THE UNIVERSITY *of* EDINBURGH

Metallosupramolecular Assemblies: Development of novel cyclometalated Pt(II) and Ir(III)-based capsules

by

Oleg Chepelin

Degree of Doctor of Philosophy

School of Chemistry

The University of Edinburgh

August, 2013

Table of Contents

Abstract and Layout of Thesis

Inspired by nature's use of self-assembled systems to carry out virtually all biological processes, chemists have taken to building simplified synthetic systems that mimic the biotic world. Although transition metal-ligand interactions are rarely used for the purpose of biological self-assembly, they have several advantages over other weak non-covalent interactions, such as pronounced directionality and significant strength. These particular attributes have allowed chemists to construct a comprehensive library of self-assembled polygons and polyhedra, using different transition metal-ligand motifs. Many of these supramolecular assemblies possess cavities of defined shape and size, which are able to accommodate guest molecules. It has further been realised that isolation of guest species from the bulk phase can lead to many interesting functions, such as containment, sensing and catalysis. Herein, a new self-assembly strategy has been used to construct novel cyclometalated Pt cages and assembly of the first known $[Ir(ppy)_2]$-based capsule has also been achieved.

Chapter 1 includes an introduction to metallosupramolecular assemblies, followed by a comprehensive review of three-dimensional architectures with accessible cavities, their synthetic strategies and applications.

Chapter 2 reports on the construction of novel Pt(II)-based trigonal prisms using an unusual, kinetically controlled protocol. By exploiting asymmetric cyclometalated 2-phenylatopyridine based platinum corner units that possess both labile and non-labile *cis*-coordination sites, trigonal prismatic stereoisomeric architectures have been selectively prepared by altering the sequence of addition of ditopic 4,4′-bipy (4,4′-bipyridine) and tritopic tpt (2,4,6-tris(4-pyridyl)-1,3,5-triazine) molecular structural components using a template free method. Collision-induced-dissociation mass spectrometry experiments were used to differentiate between the structural isomers due to their significantly different fragmentation profiles.

Chapter 3 describes the synthesis and characterisation of the first molecular capsule based on an $[Ir(ppy)_2]^+$ 90° metallosupramolecular acceptor unit. Initial work focused on pyridine-based donor ligands from which an Ir_2L_2 metallamacrocycle was assembled. However, when the highly conjugated tpt "panels" were used, due to postulated constraints in the dihedral angle, self-assembly of the Ir_6tpt_4 octahedral was

unsuccessful. The constraints in the dihedral angle were eliminated by swapping pyridine for nitrile-based ligands and following the development of a method to resolve *rac*-[(Ir(ppy)$_2$Cl)$_2$] into its enantiopure forms, homochiral Ir$_6$tcb$_4$ (tcb = 1,3,5-tricyanobenzene) octahedral capsules where realised. Photophysical studies on the Ir-capsules have shown that the ensemble of cooperative, weakly coordinating ligands can lead to luminescence not present in the comparative mononuclear analogues. X-ray crystallographic analysis revealed that the Ir capsules possess cavities large enough to accommodate 4 triflate counterions. Through a series of titration experiments the ability of the capsules to act as anion sensors was also exposed.

Further exploration into the *host-guest* chemistry of the Ir$_6$tcb$_4$ capsule is reported in Chapter 4. Subsequent experiments have shown that self-assembly is highly dependent on the counterions associated with the system. While a number of different anions (OTf^-, BF_4^-, ClO_4^-, PF_6^-) facilitate the formation of the same octahedral scaffold, when triflimide was employed as a bulkier counterion, no capsule was observed. On subsequent addition of smaller counterions, such as triflate, the same Ir$_6$tcb$_4$ cage assembles, demonstrating that the anions also act as templates. Kinetic stability experiments, undertook by monitoring the rate of scrambling of the *Δ* and *Λ*-[Ir(ppy)$_2$]$^+$ components within the preformed ensembles, show that the Ir capsules are up to 1.4×10^4 times more stable than their mononuclear analogues. The counter anions were also observed to play a crucial role in the capsule's stability with measured scrambling half-lives ranging from 4.7 mins with tetrafluoroborate to as long as 4.5 days with triflate. In contrast, the rate of ligand exchange in simple mononuclear complexes, as ascertained using EXSY NMR experiments, was found to be approximately independent of the associated anion.

Declaration

The scientific work described in the present thesis was carried out in the School of Chemistry at the University of Edinburgh between September 2009 and August 2013. Unless otherwise stated, it is the work of the Author and has not been submitted in whole or in part for any other degree or professional qualification at this or any other University or institute of learning.

Signed:……..

Date:……..

Meetings Attended and Presentations Given

1. Organic Research Seminars, School of Chemistry, University of Edinburgh, UK, 2009-2011.

Oral presentations:

a) *Multifunctional Metallosupramolecular Assemblies*, November 2009.
b) *Sequential, Kinetically Controlled Synthesis of Metallosupramolecular Stereoisomeric Assemblies*, February 2011.

2. School of Chemistry Visiting Speaker Colloquia, School of Chemistry, University of Edinburgh, UK, 2009-2013.

3. RSC Perkin Division 39th Scottish Regional Meeting, University of Edinburgh, UK, December 2010.

Poster presentation: *Sequential, Kinetically Controlled Synthesis of Metallo-supramolecular Stereoisomeric Assemblies*.

4. Mini-Symposium in Supramolecular Chemistry, Heriot-Watt University, UK, November 2011.

5. RSC Perkin Division 40th Scottish Regional Meeting, University of Edinburgh, UK, December 2011.

6. RSC Macrocyclic and Supramolecular Chemistry Meeting, University of Bath, UK, December 2011.

Poster presentation: *Cyclometalated Iridium(III) Supramolecular Assemblies*.

7. School of Chemistry, Organic Section Firbush Symposium, Firbush Point Centre, University of Edinburgh, UK, April 2012.

Oral presentation: *Coordination Driven Capsules and Cages*, April 2012. Awarded runner-up prize.

8. Mass Spectrometry (3 day course):- Principles and Practices in the 21st Century, School of Chemistry, University of Edinburgh, UK, May 2012.

9. School of Chemistry, PhD Prize Symposium, University of Edinburgh, UK, May 2012.

Oral presentation: *Coordination Driven Photoactive Ir(III) Capsules*. Awarded runner-up prize.

10. Universities of Scotland Inorganic Chemistry Conference (USIC), University of St Andrews, UK, August 2012.

Poster presentation: *Enantiopure Phenylatopyridine Iridium-Based Coordination Capsules; Remarkable Cooperative Enhancement of Luminescence Properties*.

11. Young Chem, International Congress of Young Chemists, Gdańsk, Poland, October 2012.

Oral presentation: *Coordination Driven Photoactive Ir(III) Capsules*.

12. RSC Perkin Division 41st Scottish Regional Meeting, University of St Andrews, UK, December 2012.

13. RSC Macrocyclic and Supramolecular Chemistry Meeting, Queen Mary, University of London, UK, December 2012.

Poster presentation: *Luminescent, Enantiopure, Phenylatopyridine Iridium-Based Coordination Capsules*.

14. 14th International Seminar on Inclusion Compounds, Heriot-Watt University, UK, August 2013.

Poster presentation: *Luminescent, Enantiopure, Phenylatopyridine Iridium-Based Coordination Capsules*. Awarded 1st prize.

Oral presentation: *Photoactive Iridium-Based Supramolecular Capsules*

Acknowledgements

First and foremost I would like to thank Dr. Paul Lusby for his overly generous support and supervision during my PhD and for giving me the opportunity to work for him in the first instance. Over the 4 years, Paul has been very enthusiastic about my research and has always been around to discuss exciting science, talk over problems and listen to any suggestions I may have, for this I am greatly thankful. I have learnt a great deal from him both in and outside the lab and I am particularly honoured for everything that he has taught me within the area of research and scientific writing for publication.

When I first started my PhD career, being thrown back into a chemistry lab after a year out was a little daunting. However, Dr. Sarah Pike stepped in and helped me immensely throughout my first year. I would also like to thank Sarah for her work on the initial cyclometalated Pt(II) system which I was able to elaborate and expand within the field of coordination capsules.

Towards the end of my first year I was joined by two new PhD students; Paul (Small Paul) Symmers and Dhassida (Top) Sooksawat. I would like to thank them both for their moral and intellectual support during the 2 years we worked together. Two other co-workers I would like to acknowledge are David August and Michael Burke who have always been free and keen to discuss research and, having only joined just less than a year ago, are already key members within the group.

I would further like to thank Dr. Lorna Murray and Dr. Juraj Bella who have been immensely helpful with NMR analysis and ensuring all the spectrometers were functioning 24/7. Without their tremendous help in extended NMR techniques and ensuring that the spectrometers were working in automation for fast analysis I would have been unable to accomplish half the work that I did.

Early on I was also fortunate enough to initially mentor and eventually work alongside Jakub Ujma on research in collaboration with Dr. Perdita Barran's group. The collaboration involved innovative mass spectrometry analysis and I owe a great deal of the success we achieved to both Jakub and Perdita. I would like to thank them both for all their help, training, encouragement and general banter that they and their fellow group members provided.

I would also like to thank; Dr. Anita Jones and Dr. Xiaohua Wu for their help and entrusting me with their spectrofluorometer, Prof. Alexandra Slawin for her X-ray crystallographic expertise and her patients in solving the structure of some very small crystals, Dr. Mateusz Pitak and Dr. Simon Coles also for their help with X-ray crystallography and solving the structure of the first Ir(III) capsule and last but not least Dr. Julien Michel for his computer skills in modelling and simulating the void space inside the molecular assemblies.

Outside research, I would also like to thank the other staff members that have made my work possible, in particular; Annette, Amanda and Rona for their help with the administrative side of things, chemical stores (Derek, Tim, Raymond, John and Sigita) for ensuring the chemicals (almost) always arrived the next day, computer services (David and Jim) for their IT support and the cleaners (Janet and co.) who created a very friendly, bright and clean environment to work in over the past 3 years, even on those dark dreich mornings.

Finally a special thank you to my fiancée Cara MacKenzie, soon to be Mrs Chepelin, who has always supported me, put up with my long stints at work and who has smiled and nodded along to my late night chemistry chat. Also, a wee special thank you to Inis Chepelin for staying encapsulated within mummy long enough to give his daddy adequate time to finish his thesis. For being such a good boy I dedicate this work to you.

Last but by no means least I would also like to thank my parents, siblings and grandparents for their patients with me over the last 10 years and for helping me emotionally and financially get this far.

Abbreviations

2,5-dppy	2,5-diphenylpyridine
4,4′-bipy	4,4′-bipyridine
acac	acetylacetonate
aq.	aqueous
biphen	2,2′-biphenoxide
bpe	1,2-bis(4-pyridyl)ethane
bpy	2,2′-bipyridine
CD	Circular Dichroism
CID	Collision-Induced Dissociation (MS)
COSY	Correlated Spectroscopy (NMR)
Cp	Cyclopentadienyl
Cp′	methylcyclopentadienyl
CSA	(+)-camphor-10-sulfonic acid
C^N	Bidentate ligand coordinating through a carbon and a nitrogen atom
DCE	1,2-dichloroethane
DCL	Dynamic Combinatory Library
DCM	Dichloromethane
dcmb	1,3-dicyano(5-methyl)benzene
DFT	Density Functional Theory
DMAP	4-dimethylaminopyridine
DMSO	Dimethylsulfoxide
DNA	Deoxyribonucleic Acid
DOSY	Diffusion-Ordered Spectroscopy (NMR)
dppp	1,3-(diphenylphosphino)propane
ee	enantiomeric excess
en	ethylene diamine
eq	equivalents
Et_2O	diethyl ether
EtOAc	Ethylacetate
EtOH	Ethanol
EXSY	Exchange Spectroscopy (NMR)
FAB	Fast Atom Bombardment
Fc	Ferrocene
h	hour(s)
HOESY	Heteronuclear Overhauser Effect Spectroscopy (NMR)
HPLC	High Performance Liquid Chromatography
i, *i* + 4	Hydrogen bonding between 2 amino acids separated by 4 residues
i, *i* + 7	Hydrogen bonding between 2 amino acids separated by 7 residues
IMMS	Ion-Mobility Mass Spectrometry (MS)
L	Ligand
$H_2\mathbf{L^1}$	2,6-diphenylpyridine
$H\mathbf{L^2}$	2-phenylpyridine
LR-FAB	Low Resolution Fast Atom Bombardment

M	Metal
$MeNO_2$	nitromethane
MeOH	methanol
MS	Mass Spectrometry
MS^n	Tandem MS with n stages of ion separation
min	minute(s)
MLCT	Metal-to-Ligand Charge-Transfer
nESI	nano-Electrospray Ionisation
NIR	Nitrogen Inversion/Rotation
NMR	Nuclear Magnetic Resonance
NOESY	Nuclear Overhauser Effect Spectroscopy (NMR)
NTf_2^-	trifluoromethanesulfonimide
OTf^-	trifluoromethanesulfonate
OTs^-	p-toluenesulfonate
Ph	Phenyl
ppy	2-phenylatopyridine
ppz	1-phenylatopyrazol
Py	Pyridine
PyH^+	Pyridinium cation
RNA	Ribonucleic Acid
RT	Room Temperature (23 °C)
tcb	1,3,5-tricyanobenzene
TCE	1,1,2,2-tetrachloroethane
tceb	1,3,5-tris(4-cyanophenylethynyl)benzene
T_d	achiral Tetrahedral (symmetry)
terpy	2,2′,6′,2″-terpyridine
TFE	2,2,2-trifluoroethanol
THF	Tetrahydrofuran
TLC	Thin-Layer Chromatography
TON	Turnover-Number (catalysis)
tpt	2,4,6-tris(4-pyridyl)-1,3,5-triazine
Δ-$TRISPHAT^-$	*Δ*-tris(tetrachloro-1,2-benzenediolato)phosphate(V)
UV	Ultraviolet (light)
Vis	Visible (light)
VT	Variable Temperature (NMR)
XRD	X-Ray Diffraction
Φ	emission quantum yield

NB: Conventional abbreviations for units and physical quantities are not included. Abbreviations used in the experimental sections that are not listed above are defined therein.

General Remarks in Experimental Data

Unless stated otherwise, all reagents and solvents were purchased from commercial sources and used without further purification. Dry DCM, $CHCl_3$ and THF were obtained by passing the solvent (HPLC grade) through an activated alumina column on a PureSolv™ solvent purification system (InnovativeTechnologies, Inc., MA). All reactions were carried out under a nitrogen atmosphere, unless stated otherwise. Column chromatography was carried out using Geduran® Silica 60 (particle size 40-63 μm, Merck, Germany) as the stationary phase, and TLC was performed on precoated silica gel plates (0.25 mm thick, 60 F_{254}, Merck, Germany) and observed under UV light. All chemical reactions involving Ag(I) complexes were carried out in the absence of light whenever possible.

All ^{1}H, ^{13}C and ^{19}F NMR spectra were recorded as stated on either the Bruker AV 500 or AV 400 instrument at a constant temperature of 298 K, unless otherwise stated. All DOSY experiments were performed on Bruker AV 400 (Topspin 2.1) using bipolar gradient pulses for diffusion with two spoil gradients (ledbpg2s.compensated) pulse sequence. The sequence was carried out under automated conditions where the duration of the magnetic field pulse gradient (δ) was 1.5 ms and the diffusion time (Δ) was 100 ms. Typically in each pulse field gradient NMR experiment, a series of 16 spectra on 32 K data points were collected and the eddy current delay (Te) was set to 5 ms in all experiments. The pulse gradients (g) were incremented from 2 to 95% of the maximum gradient strength in a linear ramp. The temperature was set and controlled at 298 K with an air flow of 400 L h^{-1} in order to avoid any temperature fluctuations due to sample heating during the magnetic field pulse gradients. The data was processed using Bruker Topspin 2.1.

Chemical shifts (δ) are reported in parts per million and referenced to residual solvent peaks (CD_2Cl_2: ^{1}H δ 5.32 ppm, ^{13}C δ 54.0 ppm; $CDCl_3$: ^{1}H δ 7.26 ppm, ^{13}C δ 77.2 ppm; $C_2D_2Cl_4$: ^{1}H δ 6.00 ppm, ^{13}C δ 73.8 ppm; CD_3NO_2: ^{1}H δ 4.32 ppm, ^{13}C δ 62.8 ppm). Coupling constants (*J*) are reported in hertz (Hz). The *J* value given per chemical shift, unless stated otherwise, refers to *J-J* spin coupling through three bonds (J_3). Standard abbreviations indicating multiplicity were used as follows: m = multiplet, t= triplet, dd = doublet of doublets, d = doublet, s = singlet, bs = broad singlet.

Mass spectrometry (MS) was performed on Q-Tof Ultima or Q-Tof 2 (MicromassWaters Corporation, Manchester, UK) mass spectrometers, using a nESI source, controlled using Masslynx v2.3 software. All the scans in the experimental are for positive ions. The samples were dissolved in DCE, TCE or $MeNO_2$ at 50-100 μM. Prior to analysis, instruments were calibrated using a solution (2 mg mL^{-1}) of sodium iodide in 50:50 water/isopropanol. Collision induced mass spectrometry measurements were performed with argon as the collision gas. nESI voltages were adjusted between 1.0 and 2.0 kV to optimize spray quality, while the cone voltage was typically set to 36 V. Source temperature was set at 80 °C. Energy of collision with inert gas was set to 1.6*z* eV (where *z* is the charge state of ion). nESI tips were prepared in-house from borosilicate glass capillaries (Kwik-Fil, World Precision Instruments Inc., Sarasota, FL, USA) using a Flaming/Brown Micropipette puller (Model P-97, Sutter Instrument Co., Novato, USA). Platinum wire (0.125 mm, 99.95% purity, Goodfellow Cambridge Ltd., Huntingdon, UK) was used to apply the potential to solutions. Data were analysed using MassLynx software (v4.1 Waters Corporation). Predicted isotopic distributions were calculated using Molecular Weight Calculator Version 6.48. FAB spectrometry was carried out by the MS services at the University of Edinburgh.

UV-Vis measurements were recorded on a JASCO V-670 spectrophotometer. Data was collected over a wavelength range of 270-600 nm, at a scan speed of 400 nm min^{-1}, UV bandwidth of 1.0 nm and near IR bandwidth of 4.0 nm. Samples were measured at RT and at given concentrations using a cuvette (Starna Ltd.) with a 10 mm path length.

Elemental analysis was carried out at the School of Human Sciences, London Metropolitan University.

Chapter 1

Metallosupramolecular Capsules: design, synthetic strategies and applications

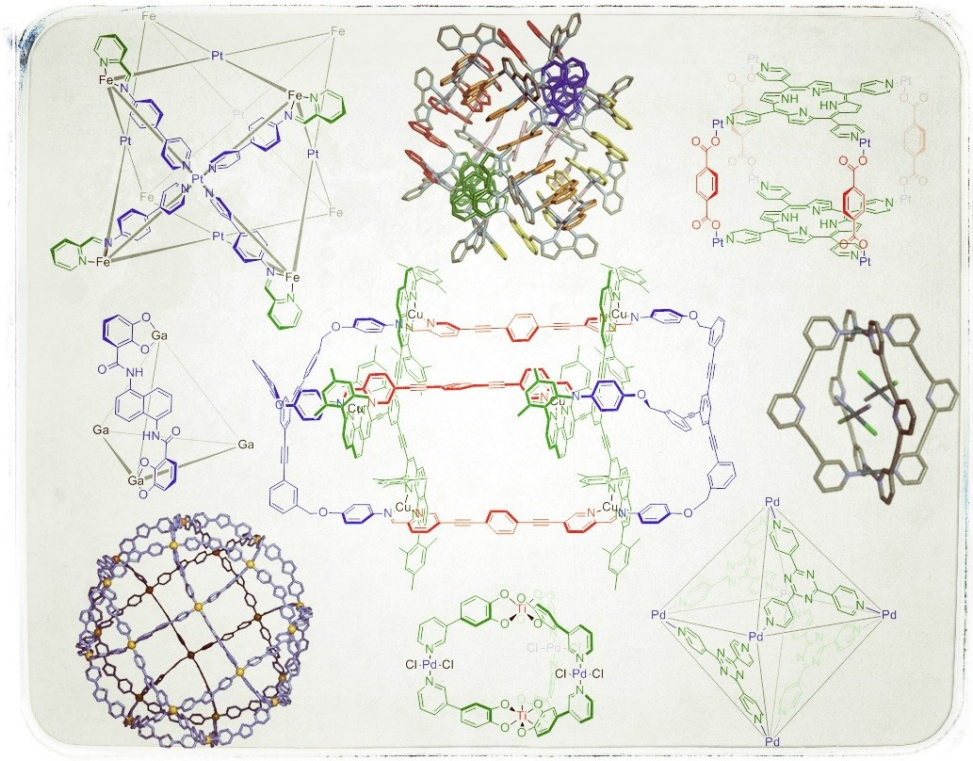

Acknowledgements

I am greatly thankful to both Dr. Paul Lusby and Dr. Christopher Campbell for proof-reading this and the following three chapters.

1.1 Synopsis

With over a 4-billion year head start, nature has developed highly efficient biological processes that rely primarily on weak intermolecular interactions. The weak, supramolecular interactions, when functioning in unison, are key in the spontaneous construction of highly specific assemblies. The ease and efficiency of self-assembly within nature has inspired chemists to build nano-sized artificial systems using abiotic strategies which mimic those found in the biological world. Initial construction primarily focused on conventional covalent chemistry to construct large molecules with complimentary hydrogen bonding motifs on the periphery that would self-assemble into discrete nano-sized architectures. However, due to the linear nature and the relative weakness of a single hydrogen bond, lengthy multi-step syntheses of the subcomponents with multiple binding sites were often required. The hydrogen-bonded assemblies were also only compatible by non-hydrogen bonding solvents and as a result the construction was often difficult and time consuming. Transition metal-ligand bonding, on the other hand, is far more versatile and with a large number of metals and ligands to choose from, with an array of different bonding angles and strengths, the number of possible assemblies is potentially limitless. Since the assembly of the first metallosupramolecular macrocycle just over 20 years ago, a vast collection of polygons and polyhedra has emerged. Initially assembled for their unique topographies, the focus has now changed to engineering and utilising these three-dimensional assemblies for various applications.

This opening chapter comprises a thorough review into discrete three-dimensional metallosupramolecular assemblies with accessible cavities, their different synthetic strategies and their many uses, in particular catalysis. The chapter also touches on the redox and photophysical properties of transition metals and how these qualities could potentially be incorporated and utilised within the supramolecular framework of the capsules.

1.2 Background

Supramolecular assemblies have evolved in biology over billions of year to function as recognition, transformation and translocation devices. Nature has utilised non-covalent molecular interactions in the form of electrostatic, hydrogen bonding, π-π stacking, hydrophobic and dispersion forces for molecular recognition and self-assembly of complex architectures. These intermolecular interactions are generally weaker than the conventional covalent bond making supramolecular assemblies potentially less stable than conventional molecular structures, kinetically more labile and geometrically more flexible. However, cooperatively, these complementary intermolecular links can form thermodynamically robust and dynamically rigid aggregates.[1]

The double-stranded helix of DNA relies on complementary base pairings to form three-dimensional supramolecular structures. Valinomycin, a naturally occurring antibiotic, transports potassium cations across the mitochondrial membrane. It too relies on multiple supramolecular interactions to bind K^+ within its macrocyclic structure for transportation through the hydrophobic environment of the membrane.[2] Enzymes, nature's nanoreactors, rely on relatively weak yet highly selective substrate recognition to promote fast reactions with high turnover numbers under mild conditions.[3] These highly proficient molecular recognition devices have fascinated and inspired the scientific community for many years, but only recently with advances in synthetic chemistry have artificial supramolecular architectures and devices started being produced.[4]

Although there are many reported organic-based three-dimensional supramolecular structures in the literature[5] this chapter will focus primarily on polyhedral architectures, with accessible cavities, assembled using metal-ligand coordination.[6] The use of these discrete assemblies as molecular containers and catalysts will also be discussed.

1.3 Three-dimensional self-assemblies

Self-assemblies are generally high order molecular structures formed by spontaneous, thermodynamically driven, enthalpically favoured rearrangement of smaller aggregates. In recent years non-covalent self-assemblies have gained great interest in

chemistry due to their aesthetically appealing architectures and potential simplicity in construction. Learning from nature, chemists started building biomimetic capsules initially using hydrogen-bonding interactions.[7] Hydrogen-bonded nano-clusters are fairly unstable and are therefore less prevalent in the literature. Their instability is generally due to a fine balance between entropic losses, due to size, versus enthalpic gains due to cooperative intermolecular interactions. The linear nature of hydrogen bonding also restricts the size of these clusters and building complexities soon became apparent. The focus thus changed to involve metal coordination.

Metal-ligand coordination is very attractive in the field of supramolecular assemblies due to three key factors:

(i) Intermolecular bonding strengths between metal centres and coordinative ligands can be tailored to range from very labile, almost dispersion-like, to very robust, covalent-like.

(ii) The well-defined geometries of metal complexes with the use of protective groups allow for angles smaller than the linear nature of H-bonding or hybridised *s* and *p* orbitals in covalent-bonds to be obtained. The 90° angle is readily accessible in square planar as well as octahedral and trigonal bipyramidal geometries.

(iii) It is generally easier and requires fewer steps to synthesise metal complexes relative to the large highly-specific ligands required in the synthesis of hydrogen-bonded systems.

Initial work on metallosupramolecular capsules used either square planar Pd(II) or Pt(II) geometries. The metal centres were exploited for their 90° angle using labile multitopic ligands while blocking of the remaining concomitant sites with kinetically inert mono- or bi-dentate auxiliaries. This method was successfully used by Fujita's group to originally build a molecular square[8] and soon after, in 1995, the first metal-directed three-dimensional cage. Stoichiometrically mixing the highly versatile *exo*-tridentate triangular 2,4,6-tris(4-pyridyl)-1,3,5-triazine "panels" (tpt)[9] with the *cis*-protected ethylenediamine palladium "connectors", $[(en)Pd(NO_3)_2]$ in an $M_3{:}L_2$ ratio, in water, led to the assembly of a discrete $M_6L_4^{12+}$ octahedral supramolecular structure **1** with T_d symmetry (Figure 1.1).[10] The presence of twelve accompanying nitrate

counteranions makes this capsule fully soluble in water, a property that has been widely exploited for the purpose of *host-guest* chemistry (*vide infra*).

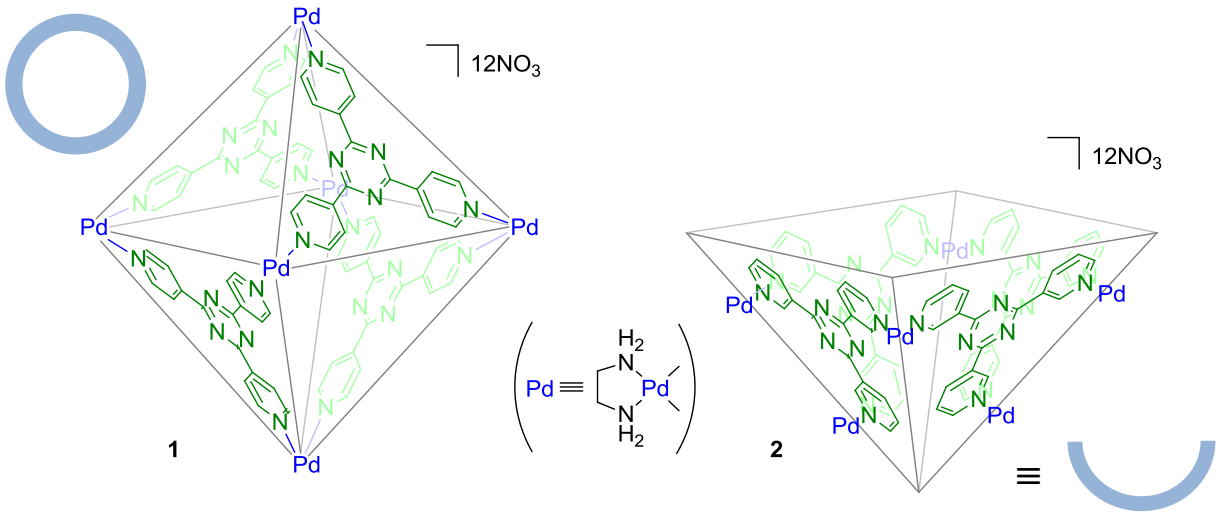

Figure 1.1. M_6L_4 prism **1** and bowl **2** reported by Fujita.[11]

By altering the *N*-donor sites on the tpt "panels" from *para*- to *meta*-, supramolecular bowl **2** could be self-assembled (Figure 1.1).[12] Interestingly, assembly **2** has also been prepared under solvent-free conditions.[13] Using a pestle and mortar, 90% isolated yields were obtained after 10 min of grinding, as opposed to 81% when heated at 70 °C in water for 30 min. The specific design of molecular polytopic "panels" of different geometries has led to the discovery of a large number of metallosupramolecular cages by Fujita's group.[11] The key to success for all these three-dimensional assemblies is the 90° angle and the dynamically rigid "panels" which ensure the assembly processes are convergent, preventing the formation of polymeric structures. The substitution of palladium(II) for the more kinetically stable platinum(II), in analogous two-dimensional assemblies, resulted in the formation of an oligomeric mixture. However when heated to 100 °C for several days, the oligomeric mixture converged into a discrete cage-like assembly which was far more kinetically robust than its palladium analogue **1**.[14]

Not all metallosupramolecular assemblies require the capping of the concomitant sites on the metal centres. For example, Shionoya's group have successfully synthesised a series of 10 different $[M_6L_8]$ cages using 10 different unsaturated metal cations with an

identical tris-monodentate ligand.[15] Using "naked" Hg(II) as the metal cation led to the formation of an M_6L_8 capsule that was coordinatively saturated. However, further addition of Hg(II) resulted in the reassembly of the M_6L_8 cage into a M_6L_4 cage constructed with unsaturated Hg(II) ions at the vertices.[16] This process was also demonstrated to be reversible by removal of Hg(II) from the system using [2.2.2]-cryptands. Other assemblies using unsaturated octahedral metal cations have also been built by Su and co-workers, using 3 or 4 rigid ditopic "clip"-like ligands with 2 metal centres.[17]

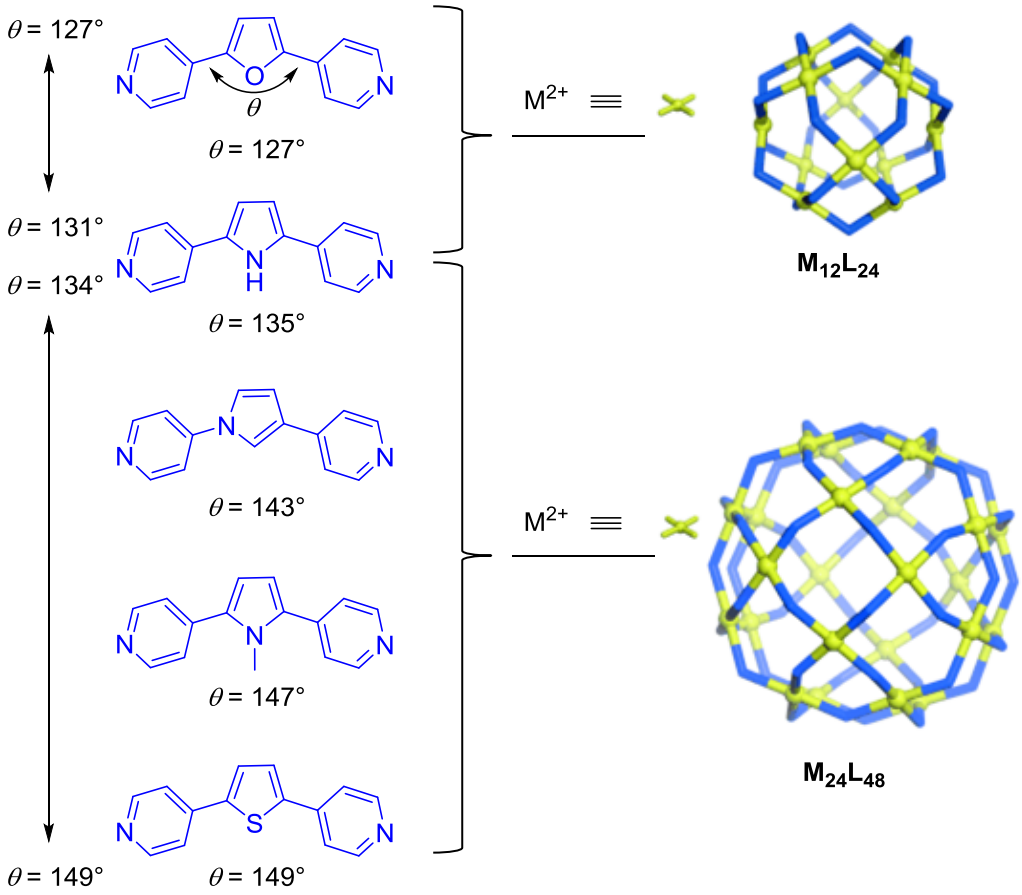

Figure 1.2. Self-assembly of $M_{12}L_{24}$ and $M_{24}L_{48}$ molecular spheres (where M^{2+} = Pd or Pt). The different angles (θ) in the di-topic ligand (L) were achieved through alterations of the central connector group. The corresponding assembly was obtained when L was mixed with M^{2+} in a 2:1 ratio. Reproduced from reference 18b.

Fujita and co-workers further demonstrated that the number of metal-acceptor sites does not have to be limited to two. By subtle alterations in the ditopic ligand coordination angle (θ), through the design of different central connector groups, Fujita

and co-workers used 4-coordinate Pd(II) or Pt(II) metal centres to assemble discrete molecular spheres as large as $M_{24}L_{48}$ (see Figure 1.2).[18]

Crowley has also utilised all four acceptor sites on Pd(II) metal centres, which when mixed with a 2 mol eq of either a ditopic pyridine ligand or a di-1,2,3-triazole "click" ligand an M_2L_4 cage or quadruply stranded helicate formed.[19] The "naked" square planar configuration of Pd(II) has also been used to build octahedral prisms using tris-*N*-donors based on a cyclotriveratrylene scaffold[20] and amide linked ligands.[21]

Stang and co-workers have developed an alternative strategy for the formation of multicomponent supramolecular assemblies which use 3 ditopic bis-Pt(II) "clips" with 2 tritopic *N*-donor ligands to assemble prism **3** (Figure 1.3).[22] The usually kinetically robust Pt(II)-pyridine bond was labilised by placing anthracene *trans* and PEt_3 ligands *cis* to the *N*-donor sites, which allowed the assemblies to form at RT. Monitoring the formation of the supramolecular entities, Stang observed initial formation of oligomeric species followed by self-correction which led to the formation of a single discrete product. Following on from the synthesis of cage **3**, Stang and co-workers constructed a plethora of discrete self-assembled architectures using a similar $Pt(PEt_3)_2$ motif.[23] Interestingly, the same group also demonstrated that when mixing multiple components in a single pot self-sorting occurred and resulted in the formation of only discrete homoleptic structures at the exclusion of less stable disordered assemblies.[24] The self-sorting processes were observed to rely on the thermodynamic preferences of the subcomponents, whereby the size of the ligands directed self-selection. In 2009, Mukherjee also reported on a very similar assembly where the Pt and N groups were interchanged to give 3 *N*-donor clips with 2 PEt_3 labilised tritopic tris-Pt(II) ligands.[25]

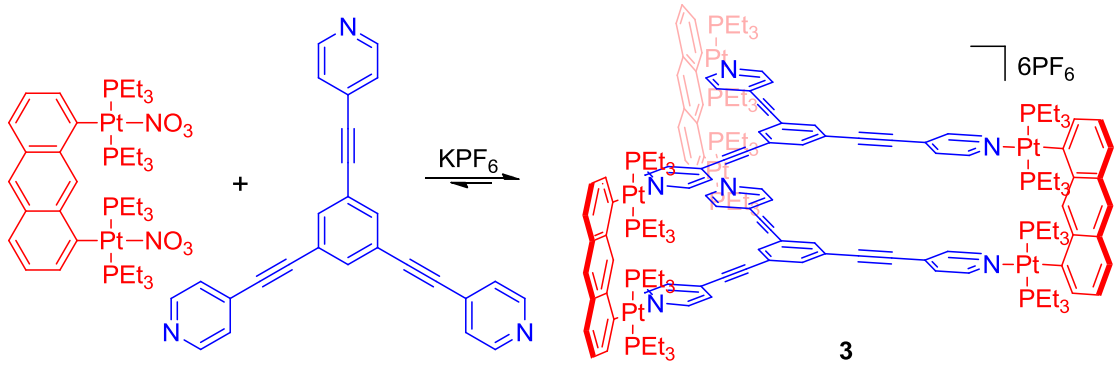

Figure 1.3. "Clip" strategy used in directing the self-assembly of **3** by Stang and co-workers.[22]

An alternative method, based on *host-guest* interactions, was first used by Fujita's group, to direct the self-assembly of more than two component metallosupramolecular systems.[26]

Host-guest chemistry involves the binding of a relatively small molecule or ion with divergent binding sites, the *guest*, to a larger framework with convergent binding sites, the *host*, *via* supramolecular interactions. Unlike self-assemblies, *host-guest* complexes are generally driven by solvophobic effects, where the encapsulation of the *guest* results in more favoured solvent-solvent interactions.[27] In nature, enzymes are probably the most famous *host-guest* systems that catalyse specific reactions by selective encapsulation of the reactive species, driven by supramolecular interactions and hydrophobic effects.[3]

Within the field of supramolecular coordination chemistry *guests* have been widely used to template the assembly of discrete architectures. In 2003 Fujita's group synthesised a prism-like cage **4** using a three-component Pt(II) system (Figure 1.4).[26] Initially when mixing the three components in a stoichiometric ratio of 2:3:6, a mixture of homoleptic Pt_4L_4 square, octahedral cage **1** and prism **4** was formed. This problem was resolved by incorporating a hydrophobic triphenylene template, which at elevated temperatures in aqueous conditions effectively drove the formation of a hydrophilic environment around itself with the self-assembly of **4**. Cage **4** showed high kinetic stability at RT, even after removal of the aromatic template. Assembly of the Pd(II)

analogue was also attempted but due to the labile nature of Pd(II) other supramolecular assemblies formed when the *guest* molecule was omitted.

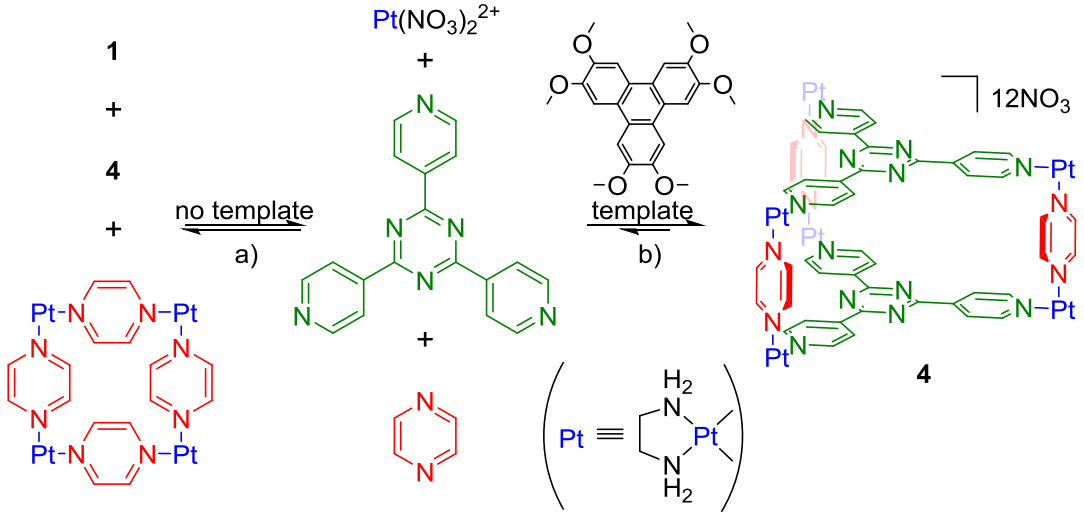

Figure 1.4. Self-assembly of trigonal prism **4** by Fujita's group. Reaction: a) without template; b) with triphenylene as template.[26]

Template-free synthesis of a trigonal prism was also achieved by adding bulky methyl groups in the *ortho*-position on a bis-pyridine ligand (see Figure 1.5).[28] This modification prevents homoleptic *cis*-coordination of the pyridine tectons due to a steric clash between the bulky methyl groups. By altering the length of the pillar ligands, Fujita and co-workers were able to lengthen the cage to allow the incorporation of multiple aromatic *guests* to form symmetrical[29] and dissymmetrical stacks.[30]

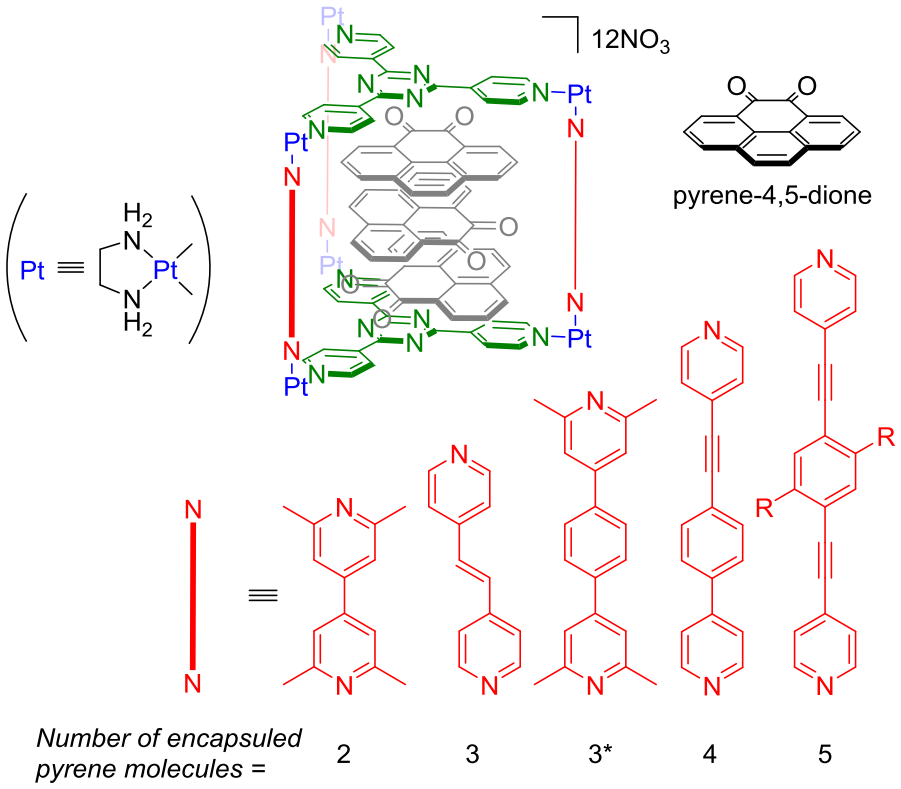

Figure 1.5. Stabilised stack of multiple pyrene based molecules within a trigonal prism of varying height. The height was adjusted using different pillared ligands of varying length as depicted above. [29] * 3 other non-pyrene aromatic molecules were encapsulated in the stack.[28] R = $OC_2H_4OCH_3$.

Recently, Stang and co-workers presented the self-assembly of a heteroleptic Pt(II) three-component tetragonal prism without the need for a template.[31] On mixing three different subunits, *cis*-$Pt(PEt_3)_2(OTf)_2$, **5a** and **5b** in a ratio of 8:4:2 a single product **5c** was formed (Figure 1.6). This spontaneous self-organisation of more than two different components, without the use of templates, is the first of its kind. The exclusive formation of **5c** without oligomerisation of the sub-units is down to the different electronic properties of the bis-carboxylate and tetrakis-pyridine ligands, **5a** and **5b**, respectively. Having two carboxylate donor groups bound in a *cis* conformation at the Pt centre was computed to be energetically disfavoured due to electrostatic repulsion between the two negatively charged groups. Although *cis*-bispyridine coordination around a square planar metal centre is common and energetically favoured, self-reorganisation occurs to maximise site occupancy, giving rise to one carboxylate and one pyridine at each metal centre.

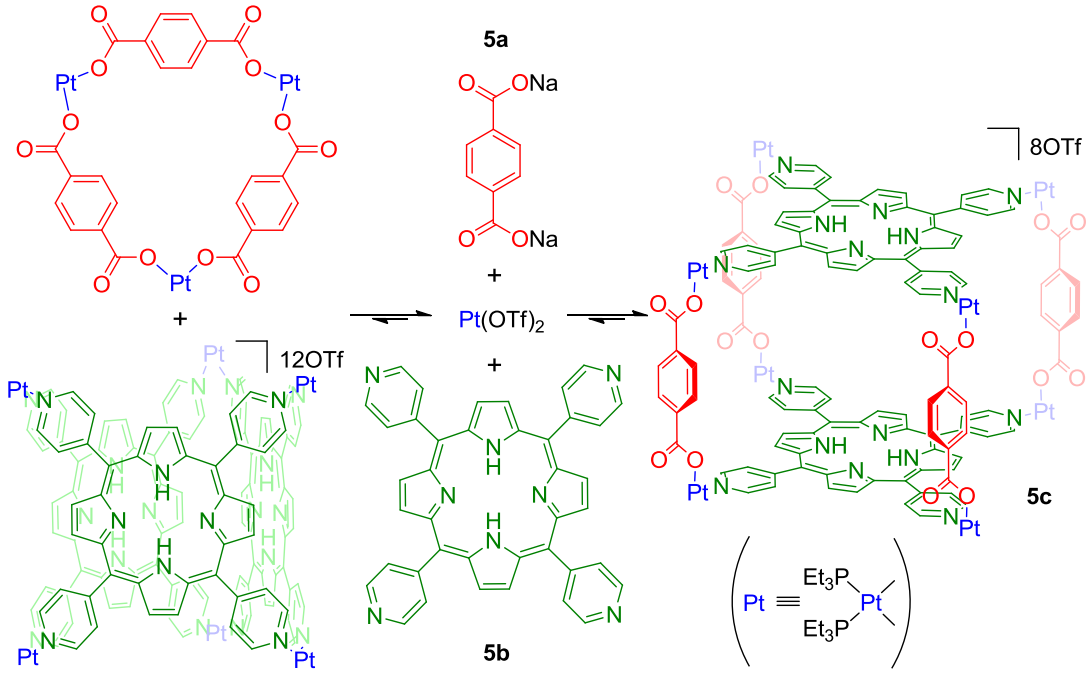

Figure 1.6. Three-component self-assembly of box **5c**. Under thermodynamic control, driven by the separation of charge at the metal centres.[31]

The charge separation strategy has also been used by Mukherjee's group in the template-free synthesis of a trigonal prism,[32] analogous in geometry to **4**, as well as Severin's group using arene "capped" Ru corner units.[33] Severin and co-workers have also used the arene "capped" Ru motif to assemble trinuclear metallamacrocycles that were linked together using dynamic covalent chemistry to form tetrahedral capsules.[34]

Often, metal-ligand interactions are either too kinetically inert, hindering the self-sorting process, or too weak, where the entropic factors for self-assembly outweigh the enthalpic gains. A number of different strategies have been applied to kinetically "lock" or "unlock" metallosupramolecular interactions, these are summarised in a comprehensive review by Thomas.[35] The following strategies used to tune the metal-ligand bond affinities are all worth bearing in mind when building three-dimensional metallosupramolecular structures:

(i) **Choice of metal**: As shown above, Pd(II) and Pt(II) complexes both have the same square planar geometry but differ in their affinity to bind ligands. Pt(II) complexes are generally more kinetically stable and form more robust supramolecular complexes, however as the Pt-pyridine bond is nearly

irreversible at RT, templates are often used in tandem to help energetically favour the self-assembly of a targeted scaffold. Likewise, the Pt-N bond can also be labilised using electron withdrawing groups in the *cis*- and *trans*-position on the metal. Within the 1st row transition metals, Fe(II), Ni(II), Zn(II) and Co(II) all favour octahedral coordination, however their affinities for ligand coordination all differ and as a consequence different assemblies are obtained.[36]

(ii) **Choice of ligand motif**: Thus far, all of the above examples have contained pyridine-based ligands. Although they are the most common monodentate ligands in the self-assembly of metallosupramolecular capsules, not too labile and not too inert, other ligands have been used in order to control the lability of the M-L bond. Metal-nitrile interactions are far weaker than those for pyridine but cooperatively self-assembly of discrete squares[37] and capsules[38] is still possible. Metal-phosphorous bonds are more kinetically inert but paired with the [Ru(tpy)Cl] motif (tpy = 2,2′,6′,2″-terpyridine)[39] or "naked" coinage metals (Cu(I), Ag(I) or Au(I))[40] spontaneous assembly of polygons and tetrahedra was respectively accomplished. Replacing labile pyridine ligands, that were used to drive discrete self-assembly, with kinetically irreversible acetylide ligands was demonstrated by Michl and co-workers as a useful technique for "locking" metallosupramolecular architectures.[41] Bidentate ligands, which generally form even stronger interactions than their monodentate counterparts, are also common in the field of metallosupramolecular assemblies. Examples that feature bidentate ligands will be discussed in the following part of this chapter.

(iii) ***Trans*- and *cis*- influence and effect**: The stability of metal-ligand bonds can be tuned simply by altering the ligand *trans* to the activated metal coordination site. σ-donor, weak-field ligands such as pyridine or amines, will stabilise, while σ-donor/π-acceptor, strong-field ligands such as carbon monoxide groups will labilise *trans*-ligands.[42] Re(I)-amine complexes are fairly inert at RT but with carbon monoxide ligands coordinated to the "capped" *trans* sites on the metal centre supramolecular assembly is achievable as demonstrated by Hupp and co-workers with their Re(I)-linked Zn-porphyrin boxes.[43] In the same manner but to a lesser extent, *cis*-effects can also be utilised to alter the binding affinity of metal complexes as

demonstrated by Stang and co-workers, who frequently use bulky, electron-withdrawing PPh_3 groups in the *cis* position to labilise Pt *N*-donor interactions.[44]

(iv) **Solvent, counterions, additives and light**: If metal-ligand bonds are relatively inert, performing the self-assembly in weakly coordinating solvents, such as THF or CH_3CN, or even under light[45] can help weaken the supramolecular interactions and enhance the rate of self-sorting. Conversely placing the supramolecular assembly in a non-coordinating solvent would lead to an inherent increase in stability. Likewise, counterion choice can dramatically alter the outcome of self-assembly. For example using weakly coordinating anions such as NO_3^- in organic solvents may allow for self-corrections to take place. Whereas replacement of NO_3^- counterions for PF_6^- may result in a mixture of different products and oligomers.[46] Coordinating additives such as 2,2,2-trifluoroethanol (TFE) have also been used by Fujita's group to temporarily labilise the Pt-pyridine bond within the self-assembly of their Pt molecular nano-spheres. Following the thermodynamically controlled self-assembly of $Pt_{12}L_{24}$, TFE was removed rendering this cuboctahedron kinetically inert.[47]

(v) **Cooperative and chelate effects**: Analogues to Velcro and DNA, a number of "seamed" supramolecular systems are stable primarily due to the combined strength of their individual intermolecular interactions.[48] Alone, these metal-ligand interactions are often readily reversible but cooperatively, stable aggregates are formed.[49] The entropic cost often heavily outbalances the enthalpic gains of a single intermolecular interaction. However, if several supramolecular interactions are present the combined enthalpic gain outweighs the relatively unchanged entropy of the system. Chelation is also an enthalpically favoured effect, giving rise to a greater number of M-L interactions without increasing the number of aggregates associated with the system.

Following on from the pioneering work by Saalfrank and co-workers,[50] Raymond's group developed a cooperatively stabilised tetrahedral M_4L_6 capsule **6** using octahedral metal centres with the chelating effect of bis-bidentate catechol ligands (Figure 1.7).[51]

Utilising the octahedral geometry of either Ga(III), Al(III), In(III), Fe(III), Ti(IV), or Ge(IV) with rigid naphthylene-amide-linked bis-catecholate ligands and a template, a racemic mixture of homochiral assemblies (*Δ,Δ,Δ,Δ* or *Λ,Λ,Λ,Λ*) were obtained. The *Δ* (or *Λ*) handedness in chirality at the metal centre would determine, due to geometric constraints, the homochiral geometry of the entire structure. Using chiral *S*-nicotinium cations resolution of the two enantiomers was possible.[52] Due to the cooperative nature of metal-ligand binding (24 metal-ligand interactions in total) assembly **6** is very robust and does not undergo racemisation even when boiled in water. Unusually for metallosupramolecular chemistry, this cage structure is anionic with a 12- charge; the presence of the 12 countercations make it water soluble, however, its large aromatic "panels" create a hydrophobic environment within the centre of the cage.

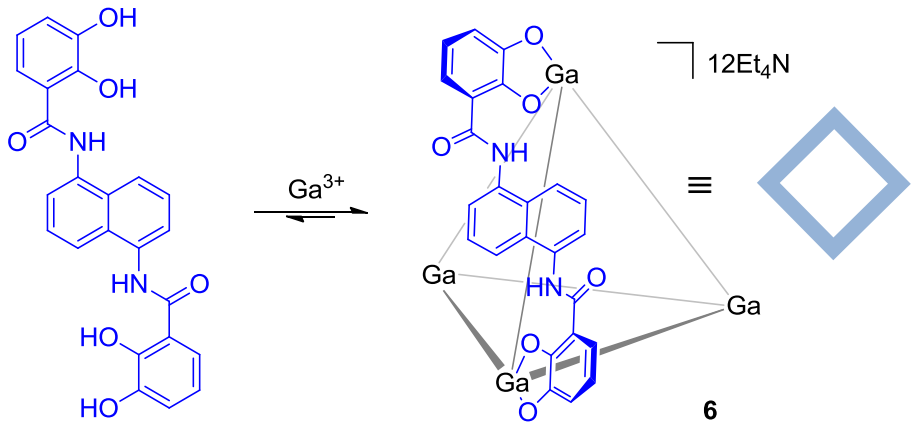

Figure 1.7. Tetrahedral homochiral [M_4L_6] capsule **6** synthesised using 6 bis-catechol ligands with 4 Ga(III) cations. Five of the six bis-catechol ligands have been removed for clarity.[51]

Symmetric [M_4L_4] clusters have also been constructed by Raymond[53] using tris-bidentate ligands and octahedral Ti(IV) or Sn(IV) metal centres and Saalfrank *et al*. using Fe(II).[54] Saalfrank *et al*. have also created a unique chiral indium *Δ,Δ,Λ,Λ*-[In_4L_4] assembly which interestingly forms from a racemic mixture of homoconfigurational (*Δ,Δ,Δ,Δ*)/(*Λ,Λ,Λ,Λ*)-*fac*-[$In_4(HL)_4$](ClO_4)$_4$ (L = tris(5,5-dimethyl-2,4-dioxohexyl)amine) stereoisomers by a simple deprotonation reaction.[55] An alternative method for the synthesis of pure homochiral clusters was reported by Cui who used chiral ligands to direct the exclusive formation of (*Δ,Δ,Δ,Δ*) or (*Λ,Λ,Λ,Λ*)-*fac* [M_4L_4] clusters with Fe(III) or Ga(III) metal centres.[56]

Moving away from tris-catecholate and other oxygen based bidentate ligands, in 2008 first Lindoy[57] and then Nitschke[58] reported on the synthesis of novel Fe_4L_6 tetrahedrons. Cage **7**, reported by Nitschke and co-workers, is formed from the *in-situ* condensation of 4,4′-diaminobiphenyl-2,2′-disulphonic acid and 2-formylpyridine to give the tris-bidentate *N*-donor ligands (Figure 1.8). The reversible nature of imine condensation gives cage **7** a unique assembly/disassembly switchable property, triggered by the pH of the aqueous solution.

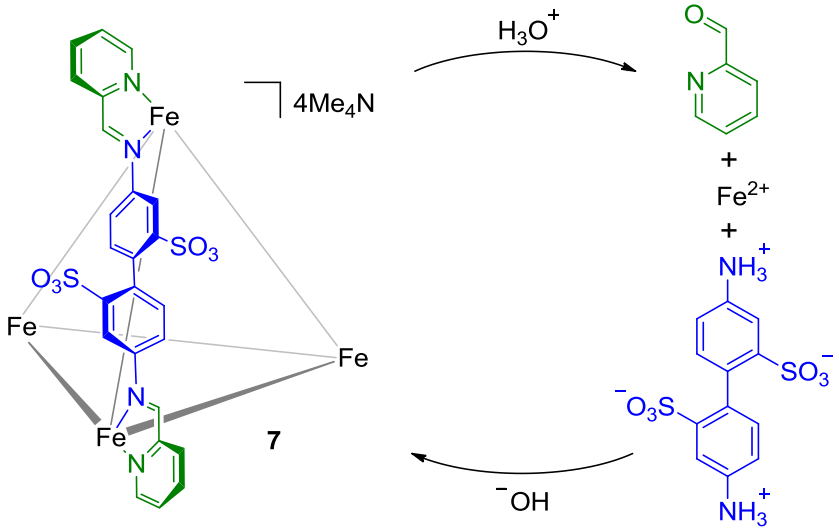

Figure 1.8. pH reversible assembly/disassembly process for cage **7** with cyclohexane as *guest* (not shown).[58] Five of the six ligands have been removed for clarity.

The "on/off" switchable property of cage **7** has led to molecular-recognition studies on the stabilisation of reactive species and capture of greenhouse gases, gold compounds and fullerenes (see section 1.4.2). Following on from the synthesis of cage **7** the Nitschke group has constructed a comprehensive library of other three-dimensional architectures all incorporating reversible bis-, tris- or tetrakis-bidentate imine-pyridine ligands.[59] The dynamic nature and sensitivity of these imine capsules to terminal amine group modification[60] and different anions and metals have been further demonstrated.[36] Exchanging Fe(II) for the more kinetically labile Co(II) and using a slightly modified bidentate ligand than the one used for the synthesis of **7** resulted in the self-assembly of a tetrahedral cage.[61] However, substituting the OTf^- counterions for ClO_4^- led to a complete geometric reassembly into a pentagonal antiprismatic structure. This pentagonal structure was also recently assembled using Fe(II) metal

centres with functionalised methoxy ligands for enhanced water solubility.[62] The self-assembly, although in equilibrium with the tetrahedral conformation during synthesis, is cooperatively "locked" at RT when isolated.

The same group also demonstrated the true capability of self-assembly with the formation of cube **8.** Using a staggering 62 subcomponents with 2 different metals in one reaction step, only a single discrete architecture formed as the thermodynamic product.[63]

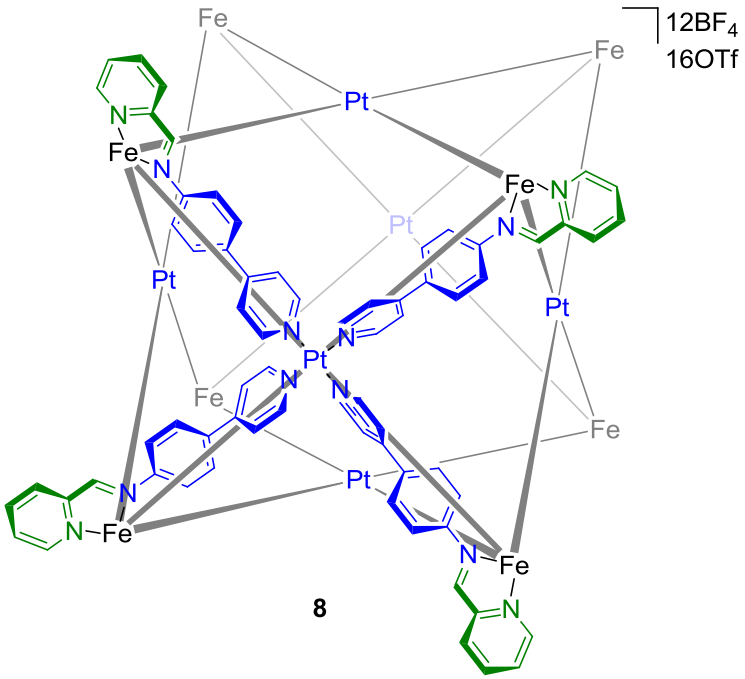

Figure 1.9. Cube **8** assembled in a single step from 62 subcomponents. Twenty of the twenty-four ligands have been removed for clarity.[63]

Recently, Schmittel and co-workers also used Schiff base condensation with the tetrahedral geometry of Cu(I) to develop capsule **9**.[64] Employing the site occupancy maximisation principle, with the use of bulky substituted phenanthroline ligands for steric control, only heteroleptic coordination was observed within the ground state (see Figure 1.10a).[65] This concept was used to build a trigonal prism with 3 bis-ditopic pyridine-aldehyde ligands and 2 tris(phenanthroline-Cu(I)) units before capping the ends with 2 trifunctional amine aggregates *via* a Schiff base condensation reaction to

form capsule **9** (see Figure 1.10b). Capsule **9** is unique in the fact that it contains one large central compartment with two smaller cavities either side.

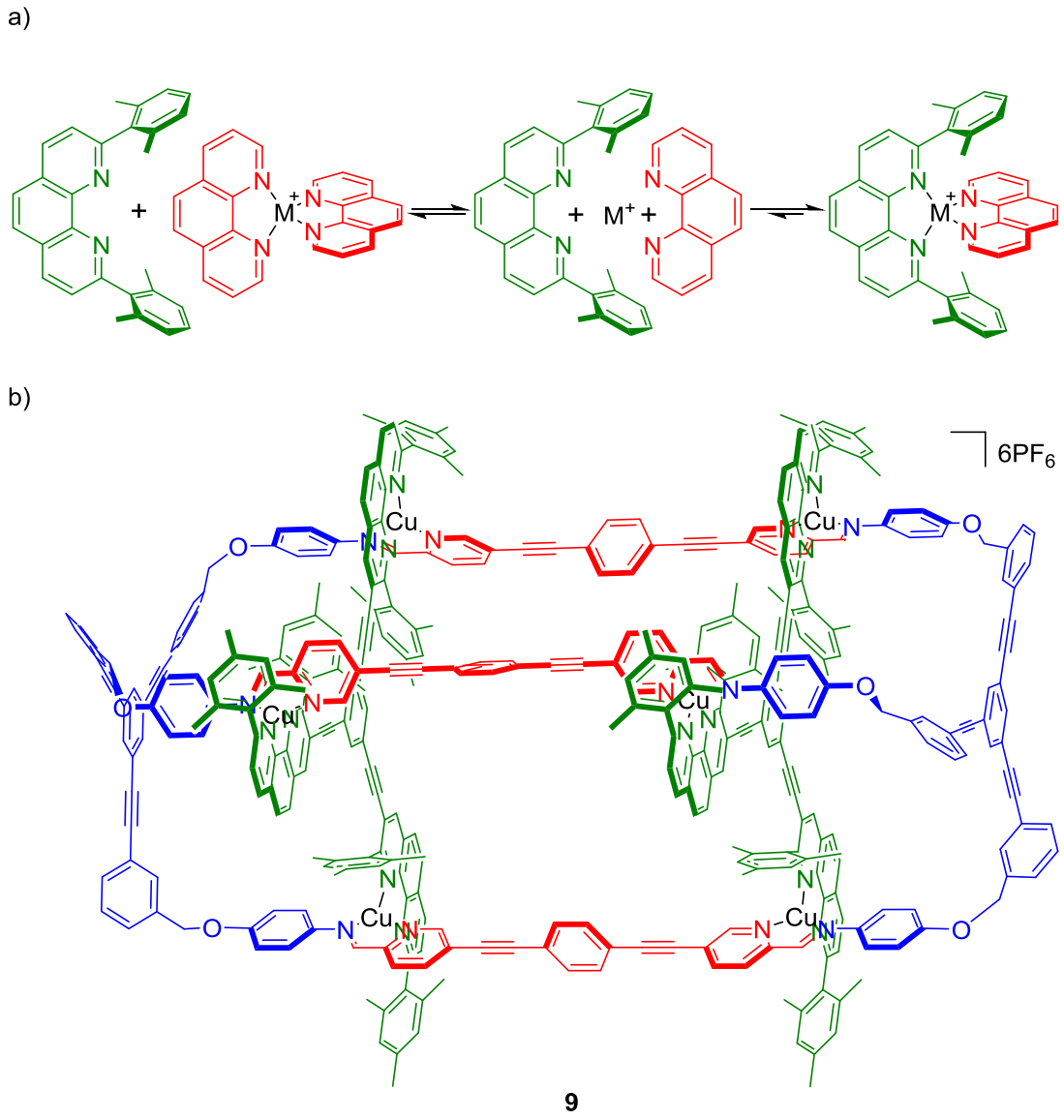

Figure 1.10. a) Illustration of how site occupancy maximisation principle with a bulky substituted phenanthroline ligand can be used to favour heteroleptic coordination. M^+ = Cu^+ or Ag^+. b) Capsule **9** with 1 large (red) and 2 small (blue) cavities.[64]

Metallo-structures using unsaturated octahedral metal centres have also been assembled by Ward, who with his team has built up a vast array of photo-active polyhedral cages using ligands with two bi-dentate pyrazolyl-pyridine *N*-donors attached to a central fluorescent aromatic group.[66] By altering the geometry of the

ligands through substitution of the central aromatic groups many different M_2:L_3 topologies were shown possible; $[M_4L_6]$ tetrahedra, $[M_8L_{12}]$ cubes, $[M_{12}L_{18}]$ truncated tetrahedral and $[M_{16}L_{24}]$ tetra-capped truncated tetrahedral. The preference for the formation of one assembly over a range of others was rationalised to be driven by secondary aromatic interactions, which were accessible due to a degree of flexibility in the ligands. The truncated tetrahedral $[M_{12}L_{18}]$ cage **10** is a good example where extensive naphthyl (electron-rich) and pyrazolyl-pyridine (electron-poor) π-stacking interactions give rise to a high-order assembly (see Figure 1.11).[67] The formation of 6 stacks, each of which contains 6 π-π interactions, enthalpically outweighs the entropically disfavoured gain in size, driving the exclusive formation of **10**.

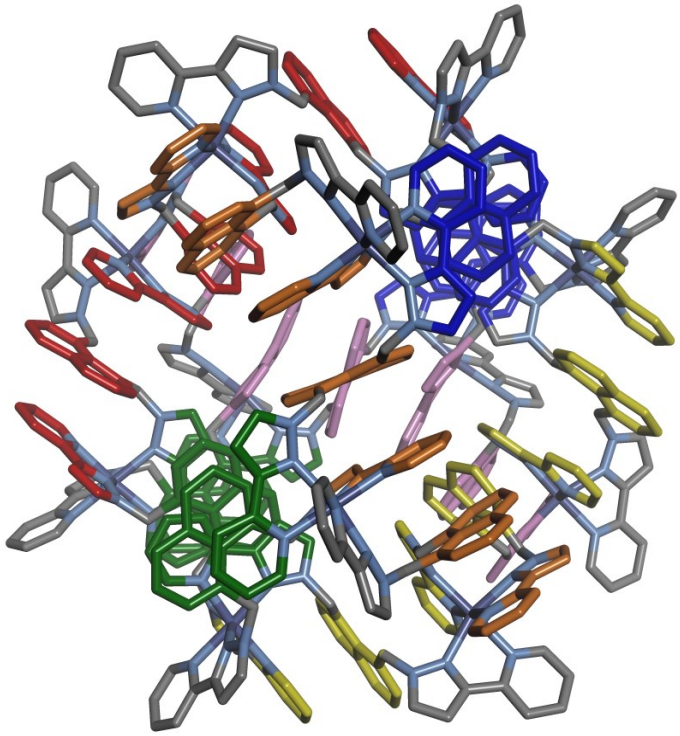

10

Figure 1.11. X-ray crystal structure of the truncated tetrahedral $[Co_{12}L_{18}]$ cage **10** with the grey carbon atoms for the 6 π-stacks are highlighted in red, green, blue, yellow, orange and pink, N atoms in light blue and Co in dark blue.[67]

The octahedral geometry of Ru(II) was also exploited by Therrien in the synthesis of metallo-prisms[68] and boxes[69]. Arenes were used as inert "capping" ligands to "block off" three of the six coordination sites on the Ru(II) metal centres. The assembly of the three-dimensional scaffolds followed the directional "clip" strategy, where ditopic

chloro-, oxalate-, benzoquinone- or thiolato-bridged arene-Ru(II) dimer "clips" spontaneously assembled with tris- or tetrakis-monodentate ligands to form the corresponding cationic prisms. By structurally altering the arene, bridging and "panelled" ligands of the Ru(II) "clips" different physical and chemical properties can be targeted, such as fluorescence detection of nitroaromatics as demonstrated by Stang's group.[70] In 2011, Therrien and co-workers reported the successful synthesis of a series of water soluble trigonal prisms **11a**-**11c** with different sized pores (see Figure 1.12).[71] Using bridged ligands of varying width (**12a**-**12c**), the pore size was altered while keeping the cavity volume constant. Cages **11a**-**11c** were used as potential drug delivery agents in a study to investigate the rate of *guest* release relative to the pore size. Unsurprisingly, out of the 3 cages, **11a** had the largest pores and the fastest *guest* release and **11c** the smallest pores and the slowest release. This work is a good illustration how selective alteration of the ligands can fine-tune the necessary chemical and physical properties targeted in an assembly.

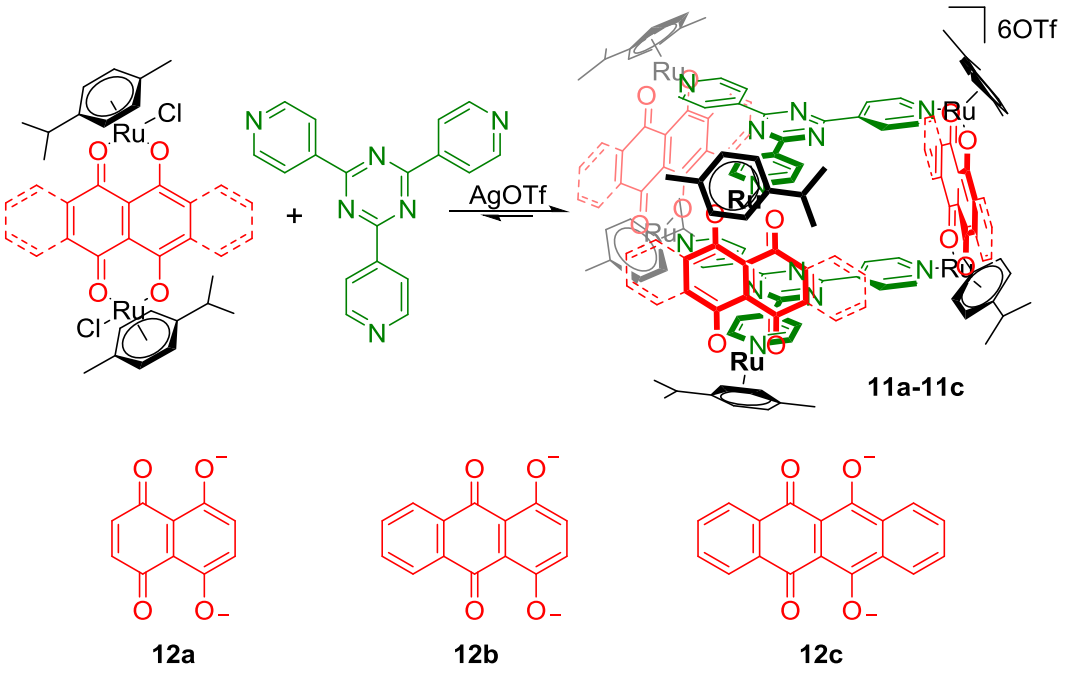

Figure 1.12. Water soluble Ru(II) prisms **11a**-**11c** constructed from 3 different corresponding bridging ligands, **12a**-**12c**, using the "clip"-strategy.[71]

In a similar manner, Jin and co-workers assembled trigonal prisms using the Ir(III) cyclopentadiene motif.[72] Self-assembly occurred in the presence of tpt driven by C-H

activation of terephthal-bis-aromatic imine ligands with $[Cp^*IrCl_2]_2$ to give a ditopic dinuclear Ir precursor. The Ir cages were similar in size and shape to **11** and encapsulation of aromatic *guests* such as $Pt(acac)_2$, pyrene, and coronene was also demonstrated.

Rhenium(I) is also known to form octahedral organometallic structures with moderately labile properties. Slone and Hupp took inspiration from nature to build the first Re-linked supramolecular Zn-porphyrin square **13** (Figure 1.13).[73]

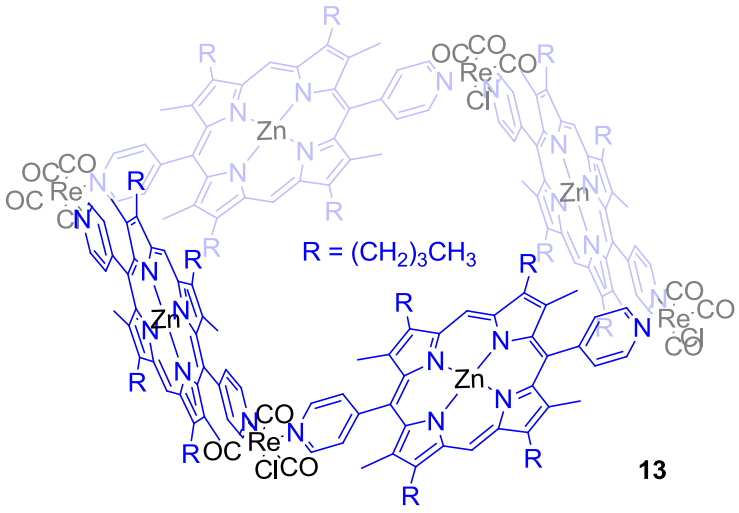

Figure 1.13. Re-linked supramolecular porphyrin square **13**.[73]

The Zn-porphyrin square is assembled using Re(I) metal corner linkers functionalised using strongly *trans*-labilising CO ligands. These molecular squares, and ultimately boxes,[74] have no charge associated with them, which has rendered their use as potential molecular sieves.[75] The molecular square **13**, although described as a two-dimensional shape, is as such three-dimensional due to the large Zn-porphyrin ligands and possesses properties that are usually associated with cage-like assemblies (see section 1.4.3). Initial attempts to synthesise a molecular box using Re as corner linkers was unsuccessful but utilising the vacant coordination sites on the Zn in the porphyrin scaffold led to the synthesis of box **14** (Figure 1.14).[74] The supramolecular structure was assembled using a 2:1 ratio of Zn-porphyrin trimers with Sn-porphyrin dimers in organic solvents. The large size of the cavity can accommodate multiple *guests* and its size, along with its asymmetry, can be adjusted by simply altering the R″ groups on the Sn-porphyrin bridging ligands.[76]

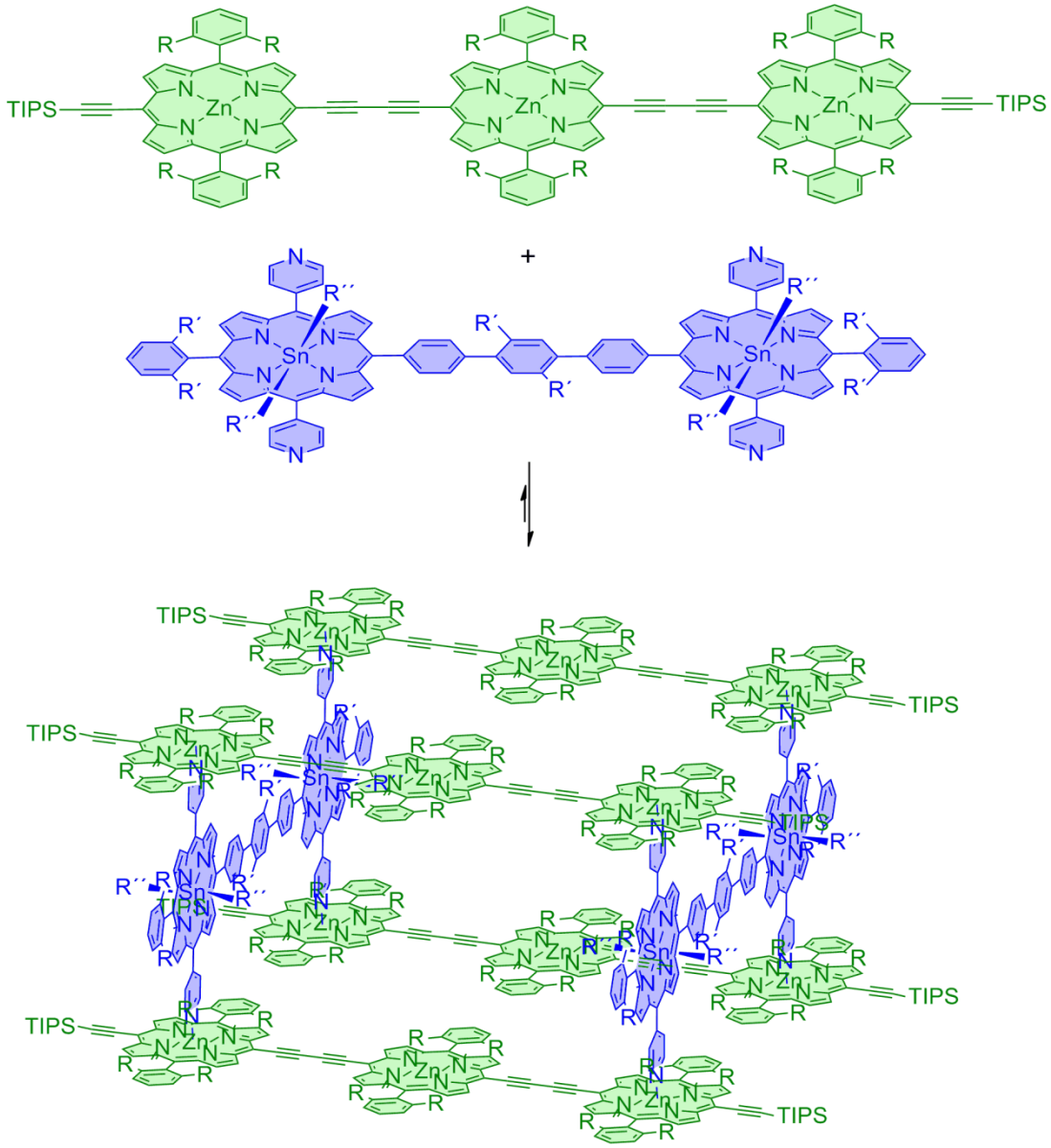

14

Figure 1.14. Rigid Zn-porphyrin box **14** as reported by Hupp. TIPS = triisopropylsilyl, R = OC_6H_{13}, R′ = OC_4H_9, R″ = 4-*tert*-butylbenzoate.[74]

Other Zn-porphyrin based assemblies have also been built by Osuka[77] and Aida[78], who both reported on two isomeric box conformations with interesting light harvesting properties.

Hupp's Zn-porphyrin metallo-assembly **14** and Nitschke's $Fe_8Pt_6L_{24}$ cube **8** are examples where more than one metal can be used to make a supramolecular capsule. The introduction of a second metal into a supramolecular array could potentially lead to unique magnetic, photoluminescent or electrochemical properties that could be accessed without the potentially tedious multistep covalent synthesis of organic ligands. By using metal centres with orthogonal binding motifs, assemblies with reduced symmetry are more easily accessible. The design principles in self-assembly of heterometallic cages tend to be very similar, whereby ligands with two orthogonal metal-binding sites are used, one soft and one hard.[70, 79] The hard donor site, such as a catechol, will fully saturate the available coordination sites of a hard metal cation, such as Ti(IV) or Ga(III), leaving the soft donor site, such as pyridine, to coordinate to a soft metal cation, such as Pd(II) or Fe(II). Reversibility in the soft donor site is still key to ensure self-correction and the formation of a discrete assembly can ensue. Ti(IV) and Pd(II) have been used in an analogous manner by Shionoya's group to construct a unique supramolecular assembly with an interconvertable structure.[80] After extensive comparative ^{1}H NMR studies on the thermodynamic stability of Ti(IV) complexes, Shionoya's team came up with a $TiHL_2(acac)$ (L = 4(3-pyridyl)catechol, acac = acetylacetonate) complex which converted into TiL_3 by selective-ligand exchange in the presence of H_2L and a strong base. By altering the basic conditions and component fraction this system was also shown to be reversible. This led to the development of a macrocyclic structure **15** that under analoguos conditions in the presence of $PdCl_2(CH_3CN)_2$ converted into a three-dimensional assembly **16** (Figure 1.15). Changing the pH with a strong acid, cage **16** could be interconverted back into **15**. The stepwise reaction pathway to **16** is under kinetic control, this was demonstrated when no single product was formed on mixing all 3 components in a single pot. The interconvertable property of cage **16** could potentially be applied as an "on/off" trigger. This stepwise ligand exchange strategy used in the self-assembly of capsules **16** has been further exploited by Shionoya, who has construct larger capsules with a further reduction in symmetry.[81]

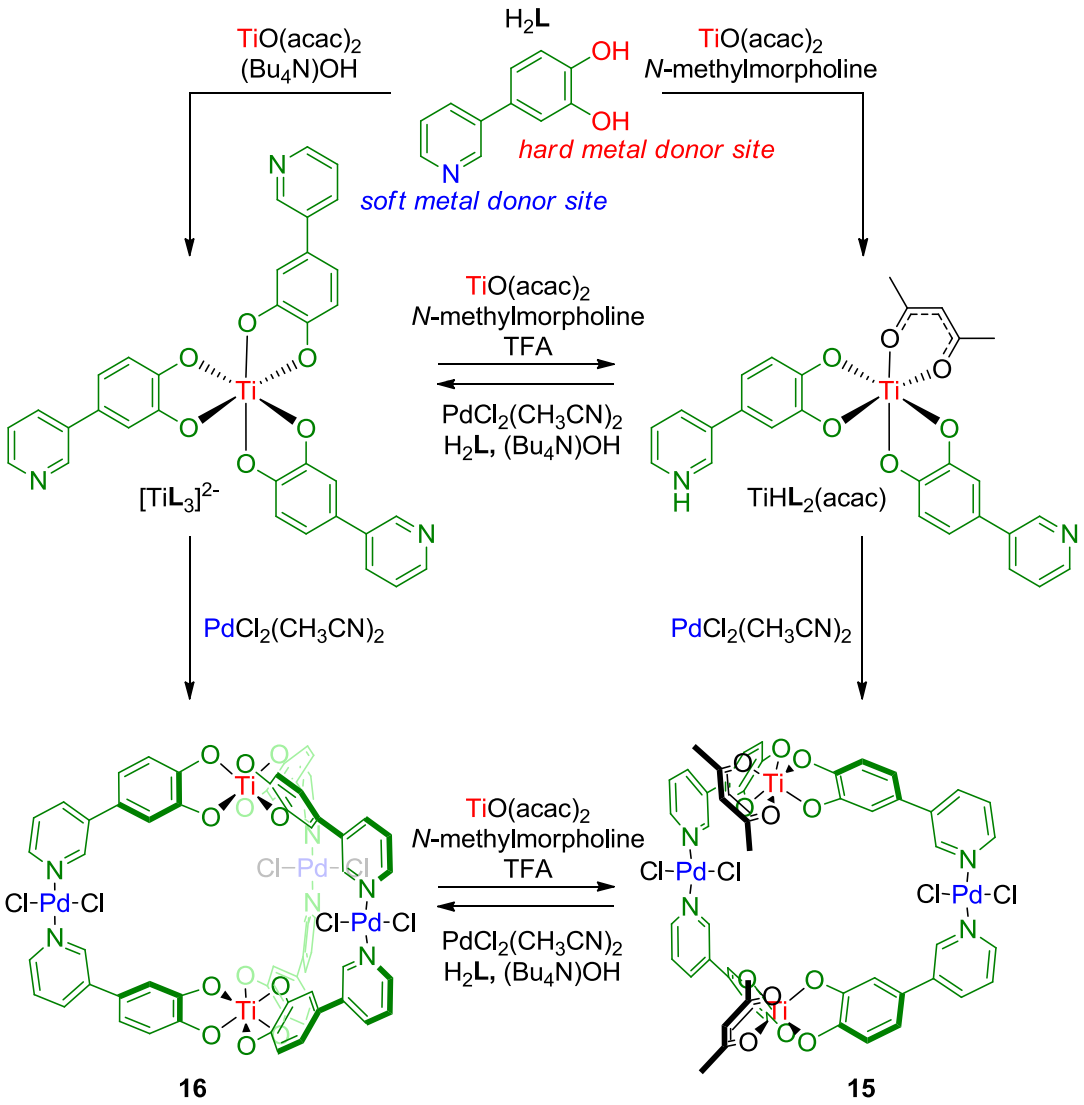

Figure 1.15. Ti(IV)Pd(II) complex with a switchable geometry between macrocycle **15** and cage **16**.[80]

A similar ligand exchange strategy has also been used by Mirkin and co-workers dubbed the "weak-link" approach. The weak-link approach uses *cis*-bidentate chelating ligands, which contain one kinetically locked bond, such as M-PPh_2, and the other a soft interaction, such as M-O or M-S, which can be broken on addition of suitable exogenous ligands. Addition of stronger coordinating ligands transforms the bidentate motif around the metal into a *trans*-monodentate interaction, expanding the assembly and producing two newly available binding sites per metal centre. Mirkin's group constructed a Rh linked macrocycle, **17**, where the bidentate phosphine and oxygen bridged ligands could be expanded by the addition of CO or CH_3CN (see Figure 1.16).[82]

The expanded forms of the macrocycle **18** and **19** could then be homocoupled to form cylindrical capsules **20** and **21** by preferential substitution of the CO or CH_3CN using 2 dinitrile or diisocyanide bridging ligands, respectively. Mirkin's group have also reported other expandable macrocycles and prisms,[83] which have been utilised, using this weak-link approach, as exogenously triggered allosteric catalysts.[84]

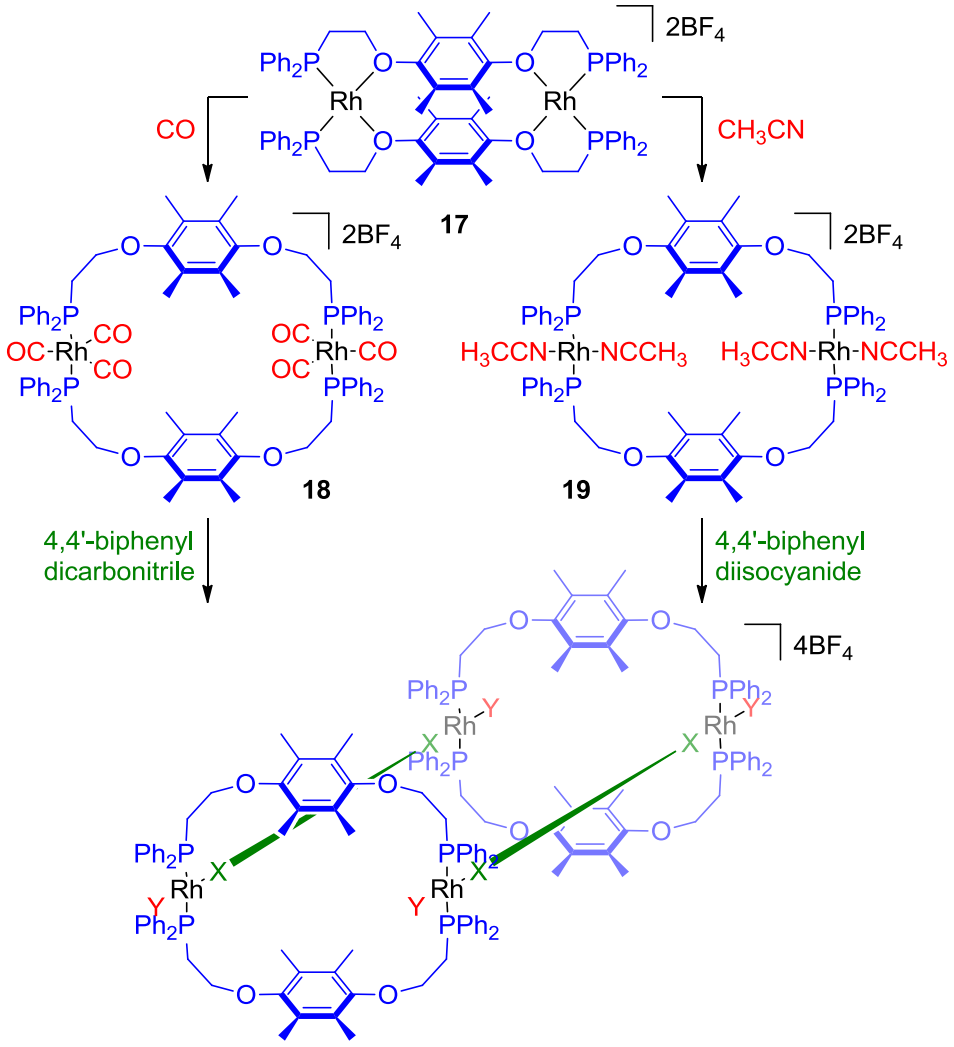

Figure 1.16. Using the weak-link approach macrocycle **17** was expanded using CO or CH_3CN to give **18** and **19**, respectively, from which cylindrical capsules **20** and **21** were assembled.[82]

All examples within this chapter were demonstrated to converge either under thermodynamic control into discrete three-dimensional assemblies (e.g. Fujita's prisms) or under a step-wise approach (e.g. Shionoya's Ti(IV)-Pd(II) cages), where a degree of kinetic control was introduced. The key strategies used to direct self-assembly of discrete entities are summarised below:

(i) **Metal choice**: Choosing a metal cation with a complimentary coordination and binding affinities for the chosen ligands is a prerequisite to successful self-assembly. For example, Nitschke demonstrated how moving across the 1st row divalent TMs produced different outcomes in self-assembly when the same ligand was used.[36] This was as a result of subtle differences in the coordination sphere and binding strength of the different metal cations. The reversibility in the metal-ligand bond is also essential for self-correction when targeting thermodynamic ground state products. Make the bond too robust or too labile and a mixture of oligomers will result.

(ii) **Ligand design**: Pre-self-assembly, ligands are often designed with pre-determined geometric information so when used in spontaneous assemblies steric hindrance prevents the formation of undesired coordination. The ligand geometry is often constrained with the use of alkynes and aromatic linkers in order to "lock" the ligand in a desirable conformation. In many instances the rigidity of the ligand has also allowed for stereochemical information to be transferred between metal centres, eradicating the formation of different stereoisomers.[51, 85] Using bulkier ligands can not only alter the ligand preference in multi-component systems but altogether prevent *cis*-coordination, as exemplified by Fujita when building multi-component prisms.[28] Hupp's group also used bulky axial ligands in the design of their box to prevent binding of the "scaffold" ligands to the inner cavity.[74] Coding the ligands with pre-determined geometrical information, along with accurate aggregate ratios, is often necessary in order to prevent oligomerisation occurring.

(iii) **Maximisation of site occupancy**: In most examples, which are under thermodynamic control, self-assembly is driven by maximisation of site occupancy with entropic and enthalpic considerations, whereby the smallest discrete assembly, which satisfies all donor/acceptor sites at a

given stoichiometry, is often preferentially formed. Depending on the number of acceptor and donor sites and the stoichiometry used within the system the size of the smallest discrete assembly sometimes turns out to be quite large, for example a triple rhomboid assembled by Stang.[86] Maximisation of site occupancy has also been referred to as "avoidance of valence frustration" by Nitschke.[87]

(iv) ***Guest*-templating**: As mentioned earlier, *guest*-templating has been used alongside thermodynamic control to kinetically "lock" supramolecular structures, however, it is more commonly used to pre-organise aggregates. When maximisation of site occupancy is not energetically favourable enough, a complimentary template can be used to lower the ground-state energy minima to a particular discrete self-assembly.[26] Demonstrated by Raymond's group in the synthesis of tetragonal prism **6**,[56] chiral *guests* can also be used as templates to selectively favour the formation of one enantiomer over the other, or as Nitschke has demonstrated using anions, one structure over another.[61]

(v) **Charge separation**: Asymmetry can be introduced into a supramolecular capsule using di- carboxylate and pyridine ligands in tandem.[31-32] Due to repulsive electronic effects of the carboxylate ligands around *cis*-protected square planar metal centres, only one carboxylate and one pyridine ligand is preferentially bound.

(vi) **Secondary inter-ligand interactions**: Although very tricky to pre-engineer within a particular self-assembly, secondary inter-ligand interactions are common within large supramolecular cages,[66] which are often formed with a degree of serendipity. The multiple secondary interactions may lead to a cooperative effect, which enthalpically favours and stabilises higher-order systems at an entropic expense.

(vii) **Site-selective ligand exchange**: Known by Stang as the "clip" strategy or by Mirkin as the "weak-link" approach, site-selective ligand exchange is a powerful technique in the directional stepwise construction of capsules that contain a reduced-degree of symmetry. The spectrochemical series is often used in this fashion, to kinetically drive the formation of desired assemblies by substitution of labile ligands (e.g. NO_3^-) for more kinetically inert aggregates (e.g. *N*-donors). However, extensive NMR analysis into the

dynamic metal-ligand exchange influenced by both the structure and properties of the metal and ligands and their combination under external stimuli is often required to build successful systems.[81]

From a growing catalogue of three-dimensional metallo-assemblies these examples were chosen due to the variety of different construction strategies used to direct and "lock" the supramolecular scaffolds. These self-assembled cages were also chosen due to their potential to act as catalysts, containers, sensors and transporters.

1.4 Functional metallosupramolecular capsules

1.4.1 Background

Initially built purely for aesthetic reasons, the focus of supramolecular design has evolved to build self-assemblies that fulfil specific applications including *guest* recognition, containment of reactive and unstable species, mediation of stoichiometric and catalytic reactions and drug carriers for biological applications.[6c, 88]

The systems to be discussed in this section all have one common key requirement which is that the metallosupramolecular assemblies are capable of encapsulating ionic or molecular *guests*.

Pioneering work in the field of *host-guest* chemistry was led by Cram who along with Lehn and Pederson received the 1987 Nobel Prize for their development and use of molecules with structure-specific interactions of high selectivity. Working primarily with covalently constructed architectures, Cram used *host* systems as containers to facilitate *guest* encapsulation and stabilise reactive and unstable aggregates by limiting the degrees-of-freedom of the *guest* within their cavities.[89]

The receptor properties of metallosupramolecular capsules were observed and the potential implications acknowledged by Fujita with the synthesis of the first capsule **1**.[10] Soon after, both Raymond[51] and Ward[90] also observed *guest* recognition of ionic species within the well-defined cavities of their respective capsules. From these studies the idea of using metallosupramolecular three-dimensional assemblies as molecular scale, size specific containers began to flourish. Their ease of synthesis and, through simple ligand and metal substitutions, adjustable dimensions and properties, were the main factors favouring the use of metal based self-assemblies as molecular vessels rather than the original covalent assemblies reported by Cram. In the same practical manner as a flask can be used in everyday life to contain, combine and store matter, these molecular capsules can be used to separate and sense materials by selective *guest* encapsulation, effectively concentrate multiple species and stabilise reactive entities by protecting them from the bulk-phase. The microenvironment of the well-defined internal cavity, due to restricted space, also has the potential to conformationally pre-

organise one or multiple *guests* such that unique phenomena, not usually present in the bulk solution, are observed.

1.4.2 Metallosupramolecular capsules as containers

Four years on from constructing their first three-dimensional self-assembly, Fujita's group began utilising cage **1** for specific applications.

In 2000 the group reported the "ship-in-a-bottle" synthesis of the short lived cyclic silanol trimer **22** by enclathration in **1** (Figure 1.17).[91]

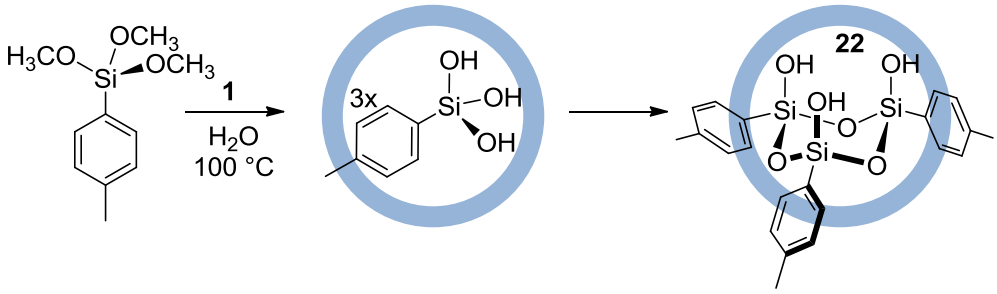

Figure 1.17. Stabilised cyclic silanol trimer **22** within cage **1**.[91]

The size specific dimension and hydrophilic cavity of **1** was ideal for encapsulation and stabilisation of three short lived phenylhydroxymethylsilane molecules hydrolysed from their methoxy derivatives prior to polymerisation in water at 100 °C. Without **1** further polymeric condensation took place. Additionally, the condensation and isolation of a specific number of trialkoxysilanes was controlled by altering the cavity size and shape of the supramolecular *hosts*.[92] This "cavity-directed synthesis" approach illustrates how supramolecular assemblies can be tailored to encapsulate a certain number of *guests* at orientations which favour specific reactions. This system is a direct mimic of the biological world where the exact product formed is pre-determined by the information encoded within the cavity size, shape and electronic properties of the enzyme.

Cage **1** has also been used to stabilise the coordinatively unsaturated 16-electron $[Cp'Mn(CO)_2]$ (Cp′ = methylcyclopentadienyl) complex **23** in order to solve a long

running debate over its coordination, which turned out to be pyramidal and not planar as originally postulated (Figure 1.18).[93]

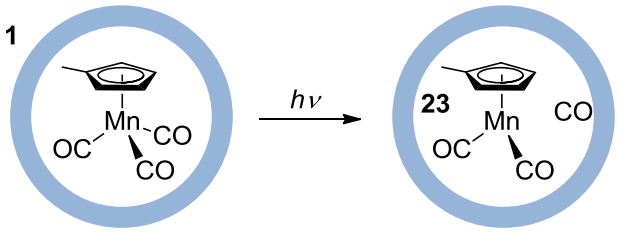

Figure 1.18. Cage **1** stabilisation of unsaturated complex **23** used to solve a long running debate over its conformation.[93]

In biology the formation of DNA duplexes under aqueous conditions is a highly efficient and specific process which is partly catalysed by the pre-organisation of base pairs within hydrophobic pockets of enzymes and partly driven by co-operative enthalpic interactions. Synthetic recognition of unstable mononucleotide duplex base pairs in water has only recently been achieved. Fujita and co-workers reported the successful stabilisation of mononucleotide duplexes in water within the hydrophobic cavity of molecular prism **4**.[94] This minimal nucleotide base pairing using artificial systems has potentially opened new synthetic routes to the synthesis of larger man-made ribosome-like transcriptional devices.

The bowl shaped assembly **2** is a more accurate representation of nature's enzymes where the hydrophobic pocket is open to bind organic molecules with no constraints on size. **2** has also been used to stabilise biological structures, such as oligopeptides as α-helices up to 17 residues long.[95] In proteins, hydrophobic cavities selectively direct the formation of α-helical secondary peptide structures through favoured intermolecular *host-guest* interactions and hydrogen bonding between the *i* and *i* + 4 residues of the peptide chains. However, outside the protein environment these polypeptides unfold due to entropic forces which outweigh the enthalpically favoured intramolecular hydrogen bonding. Bowl **2** is the correct size and shape for enclathration of *i*, *i* + 4 and *i*, *i* + 7 residues of oligopeptides, stabilising the formation of α-helices (Figure 1.19).[95c] π-π interactions between *host* and *guest* and the hydrophobic environment of this artificial enzyme is believed to be the driving force for this process.

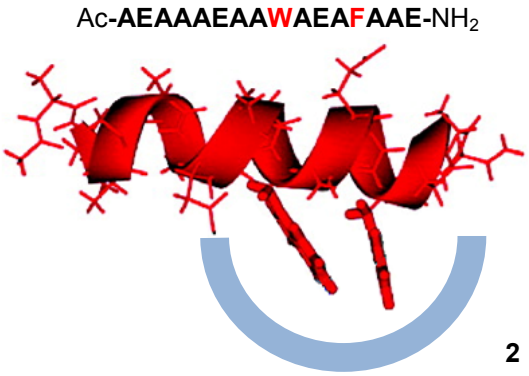

Figure 1.19. Directed formation of an α-helical secondary peptide structures within **2**. Reproduced from Ref 95c.

Raymond and co-workers have also demonstrated a wide use of applications with their anionic tetrahedral cage **6**. Water solubility, structural integrity and the ionic nature of **6** were observed to drive encapsulation of small cationic[51] and neutral[96] aggregates analogous with Fujita's cages, however, the shape, size and electrostatic properties of **6** were very different. In 2000, Raymond utilised **6** as a *host* for the quantitative formation and protection of unstable phosphonium cations in aqueous solvents.[97] Iminium cations were also stabilised in the same fashion by electrostatic driven interactions between the highly anionic cavity of *host* **6** and the positively charged cations.[98]

With a growing interest for *guest* encapsulation Raymond, in collaboration with Bergman, ran extensive experiments to establish the characteristics and mechanism for *guest* exchange within **6**.[51, 96, 99] They discovered that encapsulation depends on the size, charge, hydrophobicity and enthalpy of desolvation of the *guests* and although the different metal centres at the vertices have little conformational effect on the assembly, the encapsulated species are found to significantly distort the shape and size of the internal cavity. The encapsulation process is endothermic and driven entropically by desolvation of the *guests* through enclathration in the hydrophobic environment of the *host*. Furthermore, as the *guests* are generally too large to move freely in and out of the cavity, the process for *guest* ingress and egress was observed to occur *via* the expansion of the capsules pores and not by the rupture of the M-L bonds.

Cage **6** has also been utilised for reaction studies of nitrogen pyramidal inversion. Nitrogen inversion/rotation (NIR) within amines involves lone pair migration across the tetrahedral structure. Previously, solution NMR analysis was used to quantify the inversion free-energy barrier associated with NIR processes but due to experimental difficulties only results for amines with high inversion energy barriers were obtained. The constrained local environment of *host* **6** made the perfect tool for controlling the rate of nitrogen inversion, which along with NMR analysis was used to produce free-energy diagrams for the NIR process of monoprotonated diamines.[100]

Cage **7** has also been used by Nitschke's group to stabilise reactive aggregates.[101] White phosphorous (P_4) is highly air-sensitive and reacts with oxygen explosively to form H_3PO_4, driven by the formation of strong P-O bonds. In the presence of **7** within an aqueous solution, P_4 is encapsulated within the perfectly sized cavity by hydrophobic interactions (Figure 1.20). The stabilisation of P_4 is due to the constrained nature of the pocket which is too small for the larger P_4O_{10} to form in the presence of oxygen. Following on from the success brought about with cage **7**, Nitschke and co-workers went on to selectively encapsulate larger fullerenes from fullerene soot using a porphyrin-based cubic assembly[102] and linear Au molecules in tube-like capsules, for which encapsulation was reversible by switching the solvent.[103]

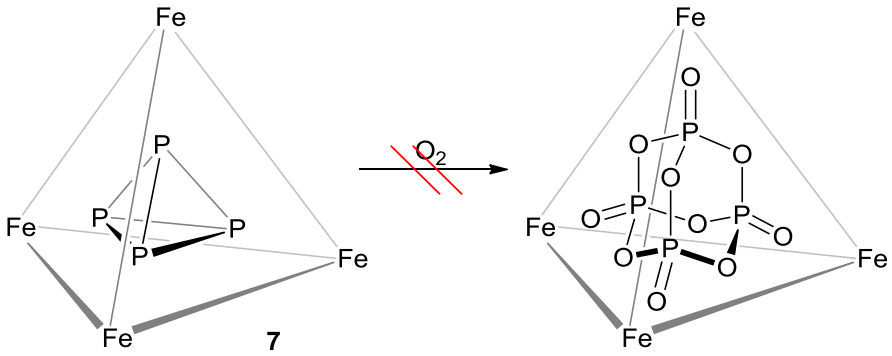

Figure 1.20. White phosphorus stabilised within cage **7**, unable to react with O_2 due to the constrained environment of the cavity.

Using *guest*-templating or steric constraints to direct the construction of Pt(II) self-assemblies at elevated temperatures, as discussed in the previous section,[26] led to the synthesis of trigonal prismatic cages of varying height (see Figure 1.5). Encapsulation of up to as many as 5 pyrene *guests* held together within a stack by their aromatic π-π

interactions was observed by Fujita and co-workers.[29] Other planar metal complexes and aromatic *guests* have also been stabilised as stacks and investigated for their unique spin crossover properties,[104] electron transport,[105] formation of metal ion arrays[106] and encapsulation of discrete polarised aromatic stacks.[107]

Likewise, Therrien's group have constructed a series of Ru-based trigonal prisms (analogous to **12**) that show an affinity for aromatic *guest* encapsulation through π-π interactions.[108] *Host-guest* chemistry studies revealed that using a large aromatic molecule, such as methyl 4-(pyren-1-yl)butanoate, results in the formation of a stable carciplex-like complex, where the *guest* is permanently bound.

Thus far, we have demonstrated how the constrained, size-specific cavity of metallosupramolecular capsules can be utilised to stabilise reactive species, intermediates and unusual products, constrain or increase the energy barrier for the rearrangement of *guests* for *in-situ* studies, selectively bind and extract aggregates from the bulk phase and permanently encapsulate *guests* to form non-covalently bonded interlocked systems. Incarceration of *guest* molecules is generally driven by hydrophobic effects in water, however, secondary intermolecular interactions are often observed in the form of Coulombic forces, π-π stacking and hydrogen-bonding.

Hydrophobically driven encapsulation within supramolecular assemblies has also been used to increase the effective molar concentration of reactive aggregates as a means to lower the reaction free-energy barriers for the formation of new products under mild conditions. The similarities between three-dimensional self-assemblies and enzyme active sites have led to the exploitation of supramolecular cages as novel reaction vessels for unique site-selective reactions and rearrangements.

1.4.3 Metallosupramolecular capsules as reaction mediators

In 1997, Rebek *et al.* were the first group to successfully exploit the enzyme-like properties of a three-dimensional supramolecular assembly. They demonstrated how their hydrogen bonded capsule could function as a microreactor for the purpose of rate enhancement in a Diels-Alder reaction between two compatible species.[109] Driven primarily by π-π interactions within a weakly-polar organic solvent the two *guest* molecules were complementary in size and shape for encapsulation within the *host*. The encapsulation effectively increased the molar concentration of the reactive species as well as pre-organising both molecules into their reactive conformations. Although, successful in increasing the rate of reaction by an impressive 200-fold the capsule had to be used in stoichiometry quantities as product inhibition was an issue. The product was complimentary in size and shape to the internal cavity of the *host* enthalpically favouring the formation of the newly formed *host-guest* complex and preventing the cage from acting as a true catalyst.

The issue of product inhibition was explored by Fujita's group who created a system where the previously reported cage **1** was recyclable after facilitating the Diels-Alder reaction between 1,4-naphthoquinone and 2-methyl-1,3-butadiene.[110] The water-soluble nature of the cage allowed the reaction to be run in an aqueous solution which gave rise to entropically driven encapsulation of the reactive species within the hydrophobic environment of the cavity of cage **1**. The effective molar concentration and pre-organisation led to a 113-fold rate enhancement for Diels-Alder reactions under stoichiometric conditions. The orthogonal solubility properties of the *host* and *guest* allowed the formed product to be isolated from cage **1** using an organic solvent and cage **1** to be reused as a molecular flask within a new reaction.

The orthogonal solubility properties between the *host* and *guest* were utilised to a greater extent in a Wacker-type oxidation process for styrenes (Figure 1.21).[111] Using a two phase system, *host* **1** was used to mediate the phase-transfer of styrene from the organic to the aqueous phase where oxidation into acetophenone occurred in the presence of Pd(II) as co-catalyst. The formed product was readily auto-excluded from the cavity of cage **1** due to an increase in water-solubility, which allows the cage to actively function as a catalyst with a turnover-number (TON) *ca.* 13. The catalytic cycle

was completed with the re-oxidation of reduced Pd(0) to Pd (II) under aerobic condition.

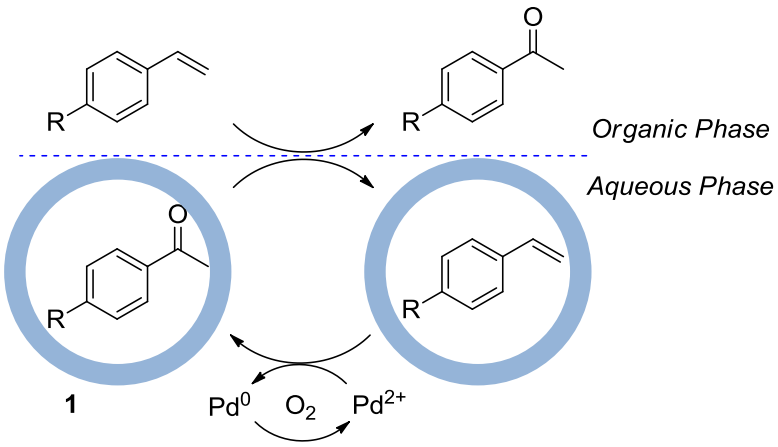

Figure 1.21. Two Phase Wacker-type oxidation of styrenes using cage **1** in the presence of a Pd(II) co-catalyst. O_2 is used to re-oxidise Pd(O).[111]

The pre-organisation capability of these molecular cages has also been shown to selectively facilitate the formation of unique regio- and stereo- selective products under cycloaddition reactions.

In solution, anthracene generally reacts with dienophiles to give the 9,10-adduct, however in the presence of cage **1** the 1,4-adduct was observed to form when using *N*-cyclohexylmaleimide (Figure 1.22).[112] The sterically constrained environment of the cavity facilitates pre-organisation of the relatively inert species into the most space saving orientations, which happens to be the ideal conformation to form the 1,4-endo-adduct *via* Diels-Alder reaction.

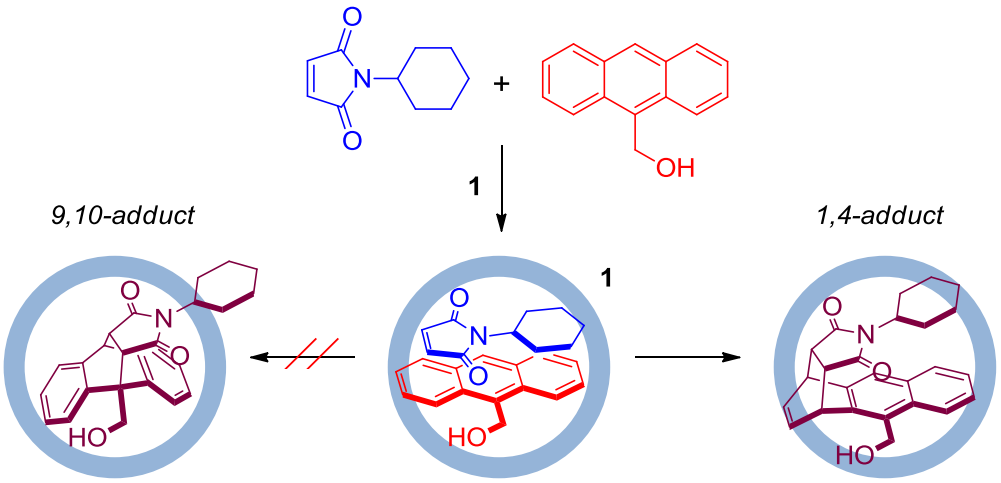

Figure 1.22. Diels-Alder reaction between *N*-cyclohexylmaleimide and 9-hydroxymethyl anthracene within cage **1** leads solely to the formation of the unusual 1,4-adduct.[112]

The geometrically constrained environment of the cavity of capsule **1** has been demonstrated by Fujita to promote other unusual, energetically disfavoured regio- and stereo- selective [2+4] cycloaddition reactions. Facilitating reactions by means of increasing the effective concentration of species using Cage **1** has not been limited to the [2+4] Diels-Alder cycloadditon, the group have also demonstrated rate enhancements in the photochemical [2+2] dimerisation reaction between heteromolecules. Originally reporting on the cross-coupling of homo-olefins,[113] Fujita went on to demonstrate that cross-photodimerisation between two different entities in the presence of cage **1** was also possible.[114] Dimerisation between two different olefins is a challenging task as the two species are often very similar in their reactivities and form a mixture of homo- and hetero- dimers. Within the hydrophobic cavity of the cage selective encapsulation of 5-ethoxy-1,4-naphthoquinone and acenaphthylene in a 1:1 ratio was observed to occur, due to the size and steric constraints of the cavity. Photoirradiation of the complex led to the exclusive formation of the *endo* dimer in 92% yield. Fujita also went on to demonstrate that the outcome of a cycloaddition reaction can be controlled by either heating or photoirradiating the reaction mixture, to give either the [2+4] or the [2+2] cycloaddition product, respectively.[115] Other photochemical cycloadditions,[116] radical additions[117] and rearrangements[118] have also been observed using cage **1** as a molecular reaction vessel.

Complete encapsulation of the reactive aggregates within molecular flasks is not crucial for reactions to take place. The bowl-shaped supramolecular assembly **2** has been used as a more efficient alternative to **1** in the photodimerisation of naphthoquinones, which led to a 98% exclusive yield of the *syn*-isomer.[113] However, as for capsule **1**, complimentary π-π and CH-π interactions between product and bowl **2** inhibit exclusion of product from the "reaction chamber" and the microreactor had to be used stoichiometrically to reach the reported yields.

Nature's enzymes that effectively increase reaction rates with high turnover numbers tend to selectively facilitate uninhibited access with complementary *host-guest* interactions to specific aggregates only. The complex structure of enzymes promotes efficient pre-organisation of *guest* entities, reducing the energy barrier to regio- and stereospecific reactions. The enzymatic cycle is completed with auto-exclusion of the product from the enzymes' open pockets, a crucial step if high turnover numbers are to be achieved.

Although the reported yields for the above reactions were high, product inhibition still remained a major problem when exploiting self-assemblies as catalysts. Fujita *et al.* have addressed this problem by successfully achieving product repulsion within the hydrophobic "open" cavity of **2** due to disfavoured product conformation. The enzyme-like hydrophobic pocket of **2** was the perfect *host* for the Diels-Alder reactions between *N*-phenylmaleimide and 9-hydroxymethyl anthracene, but rather than the 1,4-adduct being the major product when cage **1** was employed, the 9,10-adduct was exclusively formed in 99% yield (Figure 1.23).[112] This was achieved using catalyst loading at 10 mol % with an observed TON *c.a.* 10. The pocket-shape of **2** was observed to be complimentary in shape to the reactive species, pre-organising the aggregates in reactively favoured orientations. The geometry of the formed product possessed a "kink" at the 9,10-position leading to a disruption to *host-guest* π-stacking interactions as a result of a less complementary fit. Unlike the kinetically "trapped" environment of **1**, the reduced enthalpic interactions between the 9,10-adduct and **2** were over powered by the entropically favoured solvation effects, which effectively led to auto-exclusion. The destabilised "empty" cavity was re-stabilised by inclusion of further reactants, completing the catalytic cycle.

Recently, Mukherjee's group reported near identical results for the Diels-Alder reaction using a triimidazole modified bowl assembly as catalyst.[119]

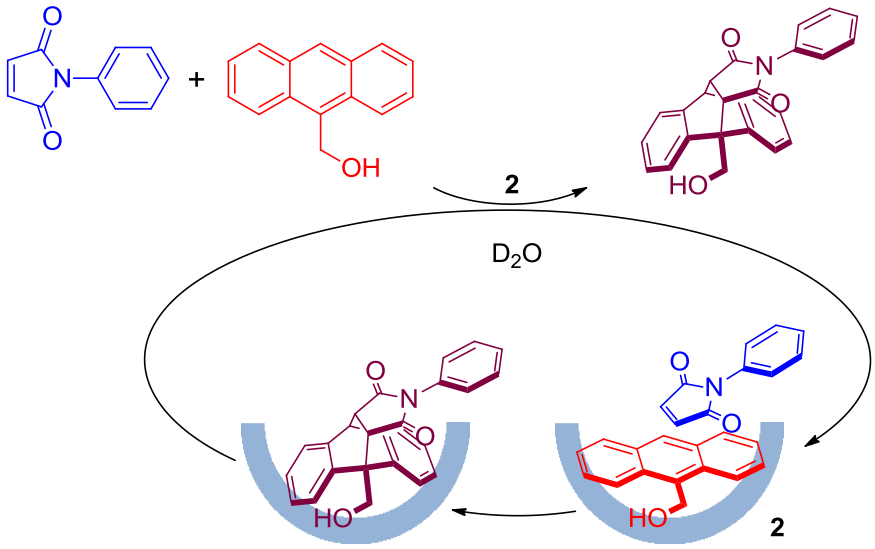

Figure 1.23. Catalytic cycle in the Diels-Alder reaction between *N*-phenylmaleimide and 9-hydroxymethyl anthracene in the presence of bowl **2**.[112]

Around the same time as Fujita, Raymond and Bergman also demonstrated the catalytic potential of prism **6** by successfully creating a catalytic cycle for the 3-aza-Cope rearrangement of enammonium cations (Figure 1.24).[120] In aqueous solutions the electrostatic attraction between the anionic *host* **6** and the cationic enammonium *guest* formed a *host-guest* complex where the constrained environment of the *host*'s cavity pre-organised the *guest* into a chair-like conformation. The chair-like geometry of the cation reduced the entropic cost for the [3,3]-sigmatropic rearrangement and reaction occurred under mild conditions. Once formed the iminium cation was preferentially replaced by an ammonium cation and hydrolysed within the bulk phase to the corresponding aldehyde, leaving prism **6** to be reused in the catalytic cycle. This system avoids product inhibition and efficient catalysis was achieved with a modest 13 mol % loading of catalyst. The aza-Cope rearrangement was also observed to obey the Michaelis-Menten model of enzyme kinetics, accelerating the reaction by a remarkable 850-fold (for R = *i*Pr, R′ = H) in the presence of **6**.[120b]

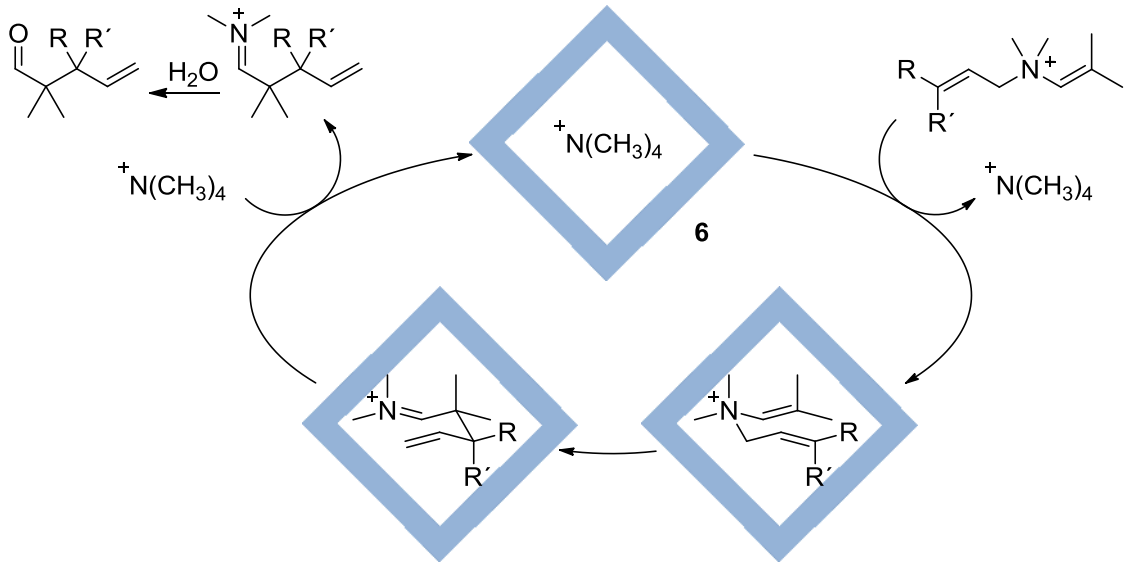

Figure 1.24. Catalytic cycle in the Aza-Cope rearrangement of enammonium cation within the cavity of *host* **6**. R = *i*Pr, R′ = H.[120]

Further catalytic cyclisation reactions with high catalytic efficiency were achieved by Raymond, Bergman and co-workers, who reported on impressive rate accelerations by up to a factor of 10^6 in the Nazarov cyclisation of pentadienols, comparable for the first time to those observed by enzymes.[121] The origin of the enzyme-like efficiency was put down to pre-organisation and stabilisation of the transition state as well as the increased basicity of the alcohol group. Inspired by enzymatic processes, the group successfully mimicked the action of terpene synthases in the cyclisation of monoterpene (±)-citronellal.[122] Under physiological pH, only the deprotonated product was observed when **6** was used as catalyst. However, in an aqueous solution, out with the hydrophobic cavity of the capsule, the hydrated form was observed as the major species. The success was attributed to the conformational control and hydrophobic environment provided by **6** in analogy to terpene synthases. Cage **6** has also been used as a highly efficient catalyst in the hydrolysis of acetals to ketones (>95% yields with 5 mol % of **6**)[123] and orthoformates to formate esters, unusually under basic condition.[124]

Recently, the full potential for these enzyme-like cage assemblies to act as environmentally benign catalysts was demonstrated in a Knoevenagel condensation.[119, 125] A reaction most commonly achieved with enzymes, Fujita and co-workers successfully used cage **1** (see Figure 1.1) to catalyse the dehydration of various

aldehydes with Meldrum's acid in a neutral homogenous aqueous solution (Figure 1.25).[125] Surprisingly, the reaction proceeded to give near stoichiometric yields with a catalytic loading of only 1 mol %. The spontaneous egress of product due to an unfavoured conformation is believed to be the driving force in this highly efficient catalytic cycle. Interestingly, no catalytic effects were observed with bowl **2**. This was attributed to the stabilisation of charge of the intermediate species by the cationic Pd(II) centres located around every portal of cage **1**.

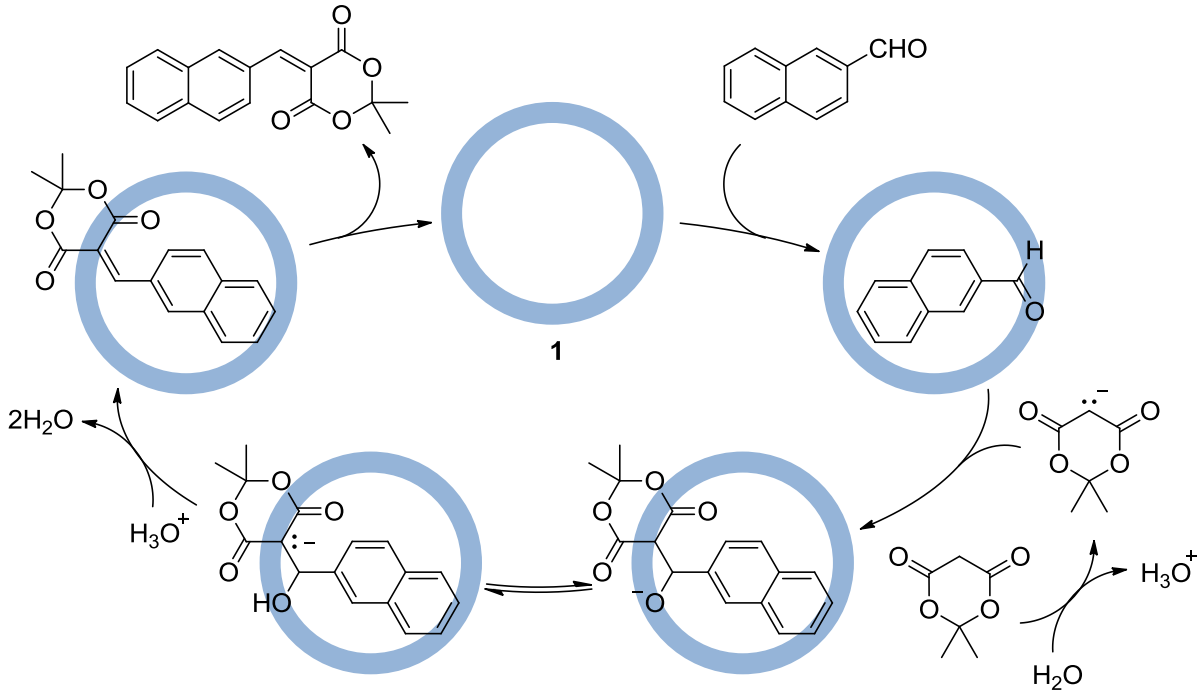

Figure 1.25. Proposed mechanism for the catalytic Knoevenagel condensation of an aldehyde with Meldrum's acid in the presence of cage **1**.[125]

Thus far, Fujita's and Raymond's supramolecular three-dimensional metallo-assemblies have been used as catalysts that have successfully facilitated a number of different regio- and stereoselective reactions in catalytic cycles with high rate enhancements and modest TONs. Another challenge in replicating the biological functionality of enzymes was to introduce chirality into the synthetic molecular flasks so that within a catalytic cycle the formation of one enantiomer of the product would be favoured over the other.

In order for self-assemblies to act as stereoselective catalysts, chiral information has to be inbuilt within the supramolecular scaffolds. Fujita's group did exactly that with cage

1 by replacing the bidentate ethylenediamine ligand of **1a** for (1*R*, 2*R*)-*N*,*N*′-dialkyle-1,2-diaminocyclohexane, **1b** and **1c** (Figure 1.26). Applying **1b** as a chiral microreactor in the asymmetric [2+2] photoaddition of 3-methylfluoranthene and *N*-cyclohexylmaleimide resulted in enantioselectivity of 50% *ee* (Figure 1.27).[126] The relatively modest enantiomeric excess was surprising as the chiral information was bestowed on the outer periphery of the cage, with little known presence in the inner cavity. For that reason it was hypothesised that the chiral auxiliaries imposed a minor geometric deformation in the triazine "panels" resulting in a chiral environment within the cavity of the cage. This system however still had the same limitations of product inhibition as observed within achiral photoaddition reactions discussed earlier.

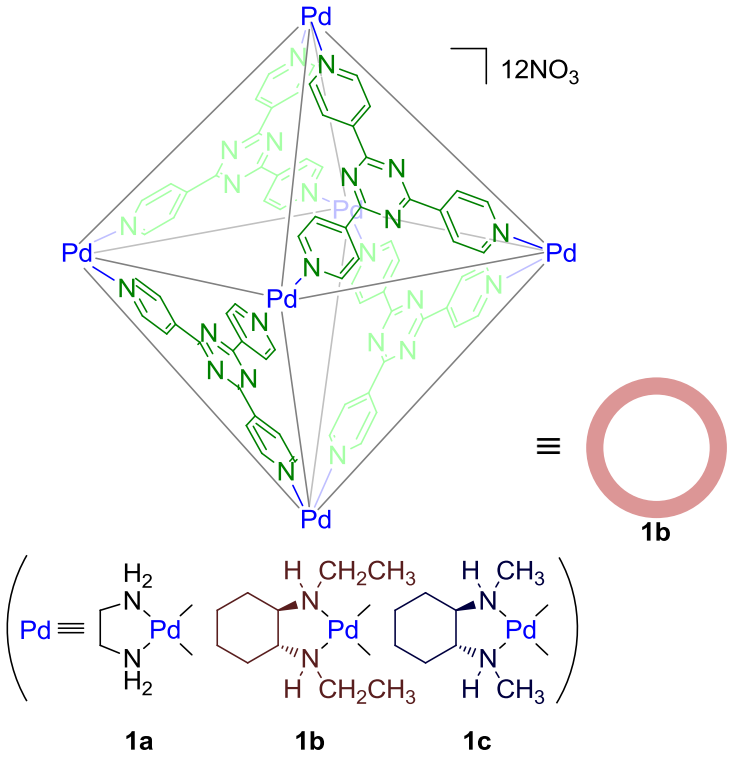

Figure 1.26. Chiral analogues **1b** and **1c** of cage **1a**.[126]

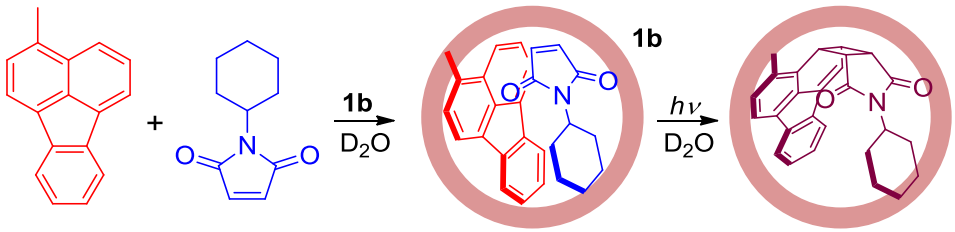

Figure 1.27. Asymmetric [2+2] photoaddition of 3-methylfluoranthene and *N*-cyclohexylmaleimide within cage **1b**.[126]

As discussed previously, tetrahedral cage **6** is chiral due to the stereogenic tris(bidentate) Ga(III) metal centre. In the presence of a chiral cation, the resolution of the *Λ* and *Δ* homochiral enantiomers was possible.[52] Chiral information transfer from **6** to substrate has recently been achieved by Raymond's group in the previously reported aza-Cope rearrangement (see Figure 1.24).[127] The aza-Cope rearrangement of emmonium cations (with different R-groups on the terminal olefin), in the presence of homochiral prism **6**, gave rise to chiral product at 78% *ee* with corresponding yields of 49%.

Hupp and co-workers took a different approach to chiral catalysis by incorporating an active achiral Mn-porphyrin catalyst (see Figure 1.28) for oxidation reactions within the chiral environment of the Zn-porphyrin square **13** and box **14**. Chirality was introduced through the R″ ligands axial to the Zn-porphyrin centres. Initially using square **13**, although an enhancement in catalytic lifetime, up to 100-fold, was observed no enantiomeric preference was visible for the epoxidation of styrenes.[128] This was believed to be due to the large torsion angles in the porphyrin "panels" of the square. Within **14** the porphyrin "panels" are far more rigid due to the geometric constrains of the box shape. In the presence of the imbedded Mn-porphyrin catalyst methyl *p*-tolyl sulphide was successfully oxidised into the corresponding sulfoxide with a modest 12% *ee* (Figure 1.29a).[76] As the active catalytic site is embedded within the constrained cavity of **14**, the size selective nature of the catalyst was also demonstrated in the preferential epoxidation of the less bulky (*Z*)-stilbene (Figure 1.29b).

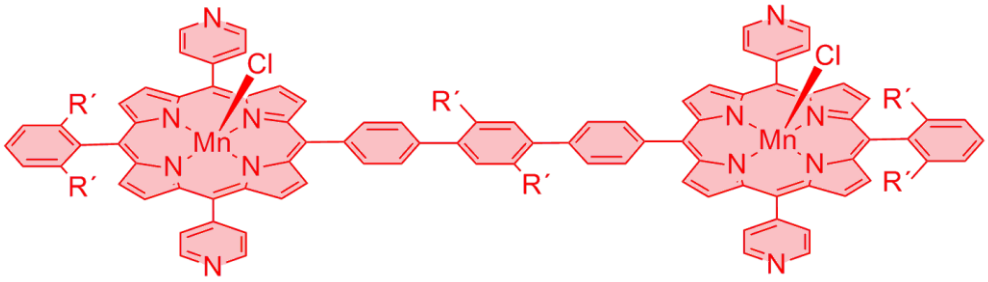

Figure 1.28. Mn-porphyrin catalyst imbedded within the cavity of **14**. R′ = OC_4H_9.

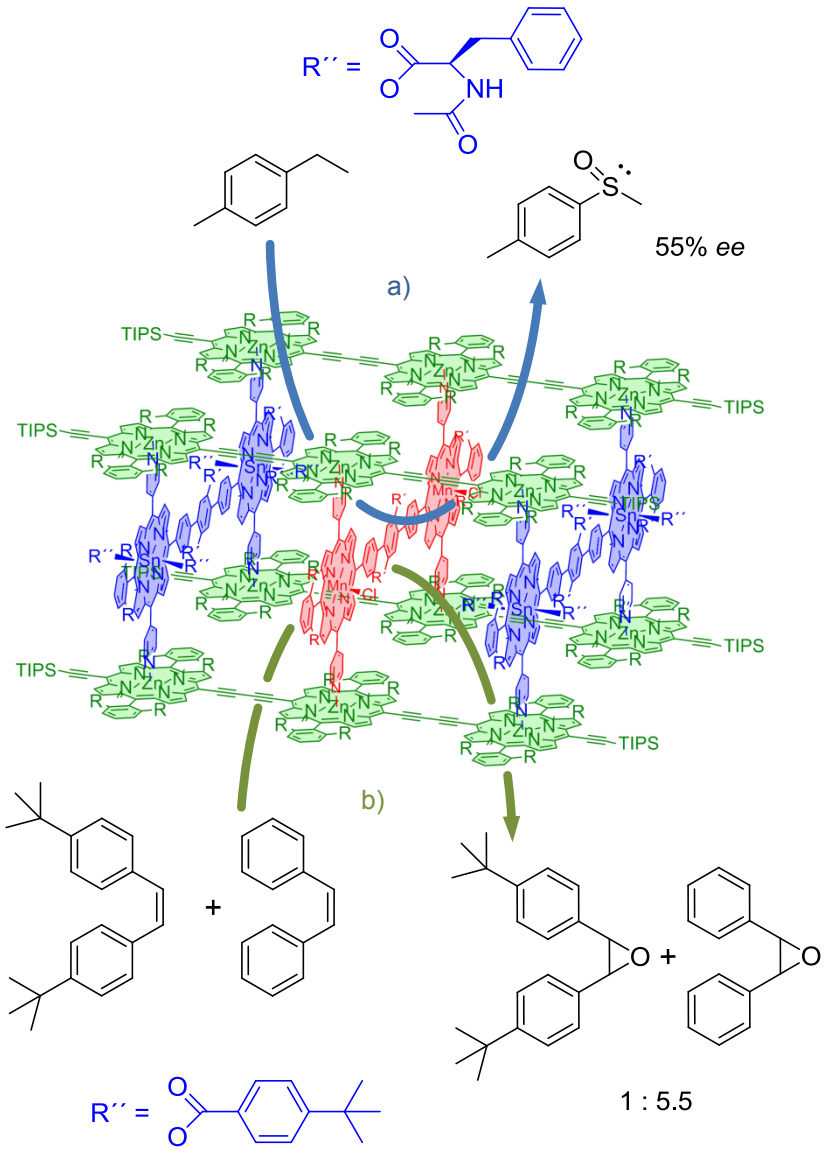

Figure 1.29. Box **14** (see Figure 1.14) used with a Mn-porphyrin catalyst (see Figure 1.28) to catalyse a) the chiral oxidation of *p*-tolyl sulphide and b) the size selective epoxidation of (*Z*)-stilbenes. TIPS = triisopropylsilyl, R = OC_6H_{13}, R′ = OC_4H_9, R″ denotes the different groups coordinated to the Sn-porphyrin ligand for reactions a) and b).[76]

This concept of incorporating an organometallic catalyst within the cavity of a molecular capsule has also been used to enhance reaction rates by increasing both the effective molar concentration of the reactive species around the active site, and selectivity, which is controlled by the well-defined cavity. First reported in a collaborative project between Raymond's and Bergman's group,[129] the size constrained chiral environment of *host* **6** with an encapsulated Ir(III) complex, was used to enhance the size and diastereomeric selectivity of C-H bond activation of various aldehydes. However, this system was stoichiometric and not catalytic due to cavity inhibition of the product. Recently, a catalytic cycle using an encapsulated Au(I)-phosphine complex within **6** for the hydroalkoxylation of allenes was accomplished.[130] Formation of the heterocyclic product was increased from 11 to 48% with the encapsulation of the $CH_3PAu(I)$ catalyst within **6**, likewise, the reaction rate was accelerated 8-fold with reported TONs as high as 67. The size- and shape-selective capability of **6** has also been used in tandem with a Rh(I) catalyst in selective isomerisation of allylic alcohols.[131]

Reaction rate enhancement and high TONs, site- and stereoselectivity and life-time durability are the main criteria by which the success of a catalyst is determined. In order to build a successful three-dimensional supramolecular catalytic system the following key points should be taken into consideration:

(i) **Concentration of reactive species**: Primarily driven by solvophobic forces, increase in the effective molar concentration of reactive aggregates within the *host's* cavity is the key concept for supramolecular cage catalysis. The hydrophobicity of the *guest* is often the driving factor in the majority of examples.

(ii) **Pre-organisation**: The constricted shape and size of the *host's* cavity guided by intermolecular *host-guest* interactions facilitates the highly selective pre-organisation of *guests* into reactive conformations. Often unusual regio- and stereo- selective reactions occur as a result. The size and shape of the cavity is pre-determined through the selective use of specific ligands and metals.

(iii) **Auto-exclusion of product(s)**: The product, if not emitted from the *host's* cavity, will inhibit any further reactions and greatly reduce the TON. Repulsion of the product has been achieved through unfavoured sterics,

repulsive electrostatic forces and increased solubility of product within the bulk phase. Without auto-exclusion the catalytic system has to be used in stoichiometric quantities.

(iv) **Chirality**: Both chiral templates and ligands have been used in the construction of chiral capsules, although in many cases, the chiral information is bound to the cage periphery with little chiral influence within the cavity. Chiral information transfer from *host* to *guest* is readily used and highly efficient within enzymes but has only recently been demonstrated possible with abiotic assemblies, however, to date the number of synthetic systems with high *ee*'s remains limited.

(v) **Charge**: The charge, which is often overlooked, has also been demonstrated crucial in some cases for stabilising ionic intermediates and facilitating auto-exclusion of product.[121, 125, 132]

Thus far, metallosupramolecular three-dimensional scaffolds have been shown to function as molecular-sized containers and reaction vessels, analogous to nature's enzymes. Despite the fact that the first abiotic metal-based capsule is nearly two decades old, it is only recently that advances in utilising these assemblies for other application have started to emerge.

1.4.4 Other applications

The notion that a chiral environment does not have to be covalently linked to the active catalyst has also been explored by Feringa *et al.* who have reported on the use of DNA linked Cu(II) assemblies in the asymmetric catalysis of a number of different reactions.[133] Enzyme-like catalysis analogous to Feringa's DNA based system has yet to be achieved with artificial self-assemblies however the arene ruthenium cage **24** reported by Therrien *et al.* has shown exactly this sort of potential.[134] Functionalised pyrene *guest* **25** (where R = propan- or butanoate) has been demonstrated to bind to the chiral *host's* cavity with a protruding "arm", capable of linking to an active catalyst (Figure 1.30). Although cage **24** is not proven to be chiral, an earlier reported trigonal prism has shown the presence of chirality in the form of a helical Bailer twist that persisted in solution without isomerism.[135]

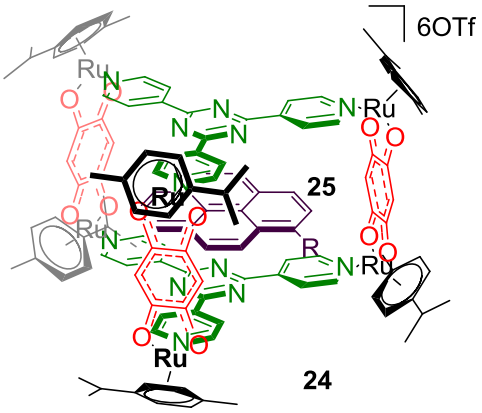

Figure 1.30. Aromatic guest **25** encapsulated within cage **24**. An R group capable of linking to an active catalyst extends outside the cavity of the *host*.[134]

Therrien and co-workers are also paving the way in utilising metallo-capsules as water-soluble drug delivery systems.[136] Incorporating cisplatin or $M(acac)_2$ (where M = Pd or Pt), potent anti-cancer drugs, into highly charged capsule **24** has facilitated "Trogen Horse-like" drug uptake into cancer cells.[134] Cage **24** was observed to be moderately cytotoxic towards human ovarian A2780 cancer cells, however, encapsulation of either the Pt/Pd complexes, or recently developed pyrenyl *guests*,[137] resulted in a significant increase in activity. The potential to functionalise the pyrenyl derivatives with better-targeting groups for specific diseases, as well as enhanced selectivity, site-specific activity and solubility is currently being investigated by the group.

Preliminary investigations into drug delivery of cisplatin by supramolecular assemblies has also recently been undertaken by Crowley and co-workers.[19b] Following the self-assembly of a water-soluble *host* **26**, two cisplatin molecules were preferentially encapsulated within the *host's* cavity, stabilised by hydrogen-bonding between the amines and the endohedral pyridines (Figure 1.31). The encapsulation of cisplatin was shown to be reversible by disassembly of cage **26** with the addition of competing DMAP ligands.

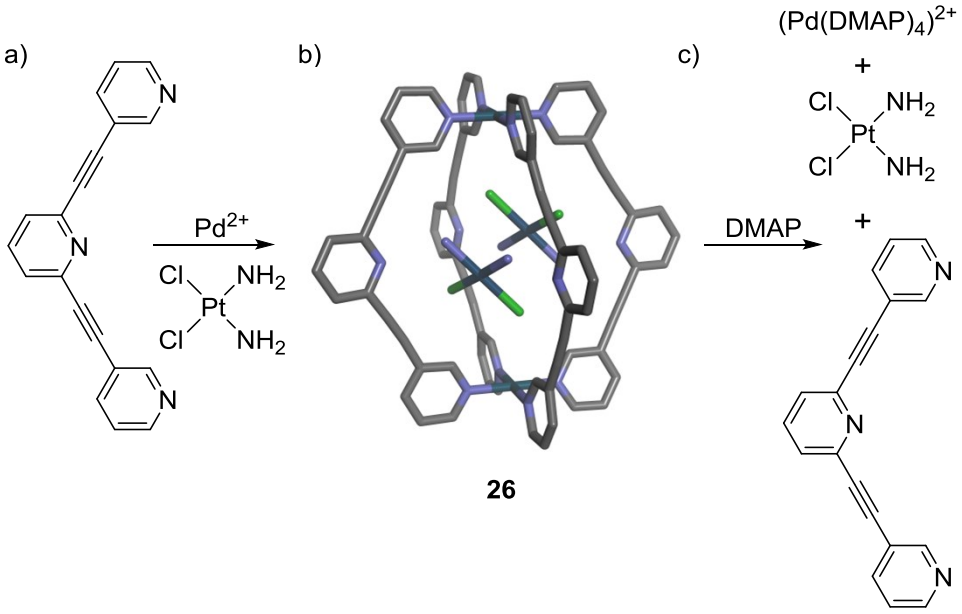

Figure 1.31. a) Spontaneous self-assembly and encapsulation of two cisplatin *guests* within cage **26**, b) X-ray crystal structure of **26** with two cisplatin *guests* and c) DMAP triggered disassembly.[19b] C atoms are highlighted in grey, N in light blue, metals in dark blue and Cl in green.

The group have recently demonstrated further potential for **26** by successfully functionalising ferrocene groups in the *exo*-position on the ligands using "click" chemistry.[138] The 1,2,3-triazol "click" moiety and ferrocene groups did not hinder self-assembly or encapsulation of cisplatin. Functionalising **26** or similar assemblies with biological targeting groups using this "click" chemistry approach could potentially lead to the next generation of very specific drug delivery systems.

Fujita and co-workers have also appended functional groups to the ligands of their $M_{12}L_{24}$ nano-capsules, but instead of sitting on the periphery the groups were attached in the *endo*-position to control the environment within the cavity. Using oligo(ethylene oxide),[139] perfluoroalkyl,[140] methyl methacrylate[141] and azobenzene[142] groups reversible La(III) absorption, fluorocarbon encapsulation and stabilisation, more efficient radical polymerisation and the control of the cavities hydrophobicity and *guest* uptake using light was respectively achieved. Recently, a glucose lined interior for these nano-spheres was also developed to favour the encapsulation of $Si(OCH_3)_4$ and $Ti(acac)_2(biphen)$ (acac = acetylacetonate, biphen = 2,2′-biphenoxide), that underwent

condensation reactions to form monodisperse SiO_2 and TiO_2 nanoparticles, respectively.[143]

1.5 Redox and optically active supramolecular assemblies

Thus far, the transition metals incorporated within the scaffold of supramolecular capsules have solely played a passive structural roll, however, transition metals are also known for their highly active redox and photochemical properties. In nature, chlorophyll in plants is probably the best known molecule for harvesting solar energy, which through a series of complicated processes transforms the captured light, *via* electrical energy transfers, into chemical energy. Envisaged by Ward,[66] utilising the metal centres within supramolecular assemblies for other applications, such as light harvesting redox-catalysis, is potentially the focal point and the next big challenge within the field of metallosupramolecular cage assemblies, yet to-date it has remained relatively unexplored.

Redox catalysis using metallo-capsules has been achieved by the likes of Su and co-workers, who reporting on C-H bond activation of various hydrocarbons using a Cu(I) cage as catalyst.[144] Although Cu(I) plays a critical role in the catalytic cycle, the only purpose the cage motif serves is in modulating the modest catalytic activity, controlled by the different associative counterions. Jung's group have also developed a water soluble capsule, $[((CH_3)_4en)Pd)_3(L)_2](BF_4)_6$ (L = 1,3,5-tris(isonicotinoyloxyethyl) cyanurate), capable of catalysing Suzuki-Miyaura C-C cross-coupling reactions without the aid of phosphine or other additives.[145] The reaction rates were enhanced when a single water molecule was encapsulated within the cavity, consistent with water-assisted effects of the Suzuki-Miyaura cross-coupling reactions. However, like the former example, the three-dimensional structure was to little advantage, as catalysis only occurred on the periphery of the cage.

Photoactive supramolecular capsules, both organic and metal containing, have also made an appearance in the literature. Mimicking the antenna modulus used for light-harvesting in biological systems, porphyrin-based self-assemblies have been extensively investigated by the Hunter,[146] Anderson[147] and Kobuke groups.[148] The first porphyrin-based three-dimensional capsules were however not assembled until

2004, when first Osuka[77] and soon after Aida[78] demonstrated the light-harvesting capability of metallosupramolecular boxes using porphyrin motif **27** (Figure 1.32). Other metal-ligand motifs that are inherently luminescent have also been used to construct optically active cage assemblies. The [$Re(CO)_3Cl$] unit **28**, reported in the self-assembly of **13**, was used by Hupp and co-workers to assemble supramolecular squares using 4,4′-bipyridine and [$M(dppp)(OTf)_2$] (M = Pd, Pt; dppp = 1,3-(diphenylphosphino)propane).[149] The Re-squares were the first reported metallamacrocycles to possess photo-excitable metal-to-ligand charge-transfer (MLCT) transitions. Sun and Lees subsequently constructed a large array of luminescent Re-base squares and triangles.[150] These metallamacrocycles were utilised as anion and small aromatic molecule sensors due to their high sensitivity to *guest* binding. Alkoxy linked Re "clips" **29** have also been used with tetratopic pyridine ligands to assemble luminescent Re-based boxes.[151] These assemblies were however only luminescent when cooled to 77 K (λ_{max} = 628 nm), due to irradiative quenching of the postulated ^{3}MLCT transitions. The first Ru(II)-based luminescent macrocycles were reported by Xu and Hong, who used a [Ru(tpy)Cl] moieties **30** (tpy = 2,2′,6′,2″-terpyridine) to assemble molecular squares and triangles.[39] The metallamacrocycles displayed ground-state absorption at 470 nm, indicative of MLCT transitions, with emission bands blue-shifted to 550 nm, relative to the mononuclear analogue at 635 nm. The two assemblies were used as sensors for 1,4-dimethoxybenzene and anisole, functioning by alterations to the luminescence quenching pathways and triggering an enhancement in emission intensity on *gues*t binding. Using similar arene-Ru(II) "clips" **31** to those used by Therrien (see Figure 1.12), Stang and co-workers assembled a series of luminescent squares[152] and trigonal prisms.[70, 153] Both MLCT within the Ru(II) "clips" and inter/intraligand $\pi \rightarrow \pi^*$ transitions between the highly conjugated pyridine-based ligands give rise to the observed luminescence, which is retained within the self-assembled scaffolds. The Ru capsules were used to detect explosive nitroaromatics, which dramatically quenched the fluorescence on encapsulation within the cavity. These assemblies were also shown to exhibit greater cytotoxicity *in vitro* then that of cisplatin. Nitroaromatic detection has also been achieved by Mukherjee's group using Pt-based prisms[25, 154] assembled using the inherently luminescent M-acetylide motif **32** (where M = Pd(II) or Pt(II)).[155] The same group also incorporated the M-acetylide motif **32** into a modified version of the Pt "clip" used by Stang (see Figure 1.3). The modified Pt "clip" was used with a linear ditopic *N,N′*-bis(4-

pyridylidene)ethylenediamine receptor ligand to assemble a luminescent rectangular assembly that was used as a sensor for 3*d* transition metal cations.[154] When a Mn(II), Fe(III), Ni(II) or Cu(II) cation was bound within the cavity of the molecular rectangle a reduction in luminescence intensity was observed due to quenching of the photoinduced electron transitions by the partially filled *d*-orbitals of the transition metals. A bis(acetylide) Pt(II) moiety has also been used to construct Pt-based squares and rectangles that display long lived phosphorescent lifetimes, with exceptionally high quantum yields.[156] The source of the luminescence within these conjugated systems is believed to be due to a combination of ^{3}MLCT excited state and $\pi \rightarrow \pi^*$ intraligand localised transitions.

Perhaps the most studied Ru(II)-based fluorophores are the polypyridyl Ru(II) **33** complexes.[157] However, possibly due to the kinetic lability of the Ru-pyridine bond, there have been very few reported supramolecular assemblies incorporating this moiety.[158] Likewise, $[Ir(ppy)_2]^+$ **34** complexes are known to be highly luminescent,[159] yet, as for $[Ru(bpy)_3]^{2+}$, very few examples of their use as supramolecular assemblies have appeared in the literature.[160]

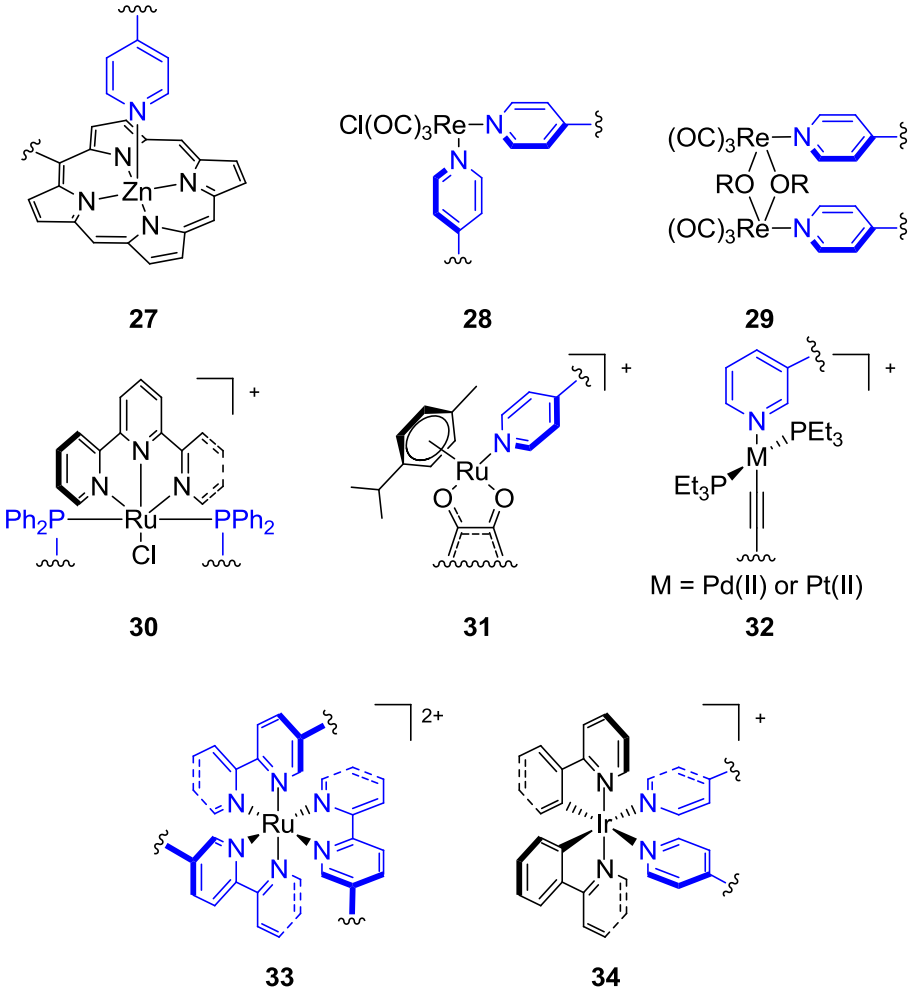

Figure 1.32. Various metal-ligand motifs used within supramolecular assembly that display photophysical activity.

Examples where the metallosupramolecular-capsules have been utilised for optically active applications have however remained limited. Light has been used as a trigger to control conformational changes of supramolecular assemblies and *vice versa* where a conformational change has resulted in a dramatic change in light emission. Recently, Clever and co-workers reported on photochromic bis-monodentate pyridyl dithienylethene ligands that with "naked" Pd(II) cations formed an M_2L_4 assembly.[161] Irradiating the capsule with light of a given wavelength the ligands undergo a conformational change, expanding or contracting the size of the capsule's cavity. This light-triggered expansion/contraction was used to control *guest* uptake/release of a dodecafluorododecaborate anion. Shionoya and co-workers have also observed optical activity with their earlier reported Hg_6L_8 assembly.[16] Interestingly the fluorescence

was coupled with the assembly's conformation change and could be turned "on" and "off" with the addition of excess Hg(II) or [2.2.2]-cryptand, respectively, due to structural alterations into the non-fluorescent Hg_6L_4 capsule. The only known example in the literature where a supramolecular "flask" plays a photo-mediated role is in the photochemical oxidation of adamantane.[162] Using cage **1**, Fujita and co-workers were able to encapsulate 4 adamantane molecules per *host* and with photoirradiation in air regio-selective oxidation was achieved at 24% yield. Extensive mechanistic studies revealed that following excitation of cage **1** a single electron was transferred from one adamantane molecule to the electron-poor tpt "panels". The adamantane radical was subsequently quenched with either residual water or oxygen to give the oxidised products 1-adamantylhydrogenperoxide or 1-adamantanol (Figure 1.33).

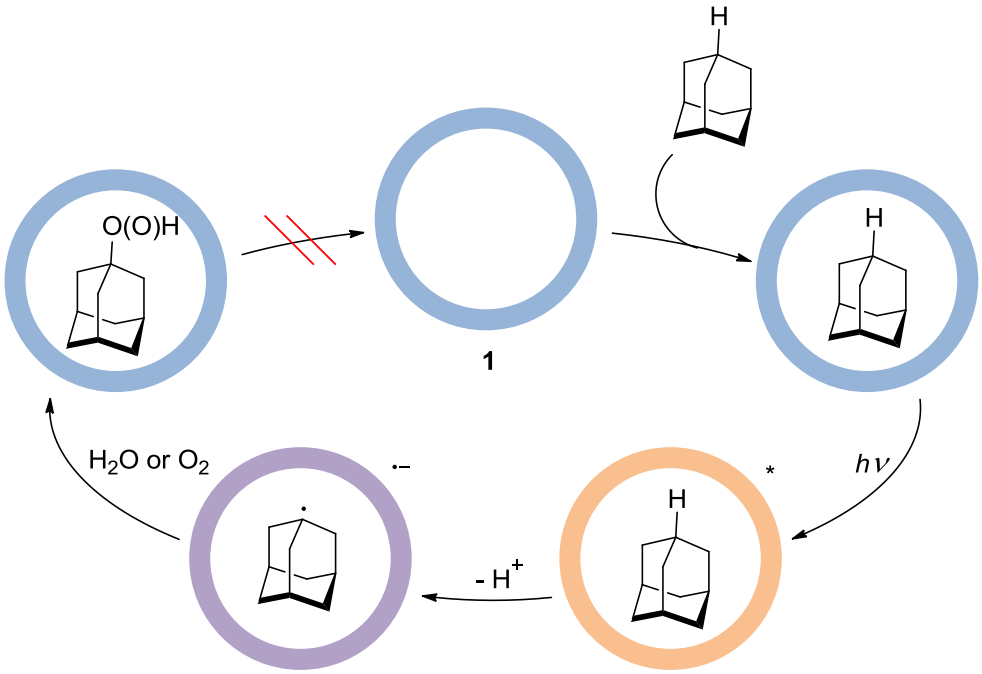

Figure 1.33. Photochemical oxidation of adamantane in the hydrophobic cavity of **1** in water.[162]

Alternative strategies in the construction of redox and optically active assemblies have used inherently photoactive ligand motifs, such as anthracene,[163] coumarin,[164] naphthyl[66] or aniline[165], or by functionalising the acceptor and/or donor building blocks of a supramolecular scaffold with photoactive groups.

Stang and co-workers have demonstrated that post-self-assembly modification was possible with a hexagonal prism, assembled using the charge separation strategy with hexatopic pyridine "panels" and ditopic carboxylate "pillars".[166] Following self-assembly with maleimide-functionalised "pillars", post synthetic covalent modification introduced ferrocene groups to the periphery of the cage, thereby bestowing redox activity on the system. Functionalisation of the self-assembly building blocks using ether or carboxylate linkers with various other groups has also been used by Stang with a plethora of different polygons and polyhedra[167] and Fujita with the $M_{12}L_{24}$ nano-spheres reported earlier.[168]

1.6 Conclusion and project targets

Inspired by nature, biological mimicry together with a bottom-up engineering approach has been used by chemists to constructing nano-sized containers and catalysts dubbed "molecular flasks" and "microreactors". As discussed in this chapter, the use of transition metal complexes to construct molecular capsules has been of great advantage due to 3 key factors: i) accessibility to a wide range of well-defined bonding angles, ii) an array of tailored bond strengths and iii) general ease in synthesis relative to conventional covalent chemistry. Since the synthesis of the first metallosupramolecular capsule in 1995, the field has been rapidly expanding and with recent innovations now includes more complex heteroleptic and heterometallic supramolecular architectures. Orthogonality in metal-ligand interactions has given access to kinetic step-wise control in the construction of three-dimensional assemblies with reduced symmetry and well-defined cavities. Finally, *host-guest* chemistry has also played a crucial role in both the synthesis, through the use of templates, and ultimately the utilisation of the capsules as *hosts* for stabilising aggregates and mediating unique and catalytic reactions. Constructing these molecular capsules for a purpose other than their unique topographies is the current focus within the literature. In particular, these capsules have shown potential use within the field of environmentally benign catalysis, opening the door to the next generation of "greener" enzyme-like reaction mediators. However, to-date, the metal centres and ligands generally play a structural role and have not been fully exploited for their potential photo-active and electrochemical

properties. Recently, examples where the metal centres and ligands serve a purpose besides maintaining the capsule's architectural integrity have started to emerge.

More often than not the specific functions of metallosupramolecular capsules reported in the literature appear to have been discovered serendipity, such as catalysis which tends to be very specific towards only a small number of reagents. The design and construction of capsules that are complimentary in conformation and electrostatic properties to specific *guests* or a purposeful function still remains a major challenge. However, one cannot forget that this is still a relatively new area of research in the field of supramolecular chemistry. With the growing number of unique designs, synthetic methods and applications so will develop the interest and intellectual understanding into how these metallosupramolecular capsules can be constructed to fulfil specific tasks and processes.

The aim of this project is to initially develop new metallosupramolecular capsules *via* a kinetically controlled approach, straying away from conventional thermodynamic one pot self-assembly reactions (Chapter 2). Secondly, the well-established optically-active cyclometalated $[Ir(ppy)_2]^+$ unit will be used to assemble the first luminescent capsule of this nature (Chapter 3), which will be thoroughly investigated for its *host-guest* chemistry coupled with its inherent photo-active properties (Chapter 4).

1.7 References

[1] a) J.-M. Lehn, *Supramolecular Chemistry*, VCH, Weinhelm, **1995**; b) D. Philp, J. F. Stoddart, *Angew. Chem. Int. Ed. Engl.* **1996**, *35*, 1154-1196; c) G. M. Whitesides, M. Boncheva, *Proc. Natl. Acad. Sci.* **2002**, *99*, 4769-4774.

[2] P. D. Beer, P. A. Gale, D. K. Smith, *Supramolecular Chemistry*, Oxford University Press, Oxford, **1999**.

[3] A. J. Kirby, *Angew. Chem. Int. Ed. Engl.* **1996**, *35*, 706-724.

[4] For a recent review on supramolecular coordinated enzyme mimics, see: M. J. Wiester, P. A. Ulmann, C. A. Mirkin, *Angew. Chem. Int. Ed.* **2011**, *50*, 114-137.

[5] Selected examples of organic-based capsules: a) L. R. MacGillivray, J. L. Atwood, *Nature* **1997**, *389*, 469-472; b) M. M. Conn, J. Rebek, *Chem. Rev.* **1997**, *97*, 1647-1668; c) Y. Liu, C. Hu, A. Comotti, M. D. Ward, *Science* **2011**, *333*, 436-440.

[6] For reviews on metallosupramolecular polyhedral assemblies, see: a) M. Schmittel, V. Kalsani, in *Functional Molecular Nanostructures, Vol. 245* (Ed.: A. D. Schlüter), Springer Berlin Heidelberg, **2005**, 1-53; b) S. J. Dalgarno, N. P. Power, J. L. Atwood, *Coord. Chem. Rev.* **2008**, *252*, 825-841; c) R. Chakrabarty, P. S. Mukherjee, P. J. Stang, *Chem. Rev.* **2011**, *111*, 6810-6918; d) Z. Laughrey, B. C. Gibb, *Chem. Soc. Rev.* **2011**, *40*, 363-386; e) T. R. Cook, Y.-R. Zheng, P. J. Stang, *Chem. Rev.* **2013**, *113*, 734-777; f) M. M. J. Smulders, I. A. Riddell, C. Browne, J. R. Nitschke, *Chem. Soc. Rev.* **2013**, *42*, 1728-1754; g) N. J. Young, B. P. Hay, *Chem. Commun.* **2013**, *49*, 1354-1379.

[7] J. Rebek, *Chem. Soc. Rev.* **1996**, *25*, 255-264.

[8] M. Fujita, J. Yazaki, K. Ogura, *J. Am. Chem. Soc.* **1990**, *112*, 5645-5647.

[9] B. Therrien, *J. Organomet. Chem.* **2011**, *696*, 637-651.

[10] M. Fujita, D. Oguro, M. Miyazawa, H. Oka, K. Yamaguchi, K. Ogura, *Nature* **1995**, *378*, 469-471.

[11] M. Fujita, M. Tominaga, A. Hori, B. Therrien, *Acc. Chem. Res.* **2005**, *38*, 369-378.

[12] M. Fujita, S.-Y. Yu, T. Kusukawa, H. Funaki, K. Ogura, K. Yamaguchi, *Angew. Chem. Int. Ed.* **1998**, *37*, 2082-2085.

[13] A. Orita, L. Jiang, T. Nakano, N. Ma, J. Otera, *Chem. Commun.* **2002**, 1362-1363.

[14] F. Ibukuro, T. Kusukawa, M. Fujita, *J. Am. Chem. Soc.* **1998**, *120*, 8561-8562.

[15] S. Hiraoka, K. Harano, M. Shiro, Y. Ozawa, N. Yasuda, K. Toriumi, M. Shionoya, *Angew. Chem. Int. Ed.* **2006**, *45*, 6488-6491.

[16] K. Harano, S. Hiraoka, M. Shionoya, *J. Am. Chem. Soc.* **2007**, *129*, 5300-5301.

[17] Z.-M. Liu, Y. Liu, S.-R. Zheng, Z.-Q. Yu, M. Pan, C.-Y. Su, *Inorg. Chem.* **2007**, *46*, 5814-5816.

[18] a) Q.-F. Sun, J. Iwasa, D. Ogawa, Y. Ishido, S. Sato, T. Ozeki, Y. Sei, K. Yamaguchi, M. Fujita, *Science* **2010**, *328*, 1144-1147; b) J. Bunzen, J. Iwasa, P. Bonakdarzadeh, E. Numata, K. Rissanen, S. Sato, M. Fujita, *Angew. Chem. Int. Ed.* **2012**, *51*, 3161-3163.

[19] a) J. D. Crowley, E. L. Gavey, *Dalton Trans.* **2010**, *39*, 4035-4037; b) J. E. M. Lewis, E. L. Gavey, S. A. Cameron, J. D. Crowley, *Chem. Sci.* **2012**, *3*, 778-784.

[20] T. K. Ronson, J. Fisher, L. P. Harding, M. J. Hardie, *Angew. Chem. Int. Ed.* **2007**, *46*, 9086-9088.

[21] D. Moon, S. Kang, J. Park, K. Lee, R. P. John, H. Won, G. H. Seong, Y. S. Kim, G. H. Kim, H. Rhee, M. S. Lah, *J. Am. Chem. Soc.* **2006**, *128*, 3530-3531.

[22] C. J. Kuehl, T. Yamamoto, S. R. Seidel, P. J. Stang, *Org. Lett.* **2002**, *4*, 913-915.

[23] Y.-R. Zheng, H.-B. Yang, K. Ghosh, L. Zhao, P. J. Stang, *Chem. Eur. J.* **2009**, *15*, 7203-7214.

[24] Y.-R. Zheng, H.-B. Yang, B. H. Northrop, K. Ghosh, P. J. Stang, *Inorg. Chem.* **2008**, *47*, 4706-4711.
[25] S. Ghosh, B. Gole, A. K. Bar, P. S. Mukherjee, *Organomet.* **2009**, *28*, 4288-4296.
[26] K. Kumazawa, K. Biradha, T. Kusukawa, T. Okano, M. Fujita, *Angew. Chem. Int. Ed.* **2003**, *42*, 3909-3913.
[27] D. J. Cram, J. M. Cram, *Container Molecules and Their Guests*, Royal Society of Chemistry, Cambridge, **1994**.
[28] M. Yoshizawa, J. Nakagawa, K. Kumazawa, M. Nagao, M. Kawano, T. Ozeki, M. Fujita, *Angew. Chem. Int. Ed.* **2005**, *44*, 1810-1813.
[29] Y. Yamauchi, M. Yoshizawa, M. Akita, M. Fujita, *J. Am. Chem. Soc.* **2010**, *132*, 960-966.
[30] T. Murase, K. Otsuka, M. Fujita, *J. Am. Chem. Soc.* **2010**, *132*, 7864-7865.
[31] Y.-R. Zheng, Z. Zhao, M. Wang, K. Ghosh, J. B. Pollock, T. R. Cook, P. J. Stang, *J. Am. Chem. Soc.* **2010**, *132*, 16873-16882.
[32] A. K. Bar, G. Mostafa, P. S. Mukherjee, *Inorg. Chem.* **2010**, *49*, 7647-7649.
[33] S. Mirtschin, A. Slabon-Turski, R. Scopelliti, A. H. Velders, K. Severin, *J. Am. Chem. Soc.* **2010**, *132*, 14004-14005.
[34] A. Granzhan, C. Schouwey, T. Riis-Johannessen, R. Scopelliti, K. Severin, *J. Am. Chem. Soc.* **2011**, *133*, 7106-7115.
[35] J. A. Thomas, *Chem. Soc. Rev.* **2007**, *36*, 856-868.
[36] I. A. Riddell, Y. R. Hristova, J. K. Clegg, C. S. Wood, B. Breiner, J. R. Nitschke, *J. Am. Chem. Soc.* **2013**, *135*, 2723-2733.
[37] J. A. Whiteford, C. V. Lu, P. J. Stang, *J. Am. Chem. Soc.* **1997**, *119*, 2524-2533.
[38] P. Jacopozzi, E. Dalcanale, *Angew. Chem. Int. Ed. Engl.* **1997**, *36*, 613-615.
[39] D. Xu, B. Hong, *Angew. Chem. Int. Ed.* **2000**, *39*, 1826-1829.
[40] S. H. Lim, Y. Su, S. M. Cohen, *Angew. Chem. Int. Ed.* **2012**, *51*, 5106-5109.
[41] A. G. L. Olive, K. Parkan, C. Givelet, J. Michl, *J. Am. Chem. Soc.* **2011**, *133*, 20108-20111.
[42] The *trans*-effect refers to the kinetic rate of substitution of the leaving group governed by the ligand in the *trans*-position on a metal centre. The *trans*-influence is the impact that the ligand has on the ground state bonding strength of the M-L bond in the *trans*-position. For a review on *cis*- and *trans*-effects of ligands, see: F. R. Hartley, *Chem. Soc. Rev.* **1973**, *2*, 163-179.
[43] J. Hupp, *Struct. Bond.* **2006**, *121*, 145-165.
[44] S. R. Seidel, P. J. Stang, *Acc. Chem. Res.* **2002**, *35*, 972-983.
[45] K.-i. Yamashita, M. Kawano, M. Fujita, *J. Am. Chem. Soc.* **2007**, *129*, 1850-1851.
[46] C. J. Kuehl, S. D. Huang, P. J. Stang, *J. Am. Chem. Soc.* **2001**, *123*, 9634-9641.
[47] D. Fujita, A. Takahashi, S. Sato, M. Fujita, *J. Am. Chem. Soc.* **2011**, *133*, 13317-13319.
[48] a) A. Ikeda, M. Yoshimura, F. Tani, Y. Naruta, S. Shinkai, *Chem. Lett.* **1998**, *27*, 587-588; b) N. P. Power, S. J. Dalgarno, J. L. Atwood, *Angew. Chem. Int. Ed.* **2007**, *46*, 8601-8604.
[49] S. Sato, Y. Ishido, M. Fujita, *J. Am. Chem. Soc.* **2009**, *131*, 6064-6065.
[50] R. W. Saalfrank, A. Stark, K. Peters, H. G. von Schnering, *Angew. Chem. Int. Ed. Engl.* **1988**, *27*, 851-853.
[51] D. L. Caulder, R. E. Powers, T. N. Parac, K. N. Raymond, *Angew. Chem. Int. Ed.* **1998**, *37*, 1840-1843.
[52] A. V. Davis, D. Fiedler, M. Ziegler, A. Terpin, K. N. Raymond, *J. Am. Chem. Soc.* **2007**, *129*, 15354-15363.

[53] C. Brückner, R. E. Powers, K. N. Raymond, *Angew. Chem. Int. Ed.* **1998**, *37*, 1837-1839.
[54] R. W. Saalfrank, H. Glaser, B. Demleitner, F. Hampel, M. M. Chowdhry, V. Schünemann, A. X. Trautwein, G. B. M. Vaughan, R. Yeh, A. V. Davis, K. N. Raymond, *Chem. Eur. J.* **2002**, *8*, 493-497.
[55] R. W. Saalfrank, H. Maid, A. Scheurer, F. W. Heinemann, R. Puchta, W. Bauer, D. Stern, D. Stalke, *Angew. Chem. Int. Ed.* **2008**, *47*, 8941-8945.
[56] T. Liu, Y. Liu, W. Xuan, Y. Cui, *Angew. Chem. Int. Ed.* **2010**, *49*, 4121-4124.
[57] C. R. K. Glasson, G. V. Meehan, J. K. Clegg, L. F. Lindoy, P. Turner, M. B. Duriska, R. Willis, *Chem. Commun.* **2008**, 1190-1192.
[58] P. Mal, D. Schultz, K. Beyeh, K. Rissanen, J. R. Nitschke, *Angew. Chem. Int. Ed.* **2008**, *47*, 8297-8301.
[59] T. K. Ronson, S. Zarra, S. P. Black, J. R. Nitschke, *Chem. Commun.* **2013**, *49*, 2476-2490.
[60] W. Meng, T. K. Ronson, J. K. Clegg, J. R. Nitschke, *Angew. Chem. Int. Ed.* **2013**, *52*, 1017-1021.
[61] I. A. Riddell, M. M. J. Smulders, J. K. Clegg, Y. R. Hristova, B. Breiner, J. D. Thoburn, J. R. Nitschke, *Nat. Chem.* **2012**, *4*, 751-756.
[62] S. Zarra, J. K. Clegg, J. R. Nitschke, *Angew. Chem. Int. Ed.* **2013**, *52*, 4837-4840.
[63] M. M. J. Smulders, A. Jiménez, J. R. Nitschke, *Angew. Chem. Int. Ed.* **2012**, *51*, 6681-6685.
[64] M. Schmittel, M. L. Saha, J. Fan, *Org. Lett.* **2011**, *13*, 3916-3919.
[65] For a recent review on heteroleptic architectures assembled using the site occupancy maximisation principle, see: S. De, K. Mahata, M. Schmittel, *Chem. Soc. Rev.* **2010**, *39*, 1555-1575.
[66] M. D. Ward, *Chem. Commun.* **2009**, 4487-4499.
[67] Z. R. Bell, J. C. Jeffery, J. A. McCleverty, M. D. Ward, *Angew. Chem. Int. Ed.* **2002**, *41*, 2515-2518.
[68] a) P. Govindaswamy, G. Süss-Fink, B. Therrien, *Organomet.* **2007**, *26*, 915-924; b) M. A. Furrer, A. Garci, E. Denoyelle-Di-Muro, P. Trouillas, F. Giannini, J. Furrer, C. M. Clavel, P. J. Dyson, G. Süss-Fink, B. Therrien, *Chem. Eur. J.* **2013**, *19*, 3198-3203.
[69] N. P. E. Barry, P. Govindaswamy, J. Furrer, G. Süss-Fink, B. Therrien, *Inorg. Chem. Commun.* **2008**, *11*, 1300-1303.
[70] M. Wang, V. Vajpayee, S. Shanmugaraju, Y.-R. Zheng, Z. Zhao, H. Kim, P. S. Mukherjee, K.-W. Chi, P. J. Stang, *Inorg. Chem.* **2011**, *50*, 1506-1512.
[71] N. P. E. Barry, O. Zava, P. J. Dyson, B. Therrien, *Chem. Eur. J.* **2011**, *17*, 9669-9677.
[72] Y.-F. Han, Y.-J. Lin, T. S. A. Hor, G.-X. Jin, *Organomet.* **2012**, *31*, 995-1000.
[73] R. V. Slone, J. T. Hupp, *Inorg. Chem.* **1997**, *36*, 5422-5423.
[74] S. J. Lee, K. L. Mulfort, X. Zuo, A. J. Goshe, P. J. Wesson, S. T. Nguyen, J. T. Hupp, D. M. Tiede, *J. Am. Chem. Soc.* **2008**, *130*, 836-838.
[75] S. Bélanger, J. T. Hupp, *Angew. Chem. Int. Ed.* **1999**, *38*, 2222-2224.
[76] S. J. Lee, S.-H. Cho, K. L. Mulfort, D. M. Tiede, J. T. Hupp, S. T. Nguyen, *J. Am. Chem. Soc.* **2008**, *130*, 16828-16829.
[77] I.-W. Hwang, T. Kamada, T. K. Ahn, D. M. Ko, T. Nakamura, A. Tsuda, A. Osuka, D. Kim, *J. Am. Chem. Soc.* **2004**, *126*, 16187-16198.
[78] A. Tsuda, H. Hu, R. Tanaka, T. Aida, *Angew. Chem. Int. Ed.* **2005**, *44*, 4884-4888.
[79] Selected examples of heterometallic capsules: a) X. Sun, D. W. Johnson, D. L. Caulder, R. E. Powers, K. N. Raymond, E. H. Wong, *Angew. Chem. Int. Ed.* **1999**,

38, 1303-1307; b) J. C. Garrison, M. J. Panzner, P. D. Custer, D. V. Reddy, P. L. Rinaldi, C. A. Tessier, W. J. Youngs, *Chem. Commun.* **2006**, 4644-4646; c) H.-B. Wu, Q.-M. Wang, *Angew. Chem. Int. Ed.* **2009**, *48*, 7343-7345; d) M. B. Duriska, S. M. Neville, J. Lu, S. S. Iremonger, J. F. Boas, C. J. Kepert, S. R. Batten, *Angew. Chem. Int. Ed.* **2009**, *48*, 8919-8922.

[80] S. Hiraoka, Y. Sakata, M. Shionoya, *J. Am. Chem. Soc.* **2008**, *130*, 10058-10059.

[81] Y. Sakata, S. Hiraoka, M. Shionoya, *Chem. Eur. J.* **2010**, *16*, 3318-3325.

[82] J. R. Farrell, C. A. Mirkin, L. M. Liable-Sands, A. L. Rheingold, *J. Am. Chem. Soc.* **1998**, *120*, 11834-11835.

[83] N. C. Gianneschi, M. S. Masar, C. A. Mirkin, *Acc. Chem. Res.* **2005**, *38*, 825-837.

[84] a) N. C. Gianneschi, P. A. Bertin, S. T. Nguyen, C. A. Mirkin, L. N. Zakharov, A. L. Rheingold, *J. Am. Chem. Soc.* **2003**, *125*, 10508-10509; b) H. J. Yoon, J. Heo, C. A. Mirkin, *J. Am. Chem. Soc.* **2007**, *129*, 14182-14183; c) M. S. Masar, N. C. Gianneschi, C. G. Oliveri, C. L. Stern, S. T. Nguyen, C. A. Mirkin, *J. Am. Chem. Soc.* **2007**, *129*, 10149-10158.

[85] a) W. Meng, J. K. Clegg, J. D. Thoburn, J. R. Nitschke, *J. Am. Chem. Soc.* **2011**, *133*, 13652-13660; b) N. Ousaka, S. Grunder, A. M. Castilla, A. C. Whalley, J. F. Stoddart, J. R. Nitschke, *J. Am. Chem. Soc.* **2012**, *134*, 15528-15537; c) N. Ousaka, J. K. Clegg, J. R. Nitschke, *Angew. Chem. Int. Ed.* **2012**, *51*, 1464-1468.

[86] J. Lee, K. Ghosh, P. J. Stang, *J. Am. Chem. Soc.* **2009**, *131*, 12028-12029.

[87] M. Hutin, G. Bernardinelli, J. R. Nitschke, *Proc. Natl. Acad. Sci.* **2006**, *103*, 17655-17660.

[88] For recent reviews on capsules utilised for various applications, see: a) M. Schmittel, V. Kalsani, *Top. Curr. Chem.* **2005**, *245*, 1-53; b) T. S. Koblenz, J. Wassenaar, J. N. H. Reek, *Chem. Soc. Rev.* **2008**, *37*, 247-262; c) M. Yoshizawa, J. K. Klosterman, M. Fujita, *Angew. Chem. Int. Ed.* **2009**, *48*, 3418-3438; d) H. Amouri, C. Desmarets, J. Moussa, *Chem. Rev.* **2012**, *112*, 2015-2041.

[89] a) E. P. Kyba, R. C. Helgeson, K. Madan, G. W. Gokel, T. L. Tarnowski, S. S. Moore, D. J. Cram, *J. Am. Chem. Soc.* **1977**, *99*, 2564-2571; b) D. J. Cram, M. E. Tanner, R. Thomas, *Angew. Chem. Int. Ed. Engl.* **1991**, *30*, 1024-1027; c) D. J. Cram, *Nature* **1992**, *356*, 29-36.

[90] J. S. Fleming, K. L. V. Mann, C.-A. Carraz, E. Psillakis, J. C. Jeffery, J. A. McCleverty, M. D. Ward, *Angew. Chem. Int. Ed.* **1998**, *37*, 1279-1281.

[91] M. Yoshizawa, T. Kusukawa, M. Fujita, K. Yamaguchi, *J. Am. Chem. Soc.* **2000**, *122*, 6311-6312.

[92] M. Yoshizawa, T. Kusukawa, M. Fujita, S. Sakamoto, K. Yamaguchi, *J. Am. Chem. Soc.* **2001**, *123*, 10454-10459.

[93] M. Kawano, Y. Kobayashi, T. Ozeki, M. Fujita, *J. Am. Chem. Soc.* **2006**, *128*, 6558-6559.

[94] T. Sawada, M. Yoshizawa, S. Sato, M. Fujita, *Nat. Chem.* **2009**, *1*, 53-56.

[95] a) S. Tashiro, M. Tominaga, Y. Yamaguchi, K. Kato, M. Fujita, *Angew. Chem. Int. Ed.* **2006**, *45*, 241-244; b) S. Tashiro, M. Tominaga, Y. Yamaguchi, K. Kato, M. Fujita, *Chem. Eur. J.* **2006**, *12*, 3211-3217; c) C. Dolain, Y. Hatakeyama, T. Sawada, S. Tashiro, M. Fujita, *J. Am. Chem. Soc.* **2010**, *132*, 5564-5565.

[96] S. M. Biros, R. G. Bergman, K. N. Raymond, *J. Am. Chem. Soc.* **2007**, *129*, 12094-12095.

[97] M. Ziegler, J. L. Brumaghim, K. N. Raymond, *Angew. Chem. Int. Ed.* **2000**, *39*, 4119-4121.

[98] V. M. Dong, D. Fiedler, B. Carl, R. G. Bergman, K. N. Raymond, *J. Am. Chem. Soc.* **2006**, *128*, 14464-14465.

[99] a) A. V. Davis, K. N. Raymond, *J. Am. Chem. Soc.* **2005**, *127*, 7912-7919; b) A. V. Davis, D. Fiedler, G. Seeber, A. Zahl, R. van Eldik, K. N. Raymond, *J. Am. Chem. Soc.* **2006**, *128*, 1324-1333; c) M. D. Pluth, D. W. Johnson, G. z. Szigethy, A. V. Davis, S. J. Teat, A. G. Oliver, R. G. Bergman, K. N. Raymond, *Inorg. Chem.* **2009**, *48*, 111-120.
[100] M. D. Pluth, R. G. Bergman, K. N. Raymond, *J. Am. Chem. Soc.* **2008**, *130*, 6362-6366.
[101] P. Mal, B. Breiner, K. Rissanen, J. R. Nitschke, *Science* **2009**, *324*, 1697-1699.
[102] W. Meng, B. Breiner, K. Rissanen, J. D. Thoburn, J. K. Clegg, J. R. Nitschke, *Angew. Chem. Int. Ed.* **2011**, *50*, 3479-3483.
[103] W. Meng, J. K. Clegg, J. R. Nitschke, *Angew. Chem. Int. Ed.* **2012**, *51*, 1881-1884.
[104] K. Ono, M. Yoshizawa, M. Akita, T. Kato, Y. Tsunobuchi, S.-i. Ohkoshi, M. Fujita, *J. Am. Chem. Soc.* **2009**, *131*, 2782-2783.
[105] M. Kiguchi, T. Takahashi, Y. Takahashi, Y. Yamauchi, T. Murase, M. Fujita, T. Tada, S. Watanabe, *Angew. Chem. Int. Ed.* **2011**, *50*, 5708-5711.
[106] T. Osuga, T. Murase, K. Ono, Y. Yamauchi, M. Fujita, *J. Am. Chem. Soc.* **2010**, *132*, 15553-15555.
[107] Y. Yamauchi, M. Yoshizawa, M. Akita, M. Fujita, *Proc. Natl. Acad. Sci.* **2009**, *106*, 10435-10437.
[108] a) J. Mattsson, P. Govindaswamy, J. Furrer, Y. Sei, K. Yamaguchi, G. Süss-Fink, B. Therrien, *Organomet.* **2008**, *27*, 4346-4356; b) J. Freudenreich, N. P. E. Barry, G. Süss-Fink, B. Therrien, *Eur. J. Inorg. Chem.* **2010**, *2010*, 2400-2405.
[109] J. Kang, J. Rebek, Jr., *Nature* **1997**, *385*, 50-52.
[110] T. Kusukawa, T. Nakai, T. Okano, M. Fujita, *Chem. Lett.* **2003**, *32*, 284-285.
[111] H. Ito, T. Kusukawa, M. Fujita, *Chem. Lett.* **2000**, *29*, 598-599.
[112] M. Yoshizawa, M. Tamura, M. Fujita, *Science* **2006**, *312*, 251-254.
[113] M. Yoshizawa, Y. Takeyama, T. Kusukawa, M. Fujita, *Angew. Chem. Int. Ed.* **2002**, *41*, 1347-1349.
[114] M. Yoshizawa, Y. Takeyama, T. Okano, M. Fujita, *J. Am. Chem. Soc.* **2003**, *125*, 3243-3247.
[115] S. Horiuchi, Y. Nishioka, T. Murase, M. Fujita, *Chem. Commun.* **2010**, *46*, 3460-3462.
[116] a) S. Karthikeyan, V. Ramamurthy, *J. Org. Chem.* **2006**, *71*, 6409-6413; b) S. Karthikeyan, V. Ramamurthy, *J. Org. Chem.* **2007**, *72*, 452-458; c) Y. Nishioka, T. Yamaguchi, M. Yoshizawa, M. Fujita, *J. Am. Chem. Soc.* **2007**, *129*, 7000-7001; d) T. Murase, S. Horiuchi, M. Fujita, *J. Am. Chem. Soc.* **2010**, *132*, 2866-2867.
[117] T. Yamaguchi, M. Fujita, *Angew. Chem. Int. Ed.* **2008**, *47*, 2067-2069.
[118] T. Furusawa, M. Kawano, M. Fujita, *Angew. Chem. Int. Ed.* **2007**, *46*, 5717-5719.
[119] D. Samanta, S. Mukherjee, Y. P. Patil, P. S. Mukherjee, *Chem. Eur. J.* **2012**, *18*, 12322-12329.
[120] a) D. Fiedler, R. G. Bergman, K. N. Raymond, *Angew. Chem. Int. Ed.* **2004**, *43*, 6748-6751; b) D. Fiedler, H. van Halbeek, R. G. Bergman, K. N. Raymond, *J. Am. Chem. Soc.* **2006**, *128*, 10240-10252; c) C. J. Hastings, D. Fiedler, R. G. Bergman, K. N. Raymond, *J. Am. Chem. Soc.* **2008**, *130*, 10977-10983.
[121] C. J. Hastings, M. D. Pluth, R. G. Bergman, K. N. Raymond, *J. Am. Chem. Soc.* **2010**, *132*, 6938-6940.
[122] W. M. Hart-Cooper, K. N. Clary, F. D. Toste, R. G. Bergman, K. N. Raymond, *J. Am. Chem. Soc.* **2012**, *134*, 17873-17876.
[123] M. D. Pluth, R. G. Bergman, K. N. Raymond, *Angew. Chem. Int. Ed.* **2007**, *46*, 8587-8589.

[124] M. D. Pluth, R. G. Bergman, K. N. Raymond, *J. Am. Chem. Soc.* **2008**, *130*, 11423-11429.
[125] T. Murase, Y. Nishijima, M. Fujita, *J. Am. Chem. Soc.* **2012**, *134*, 162-164.
[126] Y. Nishioka, T. Yamaguchi, M. Kawano, M. Fujita, *J. Am. Chem. Soc.* **2008**, *130*, 8160-8161.
[127] C. J. Brown, R. G. Bergman, K. N. Raymond, *J. Am. Chem. Soc.* **2009**, *131*, 17530-17531.
[128] M. L. Merlau, M. del Pilar Mejia, S. T. Nguyen, J. T. Hupp, *Angew. Chem. Int. Ed.* **2001**, *40*, 4239-4242.
[129] D. H. Leung, D. Fiedler, R. G. Bergman, K. N. Raymond, *Angew. Chem. Int. Ed.* **2004**, *43*, 963-966.
[130] Z. J. Wang, C. J. Brown, R. G. Bergman, K. N. Raymond, F. D. Toste, *J. Am. Chem. Soc.* **2011**, *133*, 7358-7360.
[131] D. H. Leung, R. G. Bergman, K. N. Raymond, *J. Am. Chem. Soc.* **2007**, *129*, 2746-2747.
[132] J. L. Bolliger, A. M. Belenguer, J. R. Nitschke, *Angew. Chem. Int. Ed.* **2013**, *52*, 7958-7962.
[133] A. J. Boersma, R. P. Megens, B. L. Feringa, G. Roelfes, *Chem. Soc. Rev.* **2010**, *39*, 2083.
[134] B. Therrien, G. Süss-Fink, P. Govindaswamy, A. K. Renfrew, P. J. Dyson, *Angew. Chem. Int. Ed.* **2008**, *47*, 3773-3776.
[135] P. Govindaswamy, D. Linder, J. Lacour, G. Suss-Fink, B. Therrien, *Chem. Commun.* **2006**, 4691-4693.
[136] B. Therrien, in *Chemistry of Nanocontainers, Vol. 319* (Eds.: M. Albrecht, E. Hahn), Springer Berlin Heidelberg, **2012**, pp. 35-55.
[137] a) O. Zava, J. Mattsson, B. Therrien, P. J. Dyson, *Chem. Eur. J.* **2010**, *16*, 1428-1431; b) J. Mattsson, O. Zava, A. K. Renfrew, Y. Sei, K. Yamaguchi, P. J. Dyson, B. Therrien, *Dalton Trans.* **2010**, *39*, 8248-8255; c) A. Pitto-Barry, N. P. E. Barry, O. Zava, R. Deschenaux, P. J. Dyson, B. Therrien, *Chem. Eur. J.* **2011**, *17*, 1966-1971.
[138] J. E. M. Lewis, C. John McAdam, M. G. Gardiner, J. D. Crowley, *Chem. Commun.* **2013**.
[139] M. Tominaga, K. Suzuki, T. Murase, M. Fujita, *J. Am. Chem. Soc.* **2005**, *127*, 11950-11951.
[140] S. Sato, J. Iida, K. Suzuki, M. Kawano, T. Ozeki, M. Fujita, *Science* **2006**, *313*, 1273-1276.
[141] T. Murase, S. Sato, M. Fujita, *Angew. Chem. Int. Ed.* **2007**, *46*, 1083-1085.
[142] T. Murase, S. Sato, M. Fujita, *Angew. Chem. Int. Ed.* **2007**, *46*, 5133-5136.
[143] a) K. Suzuki, S. Sato, M. Fujita, *Nat. Chem.* **2010**, *2*, 25-29; b) K. Suzuki, K. Takao, S. Sato, M. Fujita, *Angew. Chem. Int. Ed.* **2011**, *50*, 4858-4861; c) T. Ichijo, S. Sato, M. Fujita, *J. Am. Chem. Soc.* **2013**, *135*, 6786-6789.
[144] Q.-T. He, X.-P. Li, L.-F. Chen, L. Zhang, W. Wang, C.-Y. Su, *ACS Catalysis* **2012**, *3*, 1-9.
[145] T. H. Noh, E. Heo, K. H. Park, O.-S. Jung, *J. Am. Chem. Soc.* **2011**, *133*, 1236-1239.
[146] R. A. Haycock, A. Yartsev, U. Michelsen, V. Sundström, C. A. Hunter, *Angew. Chem. Int. Ed.* **2000**, *39*, 3616-3619.
[147] T. E. O. Screen, J. R. G. Thorne, R. G. Denning, D. G. Bucknall, H. L. Anderson, *J. Am. Chem. Soc.* **2002**, *124*, 9712-9713.
[148] R. Takahashi, Y. Kobuke, *J. Am. Chem. Soc.* **2003**, *125*, 2372-2373.
[149] R. V. Slone, D. I. Yoon, R. M. Calhoun, J. T. Hupp, *J. Am. Chem. Soc.* **1995**, *117*, 11813-11814.

[150] S.-S. Sun, A. J. Lees, *J. Am. Chem. Soc.* **2000**, *122*, 8956-8967.
[151] B. Manimaran, P. Thanasekaran, T. Rajendran, R.-T. Liao, Y.-H. Liu, G.-H. Lee, S.-M. Peng, S. Rajagopal, K.-L. Lu, *Inorg. Chem.* **2003**, *42*, 4795-4797.
[152] V. Vajpayee, Y. H. Song, Y. J. Jung, S. C. Kang, H. Kim, I. S. Kim, M. Wang, T. R. Cook, P. J. Stang, K.-W. Chi, *Dalton Trans.* **2012**, *41*, 3046-3052.
[153] V. Vajpayee, Y. J. Yang, S. C. Kang, H. Kim, I. S. Kim, M. Wang, P. J. Stang, K.-W. Chi, *Chem. Commun.* **2011**, *47*, 5184-5186.
[154] S. Ghosh, P. S. Mukherjee, *Organomet.* **2008**, *27*, 316-319.
[155] a) L. Sacksteder, E. Baralt, B. A. DeGraff, C. M. Lukehart, J. N. Demas, *Inorg. Chem.* **1991**, *30*, 2468-2476; b) V. W.-W. Yam, C.-H. Tao, L. Zhang, K. M.-C. Wong, K.-K. Cheung, *Organomet.* **2001**, *20*, 453-459.
[156] S. Goeb, V. Prusakova, X. Wang, A. Vezinat, M. Salle, F. N. Castellano, *Chem. Commun.* **2011**, *47*, 4397-4399.
[157] A. Juris, V. Balzani, F. Barigelletti, S. Campagna, P. Belser, A. von Zelewsky, *Coord. Chem. Rev.* **1988**, *84*, 85-277.
[158] a) P. de Wolf, S. L. Heath, J. A. Thomas, *Chem. Commun.* **2002**, 2540-2541; b) C. R. K. Glasson, G. V. Meehan, J. K. Clegg, L. F. Lindoy, J. A. Smith, F. R. Keene, C. Motti, *Chem. Eur. J.* **2008**, *14*, 10535-10538; c) N. C. Fletcher, R. T. Brown, A. P. Doherty, *Inorg. Chem.* **2006**, *45*, 6132-6134.
[159] a) I. M. Dixon, J.-P. Collin, J.-P. Sauvage, L. Flamigni, S. Encinas, F. Barigelletti, *Chem. Soc. Rev.* **2000**, *29*, 385-391; b) S. Lamansky, P. Djurovich, D. Murphy, F. Abdel-Razzaq, H.-E. Lee, C. Adachi, P. E. Burrows, S. R. Forrest, M. E. Thompson, *J. Am. Chem. Soc.* **2001**, *123*, 4304-4312.
[160] a) E. Baranoff, E. Orselli, L. Allouche, D. Di Censo, R. Scopelliti, M. Gratzel, M. K. Nazeeruddin, *Chem. Commun.* **2011**, *47*, 2799-2801; b) N. M. Ali, V. L. MacLeod, P. Jennison, I. V. Sazanovich, C. A. Hunter, J. A. Weinstein, M. D. Ward, *Dalton Trans.* **2012**, *41*, 2408-2419; c) V. Chandrasekhar, T. Hajra, J. K. Bera, S. M. W. Rahaman, N. Satumtira, O. Elbjeirami, M. A. Omary, *Inorg. Chem.* **2012**, *51*, 1319-1329.
[161] M. Han, R. Michel, B. He, Y.-S. Chen, D. Stalke, M. John, G. H. Clever, *Angew. Chem. Int. Ed.* **2013**, *52*, 1319-1323.
[162] a) M. Yoshizawa, S. Miyagi, M. Kawano, K. Ishiguro, M. Fujita, *J. Am. Chem. Soc.* **2004**, *126*, 9172-9173; b) Y. Furutani, H. Kandori, M. Kawano, K. Nakabayashi, M. Yoshizawa, M. Fujita, *J. Am. Chem. Soc.* **2009**, *131*, 4764-4768.
[163] a) R. Lin, J. H. K. Yip, K. Zhang, L. L. Koh, K.-Y. Wong, K. P. Ho, *J. Am. Chem. Soc.* **2004**, *126*, 15852-15869; b) G.-H. Ning, L.-Y. Yao, L.-X. Liu, T.-Z. Xie, Y.-Z. Li, Y. Qin, Y.-J. Pan, S.-Y. Yu, *Inorg. Chem.* **2010**, *49*, 7783-7792.
[164] S. J. Bullock, C. E. Felton, R. V. Fennessy, L. P. Harding, M. Andrews, S. J. A. Pope, C. R. Rice, T. Riis-Johannessen, *Dalton Trans.* **2009**, 10570-10573.
[165] a) A. M. Johnson, O. Moshe, A. S. Gamboa, B. W. Langloss, J. F. K. Limtiaco, C. K. Larive, R. J. Hooley, *Inorg. Chem.* **2011**, *50*, 9430-9442; b) J. B. Pollock, T. R. Cook, P. J. Stang, *J. Am. Chem. Soc.* **2012**, *134*, 10607-10620.
[166] M. Wang, W.-J. Lan, Y.-R. Zheng, T. R. Cook, H. S. White, P. J. Stang, *J. Am. Chem. Soc.* **2011**, *133*, 10752-10755.
[167] a) B. H. Northrop, H.-B. Yang, P. J. Stang, *Chem. Commun.* **2008**, 5896-5908; b) K. Ghosh, J. Hu, H. S. White, P. J. Stang, *J. Am. Chem. Soc.* **2009**, *131*, 6695-6697.
[168] a) M. Tominaga, K. Suzuki, M. Kawano, T. Kusukawa, T. Ozeki, S. Sakamoto, K. Yamaguchi, M. Fujita, *Angew. Chem. Int. Ed.* **2004**, *43*, 5621-5625; b) N. Kamiya, M. Tominaga, S. Sato, M. Fujita, *J. Am. Chem. Soc.* **2007**, *129*, 3816-3817.

Chapter 2

Sequential, kinetically controlled synthesis of multicomponent stereoisomeric Pt(II) cages

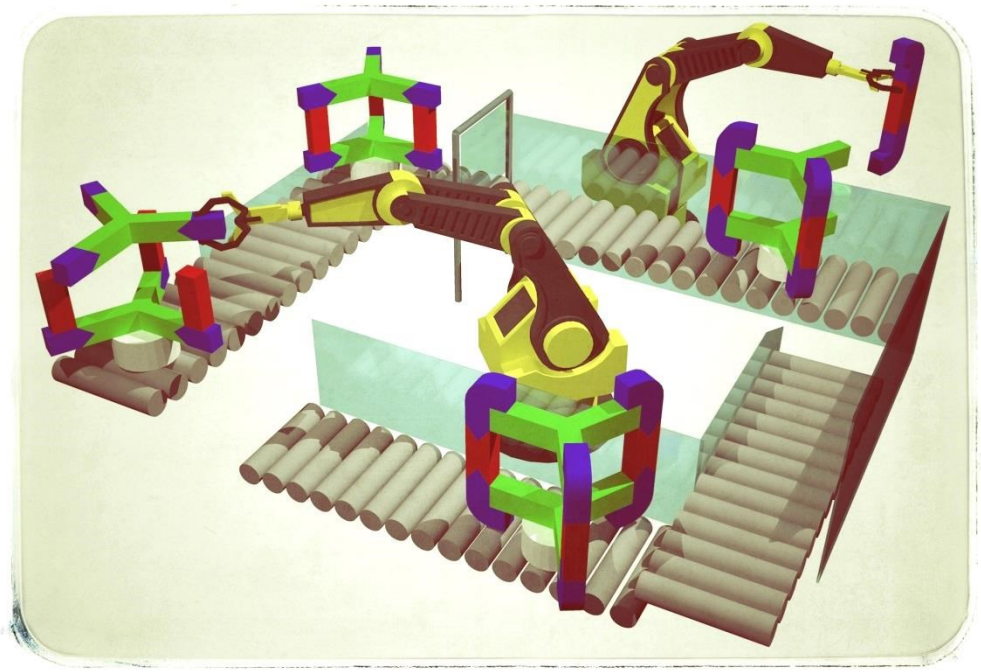

Published as *Sequential, kinetically controlled synthesis of multicomponent stereoisomeric assemblies*, O. Chepelin, J. Ujma, P. E. Barran, P. J. Lusby, *Angew. Chem. Int. Ed.* **2012**, *51*, 4194-4197.

Acknowledgements

I would like to thank Prof. Perdita Barran and Jakub Ujma for assistance with the mass spectrometry. This work was initiated by Dr. Sarah Pike, who synthesised *cis*-$[(H\mathbf{L^1}Pt)_6(4,4'\text{-bipy})_3(tpt)_2](PF_6)_6$.

2.1 Synopsis

Demonstrated herein is a kinetically controlled approach to self-assembly, in which the sequence of addition of pre-engineered molecular structural units leads to the stereoselective formation of discrete metallosupramolecular cages. Using either a phenylpyridine or a diphenylpyridine cyclometalated Pt corner unit two different sets of structural isomers were kinetically assembled by selective addion of the ligands. The kinetically stable cage isomers were characterised by their distinctly different ^{1}H NMR spectra and mass spectrometry collision-induced dissociation pathways.

2.2 Introduction

The reversibility of noncovalent and metal-ligand interactions has been widely exploited to synthesise a plethora of supramolecular and coordination-based assemblies under thermodynamic control.[1] Occasionally, entrapment in local energy minima leads to the formation of metastable products, which are often converted into lower-energy products upon prolonged reaction times.[2] In contrast, self-assembled products in nature almost always arise according to the most expedient reaction pathway, that is, are kinetically selected.[3] Herein, supramolecular structural isomers were constructed following a kinetically controlled, sequence dependent pathway, which is scarcely found in the literature.[4]

The use of platinum(II) (and other third-row transition metals) is particularly well-suited to a kinetic approach to self-assembly, not just because Pt–ligand bonds can be kinetically inert, but also because the metal ion can be conveniently tuned to produce a vast range of different ligand-exchange labilities. For instance, assemblies that utilise bis(phosphine) ligands as corner protecting groups often readily assemble at room temperature,[5] while those that exploit neutral *N*-donor bidentate ligands, such as ethylene diamine, typically require several hours at elevated temperatures to reach equilibrium.[6] Furthermore, the mechanism of labilisation, that is, the *trans* effect, is such that it is possible for a single metal centre to possess *cis* exchangeable sites with dramatically different kinetic properties. Recently a metallosupramolecular trigonal prism that possesses an unsymmetrical cyclometalated C^N corner protecting group was prepared within the Lusby group, which was assembled in two steps by treating [**L**^{1}Pt(DMSO)] (where H_2**L**^{1} = 2,6-diphenylpyridine) sequentially with 4,4′-bipy (4,4′-bipy = 4,4′-bipyridine) and tpt·3CSA (where tpt = 2,4,6-tris(4-pyridyl)-1,3,5-triazine and CSA = (+)-camphor-10-sulfonic acid; see Scheme 2.1, steps a and b).[7] The isolation of a single isomeric product *cis*-[(H**L**^{1}Pt)$_6$(4,4′-bipy)$_3$(tpt)$_2$](PF_6)$_6$ from a possible fourteen products, as indicated by the ^{1}H NMR spectrum of the hexa-PF_6^- salt (Figure 2.1a), led us to question, was this selectivity a result of each Pt centre possessing one labile and one inert exchangeable site, or was the selectivity thermodynamic in origin?

2.3 Results and Discussion

2.3.1 2,6-diphenylpyridine Pt(II) cages

In order to answer whether the formation of *cis*-[(H**L**^{1}Pt)$_6$(4,4′-bipy)$_3$(tpt)$_2$](PF$_6$)$_6$ was occurring under thermodynamic or kinetic control, the sequence in which 4,4′-bipy and tpt were added to [**L**^{1}Pt(DMSO)] was reversed. [**L**^{1}Pt(DMSO)] was first treated with a third of an eq of tpt at RT in CH_2Cl_2 to give [(**L**^{1}Pt)$_3$(tpt)] (Scheme 2.1, step c), which was then treated with 4,4′-bipy·2CSA, and after metathesis with NH_4PF_6, the hexa-PF_6^- salt was isolated in 99% yield (Scheme 2.1, step d).

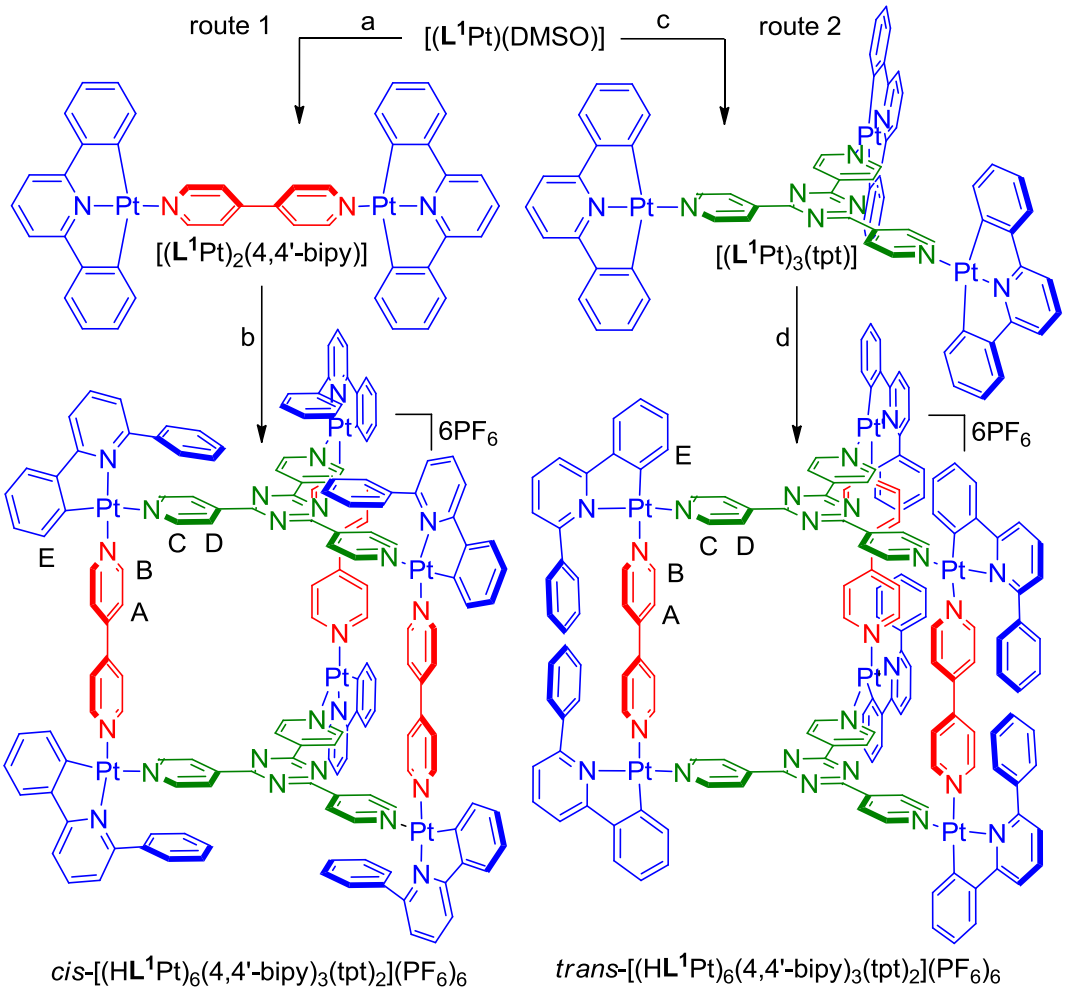

Scheme 2.1. Sequence specific control over the formation of metallosupramolecular stereochemical isomers. Conditions: a) 4,4′-bipy, CH_2Cl_2, RT, 18 h, 77%; b) (i) tpt·3CSA, CH_2Cl_2, RT, 1 h; (ii) NH_4PF_6, 97%; c) tpt, CH_2Cl_2, RT, 18 h, 85%; d) (i) 4,4′-bipy·2CSA, CH_2Cl_2, RT, 3 h; (ii) NH_4PF_6, 99%.

The ^{1}H NMR spectrum of this product (Figure 2.1b) also indicated the formation of a single species, yet there were clear differences between the spectra of the two isomers, in particular, for resonances $H_{A\text{-}E}$. The product from route 1 was assigned as *cis*-[(H**L**^{1}Pt)$_6$(4,4′-bipy)$_3$(tpt)$_2$](PF$_6$)$_6$, in which the tpt ligand is coordinated *cis* to the nitrogen of 2,6-diphenylpyridine, and the product from route 2 was assigned as *trans*-[(H**L**^{1}Pt)$_6$(4,4′-bipy)$_3$(tpt)$_2$](PF$_6$)$_6$, in which the tpt ligand is coordinated *trans* to the nitrogen of 2,6-diphenylpyridine. This absolute assignment was made on the basis that a) the resonance of the *ortho*-proton of tpt (H_C) is more deshielded in the *trans*-to-nitrogen coordination site in comparison to the *ortho*-proton 4,4′-bipy (H_B), and b) the large and small relative separations between the resonances of H_A and H_B, and between the resonances of H_C and H_D.

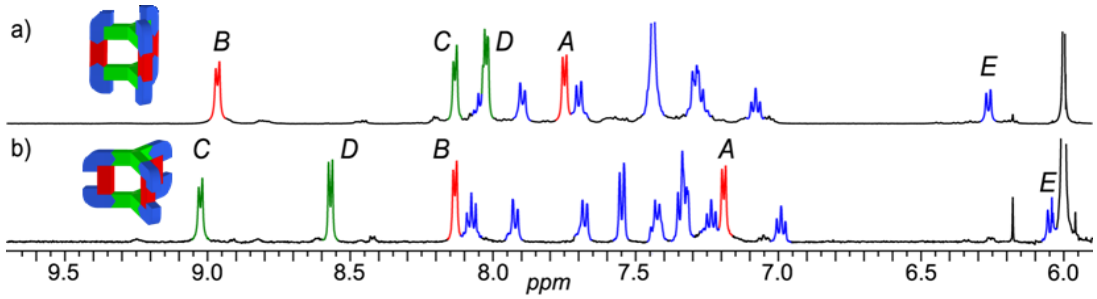

Figure 2.1. ^{1}H NMR spectra (500 MHz, $C_2D_2Cl_4$, 298 K) of a) *cis* and b) *trans*-[(H**L**^{1}Pt)$_6$(4,4′-bipy)$_3$(tpt)$_2$](PF$_6$)$_6$. The assignments correspond to the lettering shown in Scheme 2.1.

To corroborate the structural assignment of the isomers in solution, analysis was undertaken using nanoelectrospray mass spectrometry (nESI-MS). While samples of the presumed *cis* and *trans* isomers both showed identical peaks that matched the predicted isotope pattern for the intact 3+ (1360 m/z) and 2+ (2114 m/z) charged cages (see section 2.5.3), their collision-induced dissociation (CID) pathways differed significantly (see Figure 2.2). For instance, MS^2 experiments showed that with increasing kinetic energy, the isolated intact 3+ charged cage [[(H**L**^{1}Pt)$_6$(4,4′-bipy)$_3$(tpt)$_2$](PF$_6$)$_3$]$^{3+}$ of the *cis* isomer initially fragments to give ions at 1308 and 1464 m/z, which then fragment further to a dominant species at 1152 m/z (see Figure 2.2a).

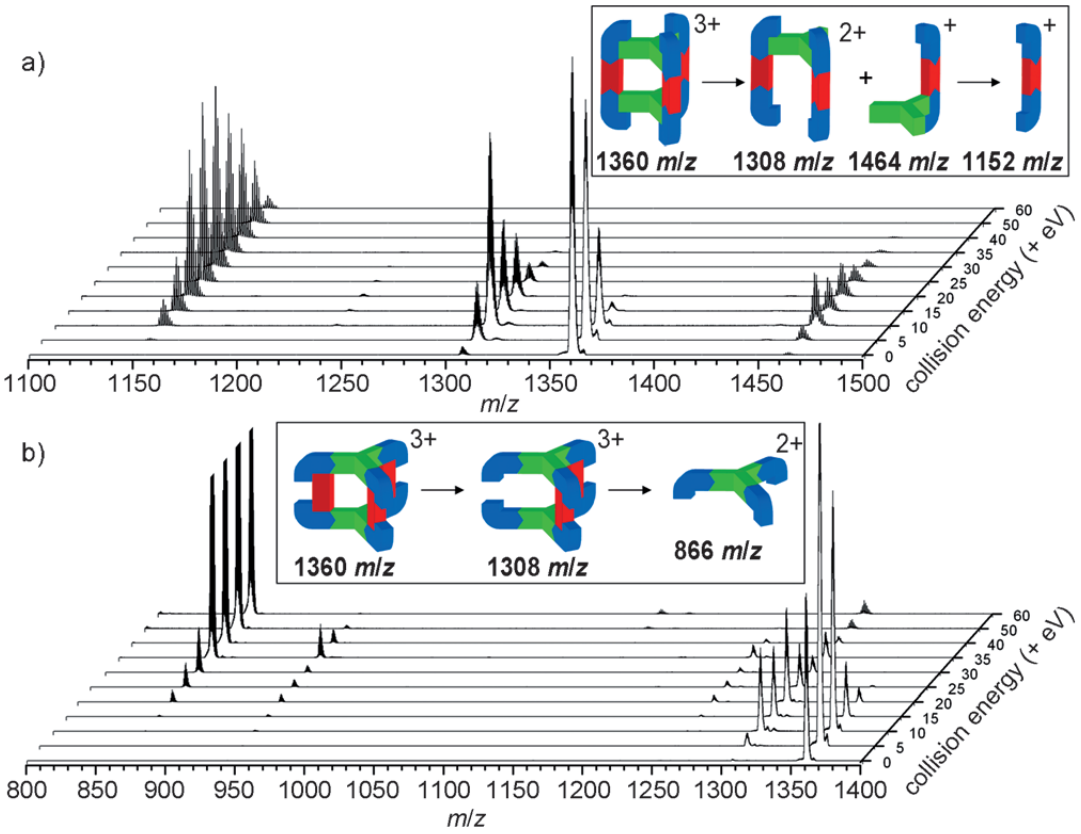

Figure 2.2. Partial nESI spectra with increasing collisional energy of the +3 intact prism (1360 *m/z*) to illuminate the CID pathways (see insets) for a) *cis* and b) *trans*-[(H**L**^{1}Pt)$_6$(4,4′-bipy)$_3$(tpt)$_2$](PF$_6$)$_6$.

Although, the singly charged peak at 1152 *m/z* unambiguously corresponds to [[(H**L**^{1}Pt)$_2$(4,4′-bipy)]PF$_6$]$^+$, and thus supports the assignment of the *cis* isomer, in which the weaker *trans*-to-phenylato Pt-tpt bond undergoes selective dissociation at lower potential, the peaks at both 1308 (+2) and 1464 (+1) *m/z* could correspond to more than one different structure with the formulas of [[(H**L**^{1}Pt)$_4$(4,4′-bipy)$_2$(tpt)](PF$_6$)$_2$]$^{2+}$ and [[(H**L**^{1}Pt)$_2$(4,4′-bipy)(tpt)]PF$_6$]$^+$, respectively. However, MS^3 experiments of both the species at 1308 and 1464 *m/z* showed the predominant appearance of the +1 ion at 1152 *m/z* ([[(H**L**^{1}Pt)$_2$(4,4′-bipy)]PF$_6$]$^+$). This finding suggests that the ions at 1308 and 1464 *m/z* correspond to tpt coordinated with two and one [(H**L**^{1}Pt)$_2$(4,4′-bipy)] unit(s), respectively, and that initial fragmentation of the cage results from cleavage of Pt-tpt bonds from adjacent panels (Figure 2.2a, inset). When the isolated 3+ ion from the *trans* isomer was subjected to the same CID experiment, a signal at 1308 *m/z* was also observed at low voltage (Figure 2.2b), yet

the different charge state (+3) indicates that the initial fragmentation involves the loss of a single 4,4′-bipy ligand to give $[[(H\mathbf{L^1}Pt)_6(4,4'\text{-bipy})_2(tpt)_2](PF_6)_3]^{3+}$ (see section 2.5.3). At higher potential, this peak diminishes with a concomitant appearance of a +2 ion at 866 *m*/*z*, which unequivocally corresponds to $[(H\mathbf{L^1}Pt)_3(tpt)]^{3+}$. This observation fits with a preferential, low-energy dissociation of the weaker Pt-4,4′-bipy bond from the *trans* isomer (Figure 2.2b, inset).

2.3.2 2-phenylpyridine Pt(II) cages

To ascertain whether a kinetic self-assembly strategy could be used if the labile coordination site isn't initially masked, we decided to also investigate the sequential addition of tpt and 4,4′-bipy to both $[(\mathbf{L^2}Pt)_2Cl_2]$ and $[(\mathbf{L^2}Pt)Cl_2]Bu_4N$, where H$\mathbf{L^2}$ is the bidentate C^N ligand 2-phenylpyridine (Scheme 2.2). The ^{1}H NMR spectrum of a mixture of $[(\mathbf{L^2}Pt)_2Cl_2]$ and 0.5 eq of 4,4′-bipy (Scheme 2.2, route 1, step a) showed the appearance of several new peaks after 5 min (Figure 2.4b); these peaks differed from those of the $[(\mathbf{L^2}Pt)_2Cl_2]$ starting material (Figure 2.4a). However, the gradual disappearance of these initial peaks and the concomitant appearance of a new set of signals, which converged to a single species after 24 h at 45 °C, was observed (Figure 2.4c). Based on the relative chemical shifts, and in particular the significant differences of H_E and H_F in the initial and final compounds (which is caused by shielding by the coordinated 4,4′-bipy ligand), it appears that *trans*-$[(\mathbf{L^2}Pt)_2(4,4'\text{-bipy})Cl_2]$ is the initial kinetic product, which rearranges into the thermodynamically (and kinetically) more-stable *cis*-$[(\mathbf{L^2}Pt)_2(4,4'\text{-bipy})Cl_2]$ (illustrated in Figure 2.3).[8] After halide extraction using AgX (where X = (+)-camphor-10-sulfonate), treatment with tpt, and then anion exchange with NH_4PF_6, *cis*-$[(\mathbf{L^2}Pt)_6(4,4'\text{-bipy})_3(tpt)_2](PF_6)_6$ was isolated in virtually quantitative yield (Scheme 2.2, route 1, step b).

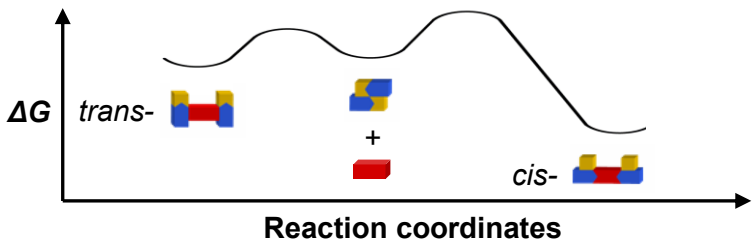

Figure 2.3. Reaction diagram for the rearrangement of $[(\mathbf{L^2}Pt)_2(4,4'\text{-bipy})Cl_2]$ from the initial *trans* isomer to the kinetically more stable *cis*.

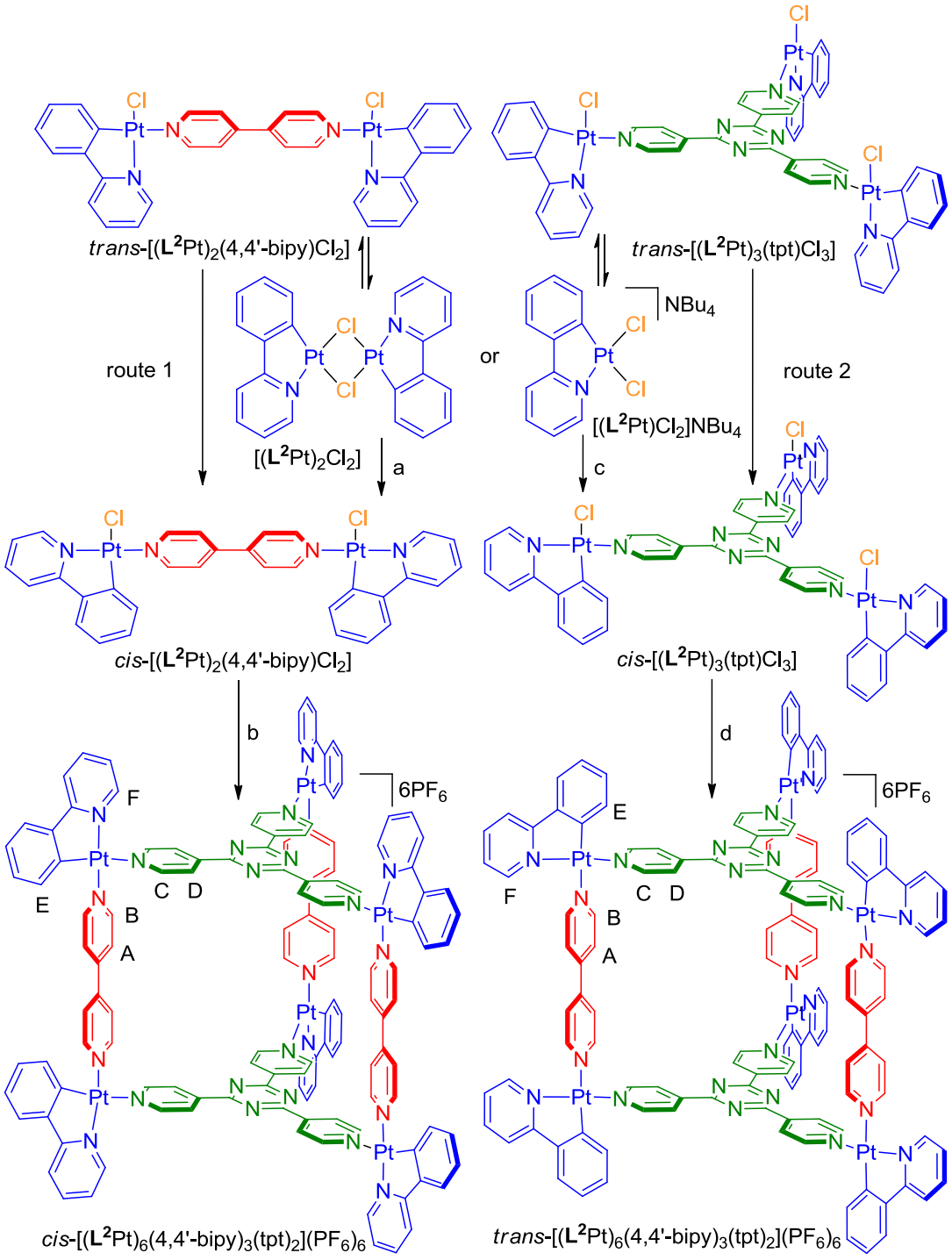

Scheme 2.2. Kinetically controlled synthesis using an "unmasked" corner protecting ligand. Conditions: a) 4,4′-bipy, $C_2H_2Cl_4$, 45 °C, 24 h; b) (i) AgX (where X = (+)-camphor-10-sulfonate), $C_2H_2Cl_4$, RT, 3 h; (ii) tpt, $C_2H_2Cl_4$, RT, 24 h; (iii) NH_4PF_6, 98% (starting from $[(\mathbf{L^2}Pt)_2Cl_2]$); c) tpt, $C_2H_2Cl_4$, 45 °C, 24 h; d) (i) AgX (where X = (+)-camphor-10-sulfonate), $C_2H_2Cl_4$, RT, 3 h; (ii) 4,4′-bipy, $C_2H_2Cl_4$, RT, 24 h; (iii) NH_4PF_6, 77% (starting from $[(\mathbf{L^2}Pt)_2Cl_2]$).

The ^{1}H NMR spectrum of this product (Figure 2.4d) again suggested the formation of a single isomer. When the sequence of addition of 4,4′-bipy and tpt to [(**L**²Pt)$_2$Cl$_2$] was switched (Scheme 2.2, route 2) a single, yet different product was obtained. A comparison of the ^{1}H NMR spectra of the two isomers showed significant differences (Figure 2.4d and 2.4e), particularly in resonances $H_{A–F}$.

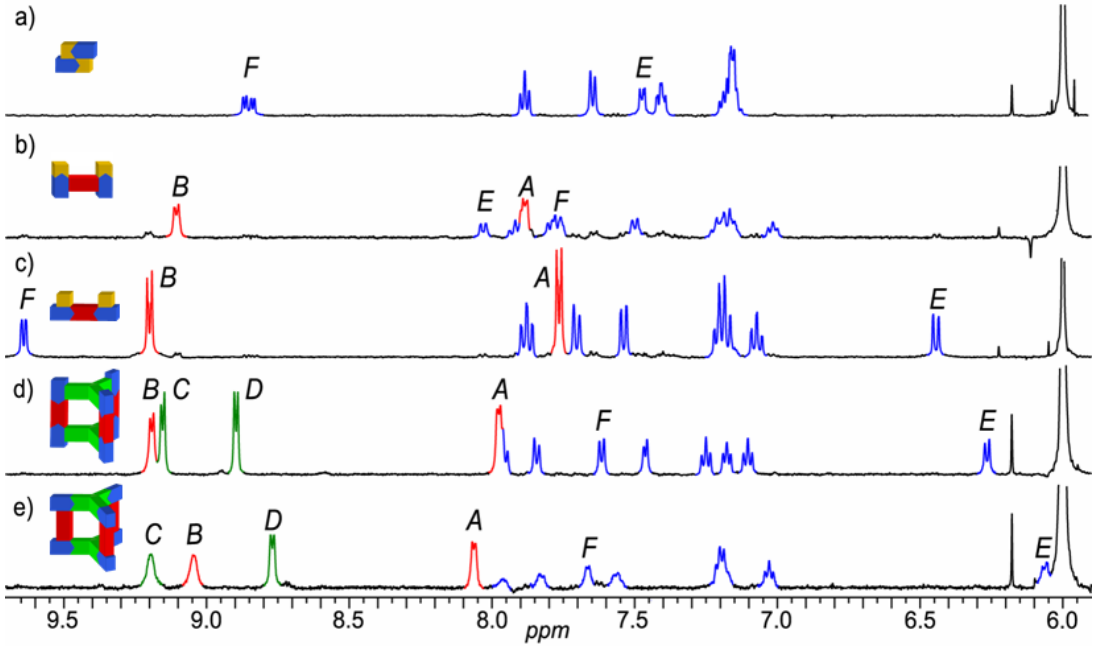

Figure 2.4. ^{1}H NMR spectra showing the kinetic self-assembly reaction starting from [(**L**²Pt)$_2$Cl$_2$] (500 MHz, $C_2D_2Cl_4$, 298 K). a) [(**L**²Pt)$_2$Cl$_2$] only; b) *trans*-[(**L**²Pt)$_2$(4,4′-bipy)Cl$_2$]; c) *cis*-[(**L**²Pt)$_2$(4,4′-bipy)Cl$_2$]; d) *cis*-[(**L**²Pt)$_6$(4,4′-bipy)$_3$(tpt)$_2$](PF$_6$)$_6$; e) *trans*-[(**L**²Pt)$_6$(4,4′-bipy)$_3$(tpt)$_2$](PF$_6$)$_6$. The assignments correspond to the lettering shown in Scheme 2.2.

The nESI mass spectra of *cis* and *trans*-[(**L**²Pt)$_6$(4,4′-bipy)$_3$(tpt)$_2$](PF$_6$)$_6$ showed identical peaks at 1208 and 1884 *m*/*z*, which matched the predicted isotope patterns for the intact +3 and +2 charged prisms, respectively (see section 2.5.3). However, in contrast to the analogous experiments with *cis* and *trans*-[(H**L**¹Pt)$_6$(4,4′-bipy)$_3$(tpt)$_2$](PF$_6$)$_6$, the CID of the *cis* and *trans* isomers of [(**L**²Pt)$_6$(4,4′-bipy)$_3$(tpt)$_2$](PF$_6$)$_6$ showed mainly peaks that did not correspond to any sensible combinations of **L**²Pt, 4,4′-bipy, tpt, and PF_6^-. Instead, the dominant CID pathway for both *cis* and *trans*-[[(**L**²Pt)$_6$(4,4′-bipy)$_3$(tpt)$_2$](PF$_6$)$_3$]$^{3+}$ involves fluoride abstraction from the PF_6^- counteranions. With the *cis* isomer, the disappearance of the 1208 *m*/*z* peak is initially accompanied by a dominant species at 1093 *m*/*z*, which corresponds to

the formula $[[(\mathbf{L^2}Pt)_4(4,4'\text{-bipy})_2(tpt)F]PF_6]^{2+}$ (Figure 2.5a). In an analogous manner to *cis* isomer of $[(H\mathbf{L^1}Pt)_6(4,4'\text{-bipy})_3(tpt)_2](PF_6)_6$, it appears that the initial fragmentation pathway involves the cleavage of the weaker Pt-tpt bonds from adjacent panels (also supported by a smaller intensity ion at 1311 *m*/*z*, which corresponds to $[[(\mathbf{L^2}Pt)_2(4,4'\text{-bipy})(tpt)]PF_6]^+$), a route that is either promoted or stabilised by abstraction of fluoride from one of the PF_6^- counteranions (Figure 2.5a, inset). MS^3 experiments show that the disappearance of this 1093 *m*/*z* ion results from the dissociation into a low-intensity ion at 873 *m*/*z*, which matches $[(\mathbf{L^2}Pt)_2(4,4'\text{-bipy})F]^+$, and subsequent MS^4 experiments show that this fragments into a singly charged ion at 505 *m*/*z*, by loss of the neutral $[(\mathbf{L^2}Pt)F]$ from $[(\mathbf{L^2}Pt)_2(4,4'\text{-bipy})F]^+$. For the *trans* isomer, the fragmentation pathway appears to first involve loss of a single 4,4′-bipy, again either promoted or stabilised by fluoride abstraction from the counter anion, to give $[[(\mathbf{L^2}Pt)_6(4,4'\text{-bipy})_2(tpt)_2F](PF_6)_2]^{3+}$ (1114 *m*/*z*), which subsequently loses another 4,4′-bipy by a fluoride promoted/stabilised route to produce $[[(\mathbf{L^2}Pt)_6(4,4'\text{-bipy})(tpt)_2F_2](PF_6)_2]^{3+}$ (1020 *m*/*z*). Again, the selective loss of 4,4′-bipy ligands from the weaker *trans*-to-phenylato coordination sites supports the formation of *trans*-$[(\mathbf{L^2}Pt)_6(4,4'\text{-bipy})_3(tpt)_2](PF_6)_6$ (Figure 2.5b, inset).

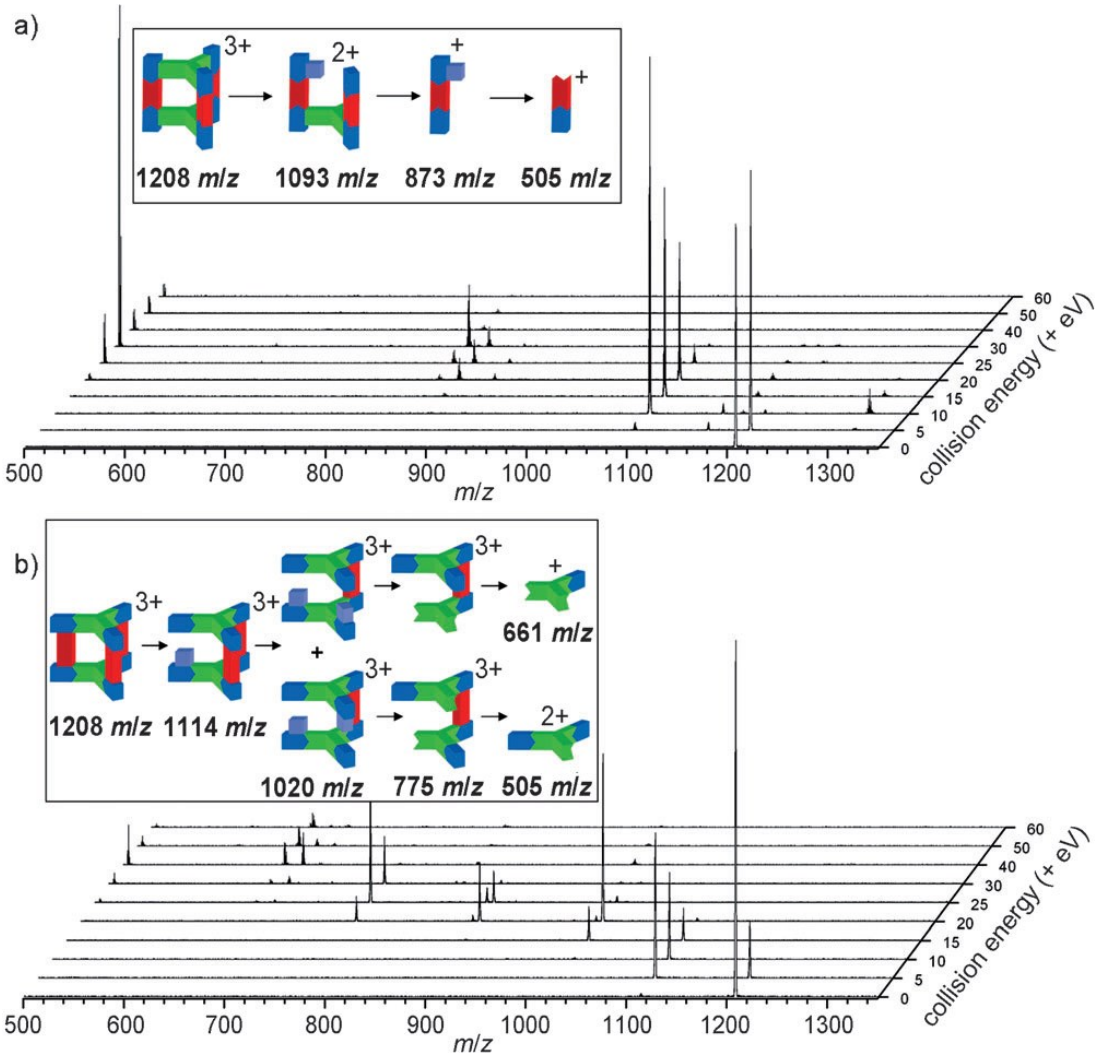

Figure 2.5. Partial nESI mass spectra with increasing collisional energy of the +3 intact prism (1208 *m/z*) to illuminate the fluoride (purple) induced CID pathways (see insets) for a) *cis* and b) *trans*-[(**L²**Pt)$_6$(4,4′-bipy)$_3$(tpt)$_2$](PF$_6$)$_6$.

The four metallosupramolecular stereochemical isomers do not undergo isomerisation, or reassemble to generate other assemblies (e.g. Pt$_4$ squares or Pt$_6$(tpt)$_4$ cages) at room temperature in solution.[9] We attribute this stability to the non-labile Pt-N bonds *trans* to the nitrogen donors of H**L¹**/**L²**; although these bonds form readily at room temperature (or just above in the case of **L²**) from the corresponding solvato/halide complexes, the activation barrier for de-coordination is such that this step is essentially irreversible under ambient conditions. Therefore the sequence in which the N-donor bridging ligands are added to the starting platinum complexes determines the stereochemical outcome of the reaction. In this regard, the synthesis of these

metallosupramolecular isomers combines elements of covalent (irreversible) synthesis and noncovalent (reversible) thermodynamically controlled assembly. It could also be expected that the isomers would show some thermodynamic bias towards either the *cis* or the *trans* form, however, heating samples of either *cis* or *trans*-[(H**L**^{1}/**L**^{2}Pt)$_6$(4,4′-bipy)$_3$(tpt)$_2$](PF$_6$)$_6$ at 80 °C for 24 h results in a complex mixture with no obvious preference for a single species. This is perhaps unsurprising as to gain greater than 95% selectivity for a single species, an energy difference greater than 1.74 kcal mol^{-1} would be required at 298 K.[10] This is in marked contrast to the sequential, kinetically controlled syntheses described herein; these syntheses give greater than 95% selectivity for single stereochemical isomers, thus highlighting the potential benefits of exploiting differences in rates of assembly, rather than simply considering ground-state energies, for the preparation of multicomponent systems.

Since the completion of this work these metallosupramolecular cages were further characterised using innovative ion mobility mass spectrometry techniques.[11]

2.4 Conclusion

The vast difference in labilities of *cis* exchangeable platinum coordination sites have been exploited to selectively synthesise multicomponent stereoisomeric assemblies using a template-free, sequential, kinetically controlled approach. This approach has the potential to generate other more complex and less symmetric coordinationally driven supramolecular assemblies. The highly shape-specific cavities could then play *host* to selective *guest* binding and catalyse regio- and stereo-specific reactions.

2.5 Experimental Section

2.5.1 General Experimental Procedure

Unless stated otherwise, all reagents and solvents were purchased from commercial sources and used without further purification. *cis*-[(H**L**^{1}Pt)$_6$(4,4′-bipy)$_3$(tpt)$_2$](PF$_6$)$_6$ was synthesised as previously described.[7] [**L**^{1}Pt(DMSO)],[12] [(**L**^{2}Pt)$_2$Cl$_2$],[8a] 2,4,6-tris(4-pyridyl)-1,3,5-triazine[13] (tpt) and AgX (where X = (+)-camphor-10-sulfonate)[14] were prepared according to the literature procedures. 4,4′-bipy·2CSA was prepared by mixing 4,4′-bipy (1 eq) with CSA (2 eq) in CH_2Cl_2, followed by removal of the solvent under reduced pressure.

2.5.2 Synthesis

2.5.2.1 Synthesis of [(HL^{1}Pt)$_6$(4,4′-bipy)$_3$(tpt)$_2$](PF$_6$)$_6$

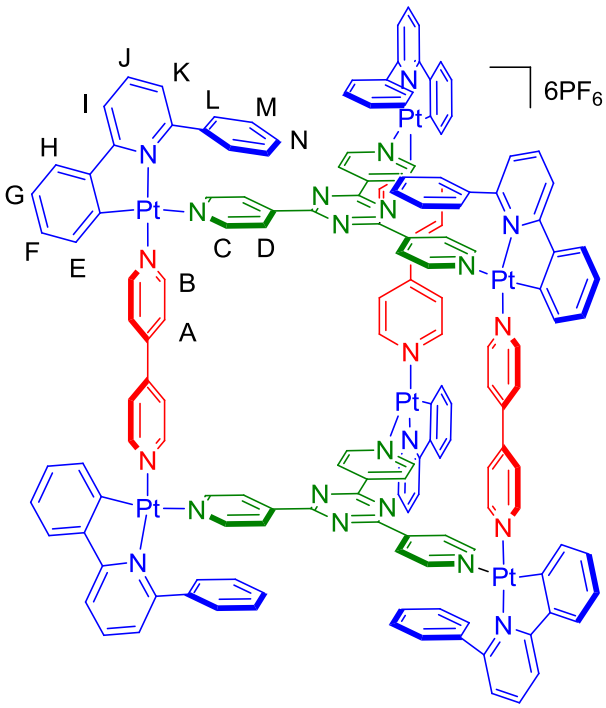

cis-[(H**L**^{1}Pt)$_6$(4,4′-bipy)$_3$(tpt)$_2$](PF$_6$)$_6$

The synthesis of *cis*-[(H**L**^{1}Pt)$_6$(4,4′-bipy)$_3$(tpt)$_2$](PF$_6$)$_6$ as reported in the literature.[7] ^{1}H NMR (500 MHz, $C_2D_2Cl_4$): 8.97 (12H, d, J = 6.5 Hz, H_B), 8.13 (12H, d, J = 6.0, H_C), 8.02

(18H, m, H_{D+J}), 7.90 (6H, d, J = 8.0 Hz, H_I), 7.74 (12H, d, J = 6.5 Hz, H_A), 7.70 (6H, d, J = 8.3 Hz, H_H), 7.44 (30H, m, H_{L+M+N}), 7.29 (12H, m, H_{G+K}), 7.08 (6H, m, H_F), 6.26 (6H, d, J = 7.2 Hz, H_E). nESI (TCE): *m/z* = 2112.1 $[(H\mathbf{L^1}Pt)_6(4,4'\text{-bipy})_3(tpt)_2(PF_6)_4]^{2+}$, 1360.1 $[(H\mathbf{L^1}Pt)_6(4,4'\text{-bipy})_3(tpt)_2(PF_6)_3]^{3+}$.

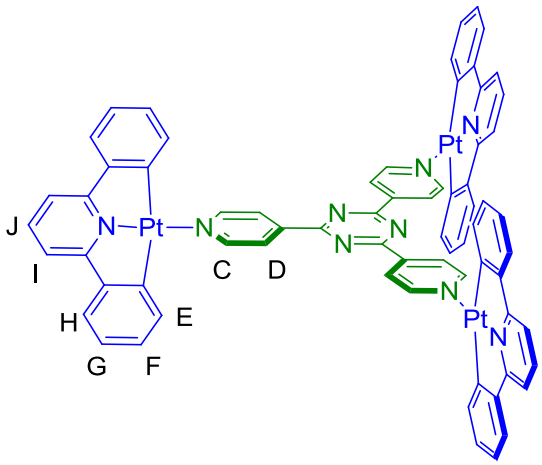

$[(\mathbf{L^1}Pt)_3(tpt)]$

$[\mathbf{L^1}Pt(DMSO)]$ (0.50 g, 1.0 mmol) was dissolved in CH_2Cl_2, to which tpt (0.10 g, 0.33 mmol) was charged. The resulting mixture was stirred for 18 h at RT, before being filtered and washed with CH_2Cl_2 (30 mL) to give the title compound as a dark purple solid (0.432 g, 85%). ^{1}H NMR (500 MHz, $C_2D_2Cl_4$): 9.33 (6H, d, J = 6.1 Hz, H_C), 8.62 (6H, d, J = 6.1 Hz, H_D), 7.55 (3H, t, J = 7.9 Hz, H_J), 7.46 (6H, d, J = 7.8 Hz, H_H), 7.30 (6H, m, H_F), 7.24 (6H, d, J = 7.9 Hz, H_I), 7.13 (6H, m, H_G), 7.03 (6H, d, J = 7.0 Hz, H_E); ^{13}C NMR (126 MHz, $C_2Cl_4D_2$): 171.0 170.0, 167.6, 154.3, 149.1, 141.2, 139.7, 132.8, 130.5, 124.9, 124.1, 124.0, 114.5; LR-FAB: *m/z* = 1586.2 $[(\mathbf{L}Pt)_3(tpt)H]^+$.

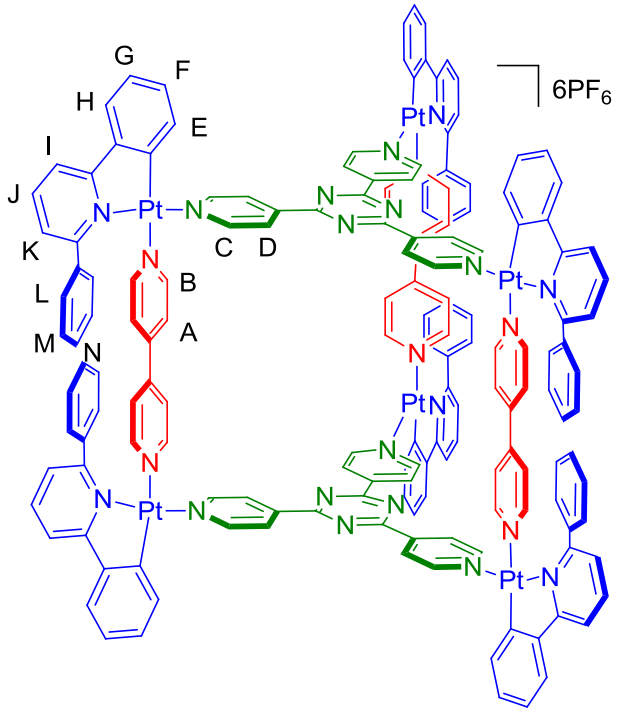

trans-[(H**L**^{1}Pt)$_6$(4,4′-bipy)$_3$(tpt)$_2$](PF$_6$)$_6$

To a suspension of [(**L**^{1}Pt)$_3$(tpt)] (57.4 mg, 0.036 mmol) in CH_2Cl_2 (7 mL) was added 4,4′-bipy·2CSA (33.7 mg, 0.054 mmol). Over 3 h, the red suspension gradually dissolved to give a clear yellow solution. The volume of solvent was reduced to *ca.* 3 mL under reduced pressure. NH_4PF_6 (59.0 mg, 0.36 mmol) in acetone (3 mL) was added to the reaction mixture and stirred at RT for 30 min. The resultant suspension was filtered off and washed with acetone, CH_2Cl_2 and Et_2O to yield a pale orange solid (80.5 mg, 99%). ^{1}H NMR (500 MHz, $C_2D_2Cl_4$): 9.02 (12H, d, J = 6.5 Hz, H_C), 8.57 (12H, d, J = 6.5 Hz, H_D), 8.13 (12H, d, J = 6.2 Hz, H_B), 8.07 (6H, m, H_J), 7.92 (6H, d, J = 8.2 Hz, H_I), 7.68 (6H, d, J = 8.1 Hz, H_H), 7.55 (12H, d, J = 7.4 Hz, H_L), 7.43 (6H, m, H_N), 7.34 (18H, m, H_{K+M}), 7.24 (6H, m, H_G), 7.19 (12H, d, J = 6.2 Hz, H_A), 6.99 (6H, m, H_F), 6.06 (6H, d, J = 7.6 Hz, H_E). nESI (TCE): m/z = 2112.1 [(H**L**^{1}Pt)$_6$(4,4′-bipy)$_3$(tpt)$_2$(PF$_6$)$_4$]$^{2+}$, 1360.1 [(H**L**^{1}Pt)$_6$(4,4′-bipy)$_3$(tpt)$_2$(PF$_6$)$_3$]$^{3+}$.

2.5.2.2 Synthesis of $[(HL^1Pt)_6(4,4'\text{-bipy})_3(tpt)_2](PF_6)_6$ and $[(L^2Pt)_6(4,4'\text{-bipy})_3(tpt)_2](PF_6)_6$

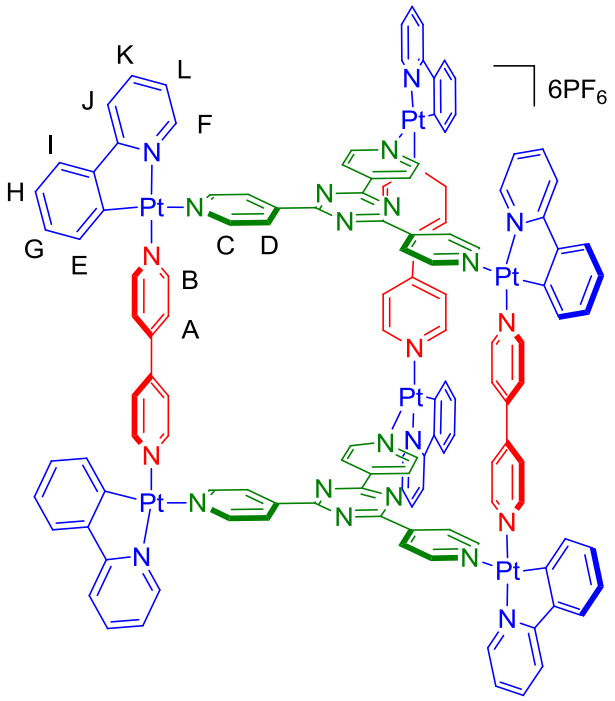

cis-$[(\mathbf{L^2}Pt)_6(4,4'\text{-bipy})_3(tpt)_2](PF_6)_6$

To a yellow suspension of $[(\mathbf{L^2}Pt)_2Cl_2]$ (99.9 mg, 0.130 mmol) in TCE (15 mL) was charged 4,4′-bipyridine (20.3 mg, 0.130 mmol). The colour of the solution and suspension changed to a brighter yellow with gentle heating at 45 °C for 24 h. AgX (where X = (+)-camphor-10-sulfonate) (97.0 mg, 0.286 mmol) was charged to the mixture, which was then stirred for a further 3 h at RT. The colour changed to a dark orange/red. The resulting AgCl was removed by filtration through celite and thoroughly washed with CH_2Cl_2. The filtrate was concentrated by the removal of CH_2Cl_2 under reduced pressure and tpt (27.0 mg, 0.0867 mmol) charged to the orange solution. Over the course of 24 h the colour of the solution changed to yellow and a fine precipitate formed. NH_4PF_6 (141.0 mg, 0.867 mmol) was added in acetone (15 mL) and the mixture changed colour to a pale yellow after 1 h. The suspension was filtered using a Buchner funnel, washed with acetone, DCM and Et_2O to yield a pale orange solid (172 mg, 98%). ^{1}H NMR (500 MHz, $C_2D_2Cl_4$): 9.19 (12H, d, J = 5.9 Hz, H_B), 9.15 (12H, d, J = 6.0 Hz, H_C), 8.90 (12H, d, J = 6.0 Hz, H_D), 8.03 – 7.93 (18H, m, H_{A+K}), 7.84 (6H, d, J = 8.6 Hz, H_J), 7.62 (6H, d, J = 8.0 Hz, H_I), 7.46 (6H, d, J = 6.4 Hz, H_F), 7.25 (6H, m, H_H), 7.18 (6H, m,

H_L), 7.10 (6H, m, H_G), 6.27 (6H, d, J = 7.6 Hz, H_E); nESI (TCE): m/z = 1884.6 [(**L**²Pt)$_6$(4,4′-bipy)$_3$(tpt)$_2$(PF$_6$)$_4$]$^{2+}$, 1208.9 [(**L**²Pt)$_6$(4,4′-bipy)$_3$(tpt)$_2$(PF$_6$)$_3$]$^{3+}$.

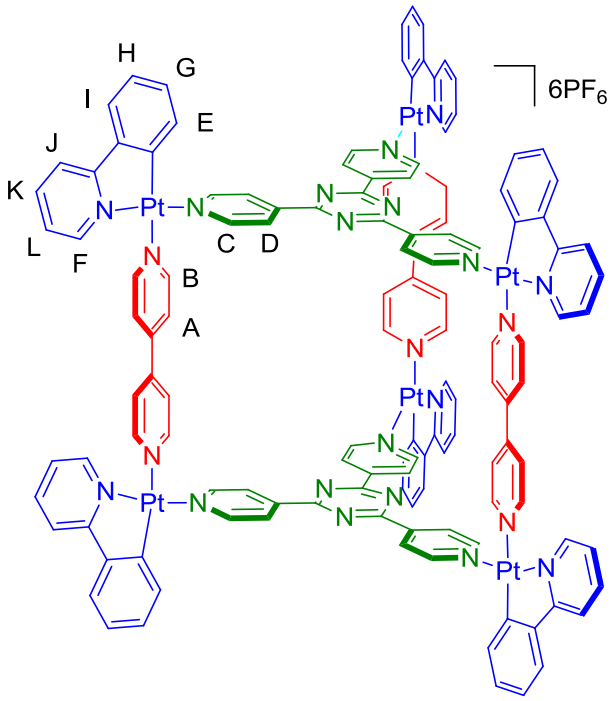

trans-[(**L**²Pt)$_6$(4,4′-bipy)$_3$(tpt)$_2$](PF$_6$)$_6$

To a yellow suspension of [(**L**²Pt)$_2$Cl$_2$] (81.5 mg, 0.106 mmol) in TCE (15 mL) was charged tpt (22.0 mg, 0.071 mmol). The colour of the solution and suspension changed to slightly orange with gentle heating at 45 °C for 24 h. AgX (where X = (+)-camphor-10-sulfonate, 79.0 mg, 0.233 mmol) was charged to the mixture, which was then stirred at RT for 3 h. The colour changed to a yellow/green. The resulting AgCl was removed by filtration through celite and thoroughly washed with CH_2Cl_2. The filtrate was concentrated by the removal of CH_2Cl_2 under reduced pressure and 4,4′-bipyridine (16.5 mg, 0.106 mmol) charged to the yellow solution. Over the course of 24 h the colour of the solution remained yellow. NH_4PF_6 (115.0 mg, 0.706 mmol) was added in acetone (15 mL) and the mixture paled slightly over 1 h. The resulting suspension was filtered using a Buchner funnel, washed with acetone, CH_2Cl_2 and Et_2O to yield a pale yellow solid. Further materiel was obtained following concentration of the filtrate under reduced pressure at 60 °C, which was again isolated following filtration and washings with acetone, CH_2Cl_2 and Et_2O (total yield from 1st and 2nd crop; 110 mg, 77%). ^{1}H NMR (500 MHz, $C_2D_2Cl_4$): 9.19 (12H, br, H_C), 9.05 (12H, br, H_B), 8.77 (12H, d, J

= 5.3 Hz, H_D), 8.06 (12H, d, J = 6.3 Hz, H_A), 7.96 (6H, br, H_K), 7.83 (6H, br, H_J), 7.67 (6H, br, H_F), 7.56 (6H, m, H_I), 7.20 (12H, m, H_{H+L}), 7.03 (6H, m, H_G), 6.06 (6H, d, J = 6.9 Hz, H_E); nESI (TCE): m/z = 1884.6 $[(\mathbf{L}^2\text{Pt})_6(4,4'\text{-bipy})_3(\text{tpt})_2(\text{PF}_6)_4]^{2+}$, 1208.9 $[(\mathbf{L}^2\text{Pt})_6(4,4'\text{-bipy})_3(\text{tpt})_2(\text{PF}_6)_3]^{3+}$.

2.5.3 Mass spectra and isotopic distribution patterns for selected peaks

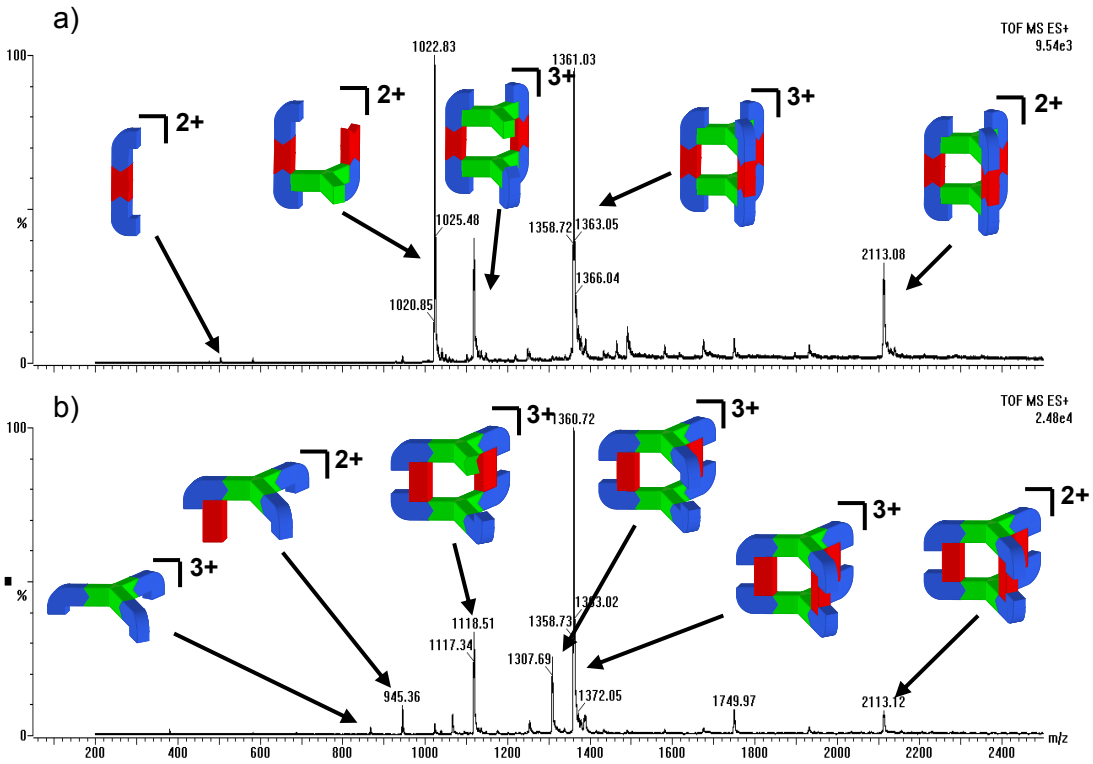

Figure 2.6. nESI (100 μM in TCE) mass spectra of a) *cis*- and b) *trans*-$[(\text{H}\mathbf{L}^1\text{Pt})_6(4,4'\text{-bipy})_3(\text{tpt})_2](\text{PF}_6)_6$. PF_6^- counterions are omitted for clarity.

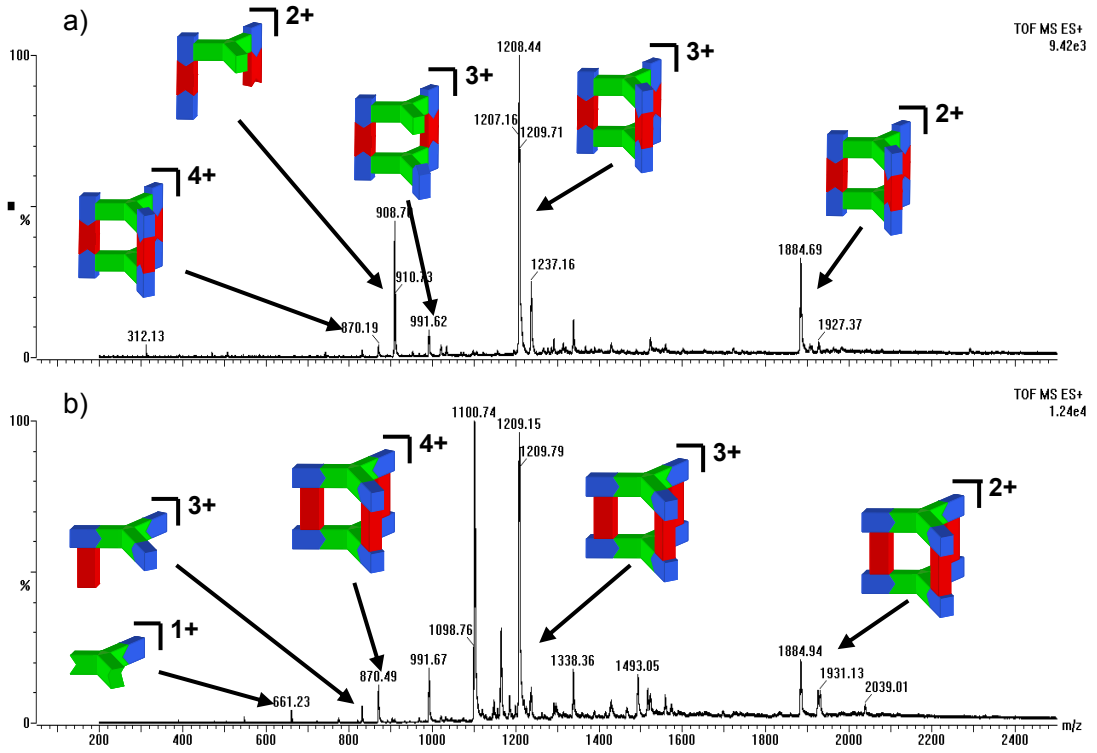

Figure 2.7. nESI (100 μM in TCE) mass spectra of a) *cis*- and b) *trans*-[(**L**²Pt)$_6$(4,4′-bipy)$_3$(tpt)$_2$](PF$_6$)$_6$. PF$_6^-$ counter ions are omitted for clarity.

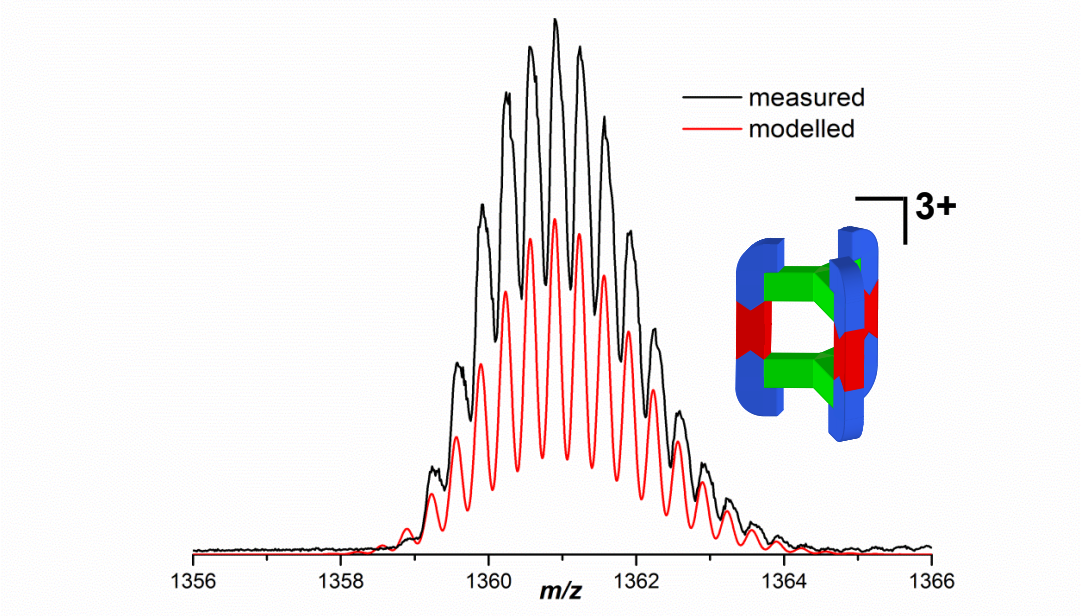

Figure 2.8. nESI-MS measured (black) versus modelled (red) isotopic distribution pattern for *cis*-[[(H**L**^{1}Pt)$_6$(4,4′-bipy)$_3$(tpt)$_2$](PF$_6$)$_3$]$^{3+}$.

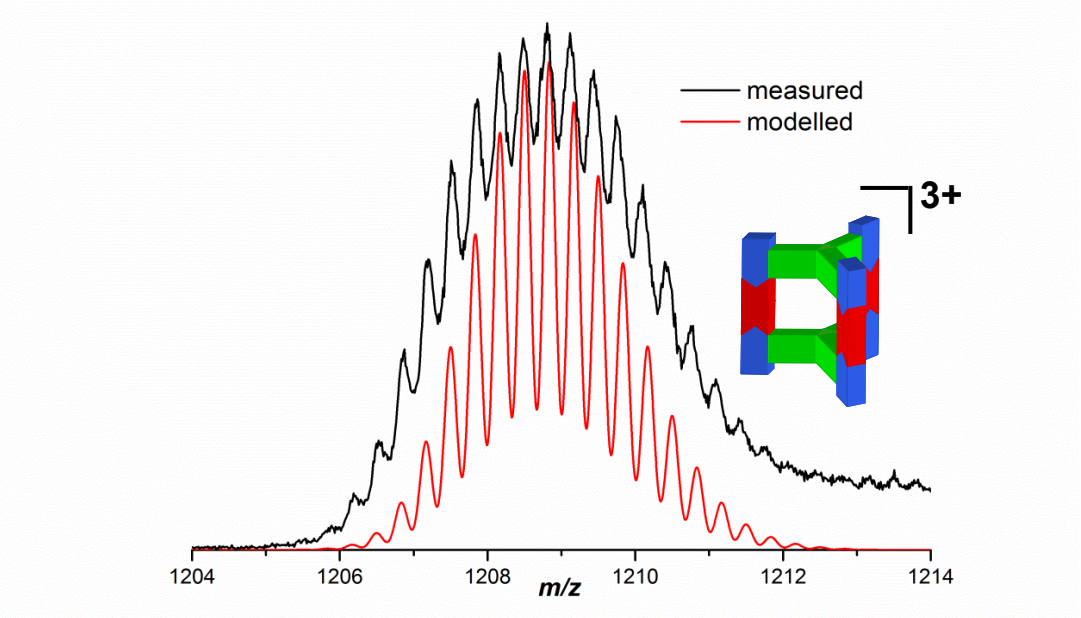

Figure 2.9. nESI-MS measured (black) versus modelled (red) isotopic distribution pattern for *cis*-[[(**L**^{2}Pt)$_6$(4,4′-bipy)$_3$(tpt)$_2$](PF$_6$)$_3$]$^{3+}$.

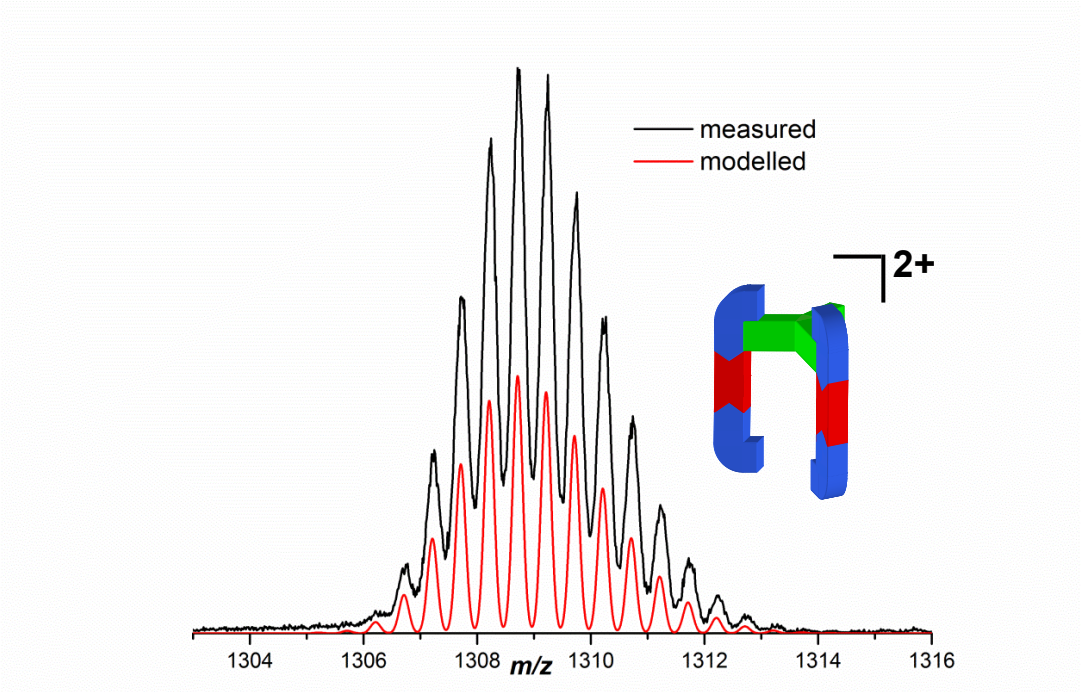

Figure 2.10. nESI-MS measured (black) versus modelled (red) isotopic distribution pattern for *cis*-[[(H**L**^{1}Pt)$_4$(4,4′-bipy)$_2$(tpt)](PF$_6$)$_2$]$^{2+}$ fragment.

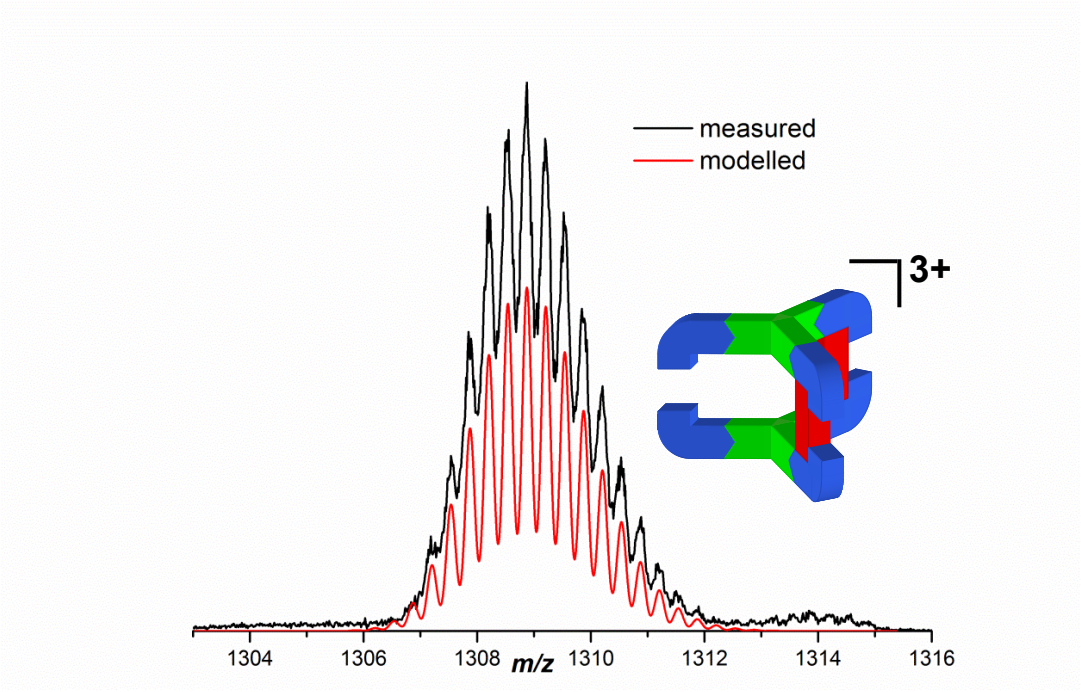

Figure 2.11. nESI-MS measured (black) versus modelled (red) isotopic distribution pattern for *trans*-[[(H**L**^{1}Pt)$_6$(4,4′-bipy)$_2$(tpt)$_2$](PF$_6$)$_3$]$^{3+}$ fragment.

2.6 Notes and References

[1] Selected examples on thermodynamically controlled self-assemblies: a) Q. F. Sun, J. Iwasa, D. Ogawa, Y. Ishido, S. Sato, T. Ozeki, Y. Sei, K. Yamaguchi, M. Fujita, *Science* **2010**, *328*, 1144-1147; b) M. Wang, Y.-R. Zheng, K. Ghosh, P. J. Stang, *J. Am. Chem. Soc.* **2010**, *132*, 6282-6283; c) S. Hiraoka, M. Kiyokawa, S. Hashida, M. Shionoya, *Angew. Chem. Int. Ed.* **2010**, *49*, 138-143; d) C. J. Hastings, M. P. Backlund, R. G. Bergman, K. N. Raymond, *Angew. Chem. Int. Ed.* **2011**, *50*, 10570-10573; e) T. Liu, Y. Liu, W. Xuan, Y. Cui, *Angew. Chem. Int. Ed.* **2010**, *49*, 4121-4124; f) A. Kaloudi-Chantzea, N. Karakostas, C. P. Raptopoulou, V. Psycharis, E. Saridakis, J. Griebel, R. Hermann, G. Pistolis, *J. Am. Chem. Soc.* **2010**, *132*, 16327-16329; g) J. Dömer, J. C. Slootweg, F. Hupka, K. Lammertsma, F. E. Hahn, *Angew. Chem. Int. Ed.* **2010**, *49*, 6430-6433; h) K. E. Allen, R. A. Faulkner, L. P. Harding, C. R. Rice, T. Riis-Johannessen, M. L. Voss, M. Whitehead, *Angew. Chem. Int. Ed.* **2010**, *49*, 6655-6658; i) X. Kuang, X. Wu, R. Yu, J. P. Donahue, J. Huang, C.-Z. Lu, *Nat. Chem.* **2010**, *2*, 461-465; j) M. Beyler, V. Heitz, J.-P. Sauvage, *J. Am. Chem. Soc.* **2010**, *132*, 4409-4417; k) J.-R. Li, H.-C. Zhou, *Nat. Chem.* **2010**, *2*, 893-898; l) J. L. Atwood, E. K. Brechin, S. J. Dalgarno, R. Inglis, L. F. Jones, A. Mossine, M. J. Paterson, N. P. Power, S. J. Teat, *Chem. Commun.* **2010**, *46*, 3484-3486; m) S. Perera, X. Li, M. Soler, A. Schultz, C. Wesdemiotis, C. N. Moorefield, G. R. Newkome, *Angew. Chem. Int. Ed.* **2010**, *49*, 6539-6544; n) J. Gao, J. Yan, S. G. Mitchell, H. N. Miras, A. G. Boulay, D.-L. Long, L. Cronin, *Chem. Sci.* **2011**, *2*, 1502-1508; o) A. Lledó, S. Kamioka, A. C. Sather, J. Rebek, *Angew. Chem. Int. Ed.* **2011**, *50*, 1299-1301; p) W. Meng, B. Breiner, K. Rissanen, J. D. Thoburn, J. K. Clegg, J. R. Nitschke, *Angew. Chem. Int. Ed.* **2011**, *50*, 3479-3483; q) A. Granzhan, C. m. Schouwey, T. Riis-Johannessen, R. Scopelliti, K. Severin, *J. Am. Chem. Soc.* **2011**, *133*, 7106-7115; r) M. Schmittel, M. L. Saha, J. Fan, *Org. Lett.* **2011**, *13*, 3916-3919; s) Y. Liu, C. Hu, A. Comotti, M. D. Ward, *Science* **2011**, *333*, 436-440; t) A. Stephenson, S. P. Argent, T. Riis-Johannessen, I. S. Tidmarsh, M. D. Ward, *J. Am. Chem. Soc.* **2011**, *133*, 858-870; u) C. R. K. Glasson, J. K. Clegg, J. C. McMurtrie, G. V. Meehan, L. F. Lindoy, C. A. Motti, B. Moubaraki, K. S. Murray, J. D. Cashion, *Chem. Sci.* **2011**, *2*, 540-543.

[2] Examples of metastable products that are converted into lower-energy products upon prolonged reaction times: a) B. Hasenknopf, J.-M. Lehn, N. Boumediene, E. Leize, A. Van Dorsselaer, *Angew. Chem. Int. Ed.* **1998**, *37*, 3265-3268; b) V. Paraschiv, M. Crego-Calama, T. Ishi-i, C. J. Padberg, P. Timmerman, D. N. Reinhoudt, *J. Am. Chem. Soc.* **2002**, *124*, 7638-7639; c) B. J. Holliday, Y.-M. Jeon, C. A. Mirkin, C. L. Stern, C. D. Incarvito, L. N. Zakharov, R. D. Sommer, A. L. Rheingold, *Organomet.* **2002**, *21*, 5713-5725; d) S. Tashiro, M. Tominaga, T. Kusukawa, M. Kawano, S. Sakamoto, K. Yamaguchi, M. Fujita, *Angew. Chem. Int. Ed.* **2003**, *42*, 3267-3270; e) A. Hori, K.-i. Yamashita, M. Fujita, *Angew. Chem. Int. Ed.* **2004**, *43*, 5016-5019; f) J. D. Badjić, S. J. Cantrill, J. F. Stoddart, *J. Am. Chem. Soc.* **2004**, *126*, 2288-2289; g) J. T. Davis, M. S. Kaucher, F. W. Kotch, M. A. Iezzi, B. C. Clover, K. M. Mullaugh, *Org. Lett.* **2004**, *6*, 4265-4268; h) A. Lohr, M. Lysetska, F. Würthner, *Angew. Chem. Int. Ed.* **2005**, *44*, 5071-5074; i) P. Mukhopadhyay, P. Y. Zavalij, L. Isaacs, *J. Am. Chem. Soc.* **2006**, *128*, 14093-14102; j) M. Yamanaka, Y. Yamada, Y. Sei, K. Yamaguchi, K. Kobayashi, *J. Am. Chem. Soc.* **2006**, *128*, 1531-1539; k) C. G. Claessens, M. J. Vicente-Arana, T. Torres, *Chem. Commun.* **2008**, 6378-6380; l) V. M. Cangelosi, T. G. Carter, L. N.

Zakharov, D. W. Johnson, *Chem. Commun.* **2009**, 5606-5608; m) W. Jiang, A. Schäfer, P. C. Mohr, C. A. Schalley, *J. Am. Chem. Soc.* **2010**, *132*, 2309-2320.

[3] a) P. Jennings, P. Wright, *Science* **1993**, *262*, 892-896; b) R. Pellarin, P. Schuetz, E. Guarnera, A. Caflisch, *J. Am. Chem. Soc.* **2010**, *132*, 14960-14970.

[4] Y. Sakata, S. Hiraoka, M. Shionoya, *Chem. Eur. J.* **2010**, *16*, 3318-3325.

[5] a) P. J. Stang, D. H. Cao, S. Saito, A. M. Arif, *J. Am. Chem. Soc.* **1995**, *117*, 6273-6283; b) A. Rang, M. Nieger, M. Engeser, A. Lützen, C. A. Schalley, *Chem. Commun.* **2008**, 4789.

[6] M. Fujita, F. Ibukuro, K. Yamaguchi, K. Ogura, *J. Am. Chem. Soc.* **1995**, *117*, 4175-4176.

[7] P. J. Lusby, P. Müller, S. J. Pike, A. M. Z. Slawin, *J. Am. Chem. Soc.* **2009**, *131*, 16398-16400.

[8] a) D. Black, G. Deacon, G. Edwards, *Aust. J. Chem.* **1994**, *47*, 217-227; Possible thermodynamic driving forces for the formation of cis-[(**L**^{2}Pt)$_2$(4,4′-bipy)Cl$_2$] may include minimisation of the repulsive interaction between partial positively charged pyridyl donors (see Y.-R. Zheng, Z. Zhao, M. Wang, K. Ghosh, J. B. Pollock, T. R. Cook, P. J. Stang, *J. Am. Chem. Soc.* **2010**, *132*, 16873-16882) and/or entropic factors related to desolvation upon lowering the dipole moment at the Pt centre (see F. Basolo, R. Pearson, *Mechanisms of inorganic reactions: a study of metal complexes in solution*, Wiley, London, **1967**).

[9] The corresponding (+)-camphor-10-sulfonate salts are also stable in 1,1,2,2-tetrachloroethane at RT.

[10] The Gibbs free energy for 95% selectivity was calculated using the Gibb free energy equation; $\Delta G = -RT\ln(K_{eq})$, where R = 1.9872 cal K^{-1} mol^{-1}, T = 298 K and K_{eq} = (95/5).

[10] J. Ujma, M. De Cecco, O. Chepelin, H. Levene, C. Moffat, S. J. Pike, P. J. Lusby, P. E. Barran, *Chem. Commun.* **2012**, *48*, 4423-4425.

[11] a) G. W. V. Cave, F. P. Fanizzi, R. J. Deeth, W. Errington, J. P. Rourke, *Organomet.* **2000**, *19*, 1355-1364; b) J. D. Crowley, I. M. Steele, B. Bosnich, *Inorg. Chem.* **2005**, *44*, 2989-2991.

[12] H. L. Anderson, S. Anderson, J. K. M. Sanders, *J. Chem. Soc., Perkin Trans. 1* **1995**, 2231-2245.

[13] J. Wasiak, J. Michalski, *Tetrahedron Lett.* **1994**, *35*, 9473-9476.

Chapter 3

Luminescent, Enantiopure, Phenylatopyridine Iridium-based Coordination Capsules

Published as *Luminescent, Enantiopure, Phenylatopyridine Iridium-Based Coordination Capsules*, O. Chepelin, J. Ujma, X. Wu, A. M. Z. Slawin, M. B. Pitak, S. J. Coles, J. Michel, A. C. Jones, P. E. Barran, P. J. Lusby, *J. Am. Chem. Soc.*, **2012**, *134*, 19334–19337.

Acknowledgements

For their contribution to this chapter I would like to thank Dr. Predita Barran and Jakub Ujma for their help with the mass spectrometry, Dr. Anita Jones and Dr. Xiaohua Wu for assistance with the luminescence measurements, Prof. Alexandra Slawin, Dr. Mateusz Pitak and Dr. Simon Coles for X-ray crystallography and Dr. Julien Michel for the occupancy calculations.

3.1 Synopsis

Herein, the first molecular capsule based on an $[Ir(ppy)_2]^+$ unit (ppy = 2-phenylatopyridine) has been prepared. Initial studies revealed that the Ir-pyridine bond is reversible at low temperatures and self-sorting pathways for the $[Ir(ppy)_2]^+$ unit with pyridine-based ligands are accessible in the self-assembly of discrete Ir structures. However, due to dihedral angle constraints at the exchangeable site on the Ir centres, assemblies using the tritopic tpt ligand (tpt = 2,4,6-tris(4-pyridyl)-1,3,5-triazine) *were unobtainable. Following the development of a method to resolve rac-$[(Ir(ppy)_2Cl)_2]$ into its enantiopure forms and replacing the tritopic pyridine ligand with the nitrile analogue, tcb (tcb = 1,3,5-tricyanobenzene), homochiral M_6L_4 octahedra were synthesised. Solution studies and X-ray diffraction show that these capsules encapsulate four of the six associated OTf- counteranions, which can be exchanged for other anionic guests. Photophysical studies have demonstrated how an ensemble of weakly coordinating ligands can lead to luminescence not present in comparable mononuclear systems.*

3.2 Introduction

The combination of transition metal ions and geometrically complementary, multitopic bridging organic ligands has led to the preparation of numerous molecular capsules and cages.[1] These assemblies possess well-defined internal cavities that promote the ingress of *guest* molecules so that interesting functions, such as catalysis or the stabilisation of reactive species may be observed.[1, 2] By and large, the transition metal ions within these systems have played solely a structural role, offering advantages such as predictable, well-defined coordination preferences and bond strength. However, transition metals and their complexes often possess many other notable features, such as interesting photophysical properties; arguably the most well-known class are the poly(pyridyl) complexes of ruthenium(II),[3] while more recently, analogous cyclometalated C^N iridium(III) complexes have found widespread use as luminescent biological probes[4] and as dopants in organic light-emitting devices.[5] Although several examples of metallocycles and dendrimers which feature $[Ru(terpy)_2]^{2+}$ and helicates which feature $[Ru(bipy)_3]^{2+}$ connections exist in the literature,[6] the use of Ru poly(pyridyl) or cyclometalated Ir complexes as structural components in metallosupramolecular assemblies, in particular polyhedral architectures, remains rare.[7] Herein, reported is the first molecular capsule based on an $[Ir(ppy)_2]^+$ (ppy = 2-phenylatopyridine) motif. We have shown that incorporation of this unit into a multimetallic array leads to a significant luminescence enhancement with respect to a comparable mononuclear complex, thus paving the way to capsules with light-harvesting functionality and the development of devices with emergent luminescent properties.

3.3 Results and Discussion

It was initially envisaged that $[Ir(ppy)_2]^+$ could be used in an analogous fashion to *cis*-protected square planar complexes, such as $[Pd(en)]^{2+}$ or $[Pt(dppp)]^{2+}$,[8] and that the ppy ligands, arranged in a *C*,*C*-*cis*-*N*,*N*-*trans* orientation, would sufficiently labilise the exchangeable sites to facilitate self-assembly.[9]

Prior to attempting the synthesis of an M_6L_4 capsule, the reversibility and self-sorting of pyridine ligands at the exchangeable sites on the $[Ir(ppy)_2]^+$ unit was investigated *via* the construction of a simpler M_2L_2 assembly.

3.3.1 $[(Ir(ppy)_2)_2(bpe)_2](OTf)_2$ metallamacrocycle

Ditopic 1,2-bis(4-pyridyl)ethane (bpe) ligand was used in the attempted synthesis of an M_2L_2 assembly, analogous to a Pd metallamacrocycle previously assembled by Fujita and co-workers.[10] On heating $[Ir(ppy)_2(CH_3CN)_2]OTf$ and bpe in $C_2H_4Cl_2$ for 18 h an orange precipitate was isolated (see Scheme 3.1a).

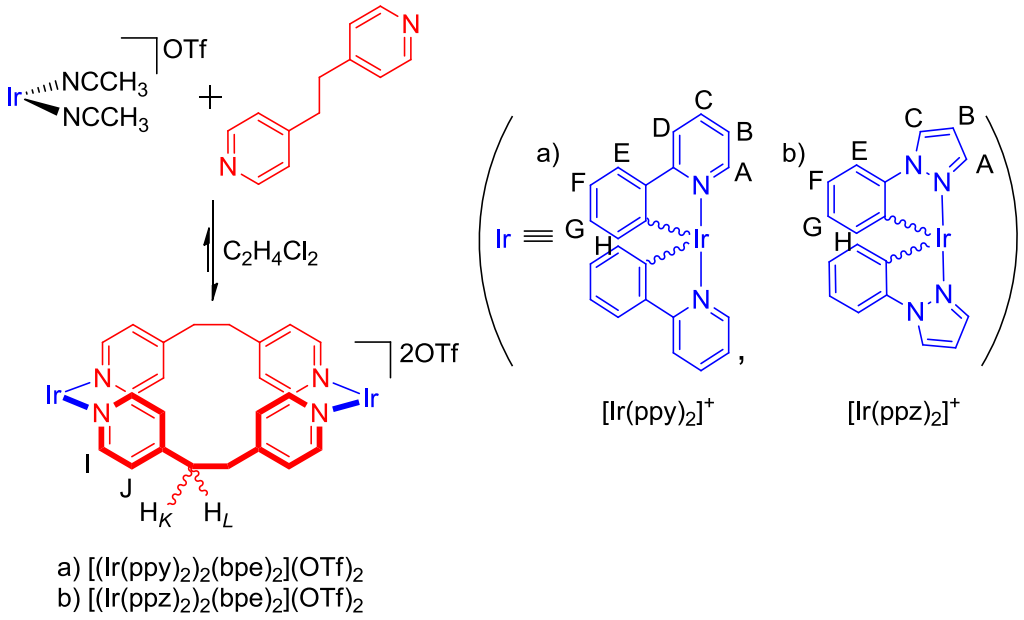

Scheme 3.1. Synthesis of heterochiral iridium metallamacrocycles $[(Ir(ppy)_2)_2(bpe)_2](OTf)_2$ and $[(Ir(ppz)_2)_2(bpe)_2](OTf)_2$ under thermodynamic control. Conditions: a) $C_2H_4Cl_2$, 50 °C, 18 h, 91%. b) $C_2H_4Cl_2$, 60 °C, 90 h, 53% (by qualitative ^1H NMR analysis).

^1H NMR revealed the formation of a symmetric assembly (see Figure 3.1a) containing twelve proton environments. All twelve ^1H signals belong to a single species with a measured diffusion coefficient log (D / m^2s^{-1}) = -9.39 and a corresponding hydrodynamic radius = 8.5 Å in CD_3NO_2 (see section 3.5.3, Figure 3.13a). Signals at 1519 and 685 m/z were observed under nESI-MS analysis, which matched the calculated isotopic distribution patterns for $[(Ir(ppy)_2)_2(bpe)_2](OTf)^+$ and $[(Ir(ppy)_2)_2(bpe)_2]^{2+}$, respectively (see section 3.5.4).

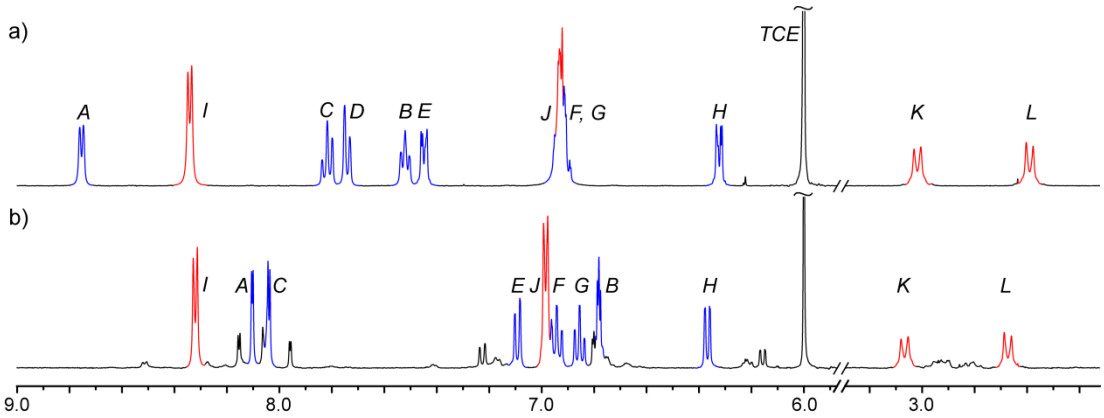

Figure 3.1. ^{1}H NMR spectra (500 MHz, $C_2D_2Cl_4$, 298 K) of a) $[(Ir(ppy)_2)_2(bpe)_2](OTf)_2$ and b) $[(Ir(ppz)_2)_2(bpe)_2](OTf)_2$.

Yellow crystals were grown by slow ether diffusion into a CH_3NO_2 solution of $[(Ir(ppy)_2)_2(bpe)_2](OTf)_2$ and from the refined X-ray diffraction (XRD) data it was observed that $[(Ir(ppy)_2)_2(bpe)_2](OTf)_2$ had crystallised in the cubic achiral space group $Ia\bar{3}$ as a racemic mixture of homochiral helicates (see Figure 3.2a).

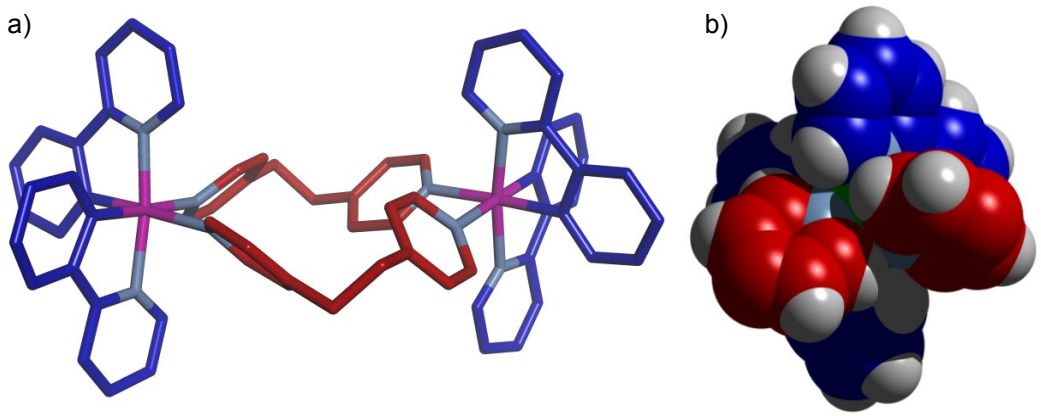

Figure 3.2. X-ray crystal structures of a) $[(Ir(ppy)_2)_2(bpe)_2]^{2+}$ and b) cross sectional space-fill view of $[(Ir(ppy)_2)_2(bpe)_2]^{2+}$, looking down the C_2 axis through the two Ir centres. The carbon atoms of ppy are shown in dark blue and bpe in red, iridium ions in magenta and nitrogen atoms in pale blue. Counterions and solvent molecules have been omitted for clarity. See section 3.5.19 for crystal data and refinement, bond lengths and angles.

Under a closer inspection, the ^{1}H NMR spectrum for $[(Ir(ppy)_2)_2(bpe)_2](OTf)_2$ (see Figure 3.1a) revealed a minor secondary splitting in the proton signals for H_E and H_H.[11]

This splitting revealed that the three possible isomers, *ΛΛ*- and *ΔΔ*- helicate and *ΛΔ*-mesocate, were all present in solution and, due to the dynamic flexibility of the bpe ligands, chiral information transfer between the two Ir centres was thus deemed not viable for this system.

The sole formation of the M_2L_2 metallamacrocycle without the formation of any higher ordered assemblies or oligomers strongly suggests that the Ir-bpe bond is kinetically reversible at low temperatures and the self-assembly process is under thermodynamic control.

3.3.2 $[(Ir(ppz)_2)_2(bpe)_2](OTf)_2$ metallamacrocycle

The synthesis of an M_2L_2 assembly using an $[Ir(ppz)_2]^+$ (ppz = 1-phenylatopyrazole) motif was also attempted to determine what effect, if any, the substitution of ppy for the ppz ligand would have on the kinetic stability. Under a similar experimental procedure as for $[Ir(ppy)_2]^+$, ^1H NMR (see Figure 3.1b) confirmed $[(Ir(ppz)_2)_2(bpe)_2](OTf)_2$ to form at 79% non-isolated yield but only after prolonged reaction times at elevated temperature. ^1H DOSY NMR confirmed the presence of a single major species with a diffusion coefficient log (D / m^2s^{-1}) = -9.39 and a hydrodynamic radius = 8.5 Å in CD_3NO_2 (see section 3.5.3, Figure 3.13b), virtually identical to the diffusion coefficient for $[(Ir(ppy)_2)_2(bpe)_2](OTf)_2$ (see section 3.5.3, Figure 3.13a). The protons $H_{I\text{-}L}$ for the coordinated bpe ligand are almost all superimposable with those for $[(Ir(ppy)_2)_2(bpe)_2](OTf)_2$, as are the phenylato protons $H_{F\text{-}H}$, however H_E is significantly shifted up field implying that the pyrazole ring is donating more electron density to the phenylato group than the pyridyl group in the ppy system. The phenylato-Ir bond is consequently weakened and, *via trans*-influence, the Ir-bpe interaction is strengthened. The greater energy input needed to form $[(Ir(ppz)_2)_2(bpe)_2](OTf)_2$, along with ^1H NMR evidence suggests that exchanging the ppy ligands for ppz increases the activation barrier to self-sorting. Further evidence that the $[(Ir(ppz)_2]^+$ unit increases the kinetic stability of a supramolecular assembly was obtained using EXSY NMR experiments in Chapter 4 (see section 4.5.7).

Given that the thermodynamically controlled synthesis of a macrocycle using the $[Ir(ppy)_2]^+$ unit and the bpe pyridine ligand was accessible at lower temperatures, a larger M_6L_4 octahedron, analogues to Fujita's Pd cage,[12] was subsequently targeted.

3.3.3 Attempted synthesis of $[(Ir(ppy)_2)_6(tpt)_4](X)_6$ octahedra

The synthesis of an M_6L_4 capsule was attempted using the commonly used 2,4,6-tris(4-pyridyl)-1,3,5-triazine (tpt) ligand[13] with the same bis(acetonitrile) iridium starting material, $[Ir(ppy)_2(CH_3CN)_2](X)$. Numerous attempts were made to synthesise $[(Ir(ppy)_2)_6(tpt)_4](X)_6$ using different counterions, solvents and a variety of different reaction conditions (see section 3.5.2.3), however, no discrete or M_6L_4 assembly was detected using either NMR or nESI-MS analysis.

Having a closer look at the ligand geometry around the iridium centres of $[(Ir(ppy)_2)_2(bpe)_2](OTf)_2$, the pyridines on the bpe ligands are positioned at a dihedral angle of ~45°, with respect to the *trans*-ppy-Ir plane (see Figure 3.2b). The ~45° dihedral twist appears to be the consequence of a steric clash between the bpe pyridines with the ppy ligands, which sit partially "overhanging" the exchangeable sites. This constrained dihedral twist would be greatly disfavoured with the conformationally "locked" planar tpt ligand within an M_6L_4 assembly. In order for the M_6L_4 assembly to form, the pyridines on the tpt ligand would need to twist out of plane; this would be energetically disfavoured due to the broken conjugation of the π system. The steric clash between the ppy and tpt ligands is believed to be the reason why the self-assembly of $[(Ir(ppy)_2)_6(tpt)_4](X)_6$ was not observed.

3.3.4 $[(Ir(ppy)_2)_6(tcb)_4](X)_6$ octahedra

In order to avoid the steric clash between the tritopic bridging ligands and the ppy on the iridium metal centres, 1,3,5-tricyanobenzene (tcb) was investigated as a less-bulky substitute for tpt. The symmetry around the cyano-groups of the tcb ligand is isotropic, which abolishes any preference the ligand may have in the dihedral angle conformation. While it was anticipated that acetonitrile displacement from $[Ir(ppy)_2(CH_3CN)_2]OTf$ by tcb to generate the M_6L_4 assembly should be entropically, if not enthalpically, favoured, initial experiments suggested only partial displacement. Instead, what is presumed to be $[(Ir(ppy)_2OTf)_2]$,[14] prepared by treating $[(Ir(ppy)_2Cl)_2]$ with silver triflate in $C_2H_4Cl_2$, was reacted with tcb in the same solvent (Scheme 3.2, route 1). While the product gave a relatively complex ^1H NMR spectrum (see Figure 3.3a), nESI-MS showed an intense 2+ peak at 2106 *m*/*z* (see section 3.5.5), which matched the predicted isotope pattern for $[\mathbf{1}\cdot 4OTf]^{2+}$. A ^1H DOSY NMR spectrum

of the product also showed that the multiple aromatic signals possessed similar diffusion coefficients (see section 3.5.6). This led to the postulation that **1**·6OTf is formed as a complex mixture of diastereoisomers[15] when the synthesis commences from racemic [(Ir(ppy)$_2$Cl)$_2$] (Scheme 3.2, route 1), and thus tcb, similarly to bpe, does not efficiently transmit stereochemical information between adjacent metal centres.

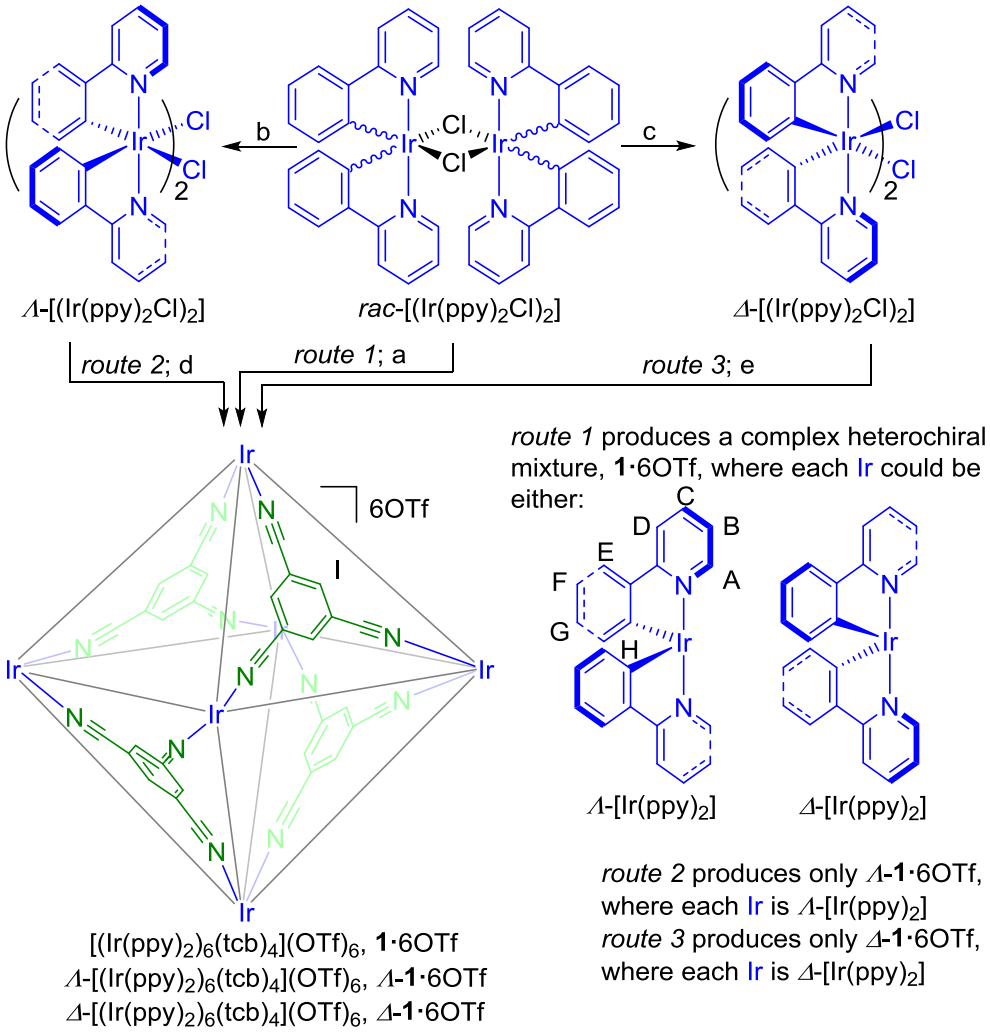

Scheme 3.2. Synthesis of heterochiral and homochiral hexanuclear iridium assemblies. Conditions: a) (i) AgOTf, $C_2H_4Cl_2$, RT, 2 h; (ii) tcb, $C_2H_4Cl_2$, RT, 4 h, 48% (starting from *rac*-[(Ir(ppy)$_2$Cl)$_2$]). b) (i) D-serine, NaOMe, MeOH, 313 K, 16 h; (ii) 1M HCl, MeOH, RT, 10 min, 50% (from *rac*-[(Ir(ppy)$_2$Cl)$_2$]). c) (i) L-serine, NaOMe, MeOH, 313 K, 16 h; (ii) 1M HCl, MeOH, RT, 10 min, 37% (from *rac*-[(Ir(ppy)$_2$Cl)$_2$]). d) (i) AgOTf, $C_2H_4Cl_2$, RT, 2 h; (ii) tcb, $C_2H_4Cl_2$, RT, 5 h, 57% (starting from *Λ*-[(Ir(ppy)$_2$Cl)$_2$]). e) (i) AgOTf, $C_2H_4Cl_2$, RT, 2 h; (ii) tcb, $C_2H_4Cl_2$, RT, 4 h, 68% (starting from *Δ*-[(Ir(ppy)$_2$Cl)$_2$]).

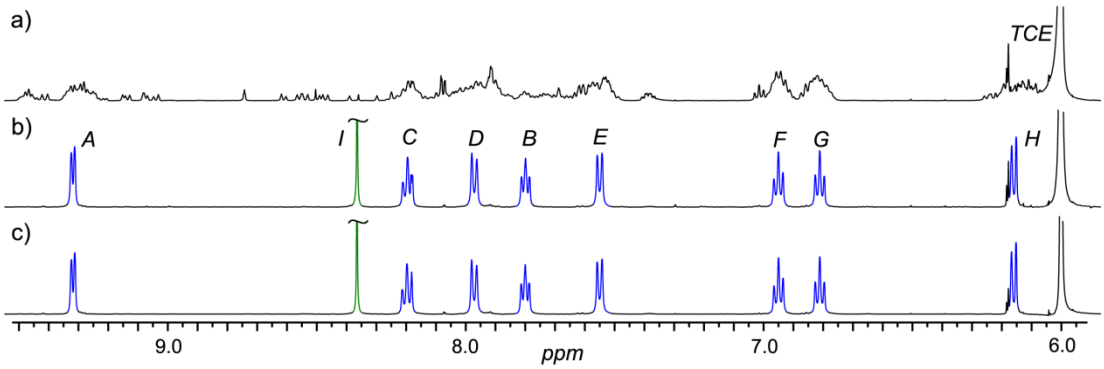

Figure 3.3. ^{1}H NMR spectra (500 MHz, $C_2D_2Cl_4$, 298 K) of a) **1**·6OTf obtained from *rac*-[(Ir(ppy)$_2$Cl)$_2$]; b) *Λ*-**1**·6OTf; c) *Δ*-**1**·6OTf. The assignments correspond to the lettering shown in Scheme 3.2.

To eliminate the problem of mixed stereoisomer formation, a preparative method to resolve *rac*-[(Ir(ppy)$_2$Cl)$_2$] into its enantiopure forms was developed. Although techniques to access enantiopure Ir compounds using either chiral ligands,[16] chiral anions[17] or resolution on a chiral phase,[18] are available thus far a method for obtaining homochiral [(Ir(ppy)$_2$Cl)$_2$] has yet to be reported. Thus, it was reasoned that complexation of the racemic iridium fragment [Ir(ppy)$_2$]$^+$ to an enantiopure amino acid would yield a diastereomeric mixture of Ir complexes that should possess different physiochemical properties. It was also postulated that the overall charge neutrality of these diastereomeric complexes would facilitate purification by chromatography on standard silica gel. We were thus delighted to find that serine complexed to Ir and produced diastereoisomers that were not only different by ^{1}H NMR spectroscopy, but also showed distinct spots *via* TLC.[19] Although these spots were close running, it was found that under conventional silica flash column chromatography conditions, significant pure quantities of the faster running species could be obtained although the slower running species was always contaminated with the less polar component. In order to overcome this, it was found that the most efficient method to obtain an iridium complex with the opposite stereochemistry was to complex the Ir to the opposite enantiomer of serine. X-ray crystallography revealed that *Δ*-[(Ir(ppy)$_2$(L-serine)] (see Figure 3.4) is the faster running diastereoisomer when L-serine was used and thus *Λ*-[(Ir(ppy)$_2$(D-serine)] is presumed, and later confirmed, to be the isolated diastereoisomer with D-serine.

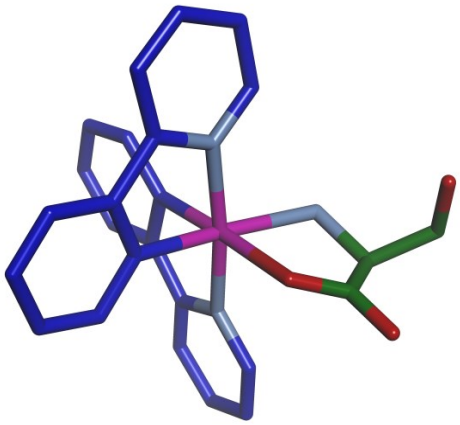

Figure 3.4. X-ray crystal structures of *Δ*-[(Ir(ppy)$_2$(L-serine)]. The carbon atoms of ppy are shown in dark blue and L-serine in green, iridium ions in magenta, nitrogen atoms in pale blue and oxygen atoms in green. See section 3.5.20 for crystal data and refinement, bond lengths and angles.

Λ- and *Δ*-[(Ir(ppy)$_2$Cl)$_2$] were readily obtained with addition of HCl (aq.) to a CH_3OH solution of the corresponding enantiopure Ir serine complexes (Scheme 3.2, steps b and c). Both [(Ir(ppy)$_2$Cl)$_2$] enantiomers (which, as expected, exhibit mirror image circular dichroism (CD) spectra; see section 3.5.7) crystallised in the chiral space group $P2_12_12_1$ upon diethyl ether diffusion into saturated dichloromethane solutions. The solid-state structures (see section 3.5.8) confirmed that no racamisation occurs when converting back to the bridged-chloride complex and the compound isolated, following resolution with D-serine, was *Λ*-[(Ir(ppy)$_2$Cl)$_2$], and L-serine was *Δ*-[(Ir(ppy)$_2$Cl)$_2$] (Scheme 3.2, steps b and c).

When the self-assembly was commenced from either *Λ*- or *Δ*-[(Ir(ppy)$_2$Cl)$_2$] (Scheme 3.2, routes 2 and 3), a precipitate was observed shortly after the addition of tcb to what are presumed to be *Δ*- and *Λ*-[(Ir(ppy)$_2$OTf)$_2$], which was then isolated after a few hours of stirring at RT. The ^{1}H NMR spectra of the two products not only were indistinguishable (see Figure 3.3b and 3.3c) but also clearly showed single species with the number and ratio of tcb-to-ppy signals consistent with the sole formation of *Λ*- and *Δ*-**1**·6OTf. CD confirmed that the two compounds were enantiomers (see section 3.5.7). The mass spectra also showed essentially a single species at 2106 m/z, which corresponds to the doubly charged [**1**·4OTf]$^{2+}$ (see section 3.5.5, Figure b and c). The surprising lack of other charge states in the mass spectra of *Λ*- and *Δ*-**1**·6OTf prompted us to look at the ^{19}F NMR spectra (see Figure 3.5a), which showed two distinct signals

at −77.45 and −79.04 ppm in a ratio of 1:2, respectively. Addition of excess Bu_4NOTf resulted in an increase in the intensity of the peak at −77.45 ppm (see Figure 3.5b), strongly suggesting that the peak at −79.04 ppm is due to encapsulated OTf^- anions. Other NMR techniques (HOESY and DOSY; see section 3.5.9) confirm this assignment and thus support the solution structure [4OTf⊂*Δ*-**1**]2OTf. Further EXSY NMR experiments have shown that the *exo* and *endo* triflates are in slow exchange and that the activation barrier for this process is 18 kcal mol^{-1} (see section 3.5.10).

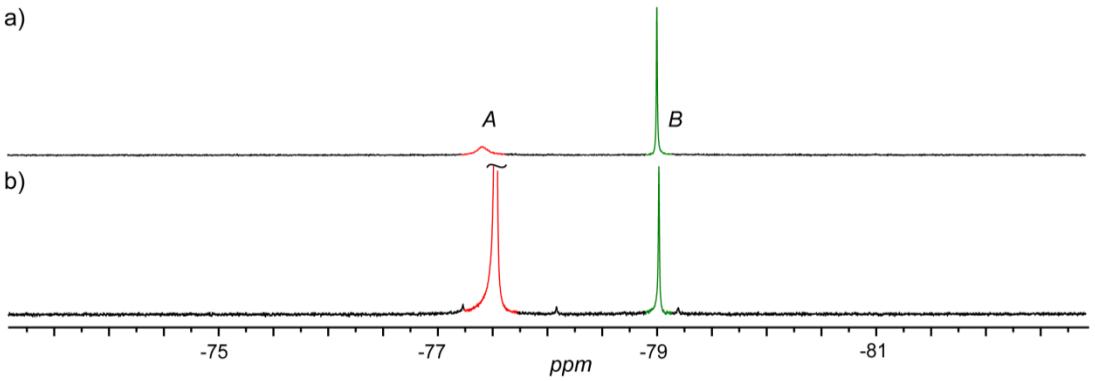

Figure 3.5. ^{19}F NMR spectra (376 MHz, $C_2D_2Cl_4$, 298 K) for a) *Λ*-**1**·6OTf (200 μM) and b) *Λ*-**1**·6OTf (200 μM) with excess Bu_4NOTf (5 mM). Green singlet (*B*) corresponds to encapsulated OTf^- and red singlet (*A*) to free OTf^-.

Corroboration of the capsule's structure was obtained from XRD using single crystals grown from benzene diffusion into a saturated dichloroethane solution of *Λ*- and *Δ*-**1**·6OTf (see Figure 3.6 for structure and section 3.5.22 for crystal data and refinement, bond lengths and angles). The solid-state structure supports the solution structure, $[4OTf⊂Δ\text{-}\mathbf{1}]^{2+}$, showing OTf^- anions located in each of the octahedron "windows". For two encapsulated triflates (with S labels 3 and 4), the S–C axis points toward the centre of these vacant windows (or, if viewed as a truncated tetrahedron, toward the vertex), forming a series of close contacts between the triflate oxygens and the hydrogen atoms attached to tcb and the *ortho*-pyridyl positions. The other encapsulated anions (with S labels 1 and 6) are positioned in a slightly more "side-on" fashion, with the cage forming short contacts between two of the oxygen atoms and one of the fluorines. It seems probable that, in solution, these two distinct triflate co-conformations participate in a low-energy exchange process, thus explaining the presence of a single "encapsulated" signal in the ^{19}F NMR spectrum at RT. The encapsulation of multiple

ions within a metallosupramolecular assembly is rare in the literature, due to repulsive anion-anion interactions, and has only been observed on a small number of occasions.[20]

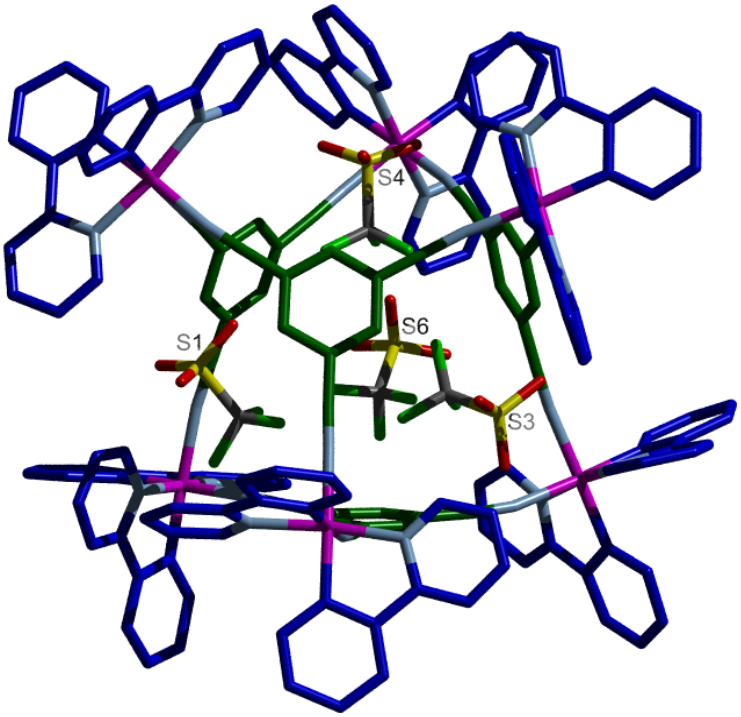

Figure 3.6. X-ray crystal structures of [4OTf⊂*Δ*-**1**]$^{2+}$. Colour code: Ir, magenta; C(ppy), blue; C(tcb), dark green; C(OTf$^-$), grey; N, light blue; O, red; S, yellow; F, light green.

To explore whether the structure and, in particular, the encapsulated anions are preserved under MS conditions, ion-mobility mass spectrometry (IMMS) measurements have been undertaken.[21] For the ions at 2106 *m*/*z*, both samples gave superimposable arrival time distributions, consistent with a single species/conformation (see section 3.5.11). The observed rotationally averaged collision cross sections for [4OTf⊂*Δ*/*Λ*-**1**]$^{2+}$ were found to be 551 and 543 Å^2, respectively, virtually within error of each other. To validate these, IMMS simulations have been carried out using structures derived from the XRD data. The values calculated using either the exact hard-spheres scattering or trajectory method, 555 and 551 Å^2, respectively, agree remarkably well with the experimental data, suggesting that the counteranions remain within the capsule upon ionisation into the gas phase.

Examples of metallocapsules which encapsulate multiple species of the same charge are very rare.[22] Clearly, the strong Coulombic attraction between the positively charged Ir vertices and negative counteranions, alongside the series of CH···X (X = O, F) hydrogen bonds (*vide supra*), is enough to overcome the repulsion between same-charge ions. It could also be that the CF_3 groups, which are "meshed" together within the centre of the cavity (C–C distances between encapsulated OTf^- counteranions range from 4.93 to 6.05 Å, with an average distance of 5.55 Å), act to insulate this charge. To probe further, we have calculated the capsule's occupancy. Based on an irregular hexadecahedron model (see section 3.5.12 for details), the volume of the empty cavity has been calculated to be 506 $Å^3$, of which the triflate counteranions occupy 280 $Å^3$, which equates to 55% filled cavity space, in line with previous observations made by Rebek.[23]

3.3.5 Photochemistry

Held under a standard long-wavelength UV lamp, 1,1,2,2-tetrachloroethane (TCE) solutions of *Λ*- and *Δ*-**1**·6OTf luminesce orange (Figure 3.7, inset b) (i) and (ii)).

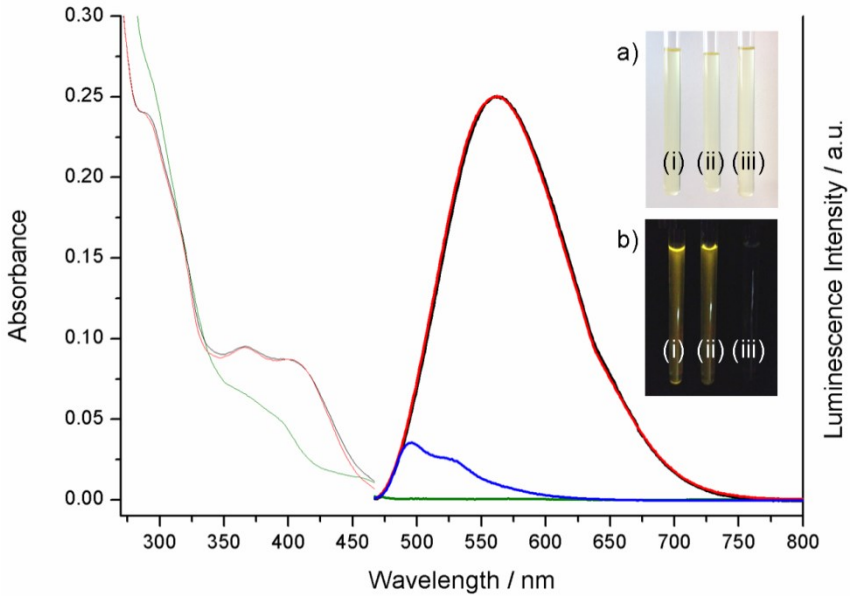

Figure 3.7. Absorption and emission (excitation at 413 nm) spectra of *Λ* and *Δ*-**1**·6OTf. *Λ* = black line; *Δ* = redline; TCE, 2 μM. For comparison, the spectra of the mononuclear $[Ir(ppy)_2(PhCN)_2]OTf$ are also shown (Ir only = green line; Ir + 3000 eq. PhCN = blue line; TCE, 12 μM). Inset: A photograph of i) *Λ*-**1**·6OTf, ii) *Δ*-**1**·6OTf and iii) $[Ir(ppy)_2(PhCN)_2]OTf$ in NMR tubes held a) in ambient lighting and b) under a UV lamp (254 nm).

As most literature Ir complexes are luminescent, the significance of the capsules' photophysical properties only becomes apparent when compared against the representative mononuclear bis(benzonitrile) complex, $[Ir(ppy)_2(PhCN)_2]OTf$ (see section 3.5.13 for ^1H NMR and UV-Vis absorption spectra).[24] Placed next to the samples of *Λ*- and *Δ*-**1**·6OTf under UV light, there is no visible luminescence from $[Ir(ppy)_2(PhCN)_2]OTf$ (Figure 3.7, inset b) (iii)) in the same solvent (at equivalent [Ir]). The absorption and emission spectra of these samples confirm these visual observations (Figure 3.7). Even with a vast excess of benzonitrile, $[Ir(ppy)_2(PhCN)_2]OTf$ is only weakly luminescent (Figure 3.7, blue line). The emission of *Λ*- and *Δ*-**1**·6OTf is also broadened and red-shifted with respect to $[Ir(ppy)_2(PhCN)_2]OTf$ (in the presence of excess benzonitrile), signifying increased charge-transfer character of the emitting state. While the quantum yields (Φ) for *Λ*- and *Δ*-**1**·6OTf, found to be 4% in air-equilibrated TCE, are comparable to those for many cyclometalated Ir(III) complexes under similar ambient conditions,[25] these often utilise either bidentate or strongly coordinating (and high ligand strength) monodentate ligands.[26] As far as we are aware, this is the first time a collection of weakly coordinating ligands has been used to inhibit nonradiative ligand dissociation pathways.[27] Interestingly, the emission intensity of *Λ*- and *Δ*-**1**·6OTf increases only marginally (by a factor of 1.1) when the samples are thoroughly degassed, in contrast to many other such Ir complexes,[25] suggesting that the metallosupramolecular architecture may also in some way inhibit collisional O_2 quenching.[25b] Alternatively, the presence of four desolvated anions located within the cavity of the capsule may provide such an efficient, alternative nonradiative decay pathway (e.g. *via* electron transfer) that the capsule is insensitive to the presence of O_2.

3.3.6 Anion exchange experiments

Preliminary investigations into the *host-guest* chemistry of $[4OTf⊂Δ/Λ\text{-}\mathbf{1}]^{2+}$ indicate that the encapsulated OTf^- anions can be exchanged for other anionic species. When Bu_4NPF_6 was titrated into a sample of $[4OTf⊂Δ\text{-}\mathbf{1}]2OTf$ in $C_2D_2Cl_4$, ^{19}F NMR spectroscopy (see Figure 3.8) shows multiple OTf^- and PF_6^- signals at low $[PF_6^-]$, indicative of mixed PF_6^--OTf^- *host-guest* complexes. At equimolar anionic concentrations, encapsulated OTf^- has mostly been displaced.

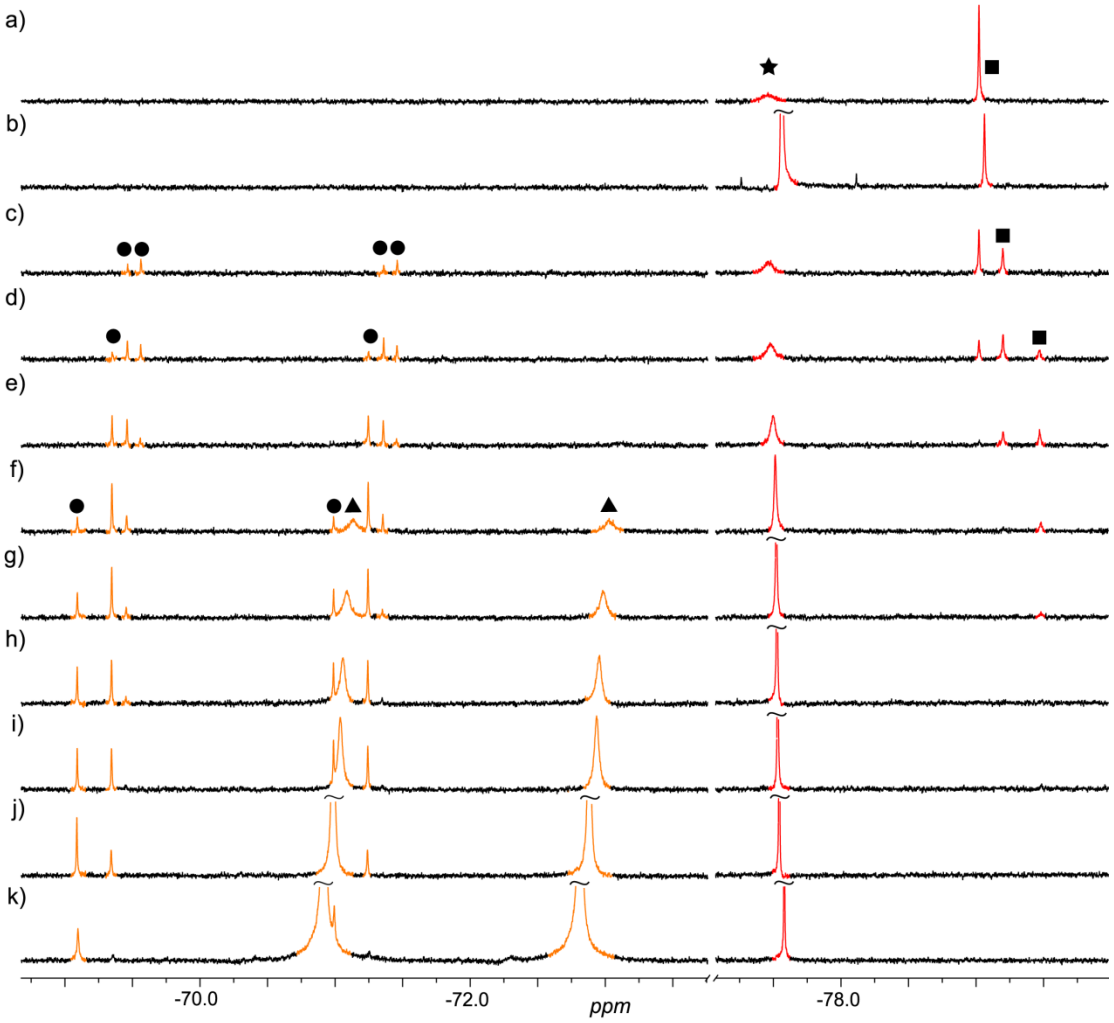

Figure 3.8. ^{19}F NMR (376 MHz, $C_2D_2Cl_4$, 298 K) spectra of Bu_4NPF_6 titration into *Δ*-**1**·6OTf: a) *Δ*-**1**·6OTf; b) *Δ*-**1**·6OTf with excess Bu_4NOTf; c) 0.8 eq Bu_4NPF_6; d) 1.6 eq; e) 3.1 eq; f) 6.8 eq; g) 9.9 eq; h) 13.0 eq; i) 17.0 eq; j) 33.4 eq; k) 94.3 eq. ★ peak for free OTf^-; ■ encapsulated OTf^-; ● encapsulated PF_6^-; ▲ free PF_6^-.

This process has also been monitored by ^{1}H NMR spectroscopy (see Figure 3.9), which shows that while the overall symmetry is preserved, the proton signals closest to the anion binding sites (the tcb hydrogen atom H_I and the *orto*- and *meta*- pyridyl sites, H_A and H_B) are noticeably shifted.

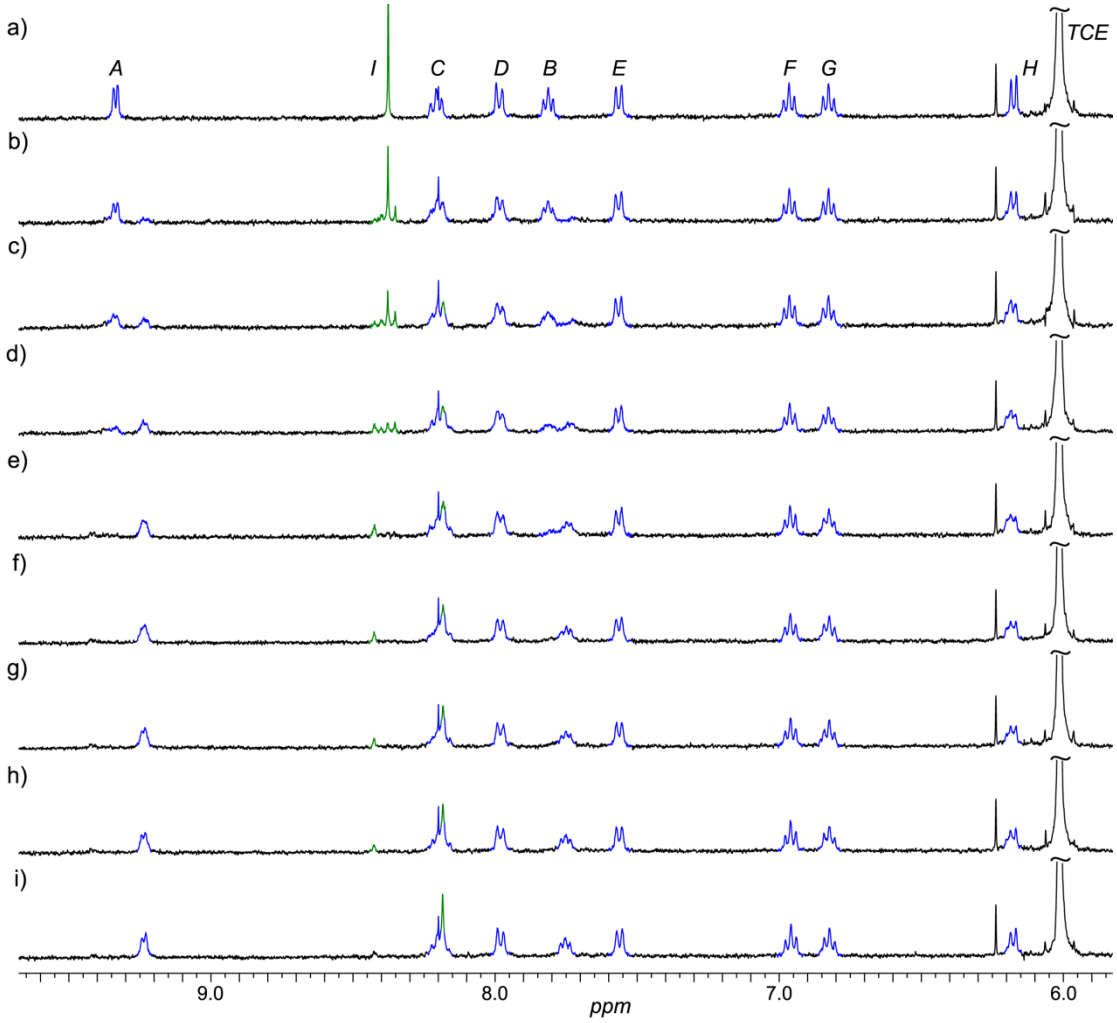

Figure 3.9. ^{1}H NMR (400 MHz, $C_2D_2Cl_4$, 298 K) spectra of Bu_4NPF_6 titration into *Δ*-**1**·6OTf: a) *Δ*-**1**·6OTf; b) *Δ*-**1**·6OTf with 0.8 eq Bu_4NPF_6; c) 1.6 eq; d) 3.1 eq; e) 6.8 eq; f) 9.9 eq; g) 13.0 eq; h) 17.0 eq; i) 33.4 eq. The assignments correspond to the lettering shown in Scheme 3.2.

Similar experiments with Bu_4NBF_4 and $Bu_4NCF_3BF_3$, and additional titrations into *Λ*-**1**·6BF_4 (see section 3.5.14), have ascertained that the overall affinity of perfluorinated anions for the cavity of [*Δ*/*Λ*-**1**]$^{6+}$ follows the sequence PF_6^- > OTf^- ≈ $CF_3BF_3^-$ > BF_4^-.[23c] Rationalisation of this affinity will be discussed in Chapter 4, however, additional DOSY and MS measurements show that the cage remains intact following *guest* exchange (see section 3.5.17 and 3.5.18). Counterion exchange for various other anions was also attempted but the assembly either decomposed or rearranged or the results were inconclusive (see section 3.5.15). An attempt to expand *host–guest* chemistry to neutral

organic species has thus far been hampered by the low solubility/stability of *Δ/Λ*-**1**$^{6+}$ in more polar solvents (see Chapter 4 for further discussion).

We have ascertained that there is communication between the luminescent properties of [*Δ/Λ*-**1**]$^{6+}$ and the cavity-bound *guests*, as evidenced by changes to the emission spectra during anion titration experiments (see Figure 3.10). When Bu_4NPF_6 was slowly added to a $C_2H_2Cl_4$ solution of *Λ*-**1**·6OTf the emission intensity dropped significantly (see Figure 3.10i). However, titrating Bu_4NOTf into *Λ*-**1**·6BF_4 had the reverse effect and an increase in the luminescence intensity was observed (see Figure 3.10ii).

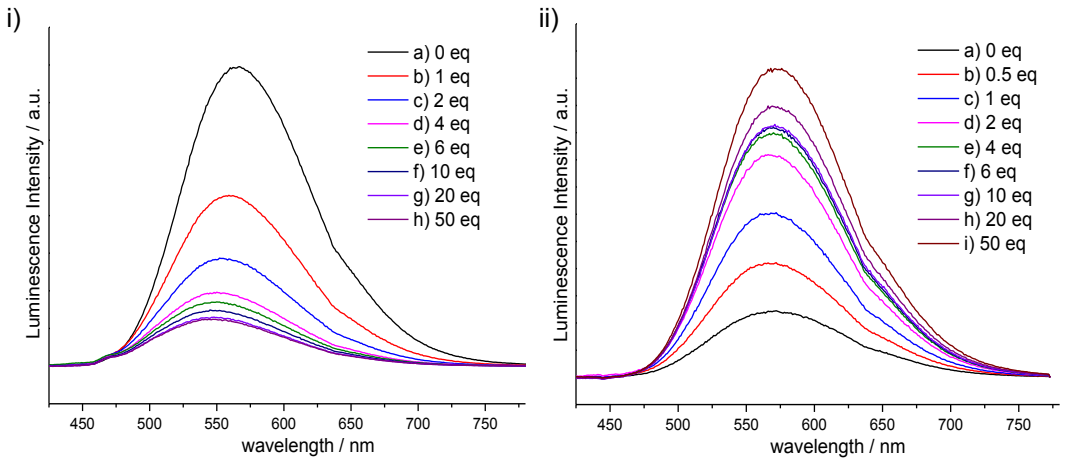

Figure 3.10. i) emission (excitation = 403 nm) spectra of Bu_4NPF_6 titration into *Λ*-**1**·6OTf: a) *Λ*-**1**·6OTf; b) *Λ*-**1**·6OTf with 1 eq Bu_4NPF_6; c) 2 eq; d) 4 eq; e) 6 eq; f) 10 eq; g) 20 eq; h) 50 eq; ii)emission (excitation = 392 nm) spectra of Bu_4NOTf titration into *Λ*-**1**·6BF_4: a) *Λ*-**1**·6BF_4; b) *Λ*-**1**·6BF_4 with 0.5 eq Bu_4NOTf; c) 1 eq; d) 2 eq; e) 4 eq; f) 6 eq; g) 10 eq; h) 20 eq; i) 50 eq. For experimental detail see section 3.5.16.

As well as showing that [*Δ/Λ*-**1**]$^{6+}$ acts as a luminescent anion sensor, this also suggests that it may be possible to tune luminescent properties of multimetallic Ir assemblies through supramolecular means rather than *via* conventional covalent modification.

3.4 Conclusion

In summary, the first molecular capsule based on an $[Ir(ppy)_2]^+$ unit has been assembled using a tritopic nitrile ligand and enantiopure Ir starting materials. The first reported method of resolving the readily used Ir bridged-chloride species into its enantiopure counterparts was demonstrated. Using the enantiomeric precursors, homochiral octahedra were assembled that displayed luminescence not present in a comparable mononuclear complex. In addition, the same capsule has demonstrated the capability of binding multiple same-charge species and that these can be exchanged for other anionic *guests*. Characteristic emission spectra were observed when different *guests* were used showing that $[\Delta/\Lambda\text{-}\mathbf{1}]^{6+}$ can act as a luminescent anion sensor.

3.5 Experimental Section

3.5.1 Experimental Procedures

3.5.1.1 General Experimental Procedure

Unless stated otherwise, all reagents and solvents were purchased from commercial sources and used without further purification. $[Ir(ppy)_2(CH_3CN)_2]OTf$,[27] 2,4,6-tris-(4-pyridyl)-1,3,5-triazine (tpt),[28] $[Ir(ppz)_2(CH_3CN)_2]OTf$, *rac*-$[(Ir(ppy)_2Cl)_2]$[29] and 1,3,5-tricyanobenzene[30] were prepared according to the literature procedures.

3.5.1.2 Ion-Mobility Mass Spectrometry (IMMS)

Ion-mobility (IM) mass spectrometry measurements were performed on a MoQ-ToF, an in-house modified[31] Q-ToF 1 (Micromass UK Ltd) fitted with nESI source. Capillary voltages were adjusted between 1 and 1.2 kV to optimise spray quality, while the cone voltage was set to 43 V. Source temperature was set at 80 °C. The energy of injection into the drift cell was set at 42 V.

Modification of instrument involved the insertion of a 5.1 cm long copper drift cell and supplementary ion optics situated post source optics and before the quadrupole analyser.[31] A potential difference can be applied across the drift cell, thus when ions are pulsed into the drift cell (which is filled with helium at pressure of ~3.5 Torr, room temperature) and drift through under the influence of this field, they are hindered by collisions with the intervening buffer gas molecules. Thus the time taken for ions to traverse the cell, in conjunction with the strength of the electric field applied across the drift cell, is due to the charge they carry and their mobility (*K*). *K* is inversely related to the rotationally averaged collision cross sections (CCS) of the ion. The ions then pass through the quadrupole and time of flight analysers and are detected by microchannel plates. The time from when ions are pulsed into the drift cell to when they are detected is therefore a combination of the time the ions spend in the drift cell (drift time) and that outside it (dead time). This is obtained from the measured mass selected arrival time distribution (ATD), and can be deconvoluted into ATDs of each individual ion.

For a given mass/charge the drift time will vary depending on its CCS but the dead time will be invariant. The ions ATD distributions are measured at 6 different values of the electric field applied to the drift cell (15-60 V). If the arrival times are plotted against P/V the intercept will be the dead time and the gradient $1/K$. After normalising for the experimental temperature and pressure inside the drift cell K can be converted into reduced mobility K_0 and this to ascertain a value for Ω using the Mason-Schamp equation below.[32]

$$K_0 = \frac{3ze}{16N_0}\left(\frac{2\pi}{\mu k_B T}\right)^{\frac{1}{2}}\frac{1}{\Omega}$$

where z is ion charge, e is electron charge, N_0 is the buffer gas number density, μ is the reduced mass of the buffer gas and ion, k_B is the Boltzmann constant, T is the effective temperature and Ω is the momentum transfer collision integral.

3.5.1.3 Ion-Mobility Simulations

Collision cross sections were simulated using MOBCAL software developed by Jarrold *et al*.[33] Two different methods of were used to calculate collision cross section of analyte ion with helium:

1. The exact hard sphere scattering (EHSS) method. The Ion is treated as a collection of overlapping spheres with radii equal to hard sphere collision distances. Orientationally-averaged momentum transfer cross section is calculated by determining the scattering angles between the incoming buffer gas atom trajectory and the departing buffer gas atom trajectory.[33] This approach ignores long range interactions between ion and gas molecule but accounts for multiple scattering.[34]

2. The trajectory method (TJM). Treats the ion as a collection of atoms, each one represented by a 12-6-4 potential. The effective potential is obtained by summing over the individual atomic contributions and then trajectories are run in this potential to obtain the scattering angle (the angle between the incoming and departing buffer gas atom trajectory). The orientationally-averaged collision integral is determined by averaging over all possible collision

geometries.[33] This method is the most rigorous and should give the most reliable estimate. TJM method accounts for long range interactions and multiple scattering.[33, 35]

3.5.1.4 Circular Dichroism (CD)

CD was performed on a JASCO J-810 spectropolarimeter. Data was collected over a wavelength range of 273-600 nm, at a scan speed of 100 nm min^{-1}, bandwidth of 1 nm and data pitch of 0.1 nm. Samples were measured at RT and at given concentrations using a 1 mm path length cuvette (Starna Ltd.). Use of the CTCB Facilities was supported by The Wellcome Trust, the Scottish University Life Sciences Alliance and the BBSRC.

3.5.1.5 Emission Spectroscopy

Steady-state luminescence spectra were measured using the Fluoromax (Horiba Jobin Yvon) photon-counting spectrofluorometer. Spectra were recorded with a bandpass of 3 nm for both excitation and emission monochromators and were corrected for variation in the excitation lamp intensity and the wavelength-dependence of the detector response. The data was further corrected with background subtraction and baseline correction. Spectral intensities were determined by integration over entire emission peaks bandwidth. Samples were measured in 1,1,2,2-tetrachloroethane (TCE) at RT using a fused silica cuvette (Starna Ltd.) with a 10 mm path length. The luminescence intensities for each sample were measured at 5 distinct absorbance values (between 0.01 and 0.1) with an excitation wavelength of 413 nm. De-aerated samples were prepared by bubbling high purity argon into the sealed cuvette for 30 min. Emission quantum yields (Φ) were determined using $[Ru(bipy)_3](PF_6)_2$ (Φ_{air} = 0.018 in acetonitrile)[36] as reference with coumarin 153 (Φ_{air} = 0.58 in ethanol)[37] as a second reference to verify the yields. The quantum yields were calculated using the expression $\Phi_X = \Phi_R(m_X/m_R)(\eta_X^2/\eta_R^2)$, where X and R denote sample being measured and reference respectively, m is the gradient from the plot of integrated luminescence intensity *vs*. absorbance and η is the refractive index of the solvent (η_{TCE} = 1.494, $\eta_{acetonitrile}$ = 1.344 and η_{EtOH} = 1.361)[38].

3.5.2 Synthesis

3.5.2.1 Synthesis of $[(Ir(ppy)_2)_2(bpe)_2](OTf)_2$

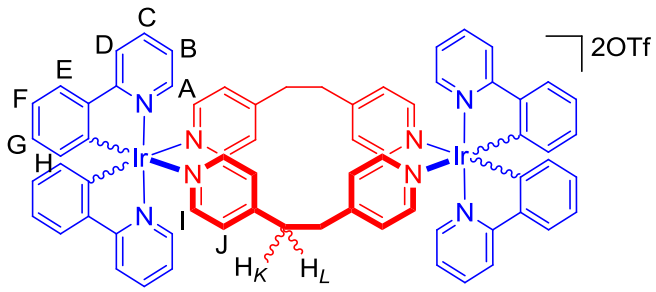

$[(Ir(ppy)_2)_2(bpe)_2](OTf)_2$

To a solution of $[Ir(ppy)_2(CH_3CN)_2]OTf$ (104.7 mg, 0.143 mmol) in $C_2H_4Cl_2$ (15 mL) was charged bpe (26.3 mg, 0.143 mmol) and the solution heated at 50 °C. After 18 h, the solution was reduced on the rotary evaporator to *ca.* 0.5 mL and the product crashed out with Et_2O diffusion, filtered and washed with Et_2O to yield an orange precipitate (81.6 mg, 68% yield). Orange crystals, suitable for X-ray crystallography, were grown with slow ether diffusion into CH_3NO_2. ^1H NMR (400 MHz, $C_2Cl_4D_2$): 8.75 (4H, d, J = 5.5 Hz, H_A), 8.34 (8H, d, J = 5.8 Hz, H_I), 7.82 (4H, m, H_C), 7.74 (4H, d, J = 7.7 Hz, H_D), 7.52 (4H, m, H_B), 7.45 (4H, m, H_E), 6.92 (16H, m, $H_{F,G,J}$), 6.32 (4H, m, H_H), 3.02 (4H, d, J_2 = 10.4 Hz, H_K), 2.59 (4H, d, J_2 = 10.4 Hz, H_L); ^{13}C NMR (126 MHz, $C_2D_2Cl_4$): 167.2, 151.1, 150.5, 149.3, 148.1, 144.1, 137.9, 131.9, 130.2, 127.3, 124.4, 123.8, 122.2, 118.9, 35.3; ^{19}F NMR (376 MHz, $C_2Cl_4D_2$): -77.30 (6F, s, OTf^-); nESI (DCE): m/z = 685.2 $[(Ir(ppy)_2)_2(bpe)_2]^{2+}$ and 1519.3 $[(Ir(ppy)_2)_2(bpe)_2](OTf)^+$; Anal. Calculated for $C_{70}H_{56}F_6Ir_2N_8O_6S_2$: C, 50.41; H, 3.38; N, 6.72%. Found: C, 50.31; H, 3.35; N, 6.77%.

3.5.2.2 Synthesis of $[(Ir(ppz)_2)_2(bpe)_2](OTf)_2$

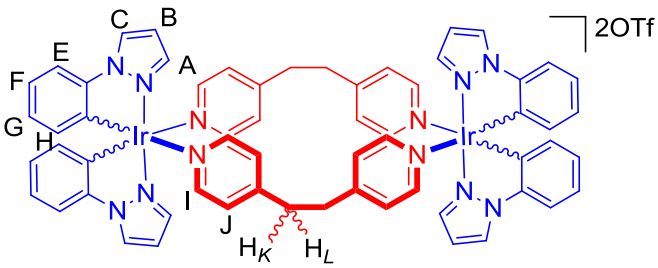

$[(Ir(ppz)_2)_2(bpe)_2](OTf)_2$

To an NMR tube was charged $[Ir(ppz)_2(CH_3CN)_2]OTf$ (5.1 mg, 0.0072 mmol) in $C_2D_2Cl_4$ (0.5 mL) and bpe (1.3 mg, 0.0072 mmol). After stirring for 16 h at RT the solution was heated for 7 h at 60 °C, a further 16 h at 75 °C and 20 h at 80 °C. Equilibrium was reached at 79% qualitative yield (by ^1H NMR). ^1H NMR (500 MHz, $C_2Cl_4D_2$): 8.32 (8H, d, J = 6.2 Hz, H_I), 8.10 (4H, d, J = 2.2 Hz, H_A), 8.04 (4H, d, J = 2.9 Hz, H_C), 7.09 (4H, m, H_E), 6.99 (8H, d, J = 6.2 Hz, H_I), 6.94 (4H, m, H_F), 6.86 (4H, m, H_G), 6.78 (4H, m, H_B), 6.37 (4H, m, H_H), 3.07 (4H, d, J_2 = 11.0 Hz, H_K), 2.67 (4H, d, J_2 = 11.0 Hz, H_L); ^{19}F NMR (376 MHz, $C_2Cl_4D_2$): -77.44 (6F, s, OTf^-); nESI (DCE): m/z = 663.2 $[(Ir(ppz)_2)_2(bpe)_2]^{2+}$ and 1475.3 $[(Ir(ppz)_2)_2(bpe)_2](OTf)^+$.

3.5.2.3 Synthesis of $[(Ir(ppy)_2)_6(tpt)_4](X)_6$

To $[Ir(ppy)_2(CH_3CN)_2]OTf$ (25.3 mg, 0.034 mmol) in $C_2H_4Cl_2$ (10 mL) as solvent was charged tpt (7.2 mg, 0.023 mmol) and the solution heated at 50 °C for 24 h. The reaction was repeated using $[Ir(ppy)_2(CH_3CN)_2]X$ (where X = (+)-camphor-10-sulfonate, PF_6^- or NO_3^-), $[(Ir(ppy)_2Cl)_2]$, $[(Ir(ppy)_2OTf)_2]$, $[Ir(2,5\text{-}dppy)_2(CH_3CN)_2]OTf$ or $[Ir(ppz)_2(CH_3CN)_2]OTf$ in CH_3NO_2, CH_2Cl_2, $C_2D_2Cl_4$, CD_3OD or D_2O at temperatures ranging from RT to reflux and reaction times from hours to days. The reaction was also attempted using solid phase grinding and a microwave reactor.

3.5.2.4 Synthesis of $[(Ir(ppy)_2)_6(tcb)_4](OTf)_6$ (1·6OTf)

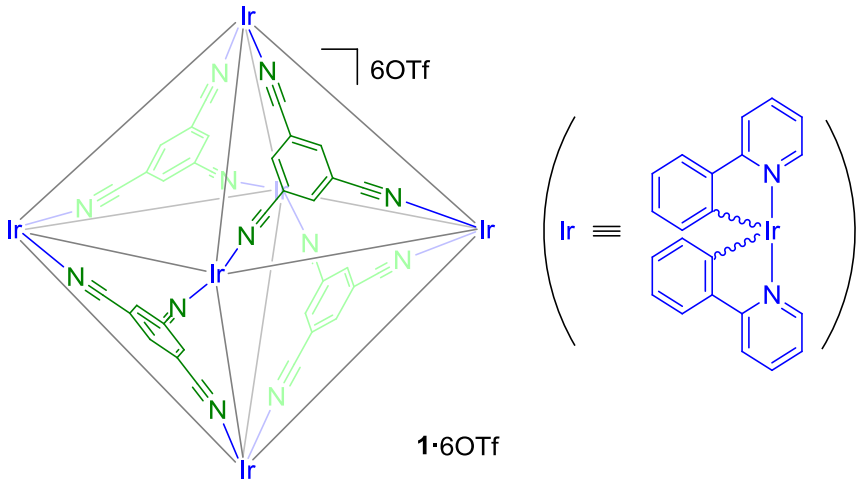

A mixture of *rac*-$[(Ir(ppy)_2Cl)_2]$ (48.3 mg, 0.0451 mmol) and AgOTf (23.2 mg, 0.0902 mmol) in $C_2H_4Cl_2$ (25 mL) were stirred at rt in a darkened flask for 2 h. The orange

solution was filtered through celite and concentrated on the rotary evaporator. The crude product was re-dissolved in $C_2H_4Cl_2$ (2 mL) and tcb (9.2 mg, 0.0601 mmol) charged. The solution was stirred for 4 h at RT. The resulting precipitate was filtered off and washed with a minimal amount of $C_2H_4Cl_2$ and Et_2O to give **1** as a yellow solid (32.4 mg, 48%). Anal. Calculated for $C_{174}H_{108}F_{18}Ir_6N_{24}O_{18}S_6$: C, 46.33; H, 2.41; N, 7.45%. Found: C, 46.23; H, 2.44; N, 7.51%; ^{1}H NMR (500 MHz, $C_2D_2Cl_4$): see Figure 3.3. nESI (DCE): *m/z* = 2106.2 $[\mathbf{1}\cdot 4OTf]^{2+}$.

3.5.2.5 Synthesis of *Δ/Λ*-[(Ir(ppy)$_2$)$_6$(tcb)$_4$](OTf)$_6$ (*Δ/Λ*-1·6OTf)

Synthesis of intermediate [(*Δ/Λ*-Ir(ppy)$_2$)(L/D-serine)] follows a similar procedure to that of R. Urban *et. Al.*[19]

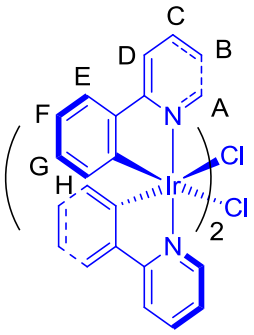

Δ-[(Ir(ppy)$_2$Cl)$_2$]

A mixture of *rac*-[(Ir(ppy)$_2$Cl)$_2$] (0.277 g, 0.26 mmol), L-serine (54.6 mg, 0.52 mmol) and NaOMe (27.9 mg, 0.52 mmol) in CH_3OH (20 mL) were stirred at 40 °C for 16 h. The solvent was removed in *vacuo* and the crude product purified using silica-gel flash column chromatography (CH_2Cl_2/CH_3OH/NEt_3 (96:3:1) as eluent). While pure fractions of the faster running diastereoisomer, *Δ*-[Ir(ppy)$_2$(L-serine)], could be obtained, the slower eluting compound, *Λ*-[Ir(ppy)$_2$(L-serine)], was always contaminated with the other isomer. The pure *Δ*-[Ir(ppy)$_2$(L-serine)] isolated from the column was dissolved in CH_3OH (5 mL) and to this was added 1M HCl solution (1 mL). A precipitate formed after 10 min at RT. This was filtered off, washed with CH_3OH and Et_2O and air dried to give a yellow solid (50.7 mg, 37% (starting from *rac*-[(Ir(ppy)$_2$Cl)$_2$]). Single crystals suitable for XRD were grown by slow vapour diffusion of Et_2O into a saturated CH_2Cl_2 solution. ^{1}H NMR (500 MHz, $C_2D_2Cl_4$): 9.17 (4H, d, *J* = 6.9 Hz, H_A), 7.90 (4H, d, *J* = 7.7 Hz, H_D), 7.79 (4H, m, H_C), 7.55 (4H, d, *J* = 6.9 Hz, H_E), 6.86 (4H, m, H_F), 6.81 (4H, m, H_B), 6.65

(4H, m, H_G), 5.95 (4H, d, J = 7.7 Hz, H_H); ^{13}C NMR (126 MHz, $C_2D_2Cl_4$): 168.0, 151.3, 144.5, 144.0, 136.5, 130.5, 129.1, 123.7, 122.3, 121.5, 118.4; nESI (DCE): m/z = 1314.4 $[(Ir(ppy)_2Cl)_2 + Bu_4N]^+$, 1701.6 $[(Ir(ppy)_2Cl)_2 + (PF_6)(Bu_4N)_2]^+$ and 2088.9 $[(Ir(ppy)_2Cl)_2 + (PF_6)_2(Bu_4N)_3]^+$.

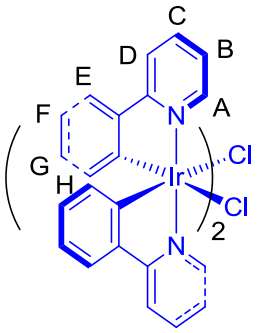

Λ-$[(Ir(ppy)_2Cl)_2]$

Λ-$[(Ir(ppy)_2Cl)_2]$ was synthesised following the same procedure as above starting with *rac*-$[(Ir(ppy)_2Cl)_2]$ (0.178 g, 0.16 mmol), D-serine (33.6 mg, 0.32 mmol) and NaOMe (17.3 mg, 0.32 mmol). Yellow solid obtained (44.2 mg, 50%). Single crystals suitable for XRD were grown by slow vapour diffusion of Et_2O into a saturated CH_2Cl_2 solution. Characterisation as for *Δ*-$[(Ir(ppy)_2Cl)_2]$.

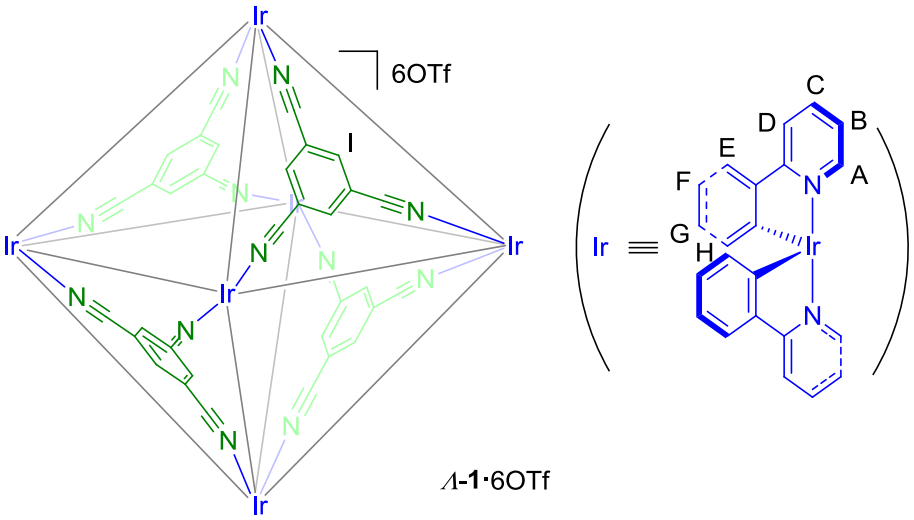

Λ-**1**·6OTf

Λ-[(Ir(ppy)$_2$)$_6$(tcb)$_4$](OTf)$_6$ (*Λ*-**1**·6OTf) was synthesised following the same procedure as for **1**·6OTf starting with *Λ*-[(Ir(ppy)$_2$Cl)$_2$] (21.0 mg, 0.020 mmol). Yellow solid obtained (16.7 mg, 57%). ^{1}H NMR (500 MHz, $C_2D_2Cl_4$): 9.32 (12H, d, *J* = 7.1 Hz, H_A), 8.36 (12H, s, H_I), 8.19 (12H, m, H_C), 7.97 (12H, d, *J* = 7.1 Hz, H_D), 7.80 (12H, m, H_B), 7.55 (12H, d, *J* = 7.8 Hz, H_E), 6.95 (12H, m, H_F), 6.81 (12H, m, H_G), 6.16 (12H, d, *J* = 7.8 Hz, H_H); ^{13}C NMR (126 MHz, $C_2D_2Cl_4$): 165.8, 152.5, 144.3, 142.6, 141.9, 139.0, 131.3, 129.5, 125.1, 124.0, 123.3, 119.5, 114.2, 112.8; ^{19}F NMR (376 MHz, $C_2Cl_4D_2$): -77.45 (6F, bs, OTf^-_{free}), -79.04 (12F, s, $OTf^-_{encapsulated}$); nESI (DCE): *m/z* = 2106.2, *Λ*-[**1**·4OTf]$^{2+}$. Anal. Calculated for $C_{174}H_{108}F_{18}Ir_6N_{24}O_{18}S_6$: C, 46.33; H, 2.41; N, 7.45%. Found: C, 46.24; H, 2.54; N, 7.51%.

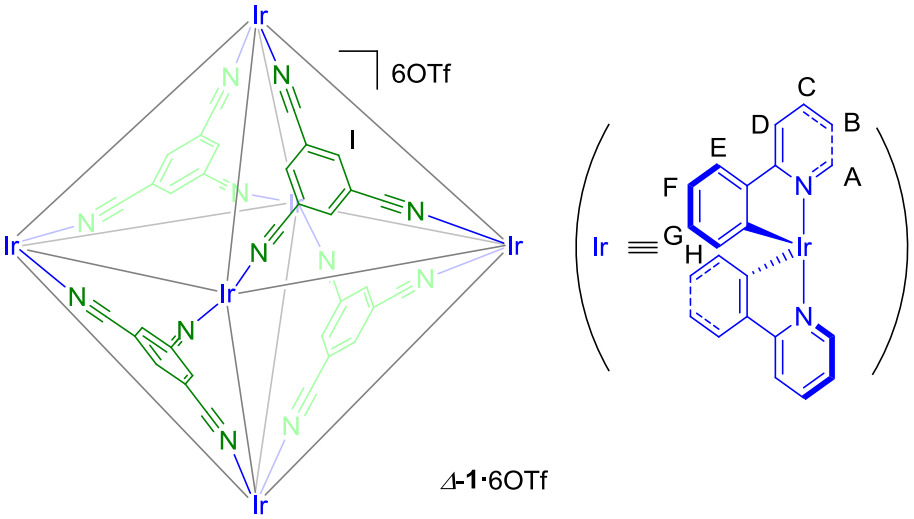

Δ-[(Ir(ppy)$_2$)$_6$(tcb)$_4$](OTf)$_6$ (*Δ*-**1**·6OTf) was synthesised from *Δ*-[(Ir(ppy)$_2$Cl)$_2$] (26.4 mg, 0.025 mmol) in an analogues fashion to *Δ*-**1**·6OTf. Yellow solid obtained (25.3 mg, 68%). Single crystals suitable for XRD were grown by slow vapour diffusion of benzene into a saturated $C_2H_2Cl_4$ solution. Anal. Calculated for $C_{174}H_{108}F_{18}Ir_6N_{24}O_{18}S_6$: C, 46.33; H, 2.41; N, 7.45%. Found: C, 46.33; H, 2.41; N, 7.45%. Further characterisation identical to *Λ*-**1**·6OTf.

3.5.2.6 Synthesis of $[Ir(ppy)_2(PhCN)_2]OTf$

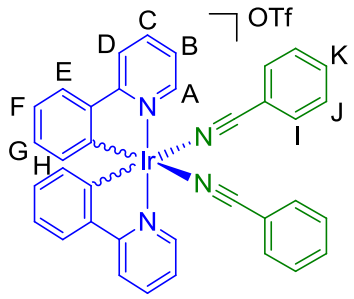

$[Ir(ppy)_2(PhCN)_2]OTf$

A mixture of *rac*-$[(Ir(ppy)_2Cl)_2]$ (30.0 mg, 0.0280 mmol) and AgOTf (14.4 mg, 0.0560 mmol) in $C_2H_4Cl_2$ (20 mL) were stirred at RT in a darkened flask for 2 h. The yellow solution was filtered through celite and concentrated on the rotary evaporator. The resultant residue was re-dissolved in $C_2H_4Cl_2$ (2 mL) and benzonitrile (9.2 mg, 0.0601 mmol) charged. The solution was stirred for 1 h at RT, concentrated on the rotary evaporator. A yellow precipitate was obtained following Et_2O diffusion into the solution, which was isolated *via* filtration (10.2 mg, 21%). ^1H NMR (500 MHz, $C_2D_2Cl_4$ + 10 eq. PhCN): 9.03 (2H, d, J = 5.7 Hz, H_A), 8.07 – 8.00 (4H, m, H_{C+D}), 7.80 – 7.40 (m, $H_{B,E,I,J,K}$ + H_{PhCN}), 7.04 (2H, m, H_F), 6.89 (2H, m, H_G), 6.20 (2H, d, J = 7.4 Hz, H_H). ^{13}C NMR (126 MHz, $C_2D_2Cl_4$ + 10 eq. PhCN): 167.1, 149.9, 143.7, 142.8, 138.9, 134.9, 133.0, 132.9 (C_{PhCN}), 132.0 (C_{PhCN}), 131.2, 130.2, 129.5, 129.1 (C_{PhCN}), 124.3, 123.6, 123.1, 119.8, 119.7, 119.1 (C_{PhCN}), 111.9 (C_{PhCN}), 109.1.

3.5.2.7 Synthesis of *Λ*-[(Ir(ppy)$_2$)$_6$(tcb)$_4$](BF$_4$)$_6$ (*Λ*-**1**·6BF$_4$)

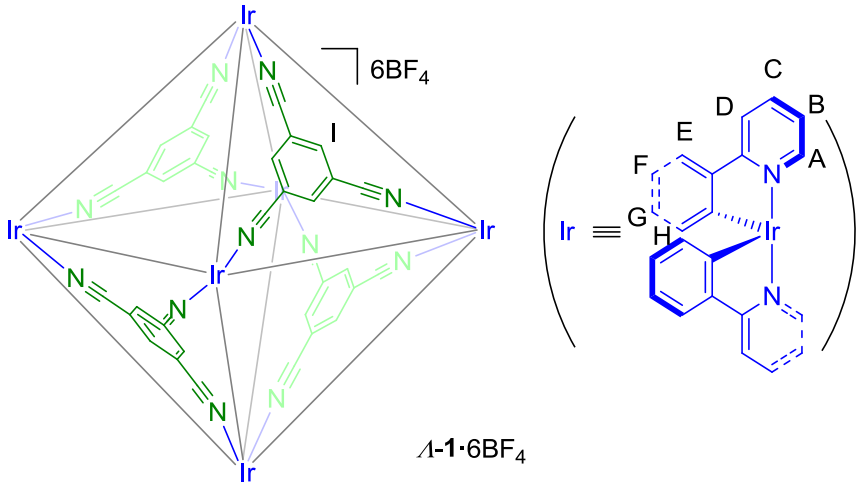

To *Λ*-[(Ir(ppy)$_2$Cl)$_2$] (16.2 mg, 0.015 mmol) was added AgBF$_4$ (5.9 mg, 0.030 mmol) in THF (5 mL) and the mixture was stirred at RT in a darkened flask for 2 h. The orange solution was filtered through celite and concentrated on the rotary evaporator. The crude product was dissolved in $C_2H_4Cl_2$ (1 mL) and tcb (3.1 mg, 0.020 mmol) charged. The solution was stirred for 4 h at RT. The resulting precipitate was filtered off and washed with a minimal amount of $C_2H_4Cl_2$ and Et_2O to give *Λ*-**1**·6BF$_4$ as a yellow solid (11.6 mg, 56%).^{1}H NMR (400 MHz, $C_2D_2Cl_4$): 9.27 (12H, d, J = 5.2 Hz, H_A), 8.20 (12H, m, H_C), 8.11 (12H, s, H_I), 7.98 (12H, d, J = 8.4 Hz, H_D), 7.86 (12H, m, H_B), 7.56 (12H, d, J = 8.3 Hz, H_E), 6.96 (12H, m, H_F), 6.83 (12H, m, H_G), 6.20 (12H, d, J = 7.4 Hz, H_H); ^{19}F NMR (376 MHz, $C_2Cl_4D_2$): -150.77 (24F, bs, BF_4^-); nESI (DCE): m/z = 1981.9 [*Λ*-**1**·4BF$_4$]$^{2+}$.

3.5.3 ^{1}H DOSY NMR for $[(Ir(ppy)_2)_2(bpe)_2](OTf)_2$ and $[(Ir(ppz)_2)_2(bpe)_2](OTf)_2$

The hydrodynamic radius of $[(Ir(ppy)_2)_2(bpe)_2](OTf)_2$ and $[(Ir(ppz)_2)_2(bpe)_2](OTf)_2$ in CD_3NO_2 was determined using ^{1}H DOSY NMR spectroscopy. From the ^{1}H DOSY NMR spectra (Figure 3.13), the measured diffusion coefficient D was used in the Stokes-Einstein equation (*equation 1*) to calculate the effective hydrodynamic radius R_H.

$$R_H = \frac{k_B T}{6\pi\eta D} \qquad (1)$$

where k_B is the Boltzmann constant, T absolute temperature and η the viscosity of the solvent. The viscosity of CD_3NO_2 not being available, that of CH_3NO_2 (0.63 mPa.s)[38] at 298 K was used instead. The diffusion coefficient and computed Stokes-Einstein radius are listed in Table 3.1.

	log D	*D* / $m^2\ s^{-1}$	Stokes-Einstein radius / Å
$[(Ir(ppy)_2)_2(bpe)_2](OTf)_2$	-9.39	4.07×10^{-10}	8.5
$[(Ir(ppz)_2)_2(bpe)_2](OTf)_2$	-9.39	4.07×10^{-10}	8.5

Table 3.1. Diffusion coefficient and computed Stokes-Einstein radius of $[(Ir(ppy)_2)_2(bpe)_2](OTf)_2$ and $[(Ir(ppz)_2)_2(bpe)_2](OTf)_2$ in CD_3NO_2 at 298 K.

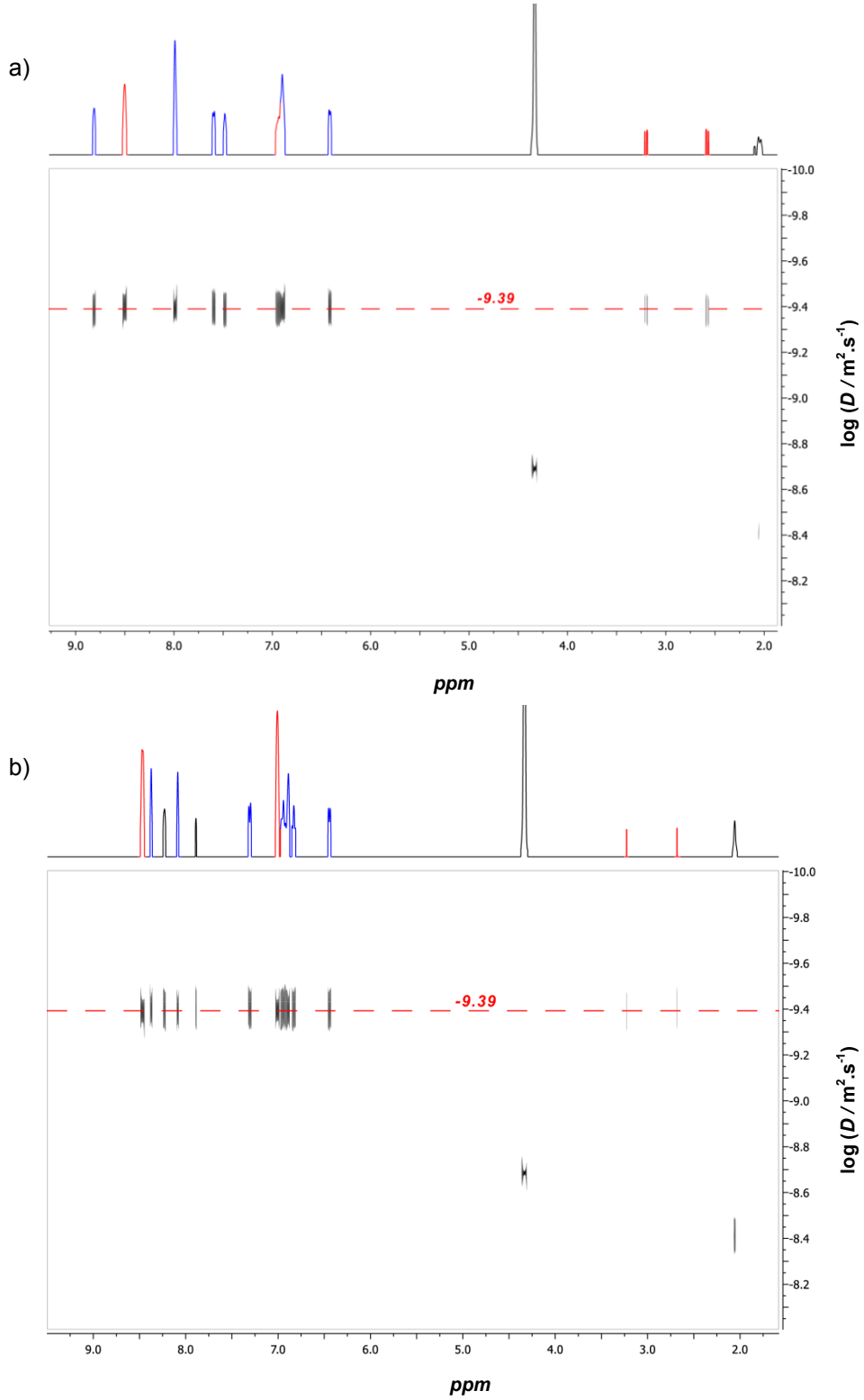

Figure 3.13. ^{1}H DOSY NMR (400 MHz, CD_3NO_2, 298 K) spectra for a) $[(Ir(ppy)_2)_2(bpe)_2](OTf)_2$ and b) $[(Ir(ppy)_2)_2(bpe)_2](OTf)_2$, with corresponding log (D / m^2s^{-1}) = -9.39 and -9.39, respectively.

3.5.4 Mass spectra and isotopic distribution patterns for $[(Ir(ppy)_2)_2(bpe)_2](OTf)_2$ and $[(Ir(ppz)_2)_2(bpe)_2](OTf)_2$.

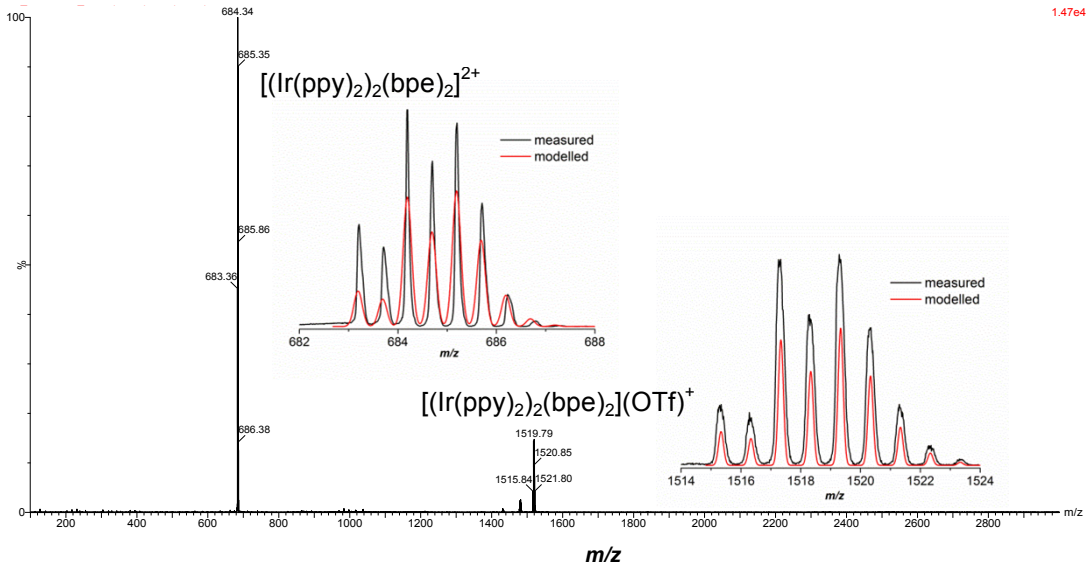

Figure 3.11. nESI mass spectra for $[(Ir(ppy)_2)_2(bpe)_2]^{2+}$ with measured (black) versus modelled (red) isotopic distribution pattern for each ion, 50 μM in $C_2H_4Cl_2$.

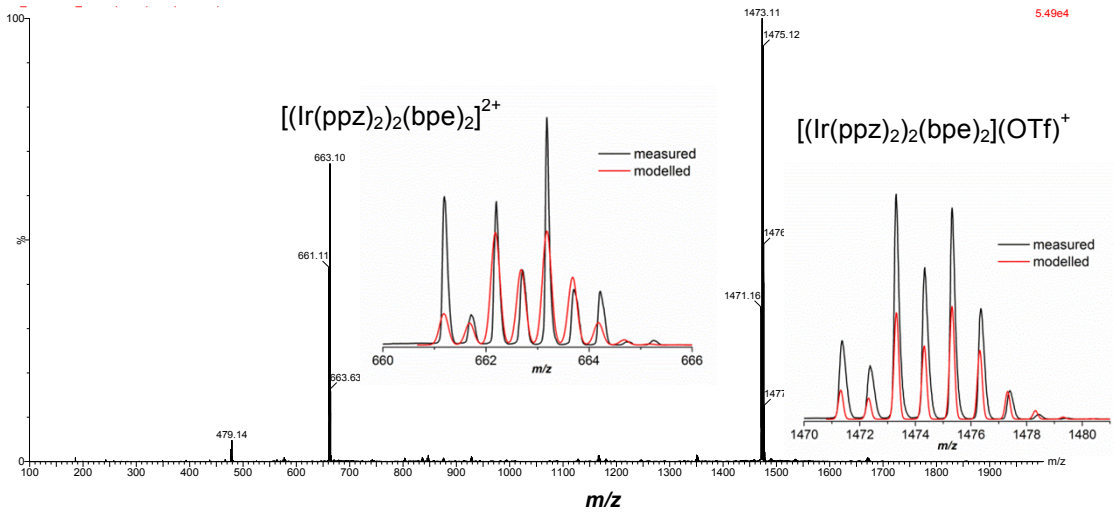

Figure 3.12. nESI mass spectra for $[(Ir(ppz)_2)_2(bpe)_2]^{2+}$ with measured (black) versus modelled (red) isotopic distribution pattern for each ion, 50 μM in $C_2H_4Cl_2$

3.5.5 Mass spectra and isotopic distribution patterns for 1·6OTf

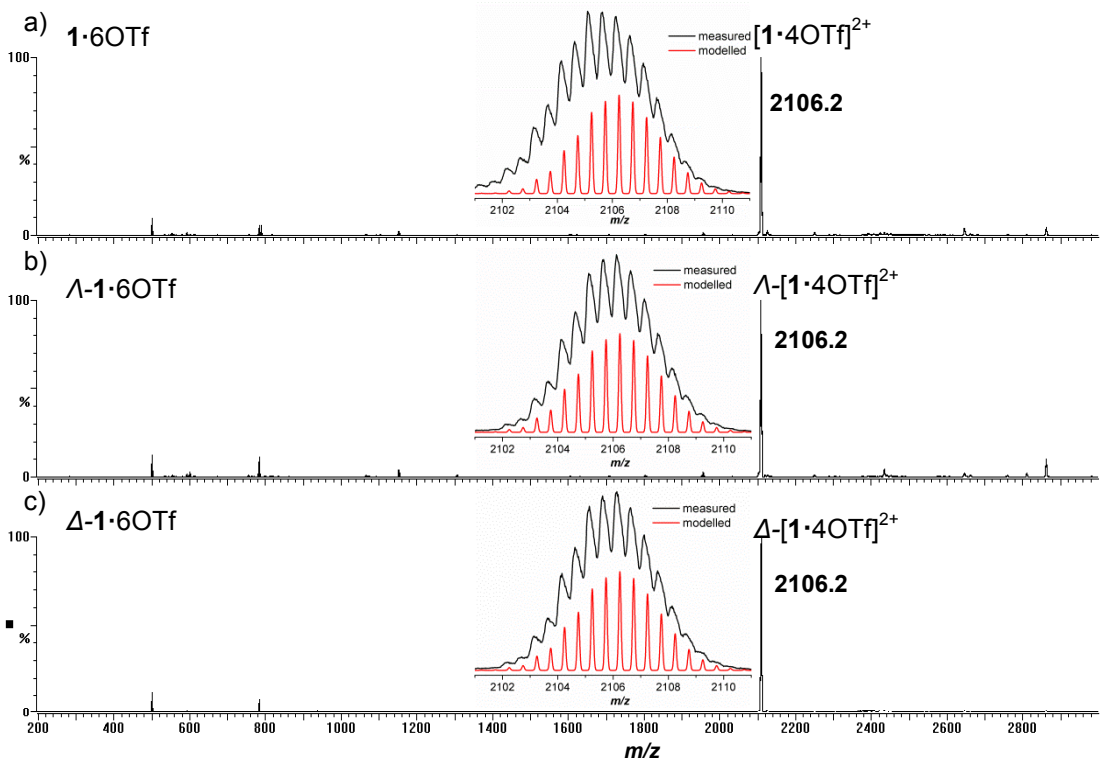

Figure 3.14. nESI mass spectra of a) **1**·6OTf, b) *Λ*-**1**·6OTf, c) *Δ*-**1**·6OTf with measured (black) versus modelled (red) isotopic distribution pattern for each [**1**·4OTf]$^{2+}$ ion, 50 μM in $C_2H_4Cl_2$.

3.5.6 ^{1}H DOSY NMR for 1·6OTf

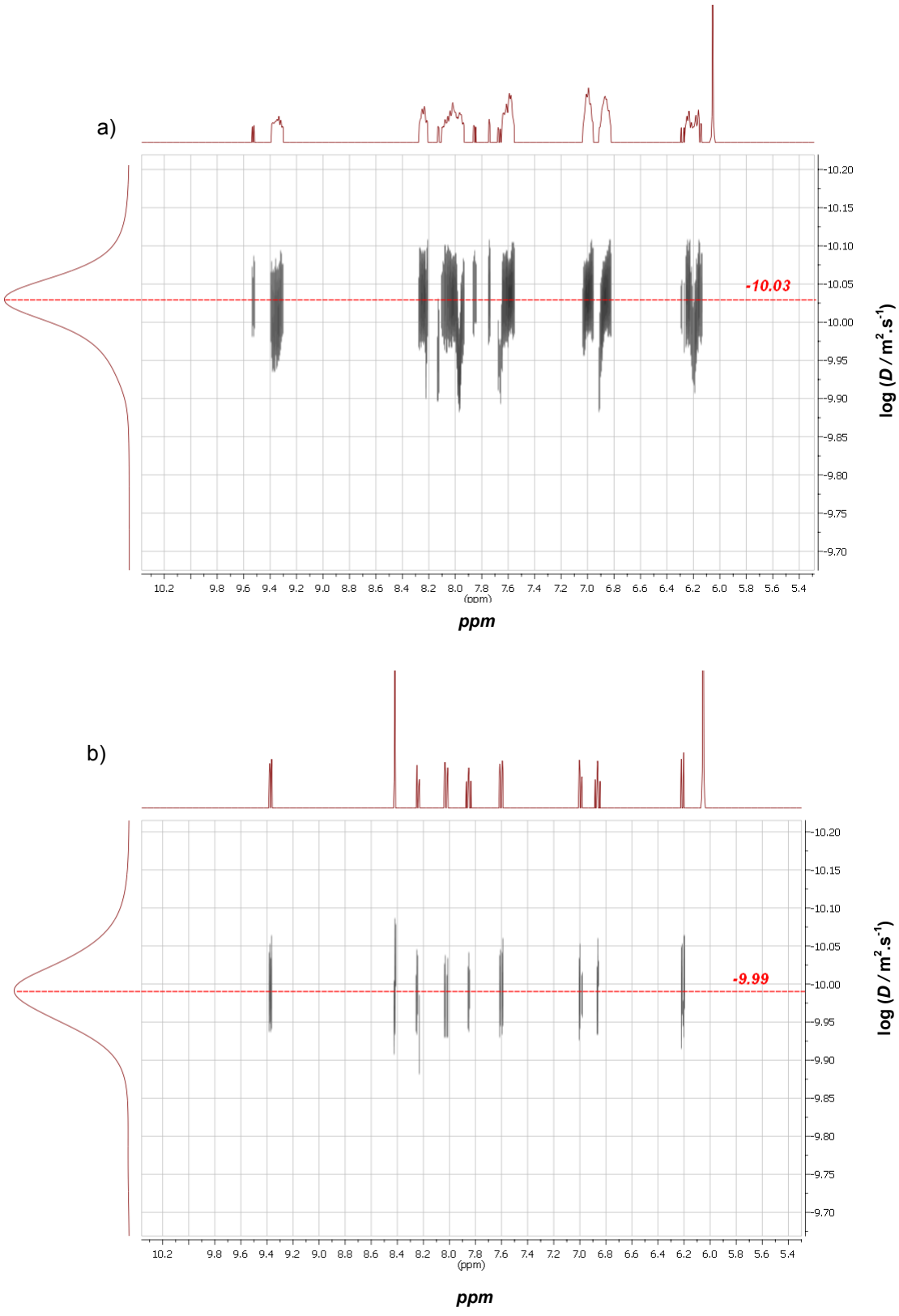

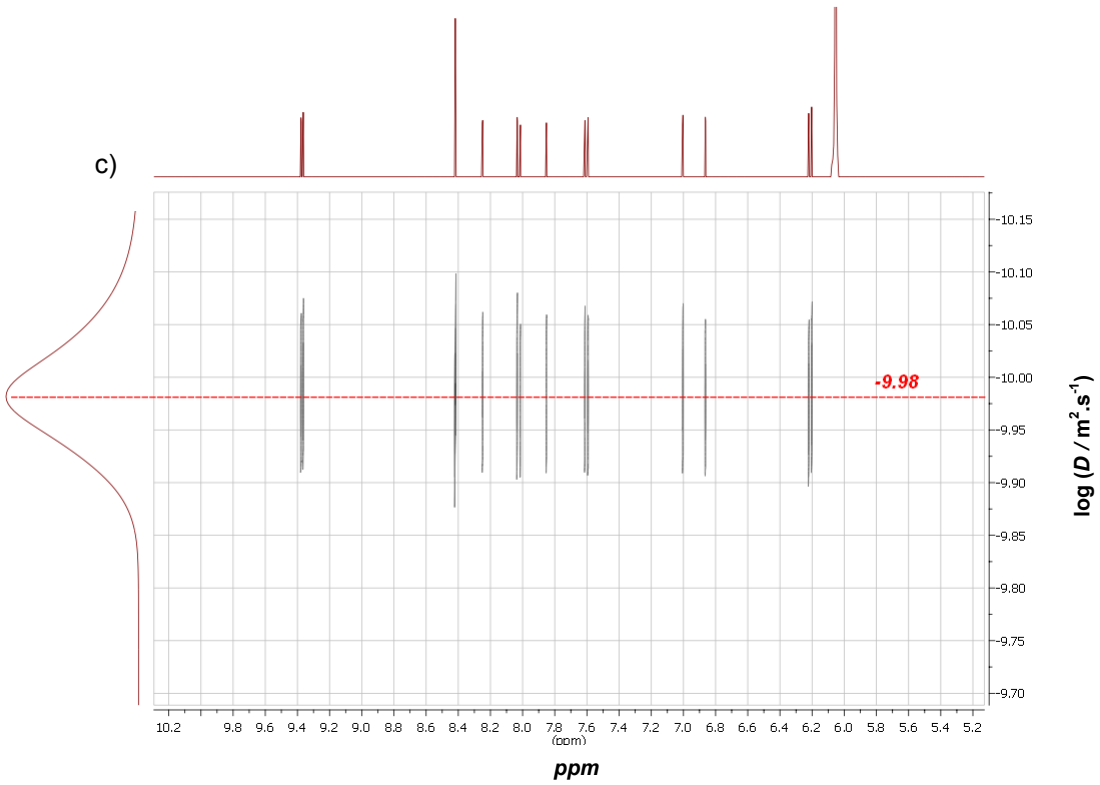

Figure 3.15. ^{1}H DOSY NMR (400 MHz, $C_2D_2Cl_4$, 298 K) spectra for a) **1**·6OTf, b) *Λ*-**1**·6OTf and c) *Δ*-**1**·6OTf, with corresponding log (D / m^2s^{-1}) = -10.03, -9.99, -9.98, respectively.

3.5.7 Circular Dichroism (CD) for selected compounds

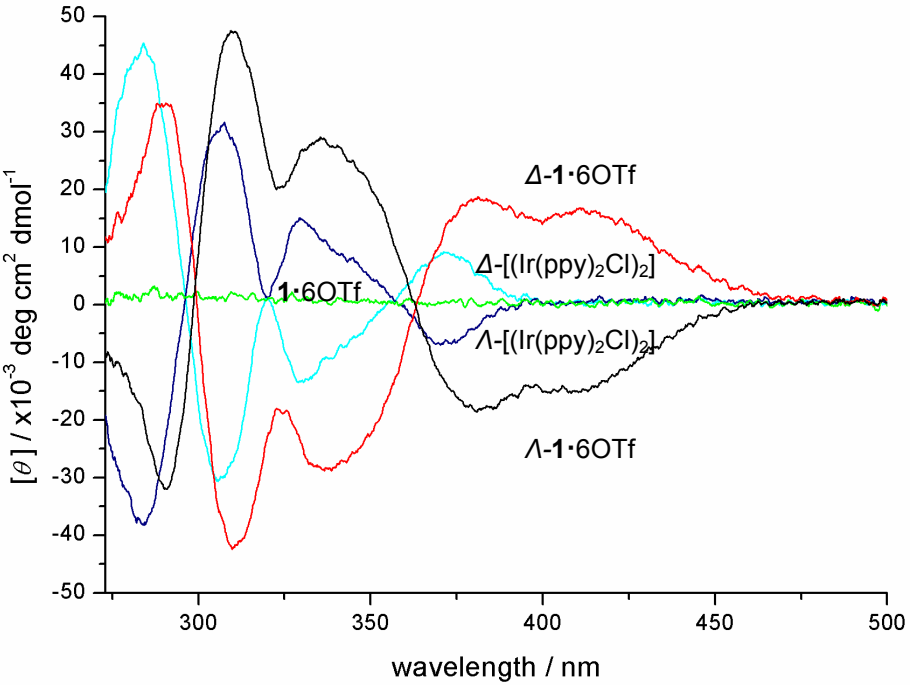

Figure 3.16. CD spectra of *Δ*-**1**·6OTf (red, 5 μM), *Λ*-**1**·6OTf (black, 5 μM), **1**·6OTf (green, 5 μM), *Δ*-[(Ir(ppy)$_2$Cl)$_2$] (light blue, 20 μM) and *Λ*-[(Ir(ppy)$_2$Cl)$_2$] (dark blue, 20 μM), (298 K, TCE).

3.5.8 X-ray crystal structures of *Λ* and *Δ*-[(Ir(ppy)$_2$Cl)$_2$]

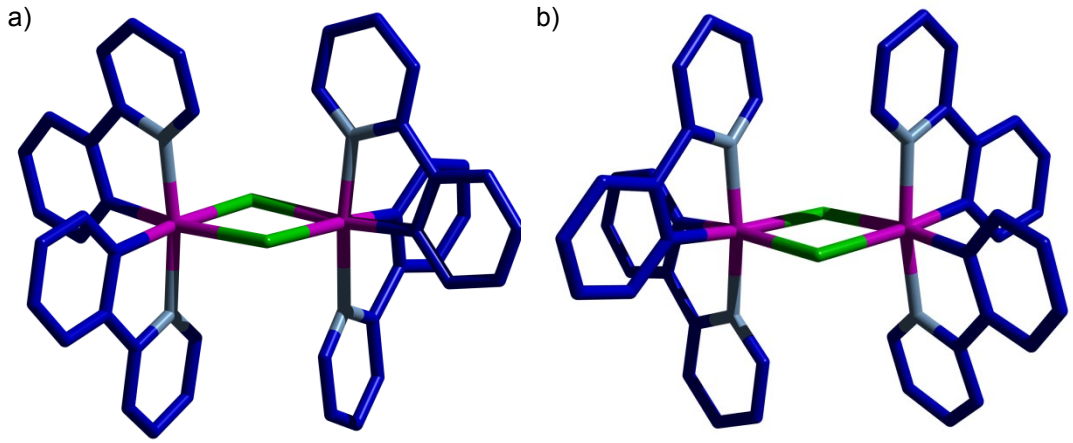

Figure 3.17. X-ray crystal structures of (a) *Λ*-[(Ir(ppy)$_2$Cl)$_2$] and (b) *Δ*-[(Ir(ppy)$_2$Cl)$_2$]. The carbon atoms of ppy are shown in dark blue, iridium ions in magenta, nitrogen atoms in pale blue and chloride ions in green. See section 3.5.21 for crystal data and refinement, bond lengths and angles.

3.5.9 ^{1}H-^{19}F HOESY and ^{19}F DOSY NMR for *Λ*-1·6OTf

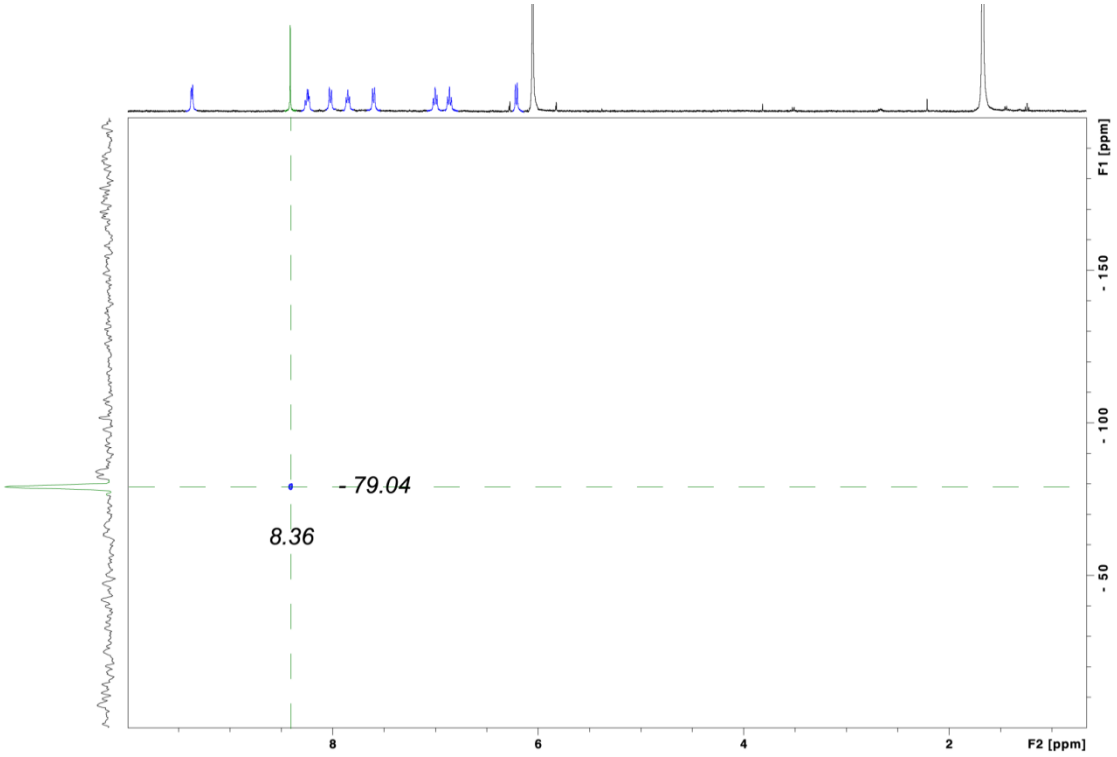

Figure 3.18. ^{19}F-^{1}H HOESY NMR spectra (376 MHz, $C_2D_2Cl_4$, 298 K) of *Λ*-**1**·6OTf (200 μM). Cross peak between the tcb ligand and the encapsulated OTf^- counterions, intercepts at 8.36 ppm and -79.04 ppm on the ^{1}H and ^{19}F NMR spectra, respectively.

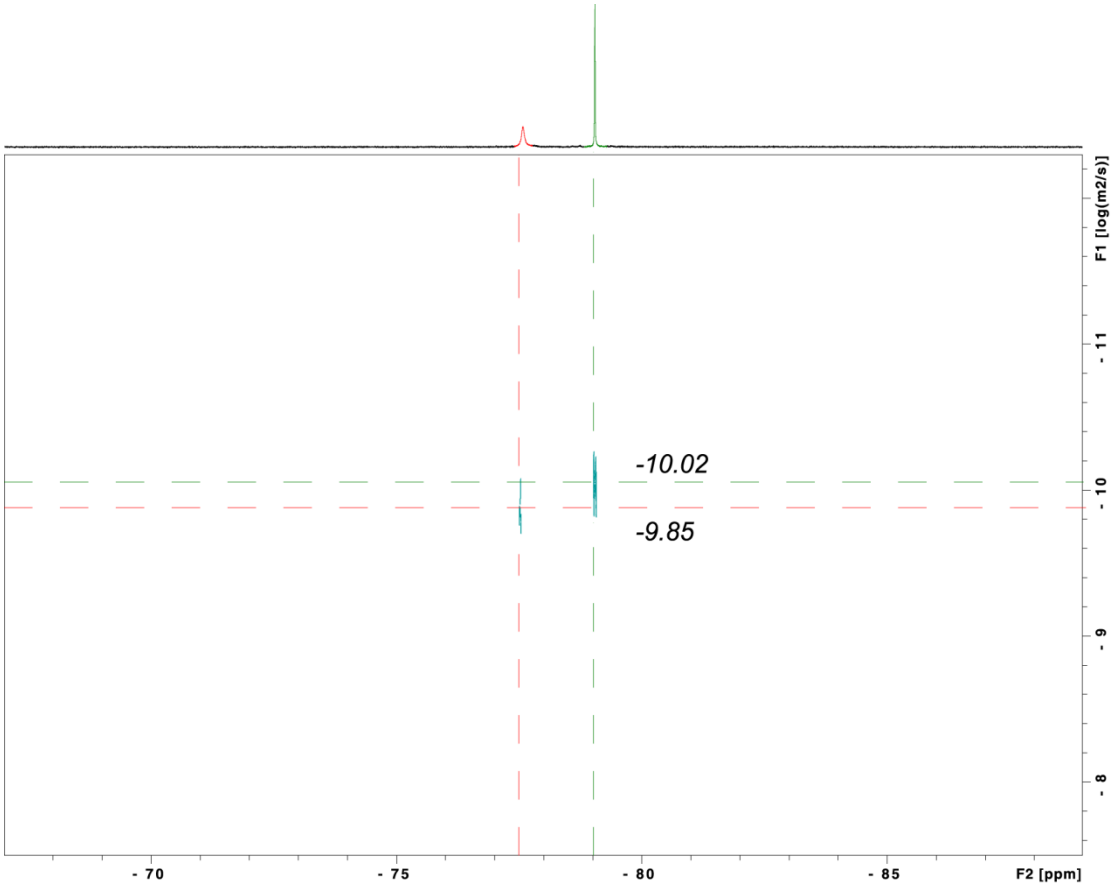

Figure 3.19. ^{19}F DOSY NMR spectra (376 MHz, $C_2D_2Cl_4$, 298 K) of *Λ*-**1**·6OTf (200 μM). Cross peak intercepts at log (D / m^2s^{-1}) = -10.02 (-79.04 ppm) and -9.85 (-77.45 ppm) for the encapsulated (green) and free OTf^- (red), respectively.

3.5.10 Exchange Spectroscopy (2D-EXSY) Investigation of *guest* binding within $\mathbf{1}^{6+}$

^{19}F 2D-EXSY was used to investigate the kinetics of exchange for [4OTf⊂*Λ*-**1**]2OTf; all spectra were recorded on a Bruker 400 MHz NMR spectrometer at 298 K with the mixing time, τ_m, set to 1.0 s. Using *equation 2* shown below, where I_{AA} and I_{BB} are the diagonal peak intensities and I_{AB} and I_{BA} are the cross-peak intensities, r was calculated. k which is the sum of the forward, k_1, and backward, k_{-1}, pseudo-first order rate constants for the *guest* exchange process was obtained using *equations 3-4*. As both processes are equal opposites ($k_1 = k_{-1}$) the observed pseudo-first order rate constant, k_{obs}, can be determined from *equation 5*. k_{obs} was used in the Eyring equation (*equation 6*) to determine the value of $\Delta G^{\ddagger}$.

$$r = \frac{(I_{AA} + I_{BB})}{(I_{AB} + I_{BA})} \qquad (2)$$

$$HG_n + G^* \underset{k_{-1}}{\overset{k_1}{\rightleftharpoons}} HG_{n-1}G^* + G \qquad (3)$$

$$k = \frac{1}{\tau_m} \times \ln \frac{r+1}{r-1} \qquad (4)$$

$$k = k_1 + k_{-1} = 2 \times k_{obs} \qquad (k_1 = k_{-1} = k_{obs}) \qquad (5)$$

$$\Delta G^{\ddagger} = -RT \ln \frac{k_{obs} h}{k_B T} \qquad (6)$$

(R = 1.9872 *cal K^{-1} mol^{-1}*, k_B = 3.30 x 10^{-24} *cal K^{-1}*, h = 1.58 x 10^{-34} *cal s*)

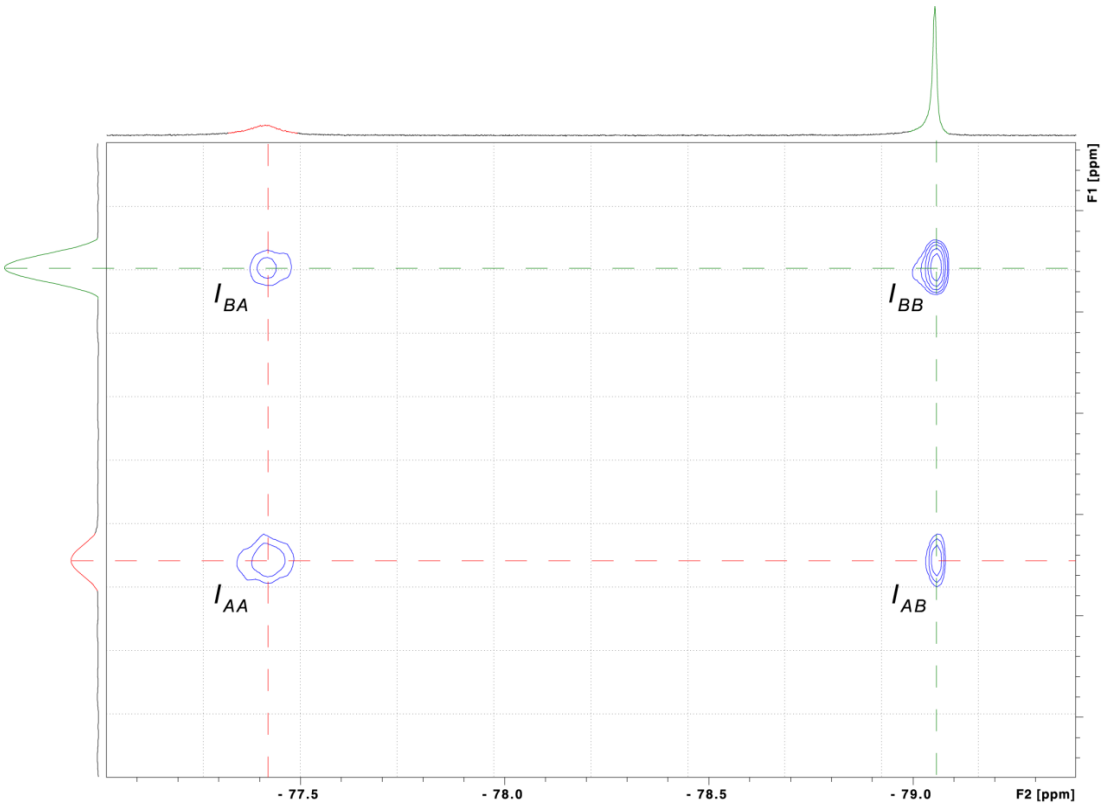

Figure 3.20. Partial ^{19}F 2D-EXSY spectrum of (376 MHz, $C_2D_2Cl_4$, 298 K) of *Δ*-**1**·6OTf.

	I_{AA}	I_{AB}	I_{BB}	I_{BA}	k_{obs} (s^{-1})	$\Delta G^{\ddagger}$ (kcal mol^{-1})
F_{OTf}	0.4716	0.2793	1.0000	0.2432	0.37	18.0

Table 3.2. Kinetic parameters of *Δ*-**1**·6OTf in $C_2D_2Cl_4$.

3.5.11 Ion-Mobility MS ATD and CCS calculations

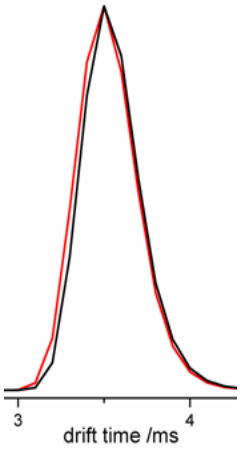

Figure 3.21. Arrival time distribution (ATD) at electric field of 4 V cm^{-1}, for *Λ*-[**1**·4OTf]$^{2+}$ (red) and *Δ*-[**1**·4OTf]$^{2+}$ (black), both at 2106 m/z.

	Λ-[**1**·4OTf]$^{2+}$	*Δ*-[**1**·4OTf]$^{2+}$
Ω_{expt} (Å^2)	551±3	543±3
Ω_{calc}^{EHSS} (Å^2)	-	555[a]
Ω_{calc}^{TJM} (Å^2)	-	551[a]

Table 3.3. Collision cross sections (CCS) for *Λ* and *Δ*-[**1**·4OTf]$^{2+}$ at 2106 m/z. [a]calculated using the XRD data for *Δ*-**1**·6OTf with solvent molecules and outer OTf^- counterions omitted. EHSS = Exact Hard Spheres Scattering, TJM = Trajectory Method.

3.5.12 Capsule occupancy calculations

A python program based on the molecular simulation library Sire was written to estimate the capsule occupancy using a numerical approach.[39] A 3-dimensional rectangular grid of cubes of 0.5 Å edge length was overlapped on the crystallographic structure of *Δ*-**1**·6OTf. An irregular hexadecahedron was then defined to cover the capsule cavity. The coordinates of the polyhedron edges were defined by the 6 iridium atoms, and four virtual sites. As shown in Figure 3.22A, the coordinate of each virtual site was taken as the geometric centre of the *meta*-pyridyl proton from three nearby three ppy groups. Any cubes on the rectangular grid whose centre did not fit inside the

hexadecahedron were then discarded. Any remaining cube whose centre was overlapped by any atom present in the crystallographic structure was then discarded. Bondi van der Waals radii were used to compute atomic overlaps (Hydrogen 1.20 Å; Carbon 1.70 Å; Nitrogen 1.55 Å; Oxygen 1.52 Å; Fluoride 1.47 Å; Sulphur 1.8 Å; Iridium 2.00 Å).[40] The free volume was then estimated by summing the volume of every remaining cube. To estimate the volume of the cavity without ligands, the calculation was repeated after removing the 4 encapsulated triflate ions present in the crystallographic structure. Similar volumes were obtained using a grid of cubes of 1.0 Å or 0.25 Å edge lengths. The volumes computed using this protocol were 506 $Å^3$ for the capsule without OTf^- *guests* (Figure 3.22B), and 226 $Å^3$ with the four OTf^- anions bound (Figure 3.22C). The cavity occupancy by the four OTf^- anions is therefore 55%.

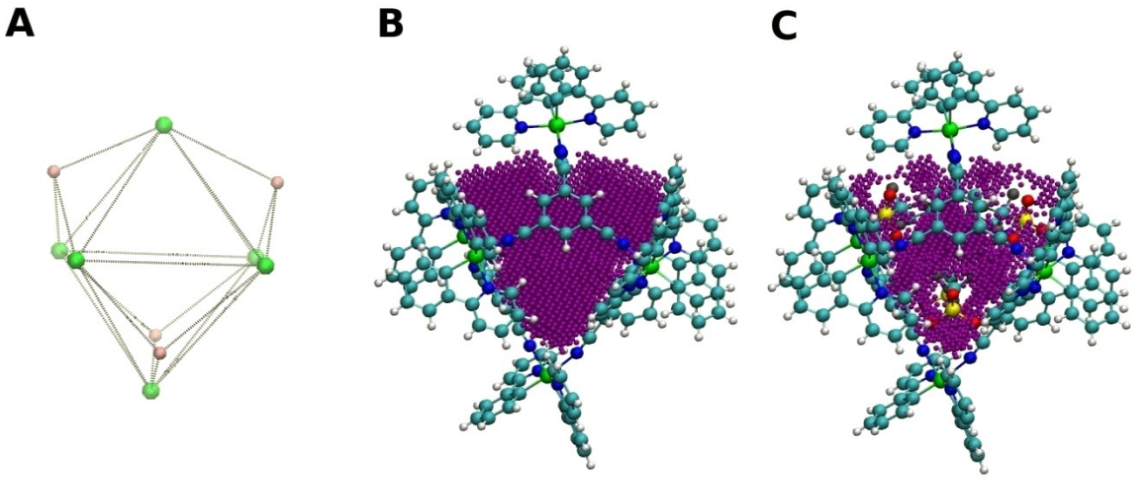

Figure 3.22. A) Cavity definition using an irregular hexadecahedron. The green spheres depict the position of iridium atoms, and the pink spheres the position of virtual sites (see main text). B) Free volume of the cavity without ligands. C) Free volume of the cavity with four OTf^- bound. Each purple sphere represents the centre of a cube of edge length 0.5 Å. Cyan spheres represent carbon atoms, white spheres hydrogen atoms, blue spheres nitrogen atoms, green spheres iridium atoms, red spheres oxygen atoms, yellow spheres sulfur atoms, gray spheres fluorine atoms. Figure created with the software VMD.[41]

3.5.13 ^{1}H NMR and UV-Vis of [Ir(ppy)$_2$(PhCN)$_2$]OTf

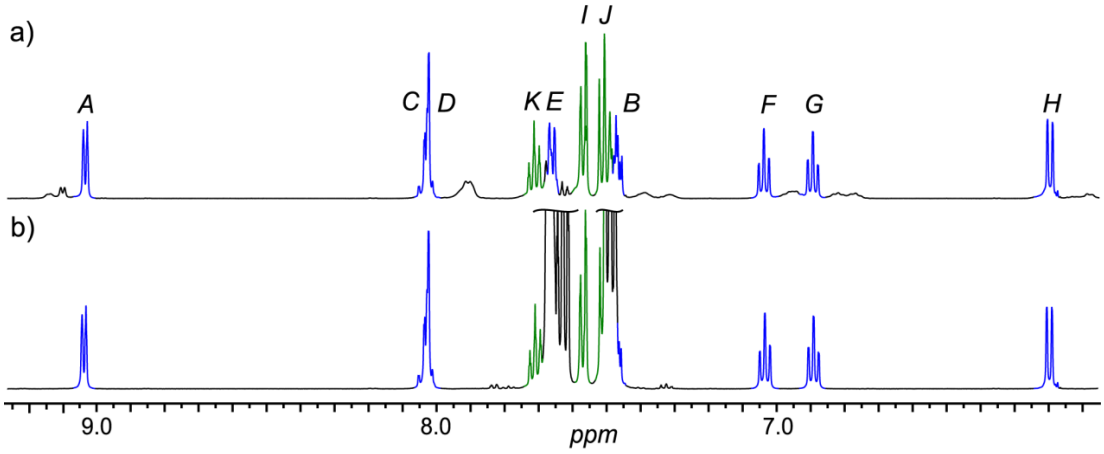

Figure 3.23. ^{1}H NMR spectra (500 MHz, $C_2D_2Cl_4$, 298 K) of a) [Ir(ppy)$_2$(PhCN)$_2$]OTf and b) [Ir(ppy)$_2$(PhCN)$_2$]OTf with excess PhCN (10 eq). See section 3.5.2.6 for assignment.

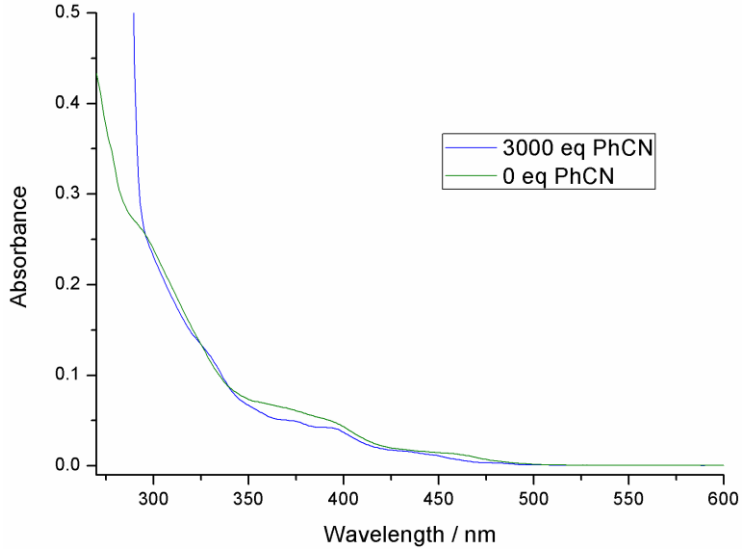

Figure 3.24. UV-Vis spectra of [Ir(ppy)$_2$(PhCN)$_2$]OTf with 0 eq PhCN (green) and 3000 eq PhCN (blue), (12 µM, 298 K, TCE).

3.5.14 *Guest* exchange experiments

Anion exchange experiments were performed by titrating a mixed $C_2D_2Cl_4$ solution of Bu_4NX / *Δ/Λ*-**1**·6X ([Bu_4NX] = 4-5 mM, [*Δ/Λ*-**1**·6X] = 100-200 μM) into a $C_2D_2Cl_4$ solution of *Δ/Λ*-**1**·6X ([*Δ/Λ*-**1**·6X] = 100-200 μM). The anion exchange experiments were monitored by ^1H and ^{19}F NMR.

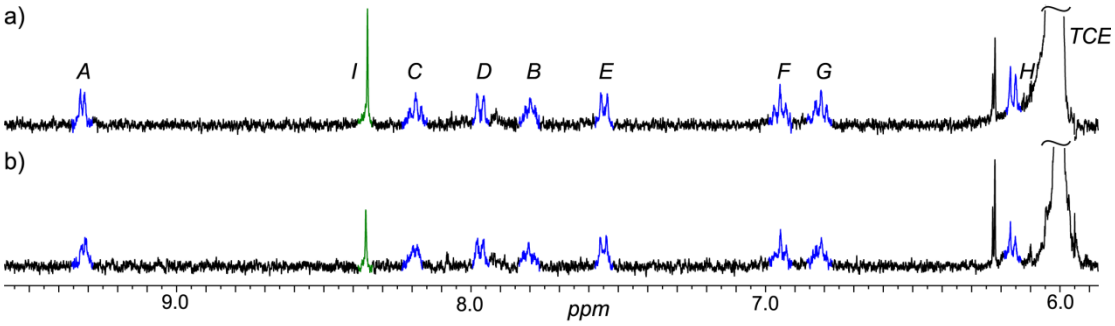

Figure 3.25. ^1H NMR (400 MHz, $C_2D_2Cl_4$, 298 K) spectra of: a) *Λ*-**1**·6OTf; b) *Λ*-**1**·6OTf with 35 eq Bu_4NBF_4. See section 3.5.2.5 for assignment.

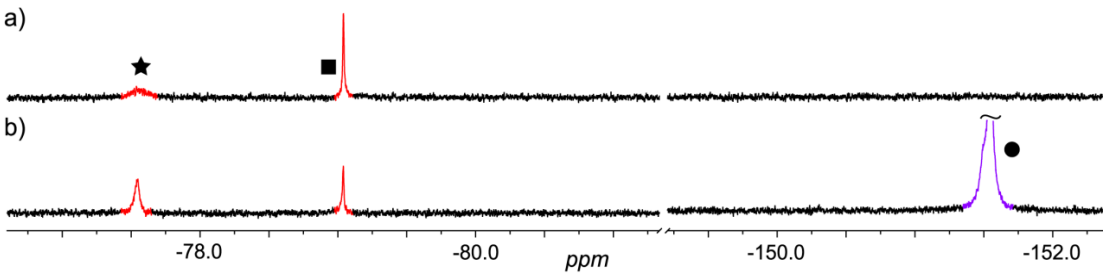

Figure 3.26. ^{19}F NMR (376 MHz, $C_2D_2Cl_4$, 298 K) spectra of: a) *Λ*-**1**·6OTf; b) *Λ*-**1**·6OTf with 35 eq Bu_4NBF_4.★ peak for free OTf^-; ■ ecapsulated OTf^-; ● encapsulated/free BF_4^- in fast exchange on the NMR timescale.

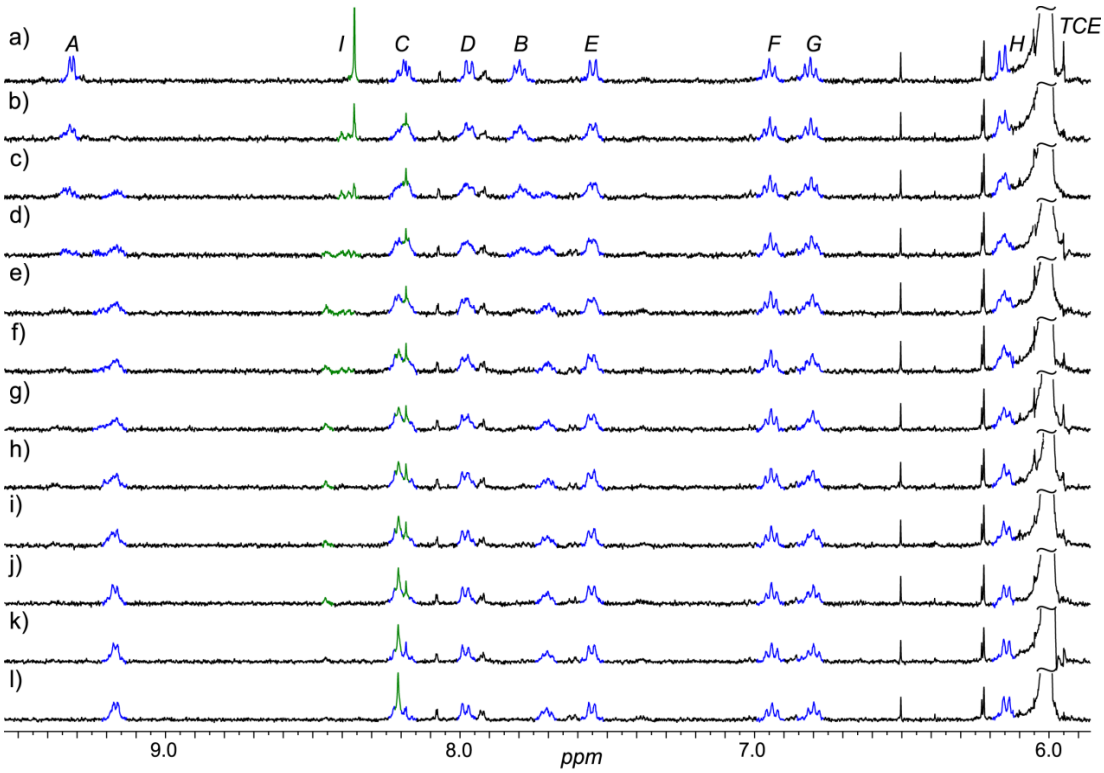

Figure 3.27. ^{1}H NMR (400 MHz, $C_2D_2Cl_4$, 298 K) spectra of $Bu_4NCF_3BF_3$ titration into *Δ*-**1**·6OTf: a) *Δ*-**1**·6OTf; b) *Δ*-**1**·6OTf with 0.7 eq Bu_4NPF_6; c) 1.9 eq; d) 3.5 eq; e) 6.2 eq; f) 8.4 eq; g) 8.8 eq; h) 12.8 eq; i) 18.5 eq; j) 25.5 eq; k) 38.1 eq; l) 76.8 eq. See section 3.5.2.5 for assignment.

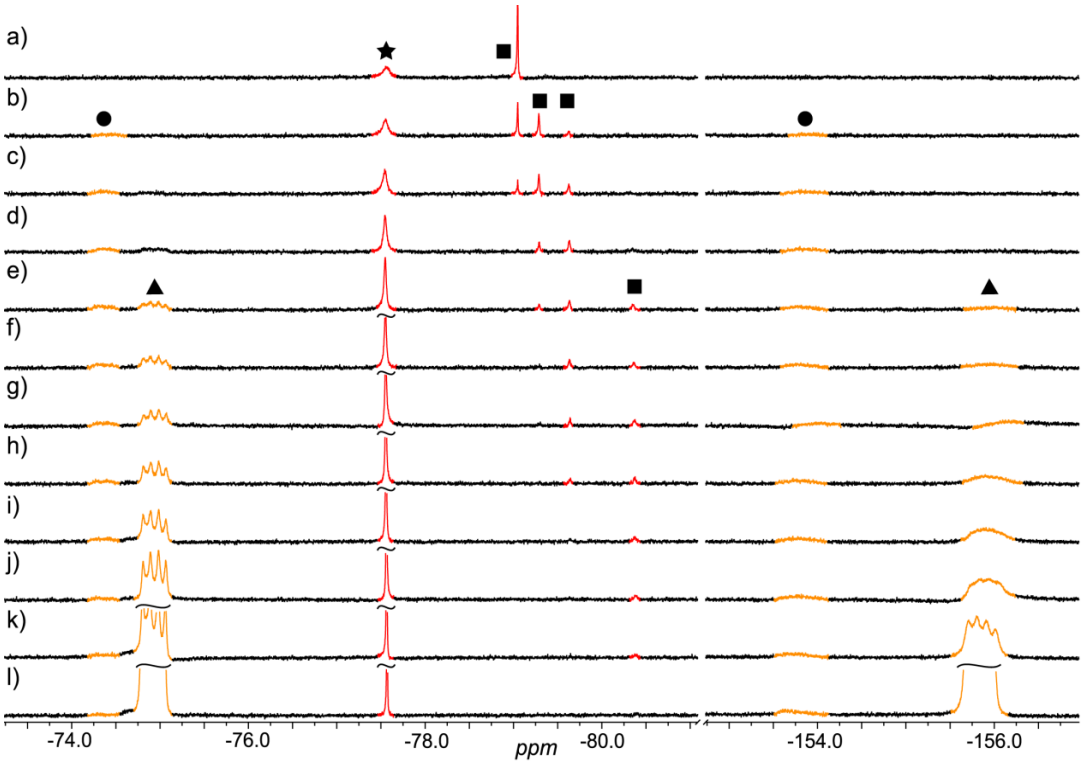

Figure 3.28. ^{19}F NMR (376 MHz, $C_2D_2Cl_4$, 298 K) spectra of $Bu_4NCF_3BF_3$ titration into *Δ*-**1**·6OTf: a) *Δ*-**1**·6OTf; b) *Δ*-**1**·6OTf with 0.7 eq Bu_4NPF_6; c) 1.9 eq; d) 3.5 eq; e) 6.2 eq; f) 8.4 eq; g) 8.8 eq; h) 12.8 eq; i) 18.5 eq; j) 25.5 eq; k) 38.1 eq; l) 76.8 eq. ★ peak for free OTf^-; ■ ecapsulated OTf^-; ● encapsulated $CF_3BF_3^-$; ▲ free $CF_3BF_3^-$.

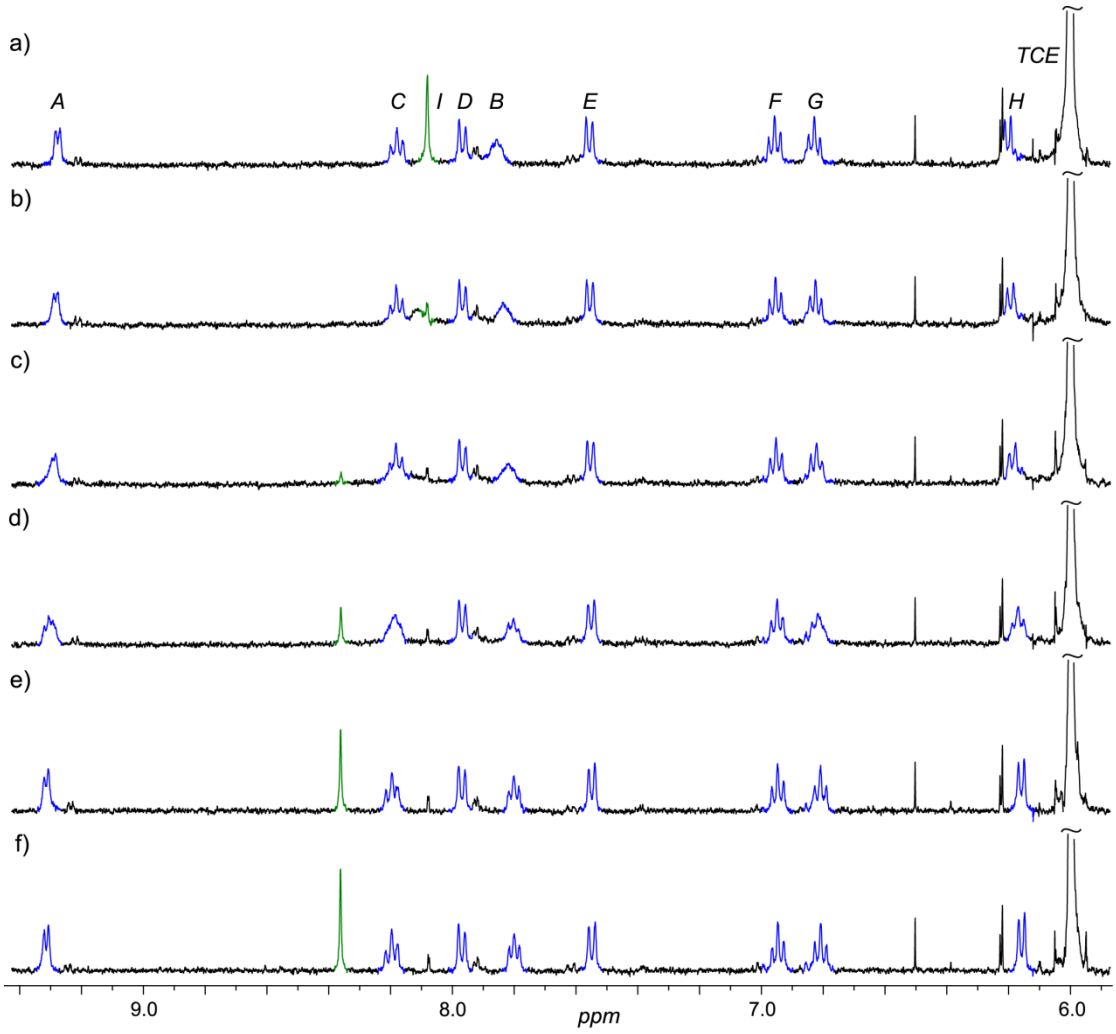

Figure 3.29. ^{1}H NMR (400 MHz, $C_2D_2Cl_4$, 298 K) spectra of Bu_4NOTf titration into *Λ*-**1**·6BF_4: a) *Λ*-**1**·6BF_4; b) *Λ*-**1**·6BF_4 with 0.8 eq Bu_4NOTf; c) 1.6 eq; d) 3.1 eq; e) 6.2 eq; f) 9.1 eq. See section 3.5.2.7 for assignment.

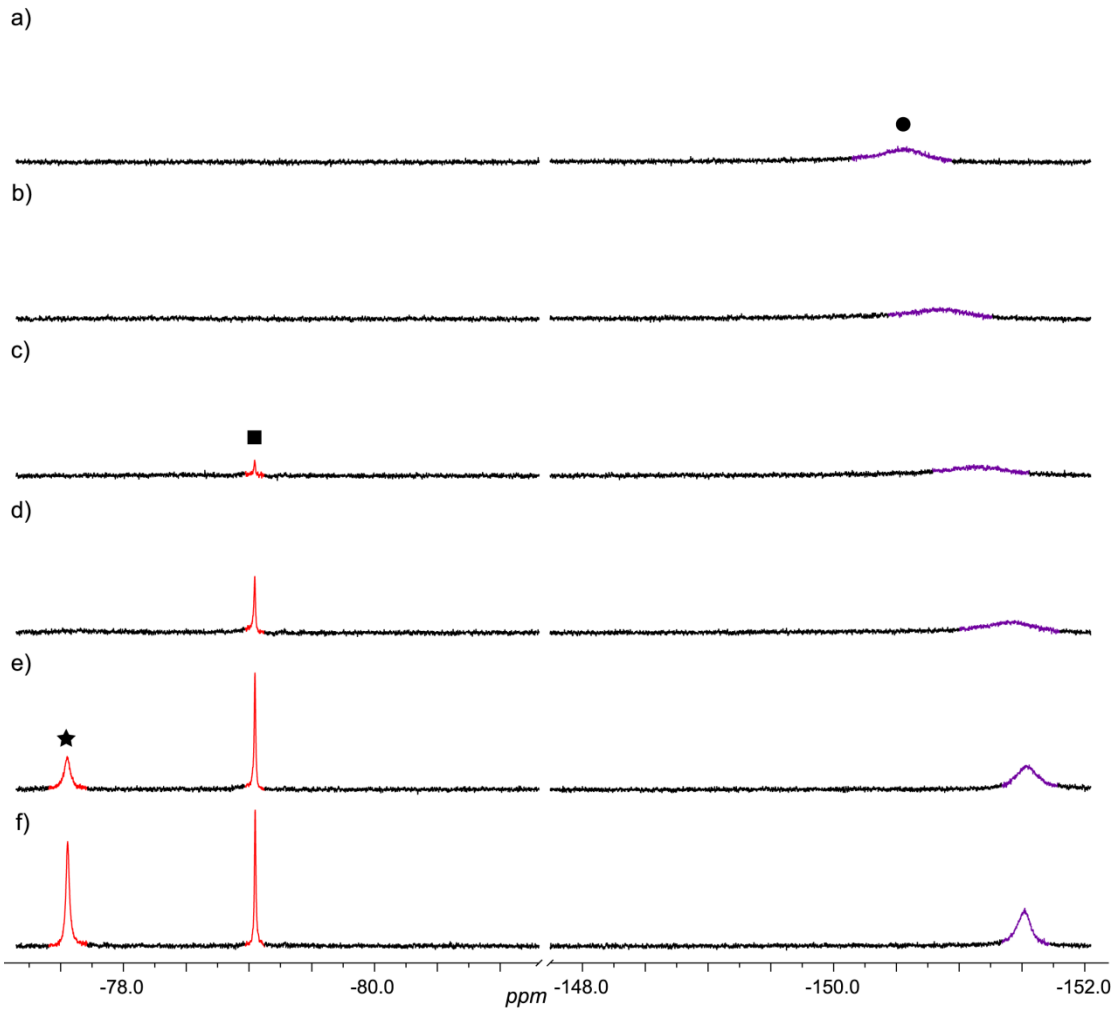

Figure 3.30. ^{19}F NMR (376 MHz, $C_2D_2Cl_4$, 298 K) spectra of Bu_4NOTf titration into *Λ*-**1**·6BF_4: a) *Λ*-**1**·6BF_4; b) *Λ*-**1**·6BF_4 with 0.8 eq Bu_4NOTf; c) 1.6 eq; d) 3.1 eq; e) 6.2 eq; f) 9.1 eq. ★ peak for free OTf^-; ■ ecapsulated OTf^-; ● encapsulated/free BF_4^- in fast exchange on the NMR timescale.

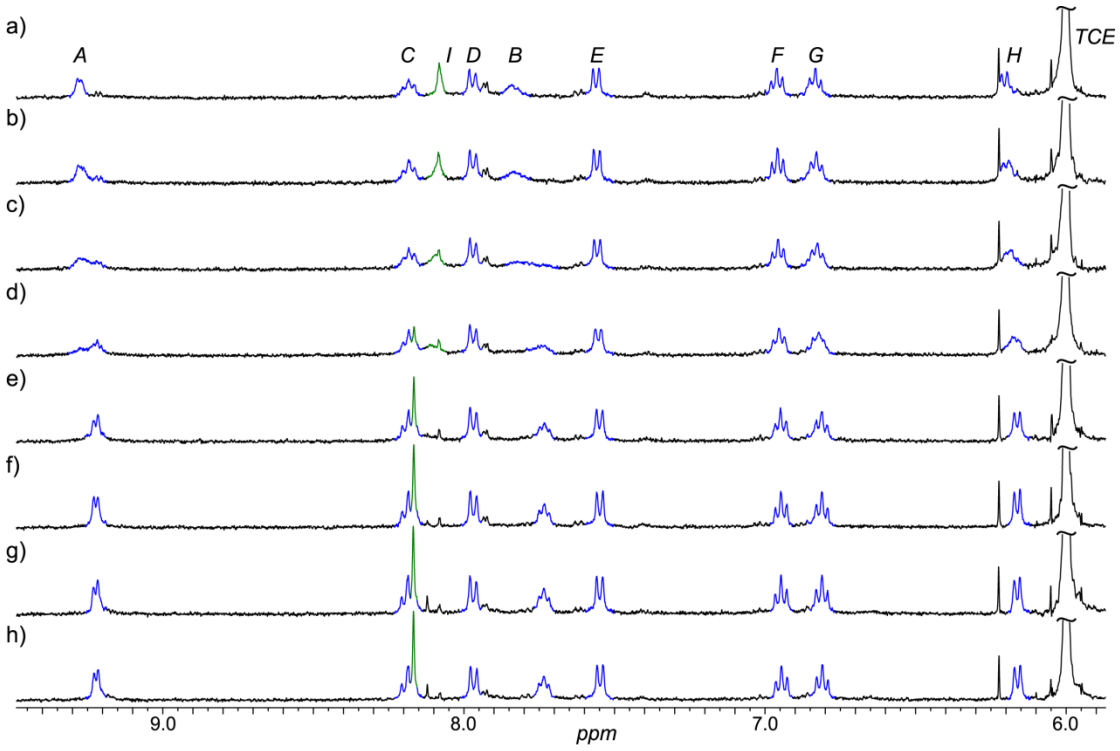

Figure 3.31. ^{1}H NMR (400 MHz, $C_2D_2Cl_4$, 298 K) spectra of Bu_4NPF_6 titration into *Λ*-**1**·6BF_4: a) *Λ*-**1**·6BF_4; b) *Λ*-**1**·6BF_4 with 0.5 eq Bu_4NPF_6; c) 0.9 eq; d) 2.0 eq; e) 3.9 eq; f) 6.2 eq; g) 7.9 eq; h) 9.5 eq. See section 3.5.2.7 for assignment.

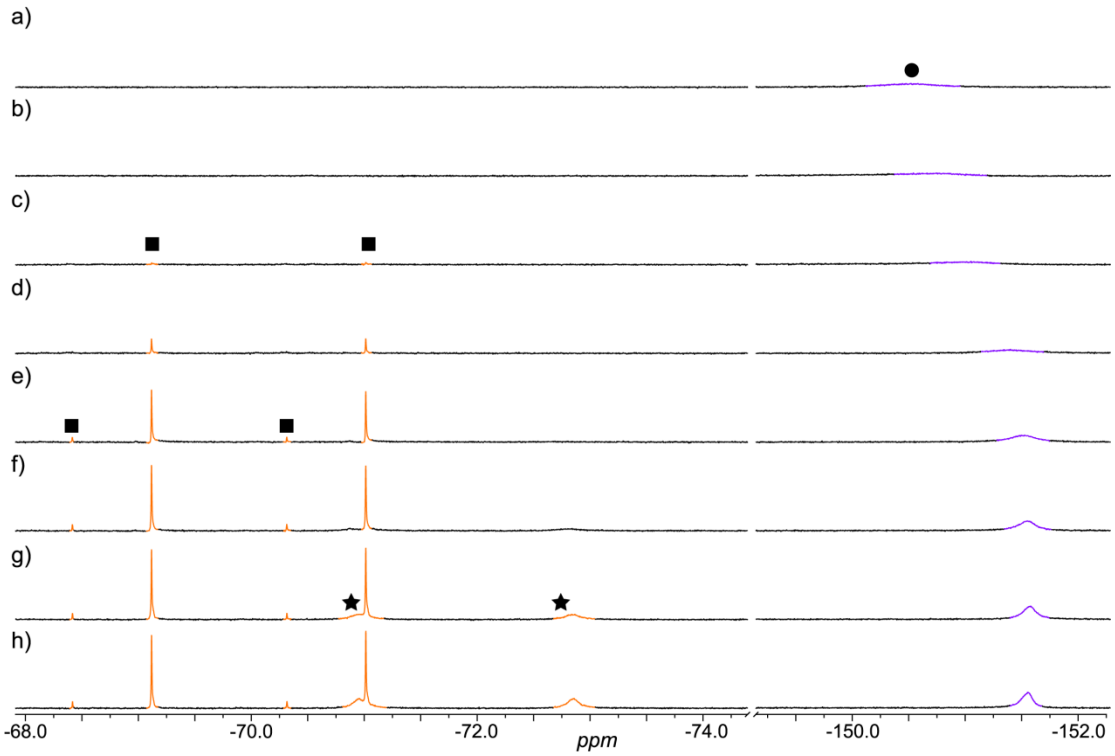

Figure 3.32. ^{19}F NMR (376 MHz, $C_2D_2Cl_4$, 298 K) spectra of Bu_4NPF_6 titration into *Λ*-**1**·6BF_4: a) *Λ*-**1**·6BF_4; b) *Λ*-**1**·6BF_4 with 0.5 eq Bu_4NPF_6; c) 0.9 eq; d) 2.0 eq; e) 3.9 eq; f) 6.2 eq; g) 7.9 eq; h) 9.5 eq. ★ peak for free PF_6^-; ■ ecapsulated PF_6^-; ● encapsulated/free BF_4^- in fast exchange on the NMR timescale.

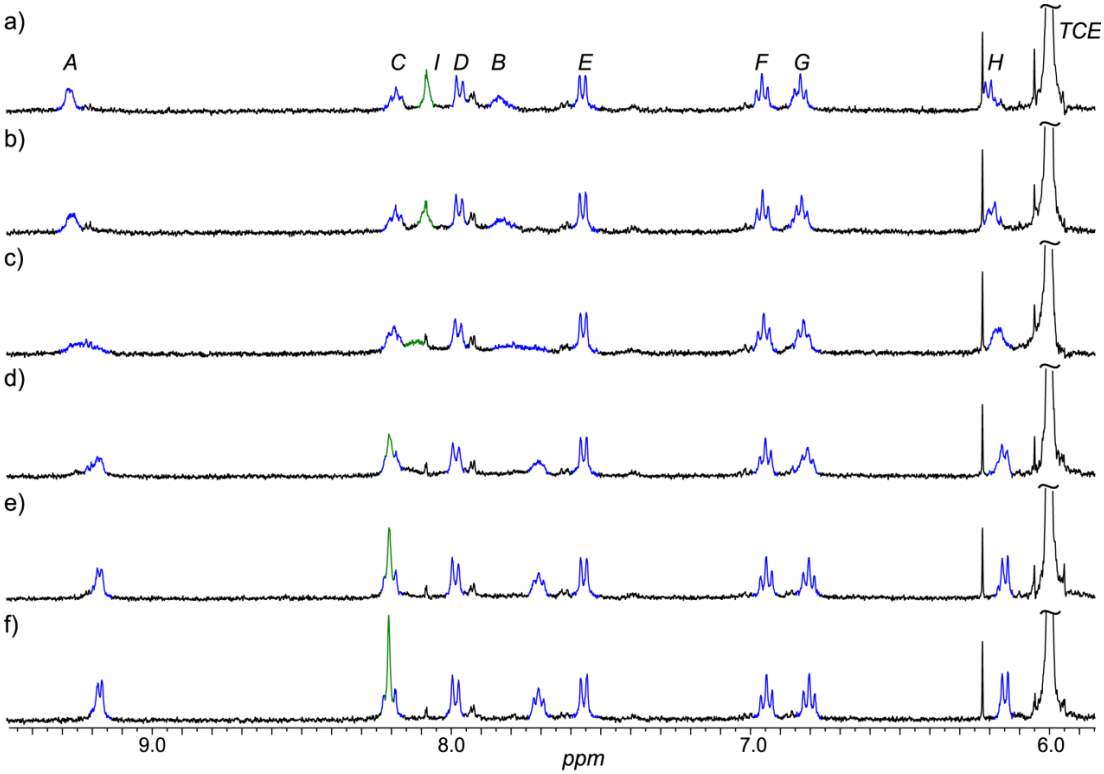

Figure 3.33. ^{1}H NMR (400 MHz, $C_2D_2Cl_4$, 298 K) spectra of $Bu_4NCF_3BF_3$ titration into *Λ*-**1**·6BF_4: a) *Λ*-**1**·6BF_4; b) *Λ*-**1**·6BF_4 with 0.4 eq Bu_4NPF_6; c) 2.0 eq; d) 3.0 eq; e) 5.4 eq; f) 9.0 eq. See section 3.5.2.7 for assignment.

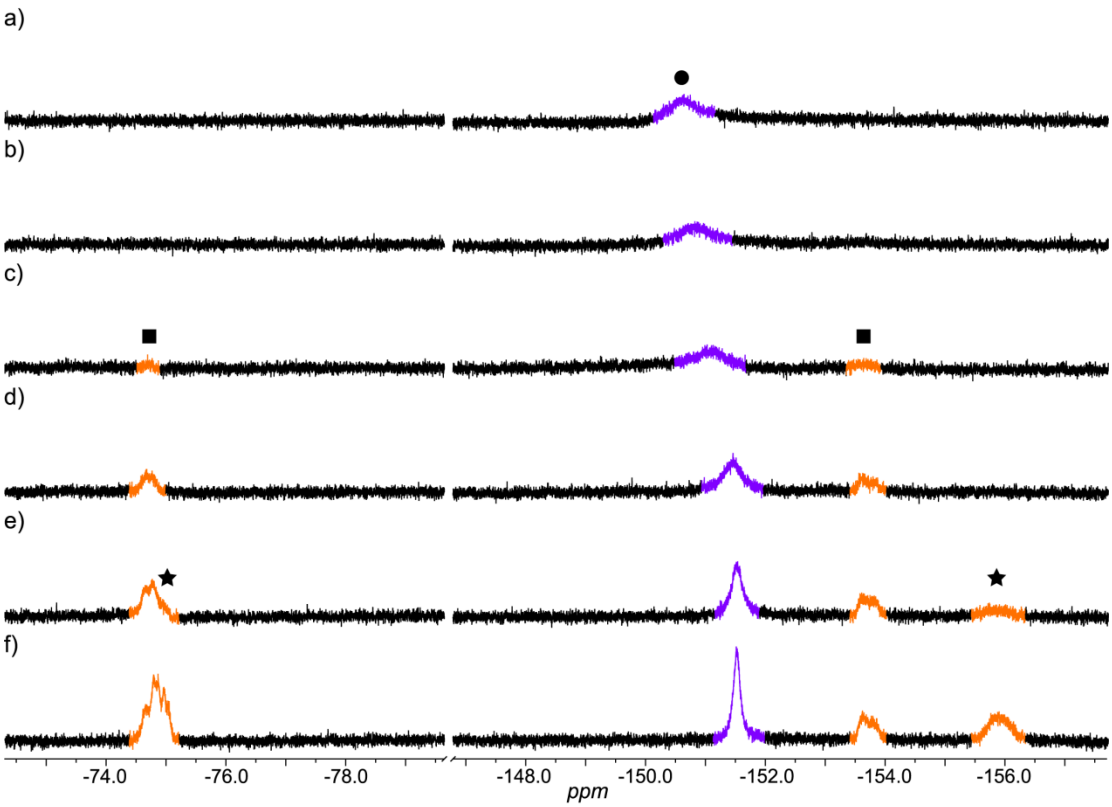

Figure 3.34. ^{19}F NMR (376 MHz, $C_2D_2Cl_4$, 298 K) spectra of $Bu_4NCF_3BF_3$ titration into *Λ*-**1**·6BF_4: a) *Λ*-**1**·6BF_4; b) *Λ*-**1**·6BF_4 with 0.4 eq Bu_4NPF_6; c) 2.0 eq; d) 3.0 eq; e) 5.4 eq; f) 9.0 eq. ★ peak for free $CF_3BF_3^-$; ■ ecapsulated $CF_3BF_3^-$; ● encapsulated/free BF_4^- in fast exchange on the NMR timescale.

3.5.15 Other attempted *guests*

The following anions and neutral *guests* (see Table 3.4) were screened for encapsulation within [*Δ*/*Λ*-**1**]$^{6+}$. All neutral and anionic *guests* (anions as their Bu_4N^+ salts) were added to a $C_2D_2Cl_4$ (unless stated otherwise) solution of either *Δ*/*Λ*-**1**·6BF_4 or *Δ*/*Λ*-**1**·6OTf.

guest	*observation*	*starting from*
OTf^-	encapsulation	*Δ*/*Λ*-**1**·6BF_4
PF_6^-	encapsulation	*Δ*/*Λ*-**1**·6BF_4
BF_4^-	encapsulation	*Δ*/*Λ*-**1**·6BF_4
ClO_4^-	encapsulation	*Δ*/*Λ*-**1**·6BF_4
$CF_3BF_3^-$	encapsulation	*Δ*/*Λ*-**1**·6BF_4
$CH_3BF_3^-$	partial encapsulation	*Δ*/*Λ*-**1**·6BF_4
$CH_3SO_3^-$	decomposition	*Δ*/*Λ*-**1**·6BF_4
OTs^-	decomposition	*Δ*/*Λ*-**1**·6OTf

NTf_2^-	re-assembled (see Chapter 4)	*Δ*/*Λ*-**1**·6BF_4
$Mo_6O_{19}^{2-}$	inconclusive, broadened NMR	*Δ*/*Λ*-**1**·6BF_4
$B_{12}F_{12}^{2-}$ caborate	decomposition	*Δ*/*Λ*-**1**·6BF_4
NO_3^-	decomposition	*Δ*/*Λ*-**1**·6BF_4
$Fc(SO_3)_2^{2-}$	decomposition	*Δ*/*Λ*-**1**·6OTf
SbF_6^-	decomposition	*Δ*/*Λ*-**1**·6BF_4
Δ-TRISPHAT$^-$	no change	*Δ*/*Λ*-**1**·6BF_4
CF_3CH_2OH	no change	*Δ*/*Λ*-**1**·6OTf
$CF_3(OH)_3$	no change	*Δ*/*Λ*-**1**·6OTf
CD_3NO_2	partial decomposition	*Δ*/*Λ*-**1**·6OTf
NO_2Ph in CD_3NO_2	no change	*Δ*/*Λ*-**1**·6OTf
MeOH	decomposition	*Δ*/*Λ*-**1**·6OTf
naphthalene	no change	*Δ*/*Λ*-**1**·6OTf

Table 3.4. *Guests* screened for encapsulation within [*Δ*/*Λ*-**1**]$^{6+}$.

3.5.16 Emission titration experiments

Anion exchange experiments were performed by titrating a mixed $C_2H_2Cl_4$ solution of Bu_4NX / *Λ*-**1**·6X ([Bu_4NX] = 0.5 mM, [*Λ*-**1**·6X] = 5 μM) into a $C_2H_2Cl_4$ solution of *Λ*-**1**·6X ([*Λ*-**1**·6X] = 5 μM). A Wavelength in the 420-370 nm region at which the absorption of mixed solution *Λ*-**1**·6X / Bu_4NX ([Bu_4NX] = 0.5 mM, [*Λ*-**1**·6X] = 5 μM) and pure *Λ*-**1**·6X ([*Λ*-**1**·6X] = 5 μM) were equal was selected for excitation.

3.5.17 ^{1}H DOSY NMR spectra of *Λ*-1·6BF$_4$ and *Λ*-1·6PF$_6$

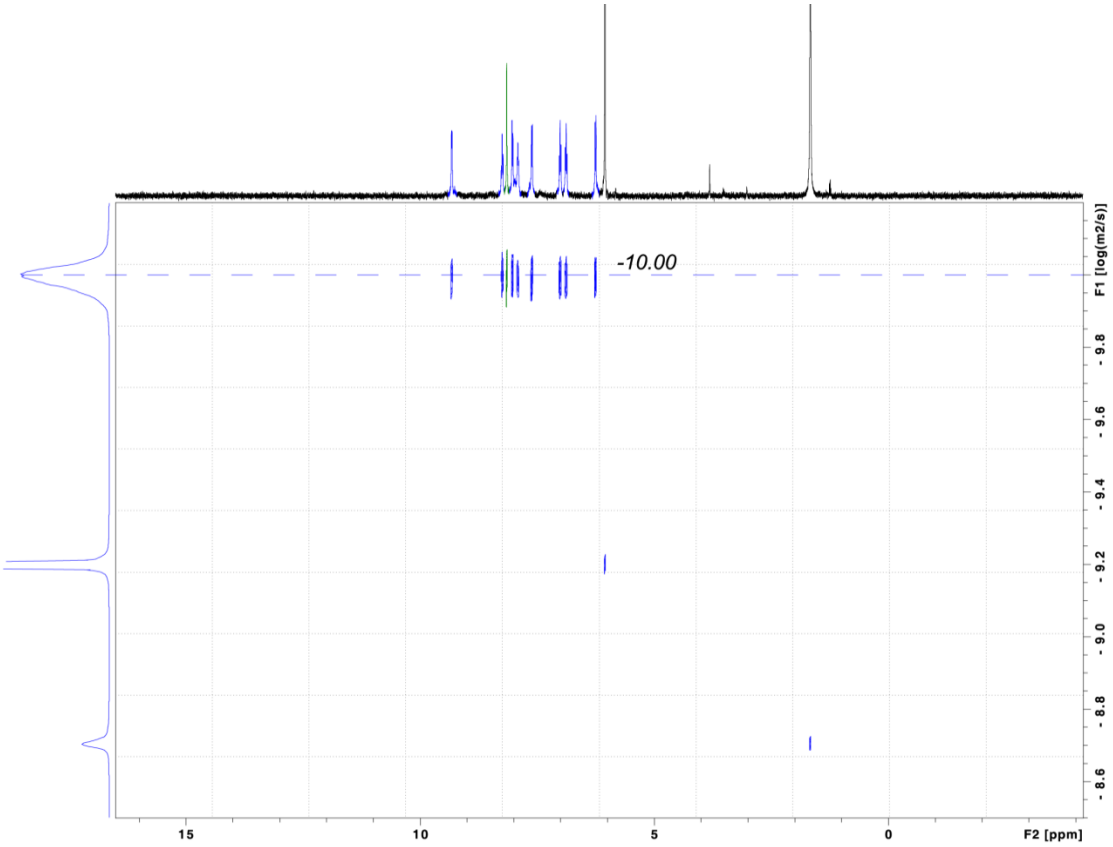

Figure 3.35. ^{1}H DOSY NMR (400 MHz, $C_2D_2Cl_4$, 298 K) spectra of *Λ*-**1**·6BF$_4$. Corresponding log (D / m^{2}s^{-1}) = -10.00.

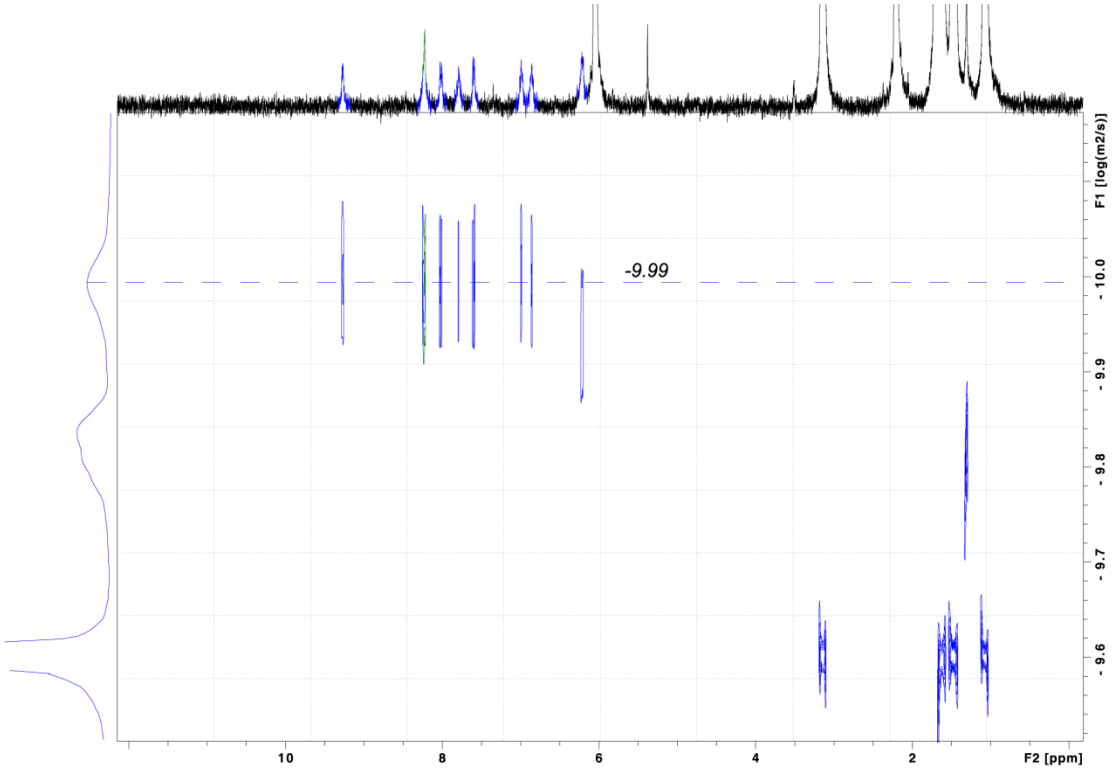

Figure 3.36. ^{1}H DOSY NMR (400 MHz, $C_2D_2Cl_4$, 298 K) spectra of *Λ*-**1**·6OTf with 30 eq Bu_4NPF_6 added. Corresponding log (D / m^2s^{-1}) = -9.99.

3.5.18 Mass spectra and isotopic distribution patterns for selected ions

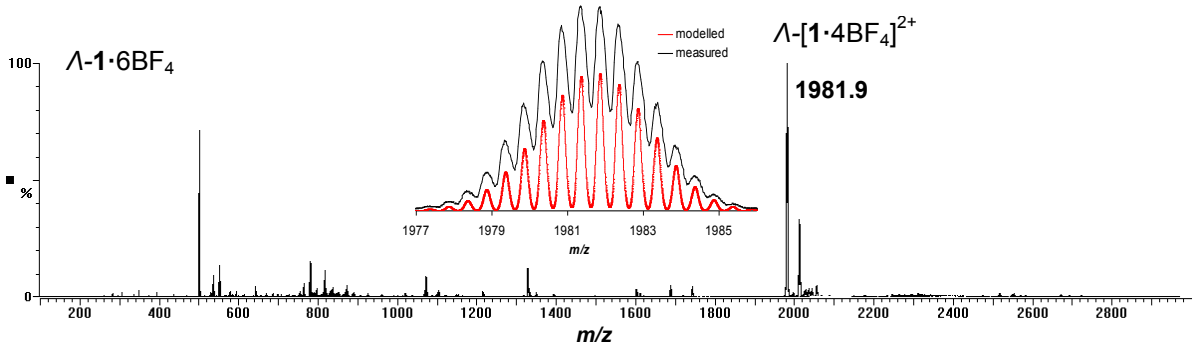

Figure 3.37. nESI mass spectra of a) *Λ*-**1**·6BF_4 with measured (black) versus modelled (red) isotopic distribution pattern for [**1**·4BF_4]$^{2+}$ ion, 50 μM in $C_2H_4Cl_2$.

3.5.19 Crystal data and structure refinement for $[(Ir(ppy)_2)_2(bpe)_2](OTf)_2$

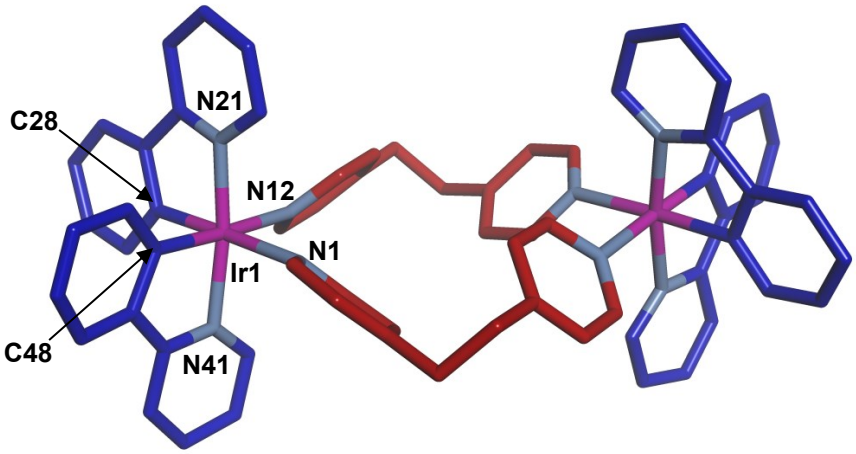

Figure 3.38. X-ray crystal structure of $[(Ir(ppy)_2)_2(bpe)_2]^{2+}$. The carbon atoms of ppy are shown in dark blue and bpe in red, iridium ions in magenta and nitrogen atoms in pale blue. Selected bond lengths [Å] and angles [°]: Ir-Ir 9.287(2), Ir1-N21 2.05(2), Ir1-N41 2.13(2), Ir1-C48 1.97(3), Ir1-C28 2.01(3), Ir1-N12 2.17(2), Ir1-N1 2.17(3), 1 N12-Ir1-N21 88.0(8), N12-Ir1-N41 97.4(8), N12-Ir1-N1 92.3(9), N1-Ir1-N21 100.3(9), N1-Ir1-N41 85.0(9), N21-Ir1-C48 90(1), N21-Ir1-C28 82(1), C48-Ir1-N41 84(1), C28-Ir1-N41 93(1), N1-Ir1-C48 91(1), N12-Ir1-C28 87(1), N1-Ir1-C28 177(1), N12-Ir1-C48 176(1).

Identification code	$[(Ir(ppy)_2)_2(bpe)_2](OTf)_2$
Empirical formula	$C_{70}H_{56}F_6Ir_2N_8O_6S_2$
Formula weight	1667.81
Temperature	93(1) K
Wavelength	0.71075 Å
Crystal system	Cubic
Space group	$Ia\bar{3}$
Unit cell dimensions	a = 36.636(4) Å α = 90°
	b = 36.636(4) Å β = 90°
	c = 36.636(4) Å γ = 90°
Volume	49172(9) $Å^3$
Z	24
Density (calculated)	1.352 g cm^{-3}
Absorption coefficient	3.365 mm^{-1}
F(000)	19680.00
Crystal Colour, Description	yellow, prism

Crystal size	0.1 × 0.1 × 0.1 mm
Theta range for data collection	3.04 to 25.33°
Index ranges	-43<=h<=44, -44<=k<=43, -44<=l<=44
Reflections collected	237542
Independent reflections	7513 [R(int) = 0.0878]
Completeness to theta = 25.33°	95.6%
Absorption correction	Multiscan
Max. and min. transmission	0.714 and 0.597
Refinement method	Full-matrix least-squares on F^2
Data / restraints / parameters	7513 / 0 / 199
Goodness-of-fit on F^2	1.158
Final R indices [I>2sigma(I)]	R1 = 0.2125
R indices (all data)	wR2 = 0.4285
Absolute structure parameter	-
Largest diff. peak and hole	5.94 and -4.52 e^- $Å^{-3}$

Table 3.5. Crystal data and structural refinement for $[(Ir(ppy)_2)_2(bpe)_2](OTf)_2$.

Special details: The unit cell comprises regions of diffused disordered solvent (benzene) which could not be modelled as discrete sites. In the crystal structure the anions are disordered and no restraints were made on the isotropic behaviour of any of the atoms. These two qualities contribute to the large values in the R indices.

3.5.20 Crystal data and structure refinement for *Δ*-[(Ir(ppy)$_2$(L-serine)]

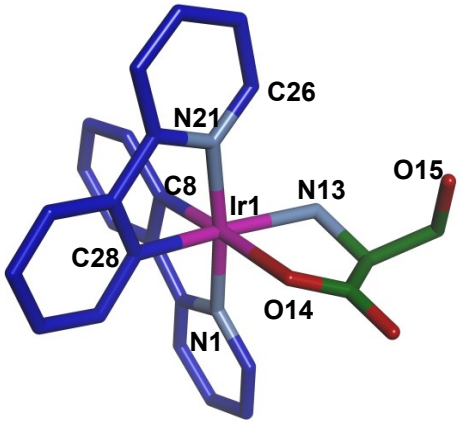

Figure 3.39. X-ray crystal structure of *Δ*-[(Ir(ppy)$_2$(L-serine)]. The carbon atoms of ppy are shown in dark blue and L-serine in green, iridium ions in magenta, nitrogen atoms in pale blue and oxygen atoms in green. Selected bond lengths [Å] and angles [°]: Ir1-O14 2.15(1), Ir1-N13 2.20(2), Ir1-N1 2.05(1), Ir1-N21 2.03(1), Ir1-N13 1.97(2), Ir1-N13 2.01 (2), N15-C26 3.21(3), O14-Ir1-N1 81.79(6), N21-Ir1-N13 96.2(6), N21-Ir1-O14 86.1(5), N21-Ir1-C28 81.1(7), C28-Ir1-N1 95.9(7), O14-Ir1-N1 94.9(5), N13-Ir1-N1 86.9(6), N21-Ir1-C8 99.1(7), C8-Ir1-N1 80.0(7), N13-Ir1-O14 77.5(5), N13-Ir1-C8 102.1(7), C8-Ir1-O14 174.8(6), C28-Ir1-N13 169.9(7), O14-Ir1-C28 92.5(6).

Identification code	*Δ*-[(Ir(ppy)$_2$(L-serine)]
Empirical formula	$C_{34}H_{33}IrN_3O_4$
Formula weight	739.87
Temperature	93(1) K
Wavelength	0.71075 Å
Crystal system	Primitive Monoclinic
Space group	$P2_1$ (#4)
Unit cell dimensions	a = 10.366(3) Å α = 90°
	b = 20.154(5) Å β = 104.730(6)°
	c = 14.904(4) Å γ = 90°
Volume	3011.1(13) Å^3
Z	4
Density (calculated)	1.632 g cm^{-3}
Absorption coefficient	4.489 mm^{-1}
F(000)	1468.0
Crystal Colour, Description	yellow, platelet

Crystal size	0.1 × 0.1 × 0.02 mm
Theta range for data collection	2.03 to 25.36°
Index ranges	-10<=h<=12, -24<=k<=17, -17<=l<=17
Reflections collected	18384
Independent reflections	9406 [R(int) = 0.0570]
Completeness to theta = 25.36°	99.0%
Absorption correction	Multiscan
Max. and min. transmission	0.914 and 0.532
Refinement method	Full-matrix least-squares on F^2
Data / restraints / parameters	9406 / 25 / 723
Goodness-of-fit on F^2	1.128
Final R indices [I>2sigma(I)]	R1 = 0.0597
R indices (all data)	R1 = 0.0639, wR2 = 0.1575
Absolute structure parameter	0.00000
Largest diff. peak and hole	5.40 and -1.81 e^- $Å^{-3}$

Table 3.6. Crystal data and structural refinement for *Δ*-[(Ir(ppy)$_2$(L-serine)].

3.5.21 Crystal data and structure refinement for *Λ*-[(Ir(ppy)$_2$Cl)$_2$] and *Δ*-[(Ir(ppy)$_2$Cl)$_2$]

Structural data were collected at 93 K using a Rigaku Saturn diffractometer (MM007 high-flux RA/MoKa radiation, confocal optic). All data collection employed narrow frames (0.3-1.0) to obtain at least a full hemisphere of data. Intensities were corrected for Lorentz polarisation and absorption effects (multiple equivalent reflections). The structures were solved by direct methods, non-hydrogen atoms were refined anisotropically with CH protons being refined in riding geometries (SHELXTL) against F^2.

CCDC 888470 and 888469 contains the supplementary crystallographic data for *Λ*-[(Ir(ppy)$_2$Cl)$_2$] and *Δ*-[(Ir(ppy)$_2$Cl)$_2$], respectively. This data can be obtained free of charge from The Cambridge Crystallographic Data Centre *via* www.ccdc.cam.ac.uk/data_request/cif.

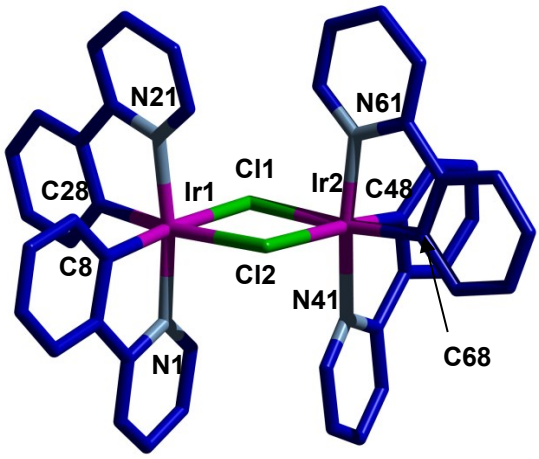

Figure 3.40. X-ray crystal structure of *Λ*-[(Ir(ppy)$_2$Cl)$_2$]. The carbon atoms of ppy are shown in blue, iridium in magenta, nitrogen in pale blue and chlorine in green. Selected bond lengths [Å] and angles [°]: Ir1-Cl1 2.5131(17), Ir1-Cl2 2.5235(16), Ir1-N1 2.050(7), Ir1-N21 2.069(7), Ir1-C8 2.003(9), Ir1-C28 1.983(8), Ir2-Cl1 2.5291(1), Ir2-Cl2 2.5249(18), Ir2-N41 2.061(6), Ir2-N61 2.044(6), Ir2-C48 1.985(8), Ir2-C68 2.004(8), Cl1-Ir1-Cl2 81.79(6), Cl1-Ir1-N1 93.01(18), Cl1-Ir1-N21 91.91(17), Cl1-Ir1 - C8 173.5(3), Cl1-Ir1-C28 92.1(2), Cl2-Ir1-N1 91.09(17), Cl2-Ir1-N21 93.4(2), Cl2-Ir1-C8 97.5(2), Cl2-Ir1-C28 171.4(2), Cl1-Ir2-Cl2 81.44(5), Cl1-Ir2-N41 92.86(18), Cl1-Ir2-N61 94.49(19), Cl1-Ir2-C48 91.6(2), Cl1-Ir2-C68 175.0(2), Cl2-Ir2-N41 94.39(17), Cl2-Ir2-N61 90.72(19), Cl2-Ir2-C48 171.6(2), Cl2-Ir2-C68 97.0(2), N21-Ir1-C8 94.6(3), N1-Ir1-C28 95.3(3), N61-Ir2-C48 94.6(3), N41-Ir2-C68 92.0(3).

Identification code	*Λ*-[(Ir(ppy)$_2$Cl)$_2$]
Empirical formula	$C_{44}H_{32}Cl_2Ir_2N_4$
Formula weight	1072.11
Temperature	93(1) K
Bond precision	C-C = 0.0130 Å
Wavelength	0.71075 Å
Crystal system	Orthorhombic
Space group	$P2_12_12_1$
Unit cell dimensions	a = 9.9782(17) Å α = 90°
	b = 12.560(2) Å β = 90°
	c = 29.008(5) Å γ = 90°
Volume	3635.4(11) Å^3
Z	4
Density (calculated)	1.959 g cm^{-3}

Absorption coefficient	7.520 mm^{-1}
F(000)	2048.0
Crystal size	0.1 × 0.03 × 0.03 mm
Theta range for data collection	1.77 to 25.38°
Index ranges	-12<=h<=12, -14<=k<=15, -32<=l<=34
Reflections collected	36752
Independent reflections	6664 [R(int) = 0.0398]
Completeness to theta = 25.38°	99.8%
Absorption correction	Multiscan
Max. and min. transmission	0.798 and 0.595
Refinement method	Full-matrix least-squares on F^2
Data / restraints / parameters	6664 / 0 / 469
Goodness-of-fit on F^2	0.996
Final R indices [I>2sigma(I)]	R1 = 0.0314
R indices (all data)	wR2 = 0.0752
Absolute structure parameter	0.001(10)
Largest diff. peak and hole	1.777 and -1.177 e^- $Å^{-3}$

Table 3.7. Crystal data and structural refinement for *Λ*-[(Ir(ppy)$_2$Cl)$_2$].

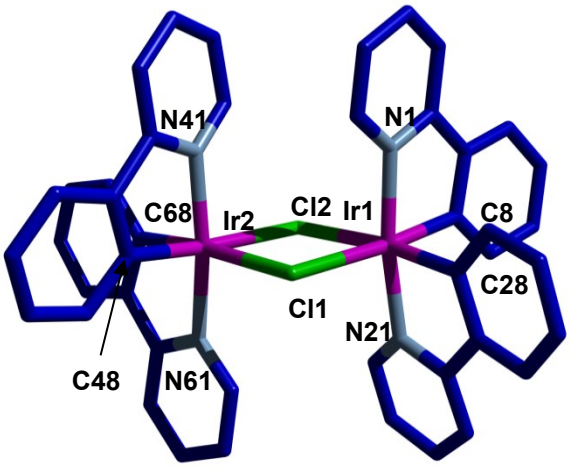

Figure 3.41. X-ray crystal structure of *Λ*-[(Ir(ppy)$_2$Cl)$_2$]. The carbon atoms of ppy are shown in blue, iridium in magenta, nitrogen in pale blue and chlorine in green. Selected bond lengths [Å] and angles [°]:Ir1-Cl1 2.5261(14), Ir1-Cl2 2.5298(13),Ir1-N1 2.056(6), Ir1-N21 2.059(5), Ir1-C8 2.007(8), Ir1-C28 1.988(6), Ir2-Cl1 2.5359(13), Ir2-Cl2 2.5328(15), Ir2-N41 2.062(5), Ir2-N61 2.044(5), Ir2-C48 1.986(6), Ir2-C68 2.002(6), Cl1-Ir1-Cl2 81.95(5), Cl1-Ir1-N1 92.84(15), Cl1-Ir1-N21 92.02(15), Cl1-Ir1-C8

173.79(19), Cl1-Ir1-C28 92.07(17), Cl2-Ir1-N1 91.38(14), Cl2-Ir1-N21 93.61(18), Cl2-Ir1-C8 97.30(17), Cl2-Ir1-C28 171.24(17), Cl1-Ir2-Cl2 81.70(4), Cl1-Ir2-N41 92.58(15), Cl1-Ir2-N61 94.64(15), Cl1-Ir2-C48 91.04(19), Cl1-Ir2-C68 175.04(17), Cl2-Ir2-N41 94.50(14), Cl2-Ir2-N61 91.20(15), Cl2-Ir2-C48 171.45(19), Cl2-Ir2-C68 97.06(17), N1-Ir1-C28 95.3(2), N21 Ir1 C8 94.2(3), N41-Ir2-C68 92.3(3), N61-Ir2-C48 93.9(3).

Identification code	*Δ*-[(Ir(ppy)$_2$Cl)$_2$]
Empirical formula	$C_{44}H_{32}Cl_2Ir_2N_4$
Formula weight	1072.11
Temperature	93(1) K
Bond precision	C-C = 0.0109 Å
Wavelength	0.71075 Å
Crystal system	Orthorhombic
Space group	$P2_12_12_1$
Unit cell dimensions	a = 10.0039(19) Å α = 90°
	b = 12.557(3) Å β = 90°
	c = 29.038(6) Å γ = 90°
Volume	3647.7(12) Å^3
Z	4
Density (calculated)	1.952 g cm^{-3}
Absorption coefficient	7.494 mm^{-1}
F(000)	2048.0
Crystal size	0.06 × 0.06 × 0.02 mm
Theta range for data collection	2.15 to 25.35°
Index ranges	-10<=h<=12, -15<=k<=15, -31<=l<=34
Reflections collected	36825
Independent reflections	6664 [R(int) = 0.0457]
Completeness to theta = 25.35°	99.8%
Absorption correction	Multiscan
Max. and min. transmission	0.8649 and 0.6626
Refinement method	Full-matrix least-squares on F^2
Data / restraints / parameters	6664 / 0 / 469
Goodness-of-fit on F^2	0.939
Final R indices [I>2sigma(I)]	R1 = 0.0255
R indices (all data)	wR2 = 0.0537
Absolute structure parameter	0.023(8)
Largest diff. peak and hole	0.646 and -0.540 e$^-$ Å^{-3}

Table 3.8. Crystal data and structural refinement for *Δ*-[(Ir(ppy)$_2$Cl)$_2$].

3.5.22 Crystal data and structure refinement for *Δ*- and *Λ*-**1**·6OTf

3.5.22.1 *Δ*-[(Ir(ppy)$_2$)$_6$(tcb)$_4$](OTf)$_6$, *Δ*-**1**·6OTf

Structural data was collected using *Rigaku AFC12* goniometer equipped with an enhanced sensitivity (HG) *Saturn724+* detector mounted at the window of an *FR-E+ SuperBright* molybdenum rotating anode generator with VHF *Varimax* optics (70μm focus). Cell determination and data collection employed *CrystalClear-SM Expert 2.0 r11* (Rigaku, 2011). The structures were solved using *SHELXL97*.[42]

CCDC 898757 contains the supplementary crystallographic data for *Δ*-**1**·6OTf. This data can be obtained free of charge from The Cambridge Crystallographic Data Centre *via* www.ccdc.cam.ac.uk/data_request/cif.

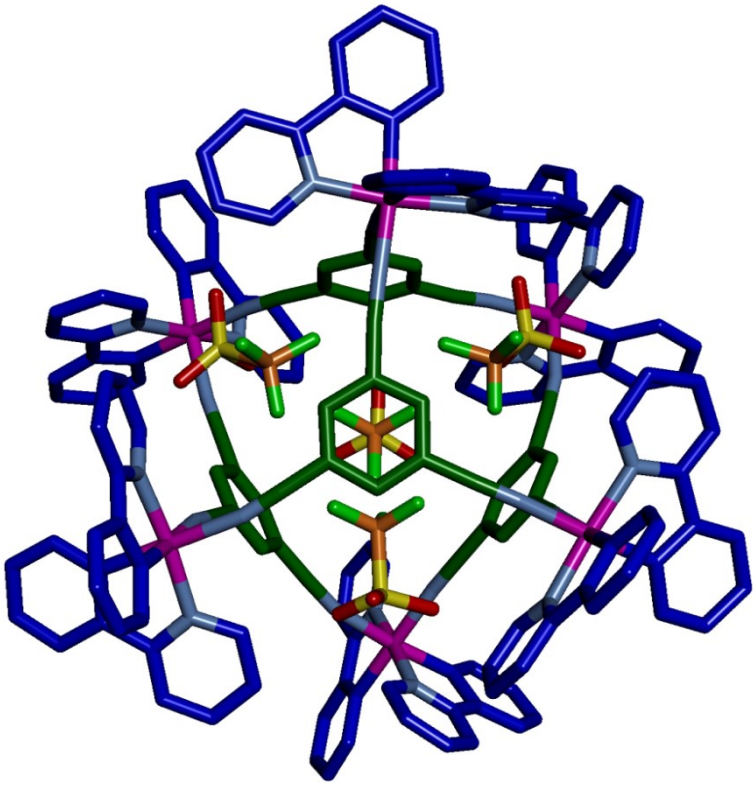

Figure 3.42. X-ray crystal structure of *Δ*-**1**·6OTf. For clarity, non-encapsulated OTf^- counteranions, solvent molecules and hydrogens have been removed. The carbon atoms of ppy are shown in blue, tcb in dark green and OTf^- carbon in orange, iridium in pink, nitrogen in pale blue, sulfur in yellow, oxygen in red and fluorine in pale green.

Identification code	*Δ*-**1**·6OTf
Empirical formula	$C_{242}H_{176}Cl_4F_{18}Ir_6N_{24}O_{19}S_6$
Formula weight	5553.43
Temperature	100(2) K
Bond precision	C-C = 0.0109 Å
Wavelength	0.71075 Å
Crystal system	Triclinic
Space group	*P*1
Unit cell dimensions	a = 18.2508(4) Å α = 84.800(6)°
	b = 19.2160(5) Å β = 63.270(5)°
	c = 20.1901(14) Å γ = 72.872(5)°
Volume	6036.4(5) $Å^3$
Z	1
Density (calculated)	1.528 g cm^{-3}
Absorption coefficient	3.469 mm^{-1}
F(000)	2736.0
Crystal Colour, Description	yellow, prism
Crystal size	0.07 × 0.07 × 0.05 mm
Theta range for data collection	3.05 to 25.03°
Index ranges	-21<=h<=17, -22<=k<=22, -24<=l<=24
Reflections collected	87282
Independent reflections	36199 [R(int) = 0.0593]
Completeness to theta = 25.03°	99.8%
Absorption correction	Semi-empirical from equivalents
Max. and min. transmission	0.8457 and 0.7933
Refinement method	Full-matrix least-squares on F^2
Data / restraints / parameters	36199 / 494 / 2648
Goodness-of-fit on F^2	1.039
Final R indices [I>2sigma(I)]	R1 = 0.0523, wR2 = 0.1296
R indices (all data)	R1 = 0.0588, wR2 = 0.1339
Absolute structure parameter	0.043(5)
Largest diff. peak and hole	2.336 and -1.265 e^- $Å^{-3}$

Table 3.9. Crystal data and structural refinement for *Δ*-**1**·6OTf.

Special details: The unit cell comprises regions of diffused disordered solvent (benzene) which could not be modelled as discrete sites. SQUEEZE[43] routine of PLATON[44] was applied to remove the contributions to the structure factors from the

solvent molecules. This improved the model quality and led to structure refinement with satisfactory convergence.

In the crystal structure several atoms are disordered. One ppy ligand has been modelled over two positions with 70:30 percent ratio. Furthermore, for disordered components (ppy ligand as well as solvent molecules) vibrational restraints (SIMU/DELU), similar displacement restraints (EADP) and distance/angle restraints DFIX/DANG and AFIX 66 were used to maintain sensible geometries and atomic displacement ellipsoids. Some atoms required ISOR restraint to approximate isotropic behaviour.

3.5.22.2 *Λ*-[(Ir(ppy)$_2$)$_6$(tcb)$_4$](OTf)$_6$, *Λ*-1·6OTf

Structural data were collected at 93 K using a Rigaku Saturn diffractometer (MM007 high-flux RA/MoKa radiation, confocal optic). All data collection employed narrow frames (0.3-1.0) to obtain at least a full hemisphere of data. Intensities were corrected for Lorentz polarisation and absorption effects (multiple equivalent reflections). The structures were solved by direct methods, non-hydrogen atoms were refined anisotropically with CH protons being refined in riding geometries (SHELXTL) against F^2.

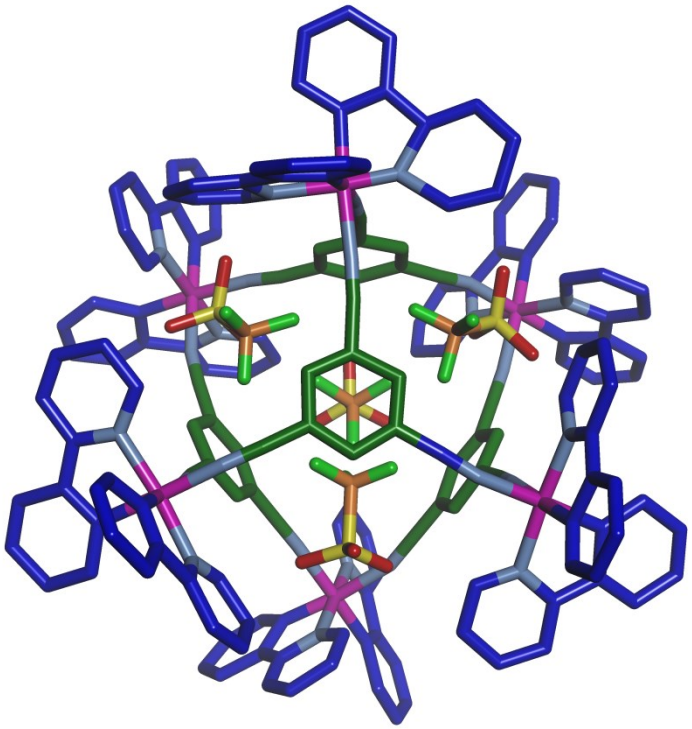

Figure 3.43. X-ray crystal structure of *Λ*-**1**·6OTf. For clarity, non-encapsulated OTf^- counteranions, solvent molecules and hydrogens have been removed. The carbon atoms of ppy are shown in blue, tcb in dark green and OTf^- carbon in orange, iridium in pink, nitrogen in pale blue, sulfur in yellow, oxygen in red and fluorine in pale green.

Identification code	*Λ*-**1**·6OTf
Empirical formula	$C_{174}H_{108}Cl_2F_{18}Ir_6N_{24}O_{18}S_6$
Formula weight	4581.47
Temperature	93(1) K
Wavelength	0.71075 Å
Crystal system	Triclinic
Space group	*P*1
Unit cell dimensions	a = 18.1600(18) Å α = 80.319(9)°
	b = 19.280(3) Å β = 63.690(6)°
	c = 20.067(3) Å γ = 73.531(8)°
Volume	6032.5(14) $Å^3$
Z	1
Density (calculated)	1.261 g cm^{-3}
Absorption coefficient	3.444 mm^{-1}
F(000)	2218.0
Crystal Colour, Description	yellow, prism

Crystal size	0.1 × 0.1 × 0.1 mm
Theta range for data collection	1.54 to 25.40°
Index ranges	-21<=h<=21, -23<=k<=23, -24<=l<=23
Reflections collected	61379
Independent reflections	35576 [R(int) = 0.0703]
Completeness to theta = 25.40°	98.9%
Absorption correction	Multiscan
Max. and min. transmission	0.444 and 0.709
Refinement method	Full-matrix least-squares on F^2
Data / restraints / parameters	35576 / 0 / 2845
Goodness-of-fit on F^2	1.509
Final R indices [I>2sigma(I)]	R1 = 0.1108
R indices (all data)	wR2 = 0.3277
Absolute structure parameter	0.078(13)
Largest diff. peak and hole	7.830 and -7.430 e^- $Å^{-3}$

Table 3.10. Crystal data and structural refinement for *Δ*-**1**·6OTf.

3.6 Notes and References

[1] For recent reviews, see: a) R. Chakrabarty, P. S. Mukherjee, P. J. Stang, *Chem. Rev.* **2011**, *111*, 6810-6918; b) M. D. Ward, P. R. Raithby, *Chem. Soc. Rev.* **2013**, *42*, 1619-1636.

[2] a) C. J. Hastings, M. P. Backlund, R. G. Bergman, K. N. Raymond, *Angew. Chem. Int. Ed.* **2011**, *50*, 10570-10573; b) T. Murase, Y. Nishijima, M. Fujita, *J. Am. Chem. Soc.* **2012**, *134*, 162-164; c) S. Horiuchi, T. Murase, M. Fujita, *J. Am. Chem. Soc.* **2011**, *133*, 12445-12447; d) P. Mal, B. Breiner, K. Rissanen, J. R. Nitschke, *Science* **2009**, *324*, 1697-1699.

[3] A. Juris, V. Balzani, F. Barigelletti, S. Campagna, P. Belser, A. von Zelewsky, *Coord. Chem. Rev.* **1988**, *84*, 85-277.

[4] K. K.-W. Lo, K. Y. Zhang, S.-K. Leung, M.-C. Tang, *Angew. Chem. Int. Ed.* **2008**, *47*, 2213-2216.

[5] M. A. Baldo, M. E. Thompson, S. R. Forrest, *Nature* **2000**, *403*, 750-753.

[6] For metallocycles which feature $[Ru(terpy)_2]^{2+}$ connections, see: a) Y.-T. Chan, X. Li, C. N. Moorefield, C. Wesdemiotis, G. R. Newkome, *Chem. Eur. J.* **2011**, *17*, 7750-7754; b) Y.-T. Chan, X. Li, J. Yu, G. A. Carri, C. N. Moorefield, G. R. Newkome, C. Wesdemiotis, *J. Am. Chem. Soc.* **2011**, *133*, 11967-11976; c) G. R. Newkome, P. Wang, C. N. Moorefield, T. J. Cho, P. P. Mohapatra, S. Li, S.-H. Hwang, O. Lukoyanova, L. Echegoyen, J. A. Palagallo, V. Iancu, S.-W. Hla, *Science* **2006**, *312*, 1782-1785; d) S.-S. Sun, A. J. Lees, *Inorg. Chem.* **2001**, *40*, 3154-3160; For helicates based on $[Ru(bipy)_3]^{2+}$ motifs, see: e) C. R. K. Glasson, G. V. Meehan, J. K. Clegg, L. F. Lindoy, J. A. Smith, F. R. Keene, C. Motti, *Chem. Eur. J.* **2008**, *14*, 10535-10538; For Ru poly(pyridyl) metallodendrimers, see: f) E. C. Constable, P. Harverson, M. Oberholzer, *Chem. Commun.* **1996**, *32*, 1821-1822.

[7] a) E. Baranoff, E. Orselli, L. Allouche, D. Di Censo, R. Scopelliti, M. Gratzel, M. K. Nazeeruddin, *Chem. Commun.* **2011**, *47*, 2799-2801; b) N. M. Ali, V. L. MacLeod, P. Jennison, I. V. Sazanovich, C. A. Hunter, J. A. Weinstein, M. D. Ward, *Dalton Trans.* **2012**, *41*, 2408-2419; c) V. Chandrasekhar, T. Hajra, J. K. Bera, S. M. W. Rahaman, N. Satumtira, O. Elbjeirami, M. A. Omary, *Inorg. Chem.* **2012**, *51*, 1319-1329; For luminescent metallopolymers, see: d) I. Eryazici, O. K. Farha, O. C. Compton, C. Stern, J. T. Hupp, S. T. Nguyen, *Dalton Trans.* **2011**, *40*, 9189-9193; For three-dimensional assemblies based on M(arene) building blocks (where M = Ru or Ir, arene = Cp*, *p*-cymene), see: e) F. Schmitt, J. Freudenreich, N. P. E. Barry, L. Juillerat-Jeanneret, G. Süss-Fink, B. Therrien, *J. Am. Chem. Soc.* **2011**, *134*, 754-757; f) Y.-F. Han, W.-G. Jia, Y.-J. Lin, G.-X. Jin, *Angew. Chem. Int. Ed.* **2009**, *48*, 6234-6238; g) S. Mirtschin, A. Slabon-Turski, R. Scopelliti, A. H. Velders, K. Severin, *J. Am. Chem. Soc.* **2010**, *132*, 14004-14005; h) V. Vajpayee, Y. J. Yang, S. C. Kang, H. Kim, I. S. Kim, M. Wang, P. J. Stang, K.-W. Chi, *Chem. Commun.* **2011**, *47*, 5184-5186.

[8] a) M. Fujita, M. Tominaga, A. Hori, B. Therrien, *Acc. Chem. Res.* **2005**, *38*, 369-378; b) S. R. Seidel, P. J. Stang, *Acc. Chem. Res.* **2002**, *35*, 972-983.

[9] a) O. Chepelin, J. Ujma, P. E. Barran, P. J. Lusby, *Angew. Chem. Int. Ed.* **2012**, *51*, 4194-4197; b) P. J. Lusby, P. Müller, S. J. Pike, A. M. Z. Slawin, *J. Am. Chem. Soc.* **2009**, *131*, 16398-16400.

[10] M. Fujita, S. Nagao, M. Iida, K. Ogata, K. Ogura, *J. Am. Chem. Soc.* **1993**, *115*, 1574-1576.

[11] V. Chandrasekhar, T. Hajra, J. K. Bera, S. M. W. Rahaman, N. Satumtira, O. Elbjeirami, M. A. Omary, *Inorg. Chem.* **2012**, *51*, 1319-1329.

[12] M. Fujita, D. Oguro, M. Miyazawa, H. Oka, K. Yamaguchi, K. Ogura, *Nature* **1995**, *378*, 469-471.
[13] B. Therrien, *J. Organomet. Chem.* **2011**, *696*, 637-651.
[14] J. R. Carlise, X.-Y. Wang, M. Weck, *Macromolecules* **2005**, *38*, 9000-9008.
[15] There are a possible four enantiomeric pairs plus two meso compounds. This, and the lower symmetry of all but the homochiral assemblies, leads to the complex ^{1}H NMR spectrum. Prolonged heating of the sample does not significantly alter the complex pattern of signals.
[16] a) A. von Zelewsky, O. Mamula, *J. Chem. Soc., Dalton Trans.* **2000**, 219-231; b) C. Hamann, A. von Zelewsky, A. Neels, H. Stoeckli-Evans, *Dalton Trans.* **2004**, 402-406; c) C. Schaffner-Hamann, A. von Zelewsky, A. Barbieri, F. Barigelletti, G. Muller, J. P. Riehl, A. Neels, *J. Am. Chem. Soc.* **2004**, *126*, 9339-9348; d) L. Yang, A. v. Zelewsky, H. P. Nguyen, G. Muller, G. Labat, H. Stoeckli-Evans, *Inorg. Chim. Acta* **2009**, *362*, 3853-3856; e) K. D. Oyler, F. J. Coughlin, S. Bernhard, *J. Am. Chem. Soc.* **2006**, *129*, 210-217; f) E. Marchi, R. Sinisi, G. Bergamini, M. Tragni, M. Monari, M. Bandini, P. Ceroni, *Chem. Eur. J.* **2012**, *18*, 8765-8773.
[17] A. Auffrant, A. Barbieri, F. Barigelletti, J. Lacour, P. Mobian, J.-P. Collin, J.-P. Sauvage, B. Ventura, *Inorg. Chem.* **2007**, *46*, 6911-6919.
[18] a) F. J. Coughlin, K. D. Oyler, R. A. Pascal, S. Bernhard, *Inorg. Chem.* **2008**, *47*, 974-979; b) X. Chen, Y. Okamoto, T. Yano, J. Otsuki, *J. Sep. Sci.* **2007**, *30*, 713-716; c) M. Ashizawa, L. Yang, K. Kobayashi, H. Sato, A. Yamagishi, F. Okuda, T. Harada, R. Kuroda, M.-a. Haga, *Dalton Trans.* **2009**, 1700-1702.
[19] R. Urban, R. Krämer, S. Mihan, K. Polborn, B. Wagner, W. Beck, *J. Organomet. Chem.* **1996**, *517*, 191-200.
[20] a) I. A. Riddell, M. M. J. Smulders, J. K. Clegg, Y. R. Hristova, B. Breiner, J. D. Thoburn, J. R. Nitschke, *Nat. Chem.* **2012**, *4*, 751-756; b) T. D. Hamilton, G. S. Papaefstathiou, L. R. MacGillivray, *J. Am. Chem. Soc.* **2002**, *124*, 11606-11607; c) I. A. Riddell, Y. R. Hristova, J. K. Clegg, C. S. Wood, B. Breiner, J. R. Nitschke, *J. Am. Chem. Soc.* **2013**, *135*, 2723-2733; d) P. N. W. Baxter, J.-M. Lehn, B. O. Kneisel, G. Baum, D. Fenske, *Chem. Eur. J.* **1999**, *5*, 113-120; e) S. Freye, J. Hey, A. Torras-Galán, D. Stalke, R. Herbst-Irmer, M. John, G. H. Clever, *Angew. Chem. Int. Ed.* **2012**, *51*, 2191-2194.
[21] a) E. R. Brocker, S. E. Anderson, B. H. Northrop, P. J. Stang, M. T. Bowers, *J. Am. Chem. Soc.* **2010**, *132*, 13486-13494; b) Y.-T. Chan, X. Li, M. Soler, J.-L. Wang, C. Wesdemiotis, G. R. Newkome, *J. Am. Chem. Soc.* **2009**, *131*, 16395-16397; c) J. Thiel, D. Yang, M. H. Rosnes, X. Liu, C. Yvon, S. E. Kelly, Y.-F. Song, D.-L. Long, L. Cronin, *Angew. Chem. Int. Ed.* **2011**, *50*, 8871-8875; d) J. Ujma, M. De Cecco, O. Chepelin, H. Levene, C. Moffat, S. J. Pike, P. J. Lusby, P. E. Barran, *Chem. Commun.* **2012**, *48*, 4423-4425.
[22] a) S. P. Argent, H. Adams, L. P. Harding, M. D. Ward, *Dalton Trans.* **2006**, *35*, 542-544; b) G. H. Clever, S. Tashiro, M. Shionoya, *Angew. Chem. Int. Ed.* **2009**, *48*, 7010-7012; c) I. A. Riddell, M. M. J. Smulders, J. K. Clegg, Y. R. Hristova, B. Breiner, J. D. Thoburn, J. R. Nitschke, *Nat. Chem.* **2012**, *4*, 751-756.
[23] a) S. Mecozzi, J. J. Rebek, *Chem. Eur. J.* **1998**, *4*, 1016-1022; b) C. J. Hastings, M. D. Pluth, S. M. Biros, R. G. Bergman, K. N. Raymond, *Tetrahedron* **2008**, *64*, 8362-8367; c) Y. R. Hristova, M. M. J. Smulders, J. K. Clegg, B. Breiner, J. R. Nitschke, *Chem. Sci.* **2011**, *2*, 638.
[24] In $C_2D_2Cl_4$, $[Ir(ppy)_2(PhCN)_2]OTf$ appears to be in a 3:1 equilibrium with a monobenzonitrile species; addition of a small excess of PhCN (10 eq) shifts the

equilibrium so that $[Ir(ppy)_2(PhCN)_2]OTf$ is the sole complex in solution (see section 3.5.13)

[25] There are only a few reported air-equilibrated quantum yields for Ir complexes, see: a) E. A. Plummer, J. W. Hofstraat, L. De Cola, *Dalton Trans.* **2003**, *22*, 2080-2084; This is because they exhibit strong O_2 quenching, e.g. for the ubiquitous $[Ir(ppy)_3]$, $\Phi = 0.71$, $\Phi_{air} = 0.03$, see: b) A. Ruggi, M. Berenguel Alonso, D. N. Reinhoudt, A. H. Velders, *Chem. Commun.* **2010**, *46*, 6726-6728.

[26] L. Flamigni, A. Barbieri, C. Sabatini, B. Ventura, F. Barigelletti, *Top. Curr. Chem.* **2007**, *281*, 143-203.

[27] B. Schmid, F. O. Garces, R. J. Watts, *Inorg. Chem.* **1994**, *33*, 9-14.

[28] H. L. Anderson, S. Anderson, J. K. M. Sanders, *J. Chem. Soc., Perkin Trans. 1* **1995**, 2231-2245.

[29] M. Nonoyama, *Bull. Chem. Soc. Jpn.* **1974**, *47*, 767-768.

[30] a) F. L. Weitl, K. N. Raymond, *J. Am. Chem. Soc.* **1979**, *101*, 2728-2731; b) A. S. Bailey, B. R. Henn, J. M. Langdon, *Tetrahedron* **1963**, *19*, 161-167.

[31] B. J. McCullough, J. Kalapothakis, H. Eastwood, P. Kemper, D. MacMillan, K. Taylor, J. Dorin, P. E. Barran, *Anal. Chem.* **2008**, *80*, 6336-6344.

[32] H. E. Revercomb, E. A. Mason, *Anal. Chem.* **1975**, *47*, 970-983.

[33] a) M. F. Mesleh, J. M. Hunter, A. A. Shvartsburg, G. C. Schatz, M. F. Jarrold, *J. Phys. Chem.* **1996**, *100*, 16082-16086; b) M. F. Mesleh, J. M. Hunter, A. A. Shvartsburg, G. C. Schatz, M. F. Jarrold, *J. Phys. Chem. A* **1997**, *101*, 968-968.

[34] A. A. Shvartsburg, M. F. Jarrold, *Chem. Phys. Lett.* **1996**, *261*, 86-91.

[35] C. Bleiholder, T. Wyttenbach, M. T. Bowers, *Int. J. Mass spectrom.* **2011**, *308*, 1-10.

[36] K. Suzuki, A. Kobayashi, S. Kaneko, K. Takehira, T. Yoshihara, H. Ishida, Y. Shiina, S. Oishi, S. Tobita, *Phys. Chem. Chem. Phys.* **2009**, *11*, 9850-9860.

[37] R. F. Kubin, A. N. Fletcher, *Chem. Phys. Lett.* **1983**, *99*, 49-52.

[38] W. M. Haynes (Ed.), *Handbook of Chemistry and Physics*, 92nd ed., CRC press, **2011**.

[39] http://siremol.org

[40] A. Bondi, *J. Phys. Chem.* **1964**, *68*, 441-451.

[41] W. Humphrey, A. Dalke, K. Schulten, *J. Mol. Graphics* **1996**, *14*, 33-38.

[42] G. Sheldrick, *Acta Cryst. Section A* **2008**, *64*, 112-122.

[43] P. van der Sluis, A. L. Spek, *Acta Cryst. Section A* **1990**, *46*, 194-201.

[44] A. Spek, *J. Appl. Crystallogr.* **2003**, *36*, 7-13.

Chapter 4

Exploration into the physical properties of the Ir(III) capsules assembled using different anions and ligands

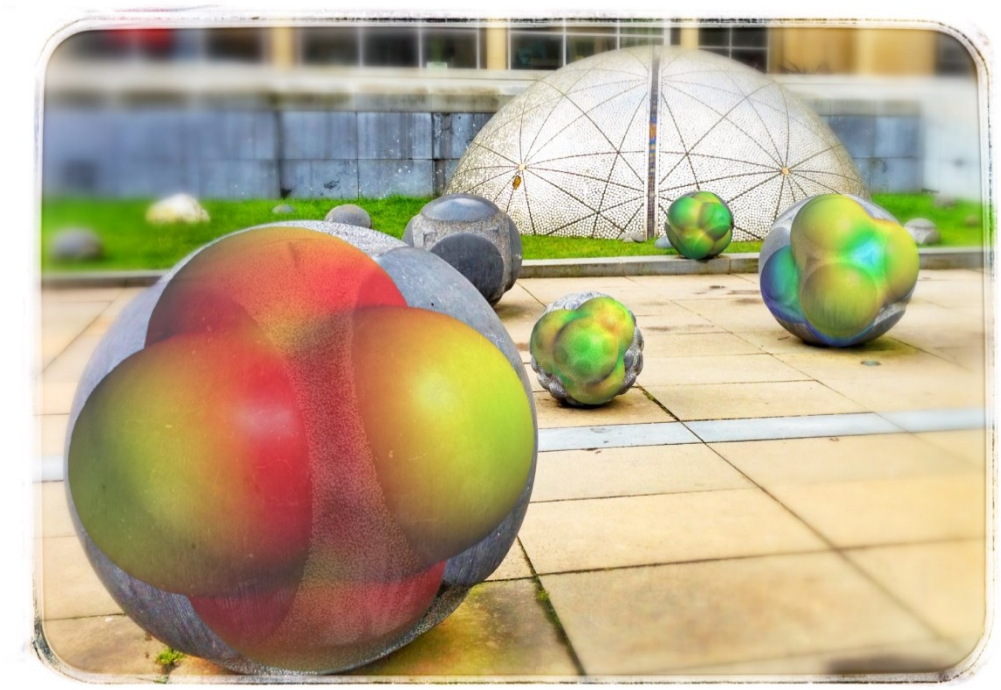

'First Conundrum', Edinburgh

Acknowledgements

I would to thank David August for his help with the synthesis and study of the $[Ir(ppy)_2(NCC_6H_4F)_2]^+$ and $[Ir(ppz)_2(NCC_6H_4F)_2]^+$ salts, Dr. Predita Barran and Jakub Ujma for their help with mass spectrometry, Prof. Alexandra Slawin for X-ray crystallography and Dr. Lorna Murray for her extensive help with NMR analysis.

4.1 Synopsis

In Chapter 3, the synthesis of the first molecular capsule based on an $[Ir(ppy)_2]^+$ metallosupramolecular 90° acceptor unit and a tritopic tricyanobenzene ligand (tcb) was described. Preliminary investigations showed that, amongst other things, four of the six associated triflate counteranions reside within the cavity of the octahedral Ir_6L_4 capsule, $\mathbf{1}^{6+}$, as evidenced by both solution and the solid state studies. In this chapter, we further explore the host-guest relationship of $\mathbf{1}^{6+}$ by preparing capsules with a wider range of counteranions (OTf^-, PF_6^-, BF_4^- and ClO_4^-). Different spectroscopic techniques indicate that a similar supramolecular structure is formed (i.e. with at least four of the six associated counteranions residing in the cavity) irrespective of the counterion used. This encapsulation allows the counteranions to not only impart different optical properties, but also markedly alter the kinetic stability of $\mathbf{1}^{6+}$. By monitoring the rate of exchange of the Δ- and Λ-$[Ir(ppy)_2]^+$ subcomponents between preformed enantiopure enantiomers of $\mathbf{1}^{6+}$, scrambling half-lives ranging from 4.7 mins with BF_4^- to as long as 4.5 days with OTf^- were observed. In the case of OTf^-, this represents a 1.4×10^4 enhancement in kinetic stability with respect to the rate of nitrile ligand exchange in a comparative mononuclear complex (as determined by NMR EXSY experiments). In further contrast to the cage scrambling experiments, the rate of ligand exchange in comparative mononuclear complexes was shown to be roughly independent of the associated counteranions. The capsule scrambling experiments have also revealed a trend in kinetic stabilities which mirrors the relative affinities of the anions for the cavity of $\mathbf{1}^{6+}$. This can be explained by differences in the inter-anion repulsive forces between the different encapsulated counteranions, as evidenced by ^1H NMR chemical shifts of the protons in environments closest to the anion binding pockets, and further supported by electrostatic potential energy models of each of the anions. The one exception appears to be PF_6^-, which exhibits a greater affinity for the cavity of $\mathbf{1}^{6+}$ and yet the half-life of scrambling of $\mathbf{1}\cdot6PF_6$ is significantly less than that of $\mathbf{1}\cdot6OTf$. This anomaly can be explained using solvophobic arguments.

In an attempt to make an "empty" cage species, assembly experiments using an Ir starting material with bulky triflimide counteranions (NTf_2^-) were also carried out. Surprisingly, rather than form a discrete assembly, the formation of a complex, dynamic combinatorial library (DCL) of aggregates was observed. However, on addition of OTf^- to the DCL, the formation of $[4OTf\subset\mathbf{1}]^{2+}$ occurred, indicating that these smaller anions clearly play a

templating-role. A similar explanation has also been used to explain why a capsule based on an extended tritopic ligand doesn't form. Further structural variations have also been explored, by investigating the self-assembly with $[Ir(ppz)_2]^+$ *(ppz = 1-phenylatopyrazol) units. While this produces the as expected* Ir_6L_4 *octahedron with tcb, the larger pore sizes result in faster exchange of guest anions and also an overall decrease in the kinetic stability with respect to* $\mathbf{1}^{6+}$*, despite further studies suggesting that the individual Ir-nitrile interaction is stronger for* $[Ir(ppz)_2]^+$ *in comparison to* $[Ir(ppy)_2]^+$*.*

4.2 Introduction

Over billions of years nature has developed highly complex dynamic chemical processes that function in tandem, often triggered by external stimuli that induce a cascade of events. In the cellular world, for example, dynamic template effects mark the start of new life in the transcription of genetic code from DNA to RNA, while apoptosis, often triggered by small molecules,[1] is a cascade of intra-cellular processes that result in cell shrinkage and eventual death. In these and many other examples, nature utilises intermolecular interactions to construct and process highly complex systems. In the abiotic world we are still far behind nature in constructing sophisticated chemical assemblies and processes, however, the recent interest in metallosupramolecular self-assembly has led to the development of highly dynamic, three-dimensional architectures that have been utilised as molecular containers.[2] Often inspired by nature, these artificial scaffolds will potentially help us unravel the mysteries within the biotic world and are already paving the way for the next generation of catalysts and sensors.

Three-dimensional metallosupramolecular assemblies are often referred to in the literature as cages and are treated as rigid, kinetically robust entities. Contrary to this description their self-assembly relies on reversible metal-ligand interactions which allow for self-sorting to take place, to ensure, occasionally with the aid of a template,[3] that the most thermodynamically favoured assembly will form. Recent studies by Nitschke and co-workers have revealed that their cages are in fact far more dynamic than initially anticipated with different polyhedra easily accessible through counterion and/or metal exchange.[4] Although the capsules often exhibit remarkable kinetic stability in solution due to cooperative effects,[5] a subtle change to the identity of the metal centre,[2d, 4, 6] ligand geometry,[7] counterions[4, 6a, 8] or even a change in solvent[9] can lead to significant structural changes to the product or, like apoptosis in cells, a weakening and complete disassembly of the three-dimensional structure altogether. Herein, we demonstrate the vital role played by the counterions and ligands in tuning the physical properties of the previously developed metallosupramolecular iridium capsule $\mathbf{1}^{6+}$.[10]

4.3 Results and Discussion

4.3.1 Synthesis and characterisation

In Chapter 3, the synthesis and characterisation of *Λ*/*Δ*-**1**$^{6+}$ utilising triflate (OTf^-) and tetrafluoroborate (BF_4^-) as the counterions was discussed. Here, two further salts of cage **1**$^{6+}$, hexafluorophosphate (PF_6^-) and perchlorate (ClO_4^-), were isolated, *via* an analogous method to the formation of **1**·6BF_4 (Scheme 4.1) and the physical properties of all 4 salts were compared.

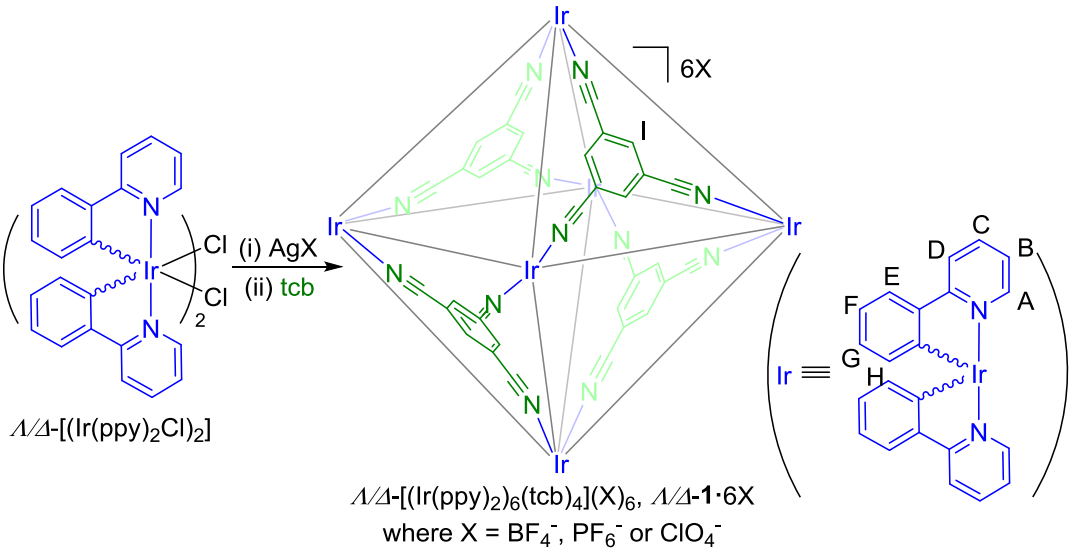

Scheme 4.1. Synthesis of *Λ*/*Δ*-**1**·6X (where X = BF_4^-, PF_6^- or ClO_4^-). Conditions: (i) AgX (where X = BF_4^-, PF_6^- or ClO_4^-), THF, RT, 2 h; (ii) tcb, $C_2H_4Cl_2$, RT, 4 h; *Λ*-**1**·6BF_4, 56%; *Δ*-**1**·6BF_4, 29%; *Λ*-**1**·6PF_6, 32%; *Δ*-**1**·6PF_6, 81%; *Λ*-**1**·6ClO_4, 62%; *Δ*-**1**·6ClO_4, 86%. Yields calculated starting from *Λ*/*Δ*-[(Ir(ppy)$_2$Cl)$_2$].

The ^{1}H NMR spectra of the two newly isolated salts confirmed the presence of highly symmetrical assemblies with 9 different aromatic proton environments, analogous to **1**·6OTf and **1**·6BF_4 (Figure 4.1). Changing the counterions associated with **1**$^{6+}$ appears to have little influence on the environments of protons H_C-H_H, which sit on the periphery of the scaffold, evident by their superimposable ^{1}H NMR chemical shifts. However, it came as no great surprise that changing the anions associated with the system significantly affected the chemical shifts of protons H_A, H_B and H_I, which are positioned next to the anion binding pockets.

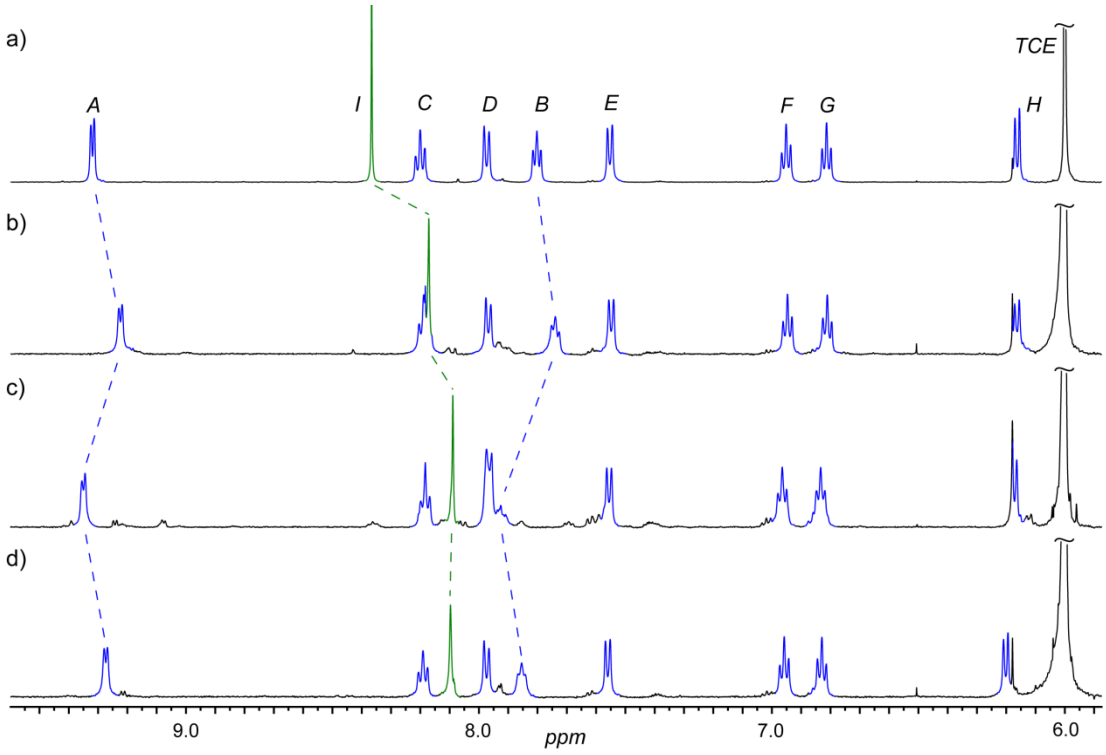

Figure 4.1. ^{1}H NMR spectra (500 MHz, $C_2D_2Cl_4$, 298 K) of a) *Λ*-**1**·6OTf, b) *Λ*-**1**·6PF_6, c) *Λ*-**1**·6ClO_4 and d) *Λ*-**1**·6BF_4. See Scheme 4.1 for peak assignment.

In addition, the different counteranions have little influence on the size of $\mathbf{1}^{6+}$, as near identical diffusion coefficients were measured for **1**·6X (where X = OTf^-, BF_4^-, PF_6^- or ClO_4^-) using ^{1}H DOSY NMR (see section 4.5.3). As had previously been observed for **1**·6OTf and **1**·6BF_4, capsules with ClO_4^- and PF_6^- counteranions only exhibit intact assemblies with 2+ charge under nESI-MS conditions (visible at 2098.3 and 2007.2 m/z, respectively), strongly suggesting that in all cases four of the six anions reside in the cavity (see section 4.5.4). However, further analysis of **1**·6PF_6 using ^{19}F NMR spectroscopy showed three sets of doublets centred at -69.37, -70.05 and -72.39 ppm (see Figure 4.2a), in contrast to **1**·6OTf, where only two signals, assignable to counteranions inside and outside the cage, were observed.

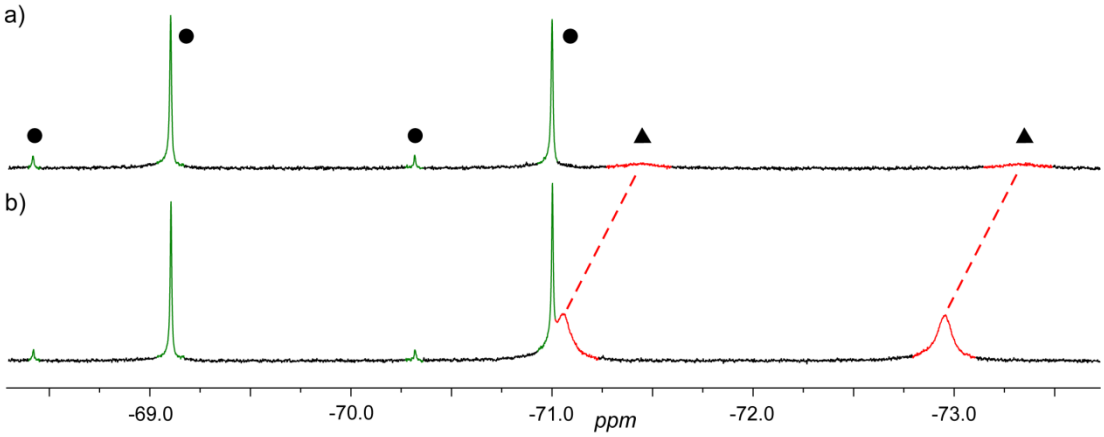

Figure 4.2. ^{19}F NMR (376 MHz, $C_2D_2Cl_4$, 298 K) spectra of a) *Λ*-**1**·6PF_6, using 1,2-difluorobenzene as internal standard the number of encapsulated (●, green) and free (▲, red) PF_6^- anions per capsule (*Λ*-**1**·6PF_6) was calculated to be 0.3, 4.4 and 1.2, respectively or qualitatively as 0.3, 4.5 and 1.2; b) *Λ*-**1**·6PF_6 with excess Bu_4NPF_6.

The ratio of PF_6^- anions in the three different environments was measured as 0.3:4.5:1.2. The broad doublet centred at -72.39 ppm (▲) increases in intensity with the addition of Bu_4NPF_6 (see Figure 4.2b), suggesting that, on average, 1.2 PF_6^- anions are associated with the outside of the capsule and 4.8 PF_6^- anions reside within the cavity in two different environments (●). In addition, the encapsulated hexafluorophophate *guests* are deshielded with respect to the unencapsulated anions, the reverse of that observed with triflate. Presumably this deshielding is caused by the formation of CH···F(P) hydrogen bonds, whereas in the case of **1**·6OTf, the cage prefers to form hydrogen bonds with the oxygen atoms of the triflate anions leaving the tcb aromatic panels to shield the CF_3 portion of this anion (see Chapter 3). Further support for this assignment comes from ^{19}F DOSY measurements and ^{19}F-^{1}H HOESY NMR analysis (see section 4.5.5), the former technique shows that both encapsulated PF_6^- signals have the same diffusion coefficients of log (D / m^2 s^{-1}) = -10.00 in $C_2D_2Cl_4$ as the ^{1}H DOSY diffusion coefficient for the scaffold (see section 4.5.3). From these results, the time-averaged 4.8 anions that are within the cavity are believed to be encapsulated by **1**$^{6+}$ in two different environments that differ based on the total number of PF_6^- anions present within the cavity. Integration of these ^{19}F signals indicates that **1**·6PF_6 is composed of [4PF_6⊂**1**](PF_6)$_2$ and [5PF_6⊂**1**]PF_6 in a ratio of 1:9 at 298 K. This integral ratio of the two ^{19}F signals was observed to change as a function of temperature (see Figure 4.3). Reducing the temperature to 243 K saw a decrease in the presence of

[5PF_6⊂**1**]PF_6 and an increase in [4PF_6⊂**1**]$(PF_6)_2$. This result suggests that while [5PF_6⊂**1**]PF_6 is enthalpically favoured, through minimising unfavourable solvent-anion interactions (*vide infra*), [4PF_6⊂**1**]$(PF_6)_2$ is preferred on entropic grounds, presumably as the loss in the number of degrees of freedom for four bound counteranions is less in comparison to binding five (i.e. two "free" anions are favoured over one, and because five encapsulated anions will experience restricted, tighter binding, than four).

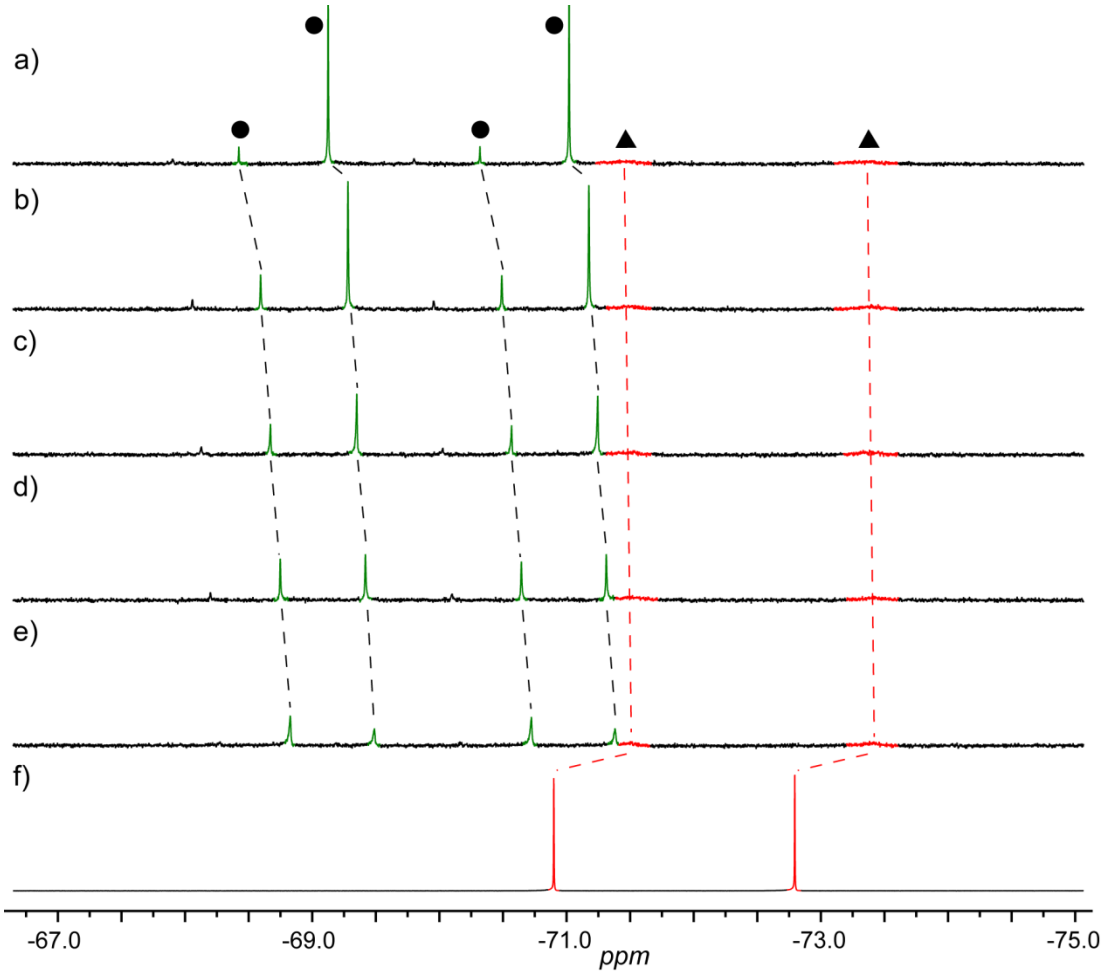

Figure 4.3. ^{19}F NMR (376 MHz, $C_2D_2Cl_4$) spectra of *Λ*-**1**·6PF_6 at a) 298 K (10:90 ratio in the integrals for the encapsulated signals), b) 273 K (20:80), c) 263 K (31:69), d) 253 K (43:57), e) 243 K (57:43) and f) spectrum of Bu_4NPF_6 at 298 K. Encapsulated (●, green) and free (▲, red) PF_6^- anions annotated accordingly in the spectra.

For **1**·6BF_4, a marginally shifted and broadened ^{19}F peak relative to Bu_4NBF_4 in $C_2D_2Cl_4$, was observed, suggesting that the BF_4^- counterions are also binding within the cavity of $\mathbf{1}^{6+}$ and are in fast exchange on the NMR timescale (see Figure 4.4). The time-averaged

signal is also deshielded with respect to free BF_4^-, suggesting that these anions form CH···F(B) hydrogen bonds with H_B, H_C and H_I, in a similar fashion to PF_6^-. The number of encapsulated BF_4^- counterions within $\mathbf{1}^{6+}$ however remained inconclusive as only partial broadening of the ^{19}F resonance was observed at the lower temperature limit of 253 K. Similarly for $\mathbf{1}\cdot 6ClO_4$, it is not possible to directly measure the number of counteranions which reside within the cavity of $\mathbf{1}^{6+}$, and the only evidence, in the absence of XRD data, for the dominance of $[4X\subset\Delta\text{-}\mathbf{1}]^{2+}$, where X = ClO_4^- or BF_4^-, is the observation of solely the dicationic species under nESI-MS conditions.

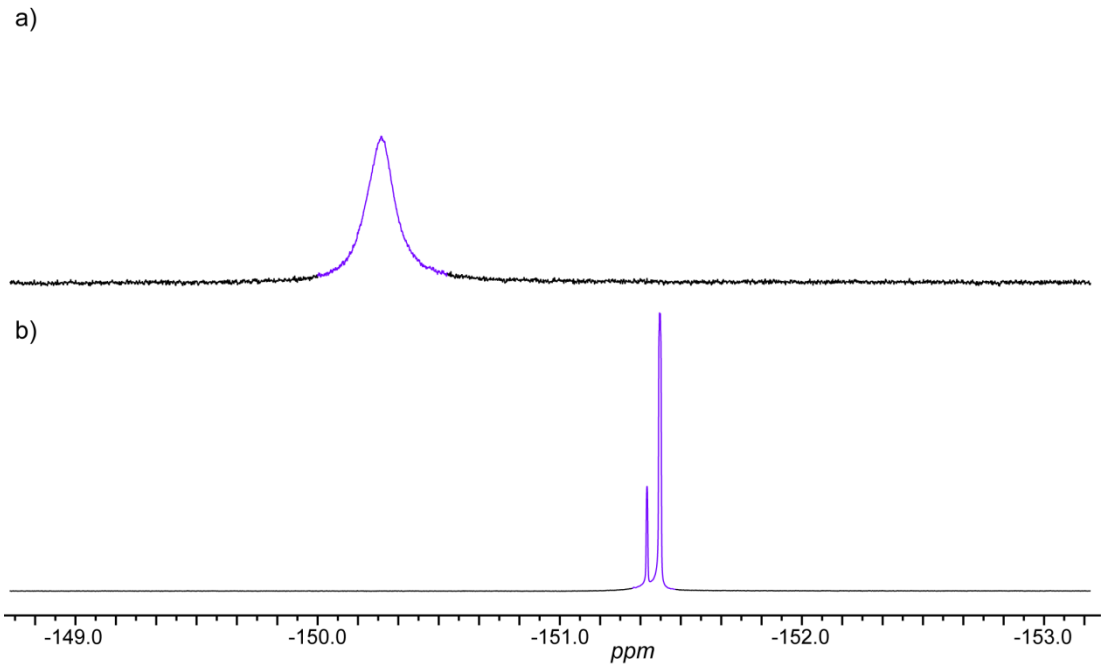

Figure 4.4. ^{19}F NMR (376 MHz, $C_2D_2Cl_4$, 298 K) spectra of a) Λ-$\mathbf{1}\cdot 6BF_4$ and b) Bu_4NBF_4.

4.3.2 Stability of $\mathbf{1}^{6+}$ and a comparison to similar mononuclear complexes

In the biotic world, large assemblies, such as double-stranded DNA, rely on multiple weak supramolecular interactions that cooperatively drive the formation of very stable, robust, structures. Abiotic metallosupramolecular assemblies also often heavily rely on cooperative effects to kinetically stabilise structures through multiple metal-ligand interactions. However, detailed investigations of these effects remain scarce.[5, 11] By measuring the ligand exchange rate between two similarly endohedrally functionalised

$M_{12}L_{24}$ assemblies, Fujita and co-workers found their nano-spheres to be remarkably stable with a half-life, $t_{1/2}$, value of 20 days, a value which is ~10^5 times more stable than the comparable monodentate Pt(II)-pyridine complex.[5] The same study also showed that part of the reason ligand scrambling between intact assemblies occurs very slowly is due to the negligible steady state concentration of free ligand; when small amounts of free ligand are added to the intact cage, the rate of scrambling increases dramatically, with a half-life, $t_{1/2}$ = 23 min. Stang and co-workers similarly showed scrambling of ligand components between a set of Pt-based polygons using 4,4′-bipy and the analogous deuterium labelled ligand.[11b] They too observed that these assemblies were remarkably stable with a ligand exchange $t_{1/2}$ of 17 days (based upon the first-order kinetic exchange rate constant k = 0.0024 h^{-1}), however, no comparison was made with a mononuclear complex making the assessment of cooperativity within their system difficult. In both of these examples, the assemblies between which the ligand exchange rates were measured were not isoenergetic, therefore the ligand exchange rate constant and the calculated overall stability are an average of the forward and reverse exchange processes. Measuring the true stability value for an ensemble of aggregates based on their exchange rates is possible when the ensembles, and the exchanging aggregates, are enantiomers of one another and the different structural isomers, which result due to scrambling, are distinguishable by analysis, such as NMR. Capsule $\mathbf{1}^{6+}$ represents an ideal candidate for such a study as both the homo-*Λ* and homo-*Δ* enantiomers are isoenergetic and the hetero-chiral assemblies, which form as a result of scrambling, have significantly different ^{1}H NMR chemical shifts to the enantiopure starting isomers.

The kinetic stabilities of **1**·6X (where X = OTf^-, PF_6^-, ClO_4^- or BF_4^-) were measured by mixing both *Λ*- and *Δ*-**1**·6X in a 1:1 ratio; as the *Λ* and *Δ*-$[Ir(ppy)_2]^+$ subcomponents scrambled the diminishing concentration of the homochiral assemblies was monitored using ^{1}H NMR spectroscopy (see Figure 4.5 for the *Λ*/*Δ*-**1**·6OTf scrambling experiment compared to **1**·6OTf obtained from *rac*-$[(Ir(ppy)_2Cl)_2]$; see section 4.5.6 for further experimental details).

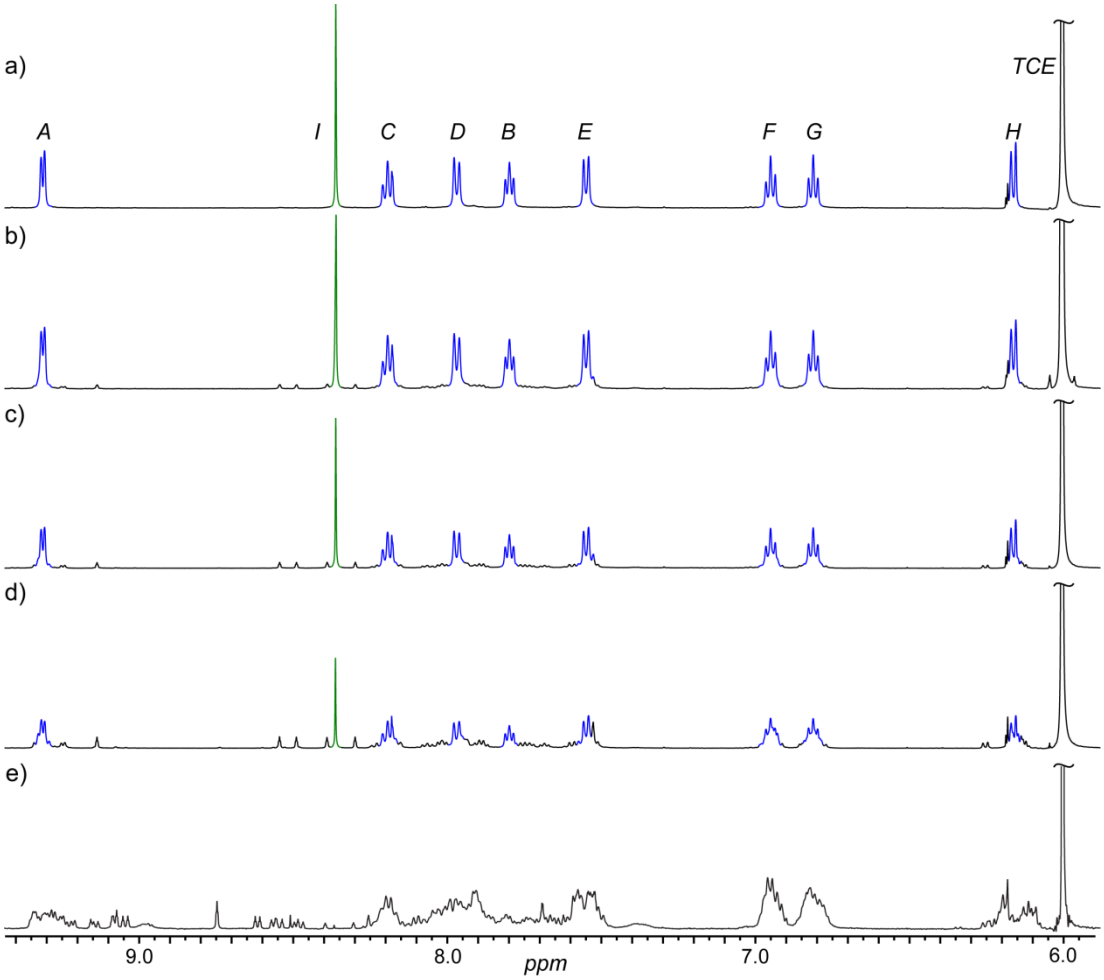

Figure 4.5. ^{1}H NMR (500 MHz, $C_2D_2Cl_4$, 298 K) spectra for the scrambling of *Λ/Δ*-**1**·6OTf, a) combined *Λ*- and *Δ*-**1**·6OTf after 0.5 h; b) 24 h; c) 48 h and d) 7 days; e) **1**·6OTf obtained from *rac*-[(Ir(ppy)$_2$Cl)$_2$]. See Scheme 4.1 for peak assignment.

Straight-line plots of (1/[*Λ/Δ*-**1**·6X]-1/[*Λ/Δ*-**1**·6X]$_0$) versus *t* with all 4 counterions (see section 4.5.6) indicated that the scrambling kinetics were second order with respect to **1**$^{6+}$. The observed exchange rate constant, k_{obs}, and half-life, $t_{1/2}$, values for **1**·6X (where X = OTf^-, PF_6^-, ClO_4^- or BF_4^-), which were derived from their corresponding plots, were observed to be highly dependent on the associated counterions (see Table 4.1). A rational of the relative stabilities of **1**$^{6+}$ is discussed in detail in section 4.3.5.

	k_{obs} / M^{-1} s^{-1}	$t_{1/2}$ / day(s)
Λ/*Δ*-**1**·6OTf	1.52×10^{-2}	4.5
Λ/*Δ*-**1**·6PF_6	3.90×10^{-2}	2.2
Λ/*Δ*-**1**·6ClO_4	11.0	0.0073
Λ/*Δ*-**1**·6BF_4	22.7	0.0033

Table 4.1. The observed exchange rate constant, k_{obs}, and half-life, $t_{1/2}$, values for **1**·6X (where X = OTf^-, PF_6^-, ClO_4^- or BF_4^-) derived from plots of $(1/[\Lambda/\Delta\text{-}\mathbf{1}\cdot6X]\text{-}1/[\Lambda/\Delta\text{-}\mathbf{1}\cdot6X]_0)$ versus t (see section 4.5.7).

	k_{obs} / s^{-1}	$\Delta G^{\ddagger}$ / kcal mol^{-1}	$t_{1/2}$ / s
$[Ir(ppy)_2(NCC_6H_4F)_2]OTf$	0.0256	19.6	27
$[Ir(ppy)_2(NCC_6H_4F)_2]PF_6$	0.0197	19.8	35
$[Ir(ppy)_2(NCC_6H_4F)_2]ClO_4$	0.0188	19.8	35
$[Ir(ppy)_2(NCC_6H_4F)_2]BF_4$	0.0255	19.6	27

Table 4.2. Kinetic parameters for NCC_6H_4F ligand exchange for $[Ir(ppy)_2(NCC_6H_4F)_2]X$ (where X = OTf^-, PF_6^-, BF_4^- and ClO_4^-) in $C_2D_2Cl_4$.

In order to ascertain how effective cooperativity is in stabilising the structure of $\mathbf{1}^{6+}$, the ligand exchange rates for **1**·6X were compared against representative mononuclear complexes, $[Ir(ppy)_2(NCC_6H_4F)_2]X$ (where X = OTf^-, PF_6^-, ClO_4^- or BF_4^-). While the exchange of nitrile ligands for the mononuclear complexes is slow on the NMR timescale, it is too quick to accurately measure *via* the same spectroscopic technique using a similar "pairs-scrambling" experiment. Instead, as the ^{19}F NMR spectrum of $[Ir(ppy)_2(NCC_6H_4F)_2]^+$ gave a signal for coordinated NCC_6H_4F that was distinct from free ligand, ^{19}F EXSY spectroscopy was used to ascertain the activation barrier to the exchange process for the different anionic salts of this mononuclear complex. The activation barrier, ΔG, observed first order rate constant, k_{obs}, and calculated half-life, $t_{1/2}$, are shown in Table 4.2. In the case of the simple mononuclear complex, the identity of the associated counterions has no significant effect on the rate of the ligand exchange process, despite the anticipated difference in coordinating abilities of the four anions.

This is in stark contrast to $\mathbf{1}^{6+}$, where the associated counteranions lead to remarkably differing kinetic stabilities (see Table 4.1). In addition, when comparing **1**·6OTf to $[Ir(ppy)_2(NCC_6H_4F)_2]OTf$, a 1.4×10^4 fold increase in the stability of ligand exchange is observed. While the enhanced stability in previous metallosupramolecular systems has been postulated to be primarily due to cooperativity between the multiple metal-ligand interactions,[5, 11b] in this system there appears to be additional parameters which stabilise the assembly. In particular the use of different counteranions appears to stabilise the structure to significantly different extents seemingly through additional non-covalent interactions between the embedded anions and the capsule's scaffold.

4.3.3 Encapsulation of OTf^- *versus* PF_6^-

In Chapter 3, the anion binding properties of capsule $\mathbf{1}^{6+}$ were explored using anion titration experiments; it was shown that this capsule preferentially binds anions in the order PF_6^- > OTf^- > BF_4^-. The activation barrier for OTf^- exchange within $[4OTf\subset\mathbf{1}](OTf)_2$ was previously measured to be 18.0 kcal mol^{-1} using ^{19}F EXSY NMR (see section 3.5.10). A similar analysis of the mixture of $[4PF_6\subset\mathbf{1}](PF_6)_2$ and $[5PF_6\subset\mathbf{1}]PF_6$ using ^{19}F EXSY NMR revealed that the energy barrier for PF_6^- exchange, 17.6 kcal mol^{-1} (see Section 4.5.7),[12] is lower than that for **1**·6OTf, suggesting that there is poor correlation between *guest* binding strength and the activation barrier to *guest* exchange. Through extensive experimental work on ion exchange, Raymond and co-workers have also revealed that the trends in ion binding affinities and exchange rates for their system do not run in parallel.[13] In this current system, there also appears to be poor correlation between *guest* binding strength and the kinetic stability of the overall ensemble, with $t_{1/2}$ of 4.5 and 2.2 days for **1**·6OTf and **1**·$6PF_6$, respectively.

The primary determinant of binding strength of *guests* within the cavities of *hosts* has often been postulated to be due to Rebek's 55% optimum cavity occupancy,[14] whereby *guests* which volumetrically fill closest to 55% of the space available within the *host* will bind strongest.[6a, 15] However, for this system, Rebek's model for ideal *guest* binding proves to be an over simplification. In Chapter 3, the 4 OTf^- counterions of $[4OTf\subset\mathbf{1}]^{2+}$ were shown to occupy an ideal 55%. However, PF_6^- anions have been shown to preferentially displace the triflate *guests* of $[4OTf\subset\mathbf{1}]^{2+}$ giving a mixture of $[4PF_6\subset\mathbf{1}]^{2+}$ and $[5PF_6\subset\mathbf{1}]^+$. Recently Nitchke's group have demonstrated that anion binding

predictions for their system using volume occupancy ratios failed when hydrogen bonding and electrostatic interactions were present.[8a] Simple calculations,[16] would appear to suggest that the volume occupancies for $[4PF_6\subset\mathbf{1}]^{2+}$ and $[5PF_6\subset\mathbf{1}]^{+}$ are 48% and 60%, respectively, and as PF_6^- binds more strongly than OTf^- this appears to contradict Rebek's theory. 55% occupancy could however be achieved with an average of 4.6 PF_6^- ions, which is close to the 4.8 encapsulated PF_6^- ions observed to exist for pure $\mathbf{1}\cdot 6PF_6$ (see section 4.3.1). Although $[5PF_6\subset\mathbf{1}]\cdot PF_6$ appears as the dominant species by ^{19}F NMR analysis, the co-existence of $[4PF_6\subset\mathbf{1}]\cdot 2PF_6$ as a minor species (see Scheme 4.2) is potentially crucial and its existence could be explained by and would support Rebek's optimum occupancy theory. This however still leaves the question why PF_6^- is preferentially encapsulated over OTf^-, yet both are estimated to occupy close to ~55%?

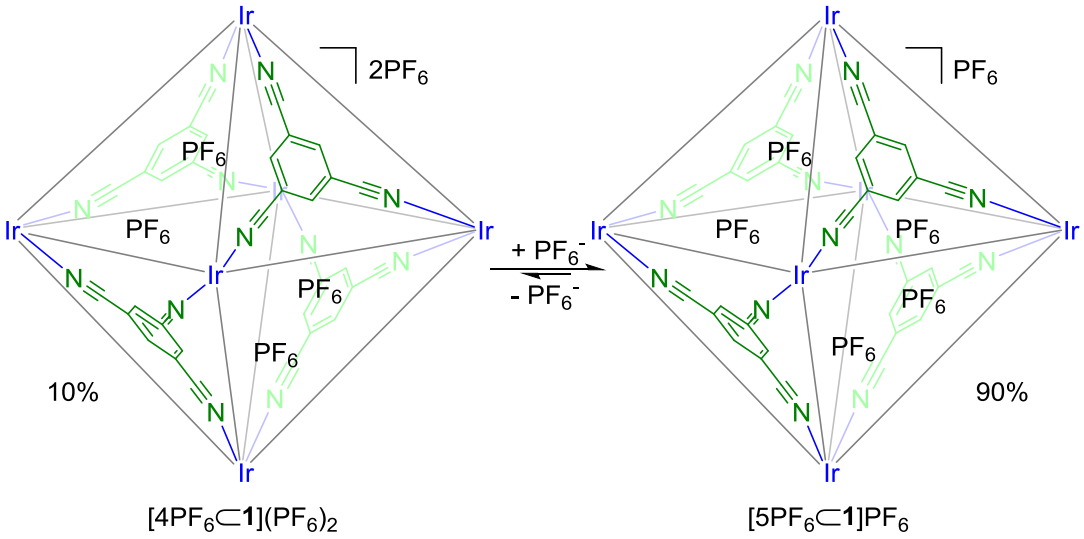

Scheme 4.2. $\mathbf{1}\cdot 6PF_6$ exists as an equilibrium between the $[4PF_6\subset\mathbf{1}](PF_6)_2$ and $[5PF_6\subset\mathbf{1}]PF_6$ species, qualitatively measured at 10% and 90% in $C_2D_2Cl_4$ at 298K, respectively. Annotated Ir (blue) ≡ $[Ir(ppy)_2]^+$.

For other metallosupramolecular capsules, anion binding affinities for cationic cavities have often been observed to follow the trend PF_6^- > OTf^- > ClO_4^- > BF_4^-, when the encapsulation process is not sterically hindered by the size or shape of the cavity.[15, 17] We now believe it is no coincidence that the anions frequently follow this trend and believe the reason behind it may be connected to solvophobic effects.

In considering the binding affinities of PF_6^-, OTf^-, ClO_4^- and BF_4^-, it appeared that the interaction of the counterions with the bulk phase had been largely ignored. The free energy of binding neutral *guests* within a metallosupramolecular *host* has been previously demonstrated to be linearly proportional to the solubility of the *guests* in the binding medium i.e. the less soluble the *guest* the greater the binding affinity to the *host*.[18] Nitschke's group have also demonstrated that in an aqueous solution CBr_4 was preferentially bound over the more water soluble CCl_4 within the hydrophobic cavity of their cage.[19] These results are consistent with the proposed hypothesis that the affinity for *guest* binding has a relationship to the solubility of the *guests* in the bulk phase, when the size and shape differences of the *guest* molecules are negligible in respect to the size and shape of the cavity.

In order to ascertain whether there is a difference in solubility between OTf^- and PF_6^- anions we decided to measure the relative solubility of the pyridinium salts (PyH·X) of the different anions in $C_2D_2Cl_4$.[20] Fully saturating the solution with the corresponding salt and using ^1H NMR for analysis, PyH·OTf appeared only partially soluble (see Figure 4.6a). In contrast, PyH·PF_6 appeared completely insoluble in $C_2D_2Cl_4$ (see Figure 4.6b), whereas the solubility of PyH·ClO_4 and PyH·BF_4 in the same solvent were significantly less than PyH·OTf but greater than PyH·PF_6 (see Figure 4.6c and 4.6d).

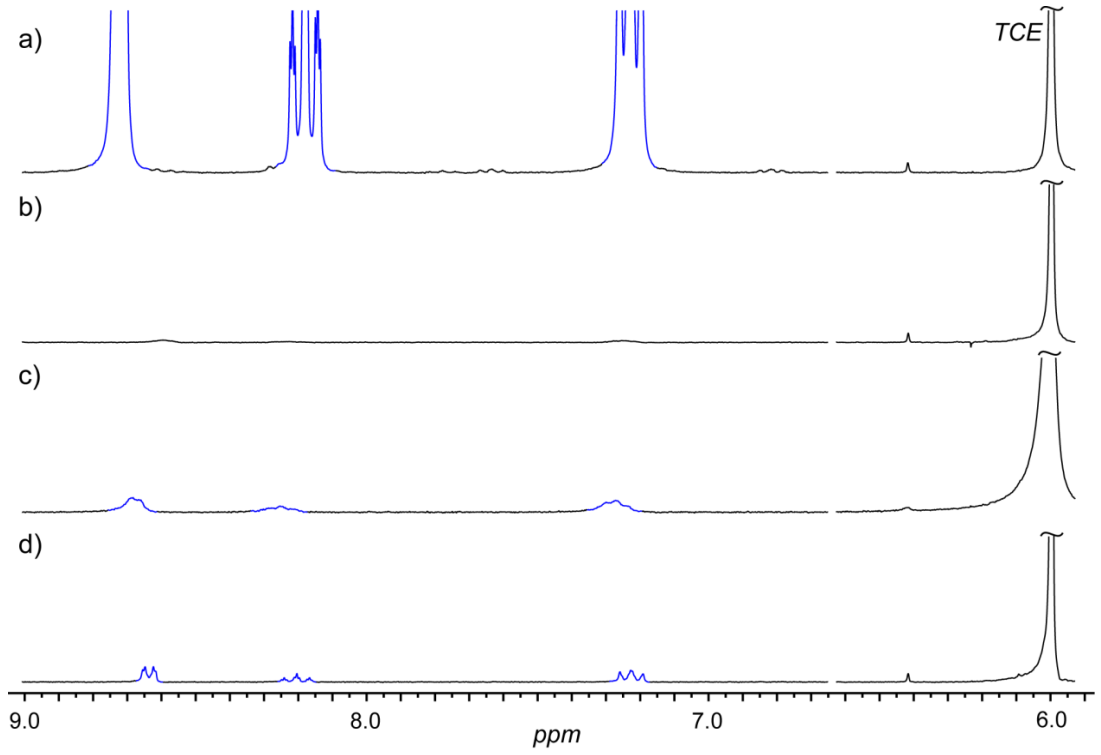

Figure 4.6. Partial ^{1}H NMR (400 MHz, $C_2D_2Cl_4$, 298 K) spectra for a) PyH·OTf, b) PyH·PF_6, c) PyH·ClO_4 and d) PyH·BF_4. All NMR samples were fully saturated with the corresponding salts and the spectra normalised.

As predicted, PF_6^- appears to be less soluble than OTf^- in $C_2D_2Cl_4$, presumably due to less favourable anion-solvent interactions. This supports the hypothesis that when the anions are in competition, PF_6^- is preferentially bound over OTf^- in the solvent free environment of the cavity of $\mathbf{1}^{6+}$ due to its greater solvophobicity in $C_2D_2Cl_4$. The solvophobicity of the different anions, however, fails to explain the observed trend in the stability of **1**·6X (where X = OTf^-, PF_6^-, ClO_4^- or BF_4^-). In order to explain this trend electrostatic potential energy surfaces were modelled for the different anions in question.

4.3.4 Modelled electrostatic potential surfaces

Computer generated molecular electrostatic potential surfaces have been used in a variety of important chemical and biological systems[21] including the prediction of non-covalent interactions such as hydrogen bond donor/acceptor ability,[22] cation-π binding strengths,[23] arene π-π stacking affinities[24] and *host-guest* recognition.[25] At

any given point on the surface of a molecule, the electrostatic potential is a measure of the electrostatic energy a positive unit test charge would experience at that point, red indicative of a more negative and blue a less negative charge.

We decided to model the electrostatic potential surfaces for the different counterions to see if electrostatic interactions could potentially explain the large differences in stability of **1**·6X (where X = OTf^-, PF_6^-, ClO_4^- or BF_4^-). The electrostatic potential surfaces for OTf^-, PF_6^-, BF_4^- and ClO_4^- were calculated using density function theory (DFT) with B3LYP/6-31G** as the basis set.[26] Observations revealed that OTf^- has a distinct dipole, which is not present for PF_6^- (see Figure 4.7a and 4.7b). PF_6^- on the other-hand has a less electronegative surface with the more negative region centred towards its core. The electrostatic potential surfaces for ClO_4^- and BF_4^- are also spherical in symmetry (see Figure 4.7c and 4.7d), however the surface for ClO_4^- is more negatively charged than PF_6^-, and BF_4^- more negatively charged than ClO_4^-.

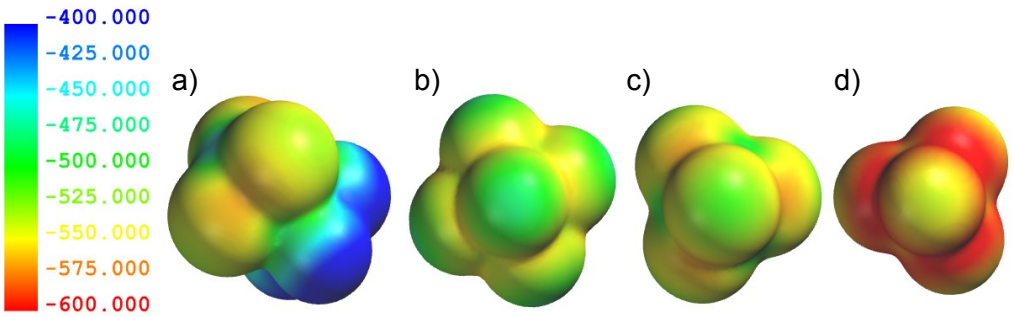

Figure 4.7. B3LYP/6-31G** calculated electrostatic potential surfaces for a) OTf^-, b) PF_6^-, c) ClO_4^- and d) BF_4^-. The rendered colour legend (kJ mol^{-1}) is generic for all 4 electrostatic potential surfaces.

4.3.5 Stability of 1^{6+} rationalised

Following on from the kinetic stability studies in section 4.3.2, the reasoning behind the differences in stability of capsules **1**·6X (where X = OTf^-, PF_6^-, ClO_4^- or BF_4^-) was explored by looking at the electrostatic potential energy surfaces of the anions (see section 4.3.4) and re-examining the X-ray crystal structure of **1**·6OTf (see section 3.5.22). From the X-ray crystal structure of **1**·6OTf, the OTf^- anions bound within $\mathbf{1}^{6+}$, are aligned with the CF_3 end pointing into the centre of the cavity and the SO_3 group out towards the capsule's "windows". The oxygens associated with the OTf^- anions appear

to hydrogen bond to both the protons on the tcb ligands and the *ortho*-proton on the pyridine of the ppy ligands, satisfying the electronegative node of the OTf^- anion (see section 3.3.4). The CH hydrogen bound OTf^- anions are also confined within a favoured tetrahedral close-packed conformation within the cavity of $\mathbf{1}^{6+}$, pre-orientated in the optimum position for hydrogen bonding. Comparing the computational models (see Figure 4.7a and 4.7b), PF_6^- on the other-hand has a spherical geometry with no net dipole and the electrostatic potential surface for PF_6^- is more electronegative than the inward pointing CF_3 group yet less electronegative than the SO_3 group on the OTf^-. The less electronegative fluorine atoms of PF_6^- mean that this anion will be a poorer hydrogen bond acceptor and, based on the modelled electrostatic potential surfaces, one would predict that PF_6^- would experience greater inter-anion repulsive forces and therefore overall weaker binding within the framework of $\mathbf{1}^{6+}$ relative to OTf^-. The attractive Coulombic forces, which are enhanced by hydrogen bonding, between the cationic framework of $\mathbf{1}^{6+}$ and the anionic core of 4 OTf^- anions for which the repulsive forces are buffered by the CF_3 groups, is believed to be the reason for the enhanced robustness of $\mathbf{1}\cdot 6OTf$ with respect to $\mathbf{1}\cdot 6PF_6$, whereas the higher affinity of PF_6^- over OTf^- for the cavity of $\mathbf{1}^{6+}$ in $C_2D_2Cl_4$ is caused by solvophobic effects.

Both ClO_4^- and BF_4^-, like PF_6^-, have spherical symmetry with no net dipole and the electrostatic potential surfaces exhibit non-directional inter-anion repulsive forces (see Figure 4.7c and 4.7d). The modelled electrostatic potential surface for BF_4^-, however, overall appears more electronegative than ClO_4^-, which in turn is more electronegative than PF_6^-, thus BF_4^- would experience greater inter-anion repulsion within the cavity than ClO_4^-, which in turn would experience greater repulsion than PF_6^-. This trend in the inter-anion repulsive forces runs in parallel to the trend observed for the stability of capsules $\mathbf{1}\cdot 6X$, $\mathbf{1}\cdot 6OTf >> \mathbf{1}\cdot 6PF_6 >> \mathbf{1}\cdot 6ClO_4 > \mathbf{1}\cdot 6BF_4$. By this analogy, the discrepancy in the stability of capsule $\mathbf{1}^{6+}$ appears to be at least partially governed by the inter-anion repulsive forces.

Interestingly, when the calculated electrostatic potential energy on the repulsive node of the anions is compared to the chemical shift of the tcb proton H_I (see Figure 4.1) an excellent linear correlation ($R^2 = 0.9998$) is observed (see Figure 4.8). The more repulsive the node of the anion, the more shielded the electron environment around proton H_I. This implies that the stability of capsule $\mathbf{1}^{6+}$ is closely related to the

electrostatic potential of the repulsive node of the associated counterions, which in turn can be predicted by the chemical shift of proton H_I on the tcb ligand.

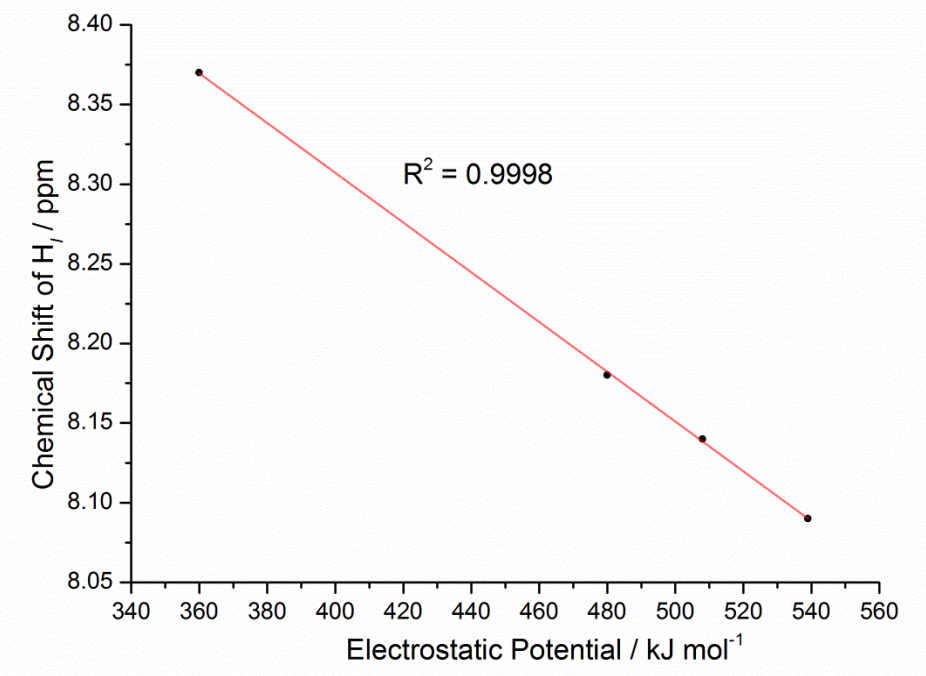

Figure 4.8. Chemical shift of H_I from the ^{1}H NMR spectra of *Λ*-**1**·6OTf, *Λ*-**1**·6PF_6, *Λ*-**1**·6ClO_4 and *Δ*-**1**·6BF_4 *verses* the calculated electrostatic potential on the repulsive node of the corresponding anion. R^2 = 0.9998.

4.3.6 Template effects

Iridium capsule $\mathbf{1}^{6+}$ has thus far displayed interesting *host-guest* chemistry with various anions. However, in order to bind neutral *guests* the capsule must either contain an empty cavity or a cavity where the ions and/or solvent molecules could be readily displaced. We therefore attempted to synthesise the empty capsule using trifluoromethanesulfonimide (NTf_2^-), a bulky anion that is potentially too large to fit inside the cationic pocket of $\mathbf{1}^{6+}$ (see Scheme 4.3).

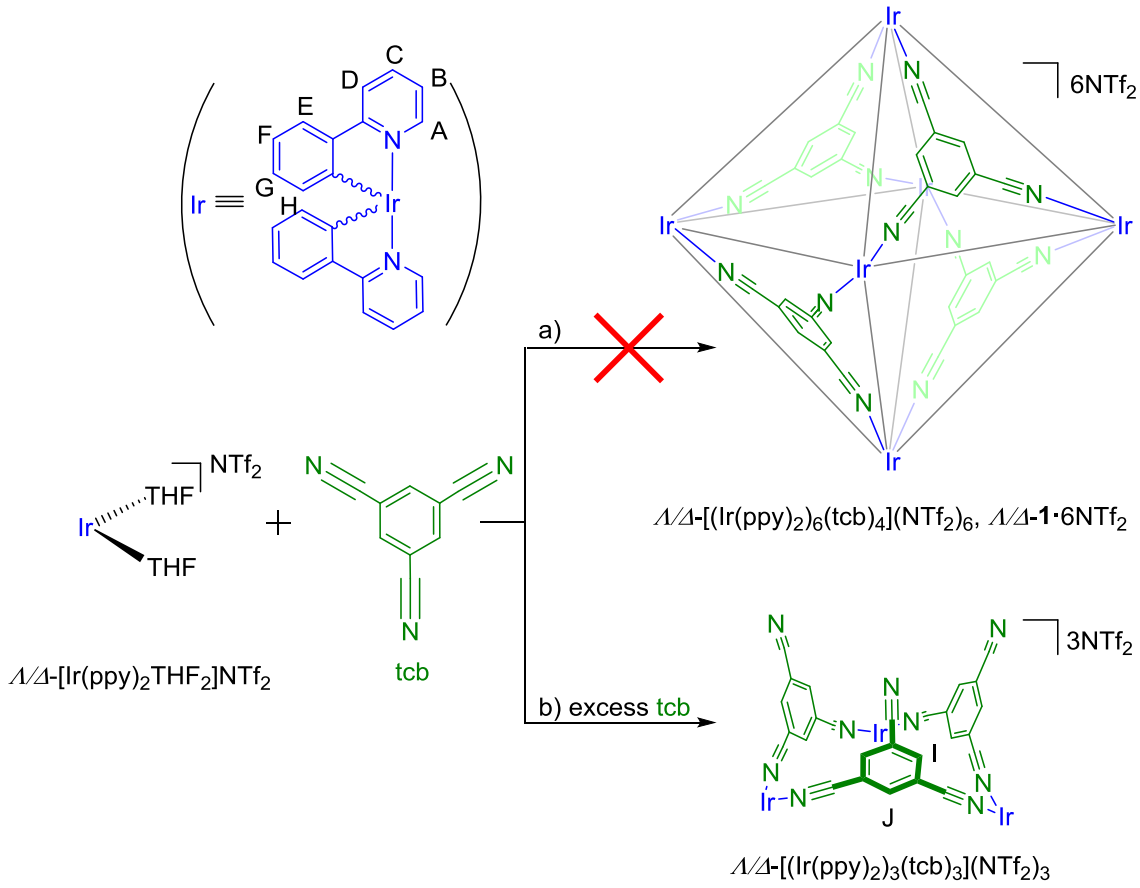

Scheme 4.3. Synthesis of *Λ*/*Δ*- **1**·6NTf$_2$ and *Λ*/*Δ*-[(Ir(ppy)$_2$)$_3$(tcb)$_3$](NTf$_2$)$_3$. Conditions: a) 3:2 stoichiometric ratio of *Λ*- or *Δ*-[(Ir(ppy)$_2$THF$_2$]NTf and tcb, $C_2H_4Cl_2$, RT and b) *Λ*- or *Δ*- [(Ir(ppy)$_2$THF$_2$]NTf with excess tcb, $C_2H_4Cl_2$, RT.

Starting from the readily synthesised *Λ*-[Ir(ppy)$_2$THF$_2$]NTf$_2$ precursor (see Figure 4.9a) in $C_2D_2Cl_4$ two thirds of an equivalents of tcb was added. A complex library of aggregates appears to form, as seen by ^{1}H NMR spectroscopy (see Figure 4.9b), and more importantly, no M_6L_4 assemblies were detected by nESI-MS analysis. However, titrating Bu$_4$NOTf into the mixture led to the broad and "messy" ^{1}H NMR spectrum converging into sharp signals (see Figure 4.9b-4.9g), superimposable with authentic **1**·6OTf. Addition of only 4 equivalents of OTf$^-$ (see Figure 4.9f), the quantity required to fill the cavity of **1**$^{6+}$, led to instantaneous formation of *Λ*-[**1**·4OTf]$^{2+}$, demonstrating the high preference in the self-assembly of the octahedral architecture over any other. What is also interesting is if a small excess of tcb is charged to the NMR sample containing the dynamic library of aggregates (Figure 4.9b) what is believed to be an open-ended form of the capsule, *Λ*-[(Ir(ppy)$_2$)$_3$(tcb)$_3$](NTf$_2$)$_3$, is observed to form (see

Figure 4.9h and Section 4.3.7). These results strongly suggest that the self-assembly of $\mathbf{1}^{6+}$ only occurs with counterions of a particular size and shape, which potentially act as templates.

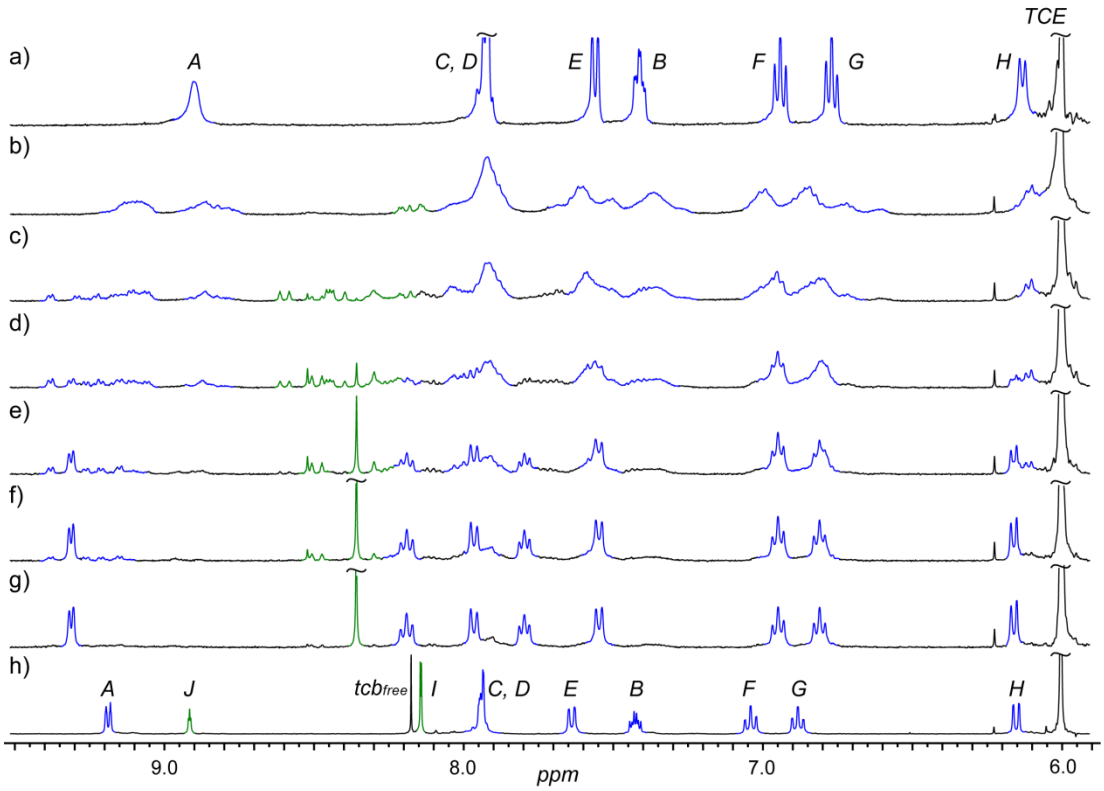

Figure 4.9. ^{1}H NMR (400 MHz, $C_2D_2Cl_4$, 298 K) spectra of a) *Λ*-[Ir(ppy)$_2$THF$_2$](NTf$_2$); b) a dynamic library of aggregates formed on addition of 3 eq of *Λ*-[Ir(ppy)$_2$](NTf$_2$) to 2 eq of tcb; dynamic library of aggregates with c) 1 eq of Bu_4NOTf; d) 2 eq; e) 3 eq; f) 4 eq; g) 6 eq and h) *Λ*-[(Ir(ppy)$_2$)$_3$(tcb)$_3$](NTf$_2$)$_3$ formed on addition of 1.3 eq of tcb to *Λ*-[Ir(ppy)$_2$THF$_2$](NTf$_2$). See Scheme 4.3 for peak assignment.

Further empirical evidence that the self-assembly of $\mathbf{1}^{6+}$ is driven by counterion templation effects was obtained by replacing tcb for a larger tritopic cyano ligand, 1,3,5-tris(4-cyanophenylethynyl)benzene (tceb), which has previously been used by Stang to create diverse Pd(II) and Pt(II)-based octahedra.[27] The larger tritopic ligand was used in an attempt to construct a capsule with wider "windows" allowing for easier anion migration in and out of the cavity. Self-assembly was attempted starting from both the [(Ir(ppy)$_2$OTf)$_2$] and [Ir(ppy)$_2$(THF)$_2$]NTf$_2$ precursors (see Scheme 4.4) but, as with NTf_2^-, no single species or M_6L_4 assemblies were detected by NMR or nESI-MS analysis. The larger assembly is believed to possess a cavity that is non-complimentary

in size and/or shape to either OTf^- or NTf_2^- counterions and, without the templation effect, the entropic costs of the larger assembly outweigh the enthalpic gains of the multiple metal-ligand interactions.

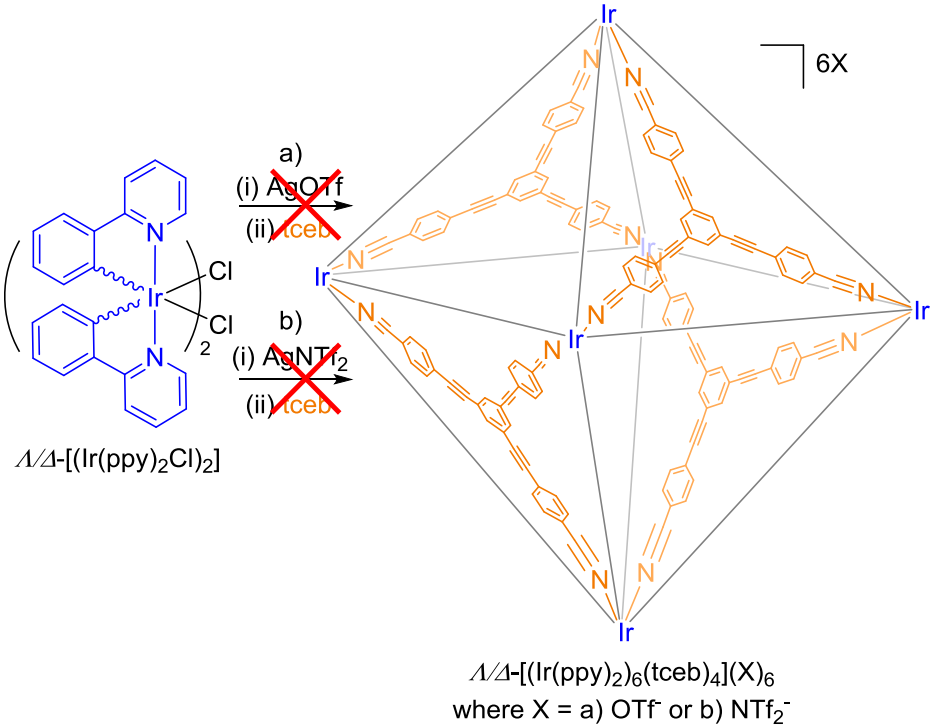

Scheme 4.4. Synthesis of *Λ/Δ*-$[(Ir(ppy)_2)_6(tceb)_4](X)_6$ (where X = a) OTf^- or b) NTf_2^-). Conditions starting from *Λ/Δ*-$[(Ir(ppy)_2Cl)_2]$: a) (i) AgOTf, $C_2H_4Cl_2$, RT, 2 h; (ii) tceb, $C_2H_4Cl_2$, RT, 24 h; b) (i) $AgNTf_2$, THF, RT, 2 h; (ii) tceb, $C_2H_4Cl_2$, RT, 24 h. Annotated Ir (blue) ≡ $[Ir(ppy)_2]^+$.

In the literature there are several instances where templates have been used to thermodynamically drive the exclusive formation of metallosupramolecular architectures by means of reducing the ground state energy of the desired assembly.[3, 28] Ions acting as templates are common in the area of coordination chemistry, specifically in the assembly of macrocycles,[29] rotaxanes, catenanes and knots[30] and other higher order assemblies.[8b, 31] The use of ions as templates in the self-assembly of metallosupramolecular capsules is also common and has been reported by the likes of Hay,[8d] Nitschke,[4, 6a] Raymond[8c] and Ward.[32] With anion templated self-assembly, there are several potential non-covalent interactions that can take place between the anions and the molecular scaffold including; hydrogen bonding, weak metal-anion and anion-π interactions[33] and/or simply Coulombic negative-positive charge attraction.

Ionic templates are often single ions of a constrained geometry. Multiple ions acting as ionic templates are far less common due to inter-ion repulsive forces, with only a small number of examples reported in the literature.[4, 6a, 34] One such example was demonstrated recently by Nitschke's group who, using NTf_2^- with Co(II) and a bis-bidentate ligand, observed the formation of a dynamic library of aggregates.[4, 6a] However, analogous to our observations with $\mathbf{1}^{6+}$, on addition of OTf^-, PF_6^-, BF_4^- or ClO_4^- a discrete Co_4L_6, Co_8L_{12} or $Co_{10}L_{15}$ assembly formed. In coordination chemistry, molecular templates have generally been used to energetically favour the self-assembly of one discrete structure from a dynamic library, however, templation effects could also be used for other useful applications, such as sensing of heavy metal cations in industry[35] and mono-disperse silica nanoparticle synthesis.[36]

Thus far, the analysis of **1**·6X has been conducted using $C_2H_4Cl_2$ or $C_2D_2Cl_4$ as solvent due to good solubility and stability. Protic solvents such as CH_3OH and aprotic coordinating solvents such as DMSO are not compatible with this system as they compete with the nitrile ligands of $\mathbf{1}^{6+}$ and facilitate decomposition of the assembly. CD_3NO_2 has also been observed to partially decompose/disassemble **1**·6OTf. However, as CD_3NO_2 is non-coordinating, the disassembly process is believed to result due to the increased solubility of OTf^- ions (presuming nitromethane will form CH···O H-bonds to OTf^-) in the solvent system, weakening the structure and destabilising the highly charged assembly. Saturating the CD_3NO_2 solution with OTf^- in the form of Bu_4NOTf, reverses this process and pushes the equilibrium to the left-hand-side leading to the reassembly of **1**·6OTf. In a mixed $CD_3NO_2/C_2D_2Cl_4$ (1:2) solvent system **1**·6OTf remains intact, however the presence of CD_3NO_2, increases OTf^- solubility and as a consequence significantly decreases the energy barrier to OTf^- exchange in and out of the cavity and potentially the number of encapsulated OTf^- anions, as evidenced by the broad ^{19}F NMR signals re-equilibrated into a 1:1 ratio (see section 4.5.8).

Re-examining the XRD data of **1**·6OTf, 4 OTf^- anions clearly form a closely packed anionic "cluster" within the cationic cavity of $\mathbf{1}^{6+}$, reducing the effective charge of the assembly from +6 to +2. $[\mathbf{1}\cdot 4OTf]^{2+}$ was also the only intact assembly cation visible by nESI-MS, implying that removal of even just one OTf^- anion from the cavity greatly destabilises the capsule. The kinetic stability of $\mathbf{1}^{6+}$ has also been demonstrated to be particularly sensitive to different anions and solvents with half-lives ranging from days to minutes. This wealth of evidence is indicative that the anions, which have been

observed to reside in the cationic pocket, not only balance the charge but are fundamentally key in stabilising and controlling the self-assembly process of $\mathbf{1}^{6+}$. It has also been demonstrated that due to their different shapes and sizes, the different anions, *in situ*, form geometrically unique anionic templates that, based on their shape, size and electrostatic potential energy surfaces, determine the stability of $\mathbf{1}^{6+}$ and whether or not $\mathbf{1}^{6+}$ forms in the first instance.

4.3.7 Metallocavitand $[(Ir(ppy)_2)_3(tcb)_3](NTf_2)_3$

In the previous section we demonstrated that the self-assembly of $\mathbf{1}^{6+}$ was counterion mediated with the NTf_2^- anion appearing either too large or of a mismatched geometry to template the formation. Adding an excess of tcb to the dynamic library of aggregates however led to the formation of what is believed to be an open-ended form of the capsule, what could be referred to as a metallocavitand.[28]

The ^{1}H NMR spectrum of *Λ/Δ*-$[(Ir(ppy)_2)_3(tcb)_3](NTf_2)_3$ (see Figure 4.9h) revealed 10 aromatic proton environments; 8 for the hydrogen atoms on the ppy and 2 on the tcb ligand. All signals appear sharp apart from H_B, which is split. The cavitand was modelled in Spartan '10 in order to try and explain the observed splitting phenomena. From the modelled structure of $[(Ir(ppy)_2)_3(tcb)_3]^{3+}$ (see Figure 4.10), the two ppy ligands are evidently inequivalent due to the reduced symmetry in this assembly relative to $\mathbf{1}^{6+}$. Proton H_B (see Figure 4.10) sits in two distinct environments, either at the base or the lip of the metallocavitand, which differ to a much greater extent than any of the other ppy proton environments. This explains why only H_B is split in the ^{1}H NMR spectrum for *Λ/Δ*-$[(Ir(ppy)_2)_3(tcb)_3](NTf_2)_3$. ^{1}H DOSY NMR confirmed that the aromatic protons all belonged to the same assembly (see section 4.5.9), with a log (D / $m^2\ s^{-1}$) of -9.86 in $C_2D_2Cl_4$ equivalent to a hydrodynamic radius of 10.9 Å, smaller than the radius of capsule $\mathbf{1}^{6+}$ and comparable to the diameter of the modelled structure (see Figure 4.10). The intact cavitand was also visible by nESI-MS (see section 4.5.10), where both the 1+ and 2+ cations for the M_3L_3 species were present. No higher order M_nL_n assemblies were observed.

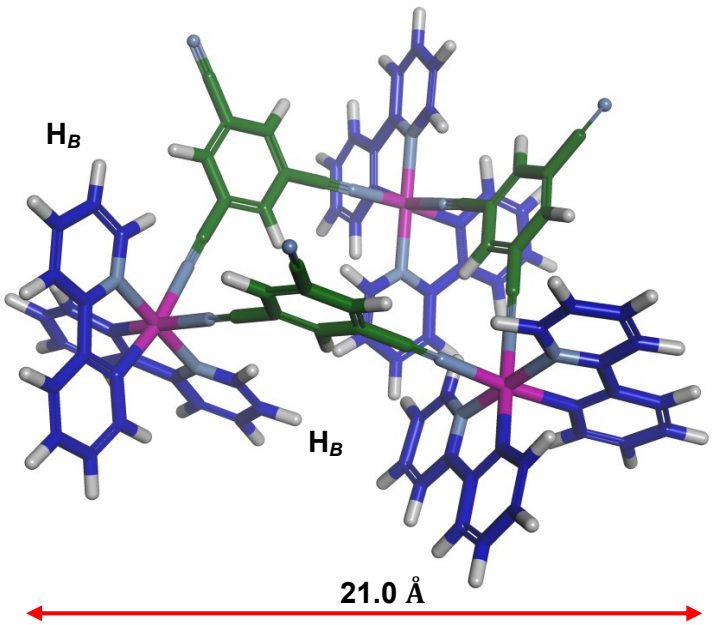

Figure 4.10. Model of *Δ*-[(Ir(ppy)$_2$)$_3$(tcb)$_3$]$^{3+}$, energy minimised in Spartan '10. Diameter measured at 21.0 Å. The two different environments for proton H$_B$ depicted.

Further evidence for the formation of [(Ir(ppy)$_2$)$_3$(tcb)$_3$](NTf$_2$)$_3$ was acquired by replacing one of the non-participating cyano groups on the tcb ligand with a methyl group, to give 1,3-dicyano(5-methyl)benzene (dcmb). Being di-topic, dcmb was predicted to only form macrocyclic assemblies of M_nL_n conformation. Following a similar experimental procedure (see Scheme 4.5) to *Δ*-[(Ir(ppy)$_2$)$_3$(tcb)$_3$](NTf$_2$)$_3$ in $C_2D_2Cl_4$, ^{1}H NMR analysis confirmed the appearance of a major species, *Δ*-[(Ir(ppy)$_2$)$_3$(dcmb)$_3$](NTf$_2$)$_3$, for which the ppy proton signals were near superimposable with those of *Δ*-[(Ir(ppy)$_2$)$_3$(tcb)$_3$](NTf$_2$)$_3$ (see section 4.5.11).

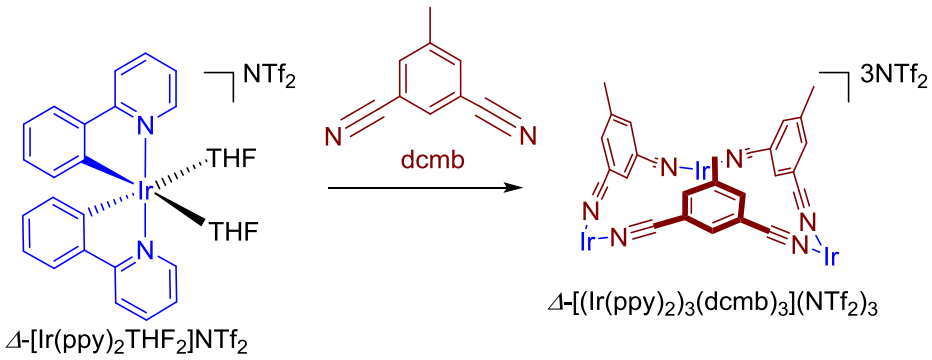

Scheme 4.5. Synthesis of *Δ*-[(Ir(ppy)$_2$)$_3$(dcmb)$_3$](NTf$_2$)$_3$, starting from *Δ*-[Ir(ppy)$_2$THF$_2$]NTf$_2$, 1 eq dcmb, $C_2D_2Cl_4$, RT. Annotated Ir (blue) ≡ *Δ*-[Ir(ppy)$_2$]$^+$.

Isolation of the metallocavitand *Λ*-[(Ir(ppy)$_2$)$_3$(tcb)$_3$](NTf$_2$)$_3$ was attempted by scaling up the reaction of *Λ*-[Ir(ppy)$_2$THF$_2$]NTf$_2$ with 1 eq of tcb in $C_2H_4Cl_2$. After 2 h at RT a precipitate was isolated from the reaction mixture which, when dissolved in $C_2D_2Cl_4$ appeared, by ^{1}H NMR analysis, to be a dynamic combinatory library of aggregates, identical in appearance to the dynamic library formed previously *in situ*. In the presence of excess tcb in $C_2D_2Cl_4$ the metallocavitand reformed as the sole product.

The instability of the metallocavitand is postulated to be due to the highly reversible nature of Ir-nitrile bond and a lack of bonding cooperativity within the system. With fewer metal-nitrile interactions than capsule **1**$^{6+}$, the entropic costs far outweigh the enthalpic gains and, without an excess of tcb to push the equilibrium to the right-hand-side, the metallocavitand exists as a dynamic library of aggregates in solution (see Scheme 4.6).

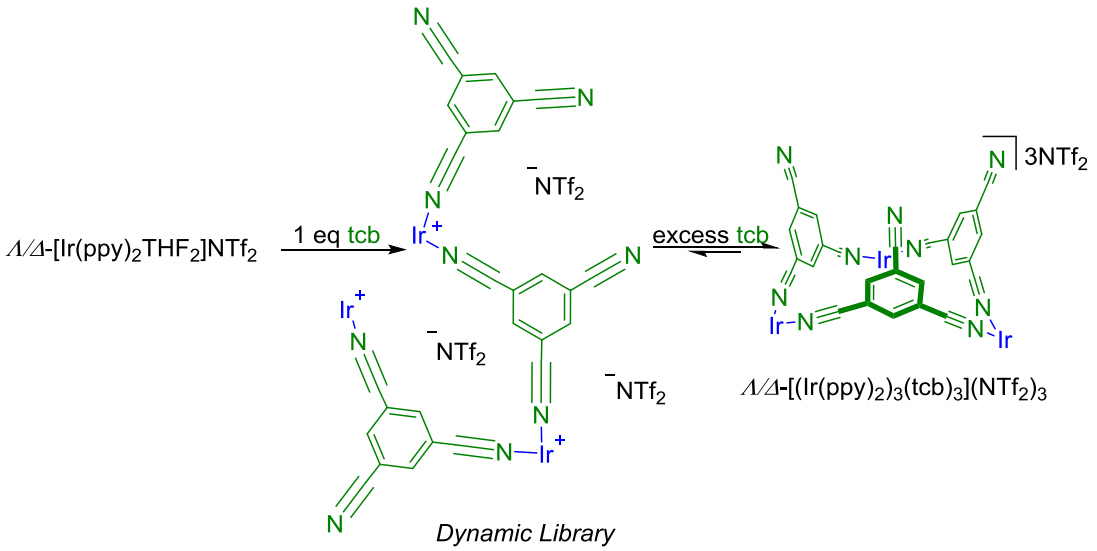

Scheme 4.6. Synthetic pathway to the self-assembly of *Λ*/*Δ*-[(Ir(ppy)$_2$)$_3$(tcb)$_3$](NTf$_2$)$_3$. Annotated Ir (blue) ≡ [Ir(ppy)$_2$]$^+$.

4.3.8 Exchanging ppy for ppz (2·6OTf)

The kinetic stability of the Ir scaffold **1**$^{6+}$ is primarily governed by the cooperativity of the multiple metal-ligand bonds with secondary interactions between the scaffold and the different counterions giving rise to the varying stability. Attempts to move the

counterions to the periphery, leaving an empty chamber, have thus far been unsuccessful.

From earlier experiments with the bpe ligand in Chapter 3, we observed that the bond between the Ir and the exchangeable ligand is more kinetically inert when 1-phenylatopyrazole (ppz) is used instead of ppy as the cyclometalating ligand. We thus compared the Ir-nitrile exchange rates between the ppz and the ppy mononuclear Ir complex using ^{19}F EXSY NMR analysis (*vide supra*). The activation barrier for Ir-nitrile exchange rate based on the ppz mononuclear analogue, $[Ir(ppz)_2(NCC_6H_4F)_2](OTf)$, was measured at 20.3 kcal mol^{-1} (see section 4.5.7), strongly supporting our previous empirical observations. We therefore reasoned, taking these experimental results into consideration, that substitution of the ppy for the ppz ligand may kinetically stabilise the metallosupramolecular scaffold to a sufficient extent to allow the anionic templates to be removed without disruption of the octahedron. Enantiopure *Λ*- and *Δ*-Ir capsules with ppz concomitant ligands, $[(Ir(ppz)_2)_6(tcb)_4](OTf)_6$ (**2**·6OTf), were subsequently synthesised and their physical properties compared to those of **1**·6OTf.

Starting from the known *rac*-$[(Ir(ppz)_2Cl)_2]$ bridged-chloride dimer and converting it into the subsequent L-serine diastereoisomers chiral resolution was this time achieved through solubility differences between the *Λ*-L and *Δ*-L diastereoisomers in CH_2Cl_2. *Λ*-$[Ir(ppz)_2$(L-serine)] appeared to be significantly more soluble in CH_2Cl_2 and was separated from the crude mixture by conventional Buchner filtration before being converted into enantiopure *Λ*-$[(Ir(ppz)_2Cl)_2]$ with 1M HCl in CH_3OH. *Δ*-$[(Ir(ppz)_2Cl)_2]$ was obtained in the same manner using D-serine. *Λ*- and *Δ*-**2**·6OTf were synthesised from *Λ*- and *Δ*-$[(Ir(ppz)_2Cl)_2]$ following an analogues experimental procedure to that for **1**·6OTf (see Scheme 4.7).

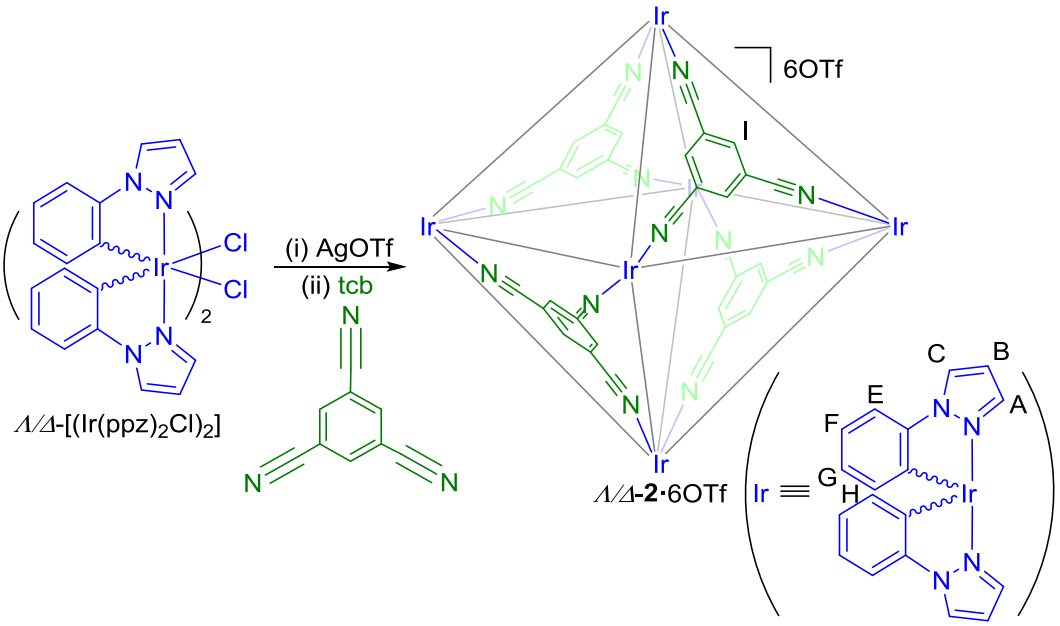

Scheme 4.7. Synthesis of *Λ*/*Δ*-**2**·6OTf. Conditions: (i) AgOTf, $C_2H_4Cl_2$, RT, 2 h; (ii) tcb, $C_2H_4Cl_2$, RT, 4 h; *Λ*-**2**·6OTf, 16% (starting from *Λ*-[(Ir(ppz)$_2$Cl)$_2$]); *Δ*-**2**·6OTf, 22% (starting from *Δ*-[(Ir(ppz)$_2$Cl)$_2$]).

The ^{1}H NMR spectrum for the two enantiomers *Λ*- and *Δ*-**2**·6OTf were identical and similar to the spectrum for *Λ*/*Δ*-**1**·6OTf (see section 4.5.12). In the aromatic region 8 different proton environments, 7 for the ppz and 1 singlet for the tcb ligand, were observed for the two enantiopure assemblies. From the ^{1}H DOSY NMR experiments, a diffusion coefficient of log (D / m^2 s^{-1}) = -9.98 was calculated (see section 4.5.12) for *Δ*-**2**·6OTf in $C_2D_2Cl_4$, a value near identical to the diffusion coefficient measured previously for **1**·6OTf (see section 3.5.6). In the gas phase under nESI-MS analysis, capsule **2**$^{6+}$, as with **1**$^{6+}$, was observed intact only as the 2+ cation, [**2**·4OTf]$^{2+}$ at 2040.2 m/z (see section 4.5.13). The appearance of only the 2+ species once again strongly suggests that 4 OTf$^-$ counterions are enclatherated in the cationic cavity of the capsule.

An X-ray crystal structure for *Δ*-**2**·6OTf (see Figure 4.11a) was obtained by slow diffusion of benzene into a saturated $C_2H_4Cl_2$ solution of **2**·$^{6+}$ (see section 4.5.14). The geometry of capsule **2**$^{6+}$ was observed to be very similar in size and shape to **1**$^{6+}$, with the largest difference being an increase in the size of the "windows" to the cavity (see Figure 4.11). Exchanging the ppy ligands on the Ir centre for the smaller ppz concomitant groups effectively increases the portal size and allows for more rapid counterion migration, as was subsequently demonstrated using ^{19}F NMR.

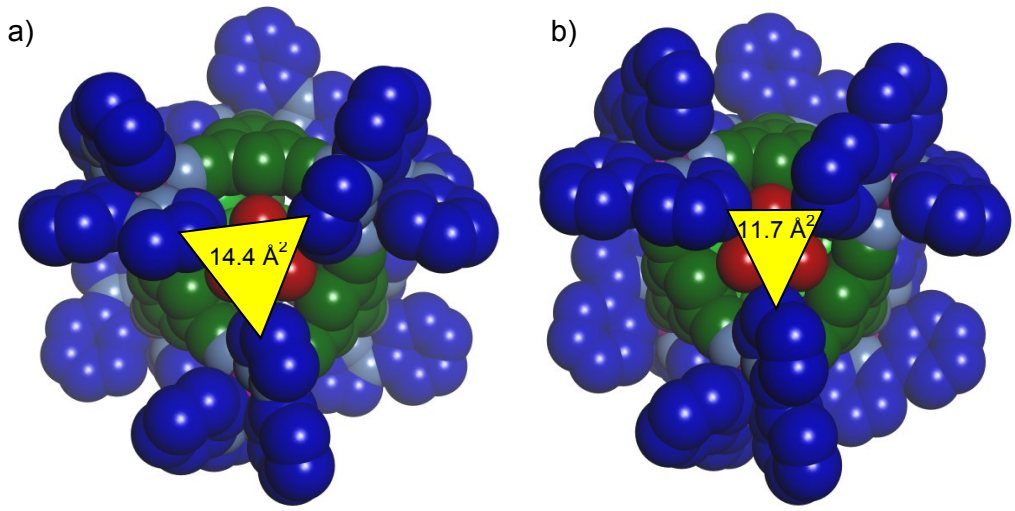

Figure 4.11. Space-fill representations of the X-ray crystal structures of a) *Δ*-**2**·6OTf and b) *Δ*-**1**·6OTf. The areas for the triangular shaped portals, highlighted in yellow, were calculated using trigonometry between the 3 *meta*-carbons on the pyrazole and pyridine rings of the ppz and ppy ligands, respectively. Portal areas were calculated as a) 14.4 Å^2 and b) 11.7 Å^2. The carbon atoms of ppy are shown in blue, tcb in dark green and OTf$^-$ carbons in orange, iridium in pink, nitrogen in pale blue, sulfur in yellow, oxygen in red and fluorine in pale green. Hydrogens have been omitted for clarity.

The ^{19}F NMR spectrum for *Δ*-**2**·6OTf revealed a broad, partially split, fluorine signal at RT, indicative of fast anion exchange on the NMR timescale and a lower energy barrier to anion encapsulation, relative to *Δ*-**1**·6OTf (see Figure 4.12). The fast anion exchange was monitored and a coalescence temperature of 30 °C was determined using VT NMR (see section 4.5.15). The rate constant for OTf$^-$ exchange was determined using ^{19}F EXSY NMR and a change in Gibbs free energy of 15.8 kcal mol^{-1} calculated (see section 4.5.7). The energy barrier to OTf$^-$ exchange for **2**·6OTf was 2.1 kcal mol^{-1} lower than for **1**·6OTf, most likely due to less hindered anion migration in and out of the cavity through the larger portals in the scaffold.

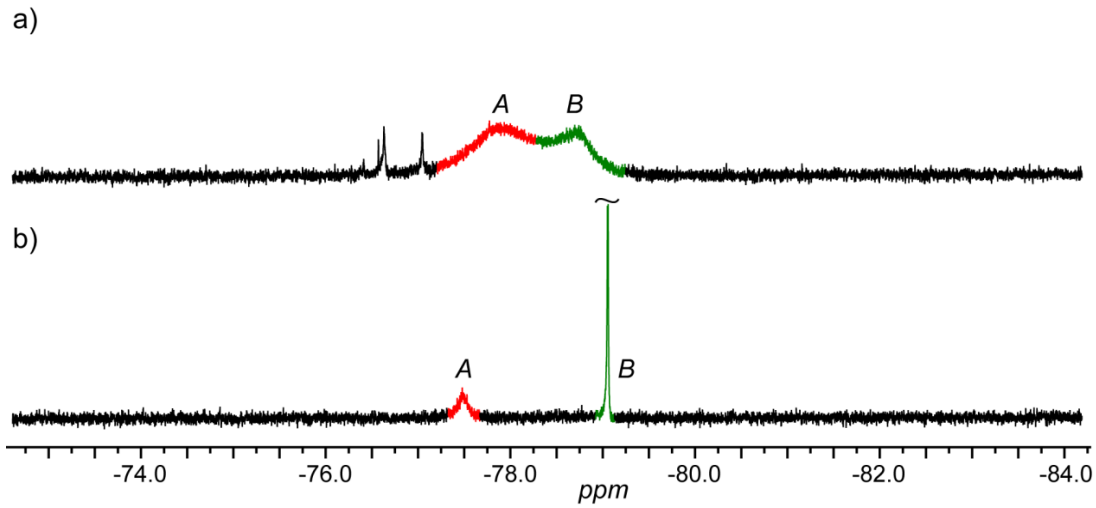

Figure 4.12. ^{19}F NMR spectra (376 MHz, $C_2D_2Cl_4$, 298 K) for a) *Δ*-**2**·6OTf and b) *Δ*-**1**·6OTf. Green singlet (*B*) corresponds to encapsulated OTf^- and red singlet (*A*) is for free OTf^-.

The effect the larger portals have on the stability of the Ir capsule, given that the Ir-nitrile interaction has been demonstrated to be stronger with the ppz ligands but the anion encapsulation weaker, was investigated next.

The stability of **2**·6OTf was measured, as for **1**$^{6+}$, by mixing *Λ*- and *Δ*-**2**·6OTf in equal proportions and, using ^{1}H NMR, recording the decreasing concentration of the intact homochiral assemblies with time. From a straight-line plot of *t* versus (1/[*Λ*/*Δ*-**2**·6OTf]-1/[*Λ*/*Δ*-**2**·6OTf]$_0$) the $t_{1/2}$ for **2**·6OTf was calculated as 1.9 days, less than half the value of **1**·6OTf (see section 4.5.16). The diminished stability of **2**·6OTf, relative to **1**·6OTf, is believed to be due to the larger portal size in the scaffold, leading to weaker anion binding affinities, a reduced barrier to anion exchange and a more rapid flux of anions in and out of the cavity. Hydrogen bonding and potentially other weak intermolecular interactions between the encapsulated OTf^- anions and the tcb and ppy ligands have been postulated key in stabilising the assembly of **1**$^{6+}$. In the case of **2**$^{6+}$, these interactions are still present but with a conformational and chemical change in the scaffold – exchange of the pyridyl groups for pyrazole – the interactions are potentially weaker. The combination of weaker interactions between the OTf^- anions and the scaffold and the less sterically hindered barrier to anion exchange, both of which destabilise the assembly, appear to outweigh the enthalpic gains of the enhanced Ir-

nitrile bond strength for the $[Ir(ppz)_2]^+$ motif. As a result capsule **2**·6OTf has been demonstrated to be less stable than capsule **1**·6OTf.

4.3.9 Photophysical Properties

The $[Ir(ppy)_2]^+$ moiety has been extensively used to construct luminescent complexes which exhibit high quantum yields. In Chapter 3, the luminescent properties of capsule **1**·6OTf were first investigated and titration with different anions was demonstrated to alter the emission intensity of the capsule. Although, both PF_6^- and BF_4^- anions were observed to qualitatively quench the emission of **1**·6OTf, no absolute values in the quantum yields of **1**·6PF_6 and **1**·6BF_4 were calculated.

Preliminary measurements have revealed that the maximum emission wavelength (λ_{max}) for **1**·6BF_4 is slightly blue shifted and **1**·6PF_6 and **1**·6ClO_4 slightly red shifted relative to **1**·6OTf (see Figure 4.13). Air equilibrated quantum yields for the 3 new salts were measured to be lower than the yields observed for **1**·6OTf, ranging between 0.6-1.2% (see section 4.5.17). These experimental results were in agreement with the titration experiments conducted in Chapter 3. The luminescent data for $\mathbf{1}^{6+}$ with various counter ions appears to have little correlation to the kinetic stabilitie of the capsule or the vibrational stretching frequencies of the 4 anions,[37] except for **1**·6OTf that is most stable and has the highest quantum yield. With a 100 fold excess of tcb in $C_2H_2Cl_4$, the Ir cavitand, *Δ*-[$(Ir(ppy)_2)_3$(tcb) $_3$]$(NTf_2)_3$, was demonstrated to maintain the luminescent properties of **1**·6OTf, but once again with a reduced quantum yield (Φ = 0.6%) (see section 4.5.17).

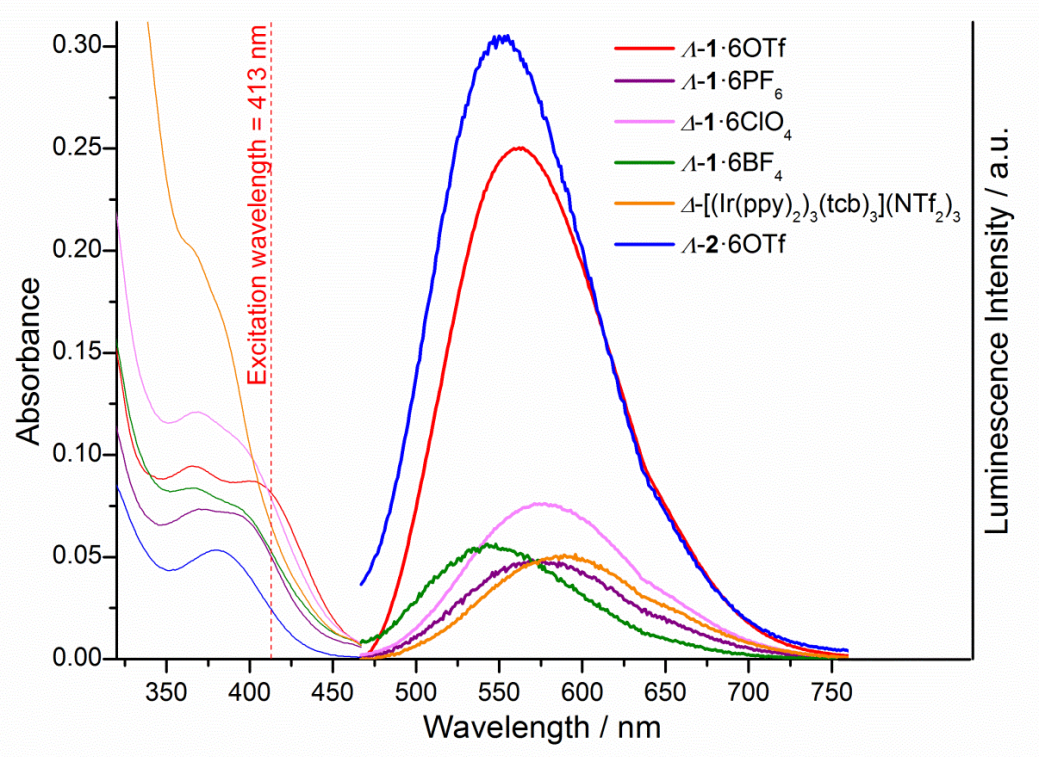

Figure 4.13. Absorption and emission (excitation 413 nm) spectra of *Λ*-**1**·6OTf (2 μM), *Λ*-**1**·6PF_6 (2 μM), *Δ*-**1**·6ClO_4 (2 μM), *Λ*-**1**·6BF_4 (2 μM), *Δ*-[$(Ir(ppy)_2)_3(tcb)_3$]$(NTf_2)_3$ (6 μM with 100 eq of tcb) and *Λ*-**2**·6OTf (1.2 μM) in $C_2H_2Cl_4$.

The inherent luminescent properties of analogous cationic Ir complexes have been demonstrated to arise primarily due to MLCT transitions. The λ_{max} and quantum yields are subsequently tuned by altering the HOMO-LUMO gap of the complexes using an array of different ligands. Substituting for a more electron withdrawing ligand often leads to a blue shift in emission. Emission spectroscopy for **2**·6OTf was consistent with the literature, with an observed λ_{max} blue shifted to 551 nm, relative to **1**·6OTf (λ_{max} = 560 nm). The blue shift is believed to be due to the greater electron withdrawing nature of the ppz ligand, with respect to the ppy. The quantum yield for **2**·6OTf was measured at 5.7%, an increase of 1.6% on the quantum yield of **1**·6OTf (see section 4.5.17). This result was surprising given that **1**·6OTf is more stable than **2**·6OTf, and as a result ligand dissociation as a means to luminescence quenching would be expected to be more profound for **2**·6OTf.

These preliminary results suggest that the quantum yields for the Ir assemblies are primarily governed by the anions and the auxiliary ligands on the Ir metal-centres and not the kinetic stabilities of the assemblies.

4.4 Conclusion

In conclusion, the vital roles played by the counterions in facilitating self-assembly and stabilising the assembled structures of $\mathbf{1}^{6+}$ have been explored. The stability of $\mathbf{1}^{6+}$ was demonstrated to be particularly sensitive to different counterions with measured stability half-lives ranging from 4.5 days (for $\mathbf{1}\cdot 6OTf$) to 5 mins (for $\mathbf{1}\cdot 6BF_4$). Irrespective of the counterions, a large reduction in the ligand exchange rate (up to 1.4×10^4 fold) was still observed when comparing capsule $\mathbf{1}^{6+}$ to similar mononuclear complexes. Modelled electrostatic potential energy surfaces were used to explain the observed differences in the stability of $\mathbf{1}^{6+}$ when OTf^-, PF_6^-, ClO_4^- or BF_4^- were used as counterions. These small non-coordinating anions were shown to form complimentary templates that mediate the self-assembly of $\mathbf{1}^{6+}$, however, using a bulkier NTf_2^- anion led to the formation of a unique Ir metallocavitand. The metallocavitand maintained the photoluminescent properties associated with the corresponding capsules but was observed to be far less stable, most likely due to the reduced number of metal-ligand interactions and counteranion binding in the structure. Exchanging the ppy concomitant ligands on the Ir metal centres for ppz increased the rate of anion migration in and out of the capsule's cavity, destabilising the assembly as a consequence. The luminescence quantum yields were however enhanced indicating that the irradiative quenching associated with these Ir capsules is not directly proportional to their kinetic stabilities.

4.5 Experimental Section

4.5.1 General Experimental Procedure

Unless stated otherwise, all reagents and solvents were purchased from commercial sources and used without further purification. *rac*-[$(Ir(ppy)_2Cl)_2$],[38] *rac*-[$(Ir(ppz)_2Cl)_2$][39] and 1,3,5-tricyanobenzene (tcb)[40] were prepared according to the literature procedures.

4.5.2 Synthesis

4.5.2.1 Synthesis of *Λ/Δ*-[$(Ir(ppy)_2)_6(tcb)_4$](OTf)$_6$ (*Λ/Δ*-**1**·6OTf)

Experimental procedure for the synthesis of *Λ*- and *Δ*-[$(Ir(ppy)_2)_6(tcb)_4$](OTf)$_6$ (*Λ/Δ*-**1**·6OTf) is discribed in section 3.5.2.5.

4.5.2.2 Synthesis of *Λ/Δ*-[$(Ir(ppy)_2)_6(tcb)_4$](BF_4)$_6$ (*Λ/Δ*-**1**·6BF_4)

Experimental procedure for the synthesis of *Λ*-[$(Ir(ppy)_2)_6(tcb)_4$](BF_4)$_6$ (*Λ*-**1**·6BF_4) is discribed in section 3.5.2.7.

Starting from *Δ*-[$Ir(ppy)_2Cl)_2$] (8.9 mg, 0.008 mmol), the *Δ*-enantiomer was synthesised following the same procedure as for *Λ*-**1**·6BF_4. Yellow solid obtained (3.3 mg, 29%). Characterisation was identical to *Λ*-**1**·6BF_4.

4.5.2.3 Synthesis of *Λ*/*Δ*-[(Ir(ppy)$_2$)$_6$(tcb)$_4$](PF$_6$)$_6$ (*Λ*/*Δ*-**1**·6PF$_6$)

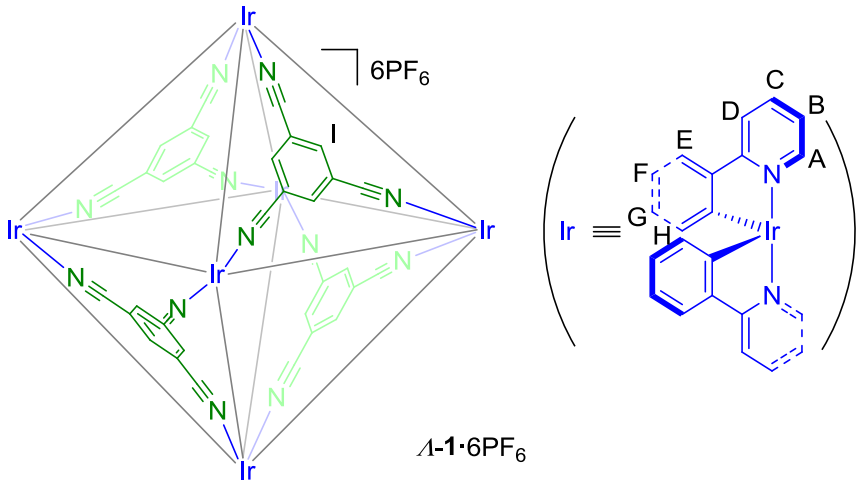

To *Λ*-[(Ir(ppy)$_2$Cl)$_2$] (21.0 mg, 0.020 mmol) was added AgPF$_6$ (9.9 mg, 0.040 mmol) in THF (5 mL) and the mixture stirred at RT in a darkened flask for 2 h. The orange solution was filtered through celite and concentrated under pressure. The crude product was dissolved in $C_2H_4Cl_2$ (1 mL), tcb (4.0 mg, 0.026 mmol) charged and the solution stirred for 4 h at RT. The resulting precipitate was filtered off and washed with a minimal amount of $C_2H_4Cl_2$ and Et_2O to give *Λ*-**1**·6PF$_6$ as a yellow solid (9.4 mg, 32%). ^{1}H NMR (400 MHz, $C_2D_2Cl_4$): 9.22 (12H, d, J = 5.7 Hz, H$_A$), 8.19 (12H, m, H$_C$), 8.17 (12H, s, H$_I$), 7.97 (12H, d, J = 7.9 Hz, H$_D$), 7.74 (12H, m, H$_B$), 7.55 (12H, d, J = 8.3 Hz, H$_E$), 6.95 (12H, m, H$_F$), 6.81 (12H, m, H$_G$), 6.16 (12H, d, J = 7.1 Hz, H$_H$); ^{19}F NMR (376 MHz, $C_2Cl_4D_2$): -69.37 (1.8F, d, J_{FP} = 715 Hz, 0.3PF$_6^-$), -70.05 (27.0F, d, J_{FP} = 714 Hz, 4.5PF$_6^-$), -72.39 (7.2F, d, J_{FP} = 707 Hz, 1.2PF$_6^-$); nESI *m*/*z*: 2098.3 [*Λ*-**1**·4PF$_6$]$^{2+}$.

Starting from *Δ*-[Ir(ppy)$_2$Cl)$_2$] (8.5 mg, 0.008 mmol), the *Δ*-enantiomer was synthesised following the same procedure as for *Λ*-**1**·6PF$_6$ above. Yellow solid obtained (9.6 mg, 81%). Characterisation was identical to *Λ*-**1**·6PF$_6$.

4.5.2.4 Synthesis of *Λ*/*Δ*-[(Ir(ppy)$_2$)$_6$(tcb)$_4$](ClO$_4$)$_6$ (*Λ*/*Δ*-**1**·6ClO$_4$)

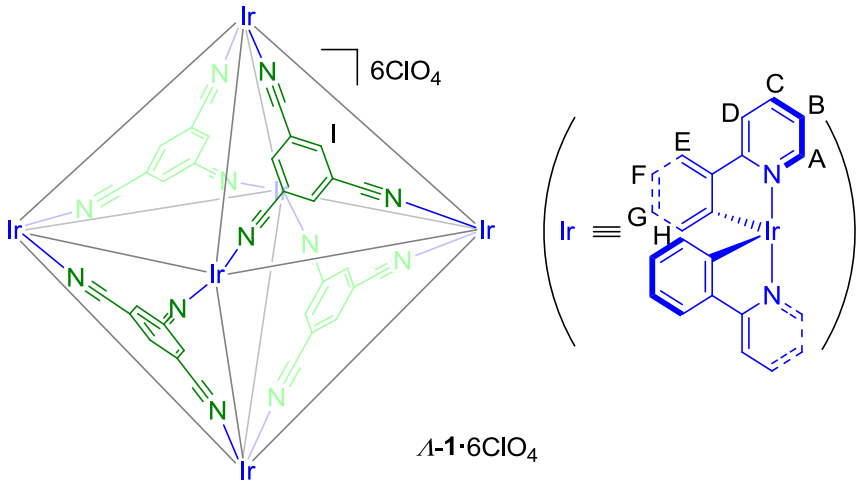

The synthesis of *Λ*-**1**·6ClO$_4$ followed a similar experimental procedure to *Λ*-**1**·6PF$_6$, starting with *Λ*-[Ir(ppy)$_2$Cl)$_2$] (16.7 mg, 0.016 mmol) and using AgClO$_4$ (6.4 mg, 0.032 mmol) instead of AgPF$_6$. Yellow solid obtained (13.6 mg, 62%). ^{1}H NMR (500 MHz, $C_2D_2Cl_4$): 9.35 (12H, d, J = 5.5 Hz, H$_A$), 8.19 (12H, m, H$_C$), 8.09 (12H, s, H$_I$), 7.94 (24H, m, H$_{B+D}$), 7.56 (12H, d, J = 8.0 Hz, H$_E$), 6.96 (12H, m, H$_F$), 6.84 (12H, m, H$_G$), 6.17 (12H, d, J = 7.4 Hz, H$_H$); nESI *m/z*: 2007.2 [*Λ*-**1**·4ClO$_4$]$^{2+}$. Anal. Calculated for $C_{168}H_{108}Cl_6Ir_6N_{24}O_{24}$: C, 47.90; H, 2.58; N, 7.98%. Found: C, 47.75; H, 2.47; N, 7.93%.

Starting from *Δ*-[Ir(ppy)$_2$Cl)$_2$] (16.5 mg, 0.015 mmol), the *Δ*-enantiomer was synthesised following the same procedure as for *Λ*-**1**·6ClO$_4$. Yellow solid obtained (18.6mg, 86%). Characterisation was identical to *Λ*-**1**·6ClO$_4$.

4.5.2.5 Synthesis of [Ir(ppy)$_2$(NCC$_6$H$_4$F)$_2$](X) where X = OTf$^-$, PF$_6^-$, ClO$_4^-$ and BF$_4^-$

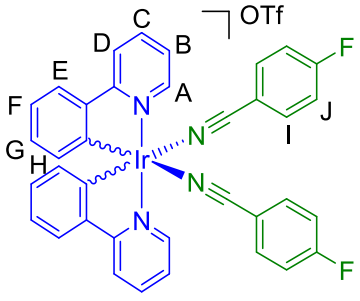

[(Ir(ppy)$_2$Cl)$_2$] (63.6 mg, 0.059 mmol) and AgOTf (30.5 mg, 0.118 mmol) were dissolved in $C_2H_4Cl_2$ (30 mL). The solution was stirred at room temperature in a darkened flask for 2 h. The mixture was filtered through celite and washed with $C_2H_4Cl_2$. The filtrate was concentrated (~4 mL) and 4-fluorobenzonitrile (NCC_6H_4F) (28.6 mg, 0.236 mmol) was charged. After 1 h at RT, the solution was concentrated to 0.5 mL and the product was precipitated out of solution with Et_2O. The resultant yellow solid was filtered and washed with Et_2O to yield [Ir(ppy)$_2$(NCC_6H_4F)$_2$]OTf (39.6 mg, 37%). ^{1}H NMR (400 MHz, $C_2D_2Cl_4$ + 10 eq NCC_6H_4F): 9.06(2H, d, J = 5.4 Hz, H_A), 8.03 (4H, m, H_{C+D}), 7.75-7.58 (m, H_{E+I} + $H_{NCC_6H_4F}$), 7.50 (2H, m, H_B), 7.26-7.14 (m, H_J + $H_{NCC_6H_4F}$), 7.03 (2H, m, H_F), 6.89 (2H, m, H_G), 6.19 (2H, d, J = 7.6Hz, H_H); ^{19}F NMR (376 MHz, $C_2D_2Cl_4$ + 10 eq NCC_6H_4F): -77.41 (18F, s, OTf^-), -96.98 (2F, s, $NCC_6H_4F_{bound}$), -101.60 (s, $NCC_6H_4F_{free}$).

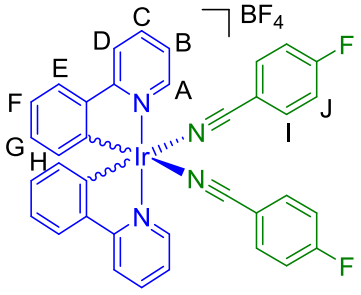

[Ir(ppy)$_2$(NCC_6H_4F)$_2$]BF_4

[(Ir(ppy)$_2$Cl)$_2$] (23.2 mg, 0.022 mmol) and $AgBF_4$ (8.6 mg, 0.044 mmol) were dissolved in THF (10 mL). The solution was stirred at RT in a darkened flask for 2 h. The mixture was filtered through celite and washed with THF. The filtrate was concentrated and redissolved in $C_2H_4Cl_2$ (3 mL). NCC_6H_4F (10.6 mg, 0.088 mmol) was charged and the solution was stirred at room temperature for 1 h. The solution was concentrated to ~0.5 mL and the product was precipitated out of solution with Et_2O. The resultant yellow solid was filtered and washed with Et_2O to yield [Ir(ppy)$_2$(NCC_6H_4F)$_2$]BF_4 (22.0 mg, 61%). ^{1}H NMR (400 MHz, $C_2D_2Cl_4$ + 10 eq FC_6H_4CN): 9.09 (2H, d, J = 5.7 Hz, H_A), 8.05 (4H, m, H_{C+D}), 7.76-7.63 (m, H_{E+I} + $H_{NCC_6H_4F}$), 7.52 (2H, m, H_B), 7.26-7.15 (m, H_J + $H_{NCC_6H_4F}$), 7.06 (2H, m, H_F), 6.93 (2H, m, H_G), 6.22 (2H, d, J = 7.5Hz, H_H); ^{19}F NMR (376 MHz, $C_2D_2Cl_4$ + 10 eq NCC_6H_4F): -97.12 (2F, s, $NCC_6H_4F_{bound}$), -101.15 (s, $NCC_6H_4F_{free}$), -151.60 (24F, s, BF_4^-).

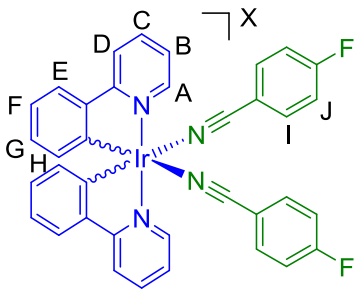

$[Ir(ppy)_2(NCC_6H_4F)_2]X$
(where X = PF_6^- or ClO_4^-)

$[Ir(ppy)_2(NCC_6H_4F)_2]PF_6$ and $[Ir(ppy)_2(NCC_6H_4F)_2]ClO_4$ were synthesised starting from $[(Ir(ppy)_2Cl)_2]$ and AgX (where X = PF_6^- and ClO_4^-, respectively) following an analogous procedure to $[Ir(ppy)_2(NCC_6H_4F)_2]BF_4$ above.

Starting from *rac*-$[Ir(ppy)_2Cl)_2]$ (60.1 mg, 0.056 mmol), $[Ir(ppy)_2(NCC_6H_4F)_2]PF_6$ was synthesised as a yellow solid (29.6 mg, 30% yield). ^{1}H NMR (400 MHz, $C_2D_2Cl_4$ + 10 eq NCC_6H_4F): 9.07 (2H, d, J = 5.7 Hz, H_A), 8.02 (4H, m, H_{C+D}), 7.76-7.61 (m, H_{E+I} + $H_{NCC_6H_4F}$), 7.49 (2H, m, H_B), 7.25-7.12 (m, H_J + $H_{NCC_6H_4F}$), 7.03 (2H, m, H_F), 6.88 (2H, m, H_G), 6.20 (2H, d, J = 7.6Hz, H_H); ^{19}F NMR (376 MHz, $C_2D_2Cl_4$ + 10 eq NCC_6H_4F): -71.94 (6F, d, J_{FP} = 713.8 Hz, PF_6^-), -97.28 (2F, s, $NCC_6H_4F_{bound}$), -101.60 (s, $NCC_6H_4F_{free}$).

Starting from *rac*-$[Ir(ppy)_2Cl)_2]$ (60.5 mg, 0.056 mmol), $[Ir(ppy)_2(NCC_6H_4F)_2]ClO_4$ was synthesised as a yellow solid (4.9 mg, 5% yield). ^{1}H NMR (400 MHz, $C_2D_2Cl_4$ + 10 eq NCC_6H_4F): 9.06 (2H, d, J = 5.6 Hz, H_A), 8.06 (4H, m, H_{C+D}), 7.73-7.62 (m, H_{E+I} + $H_{NCC_6H_4F}$), 7.48 (2H, m, H_B), 7.25-7.14 (m, H_J + $H_{NCC_6H_4F}$), 7.03 (2H, m, H_F), 6.88 (2H, m, H_G), 6.19 (2H, d, J = 7.6Hz, H_H); ^{19}F NMR (376 MHz, $C_2D_2Cl_4$ + 10 eq NCC_6H_4F): -97.25 (2F, s, $NCC_6H_4F_{bound}$), -101.59 (s, $NCC_6H_4F_{free}$).

4.5.2.6 Synthesis of PyH·PF_6, PyH·ClO_4 and PyH·BF_4

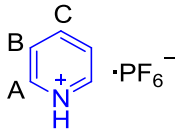

PyH·PF_6

Pyridinium chloride (0.167 g, 1.44 mmol) and $AgPF_6$ (0.364 g, 2.88 mmol) were mixed in $C_2H_4Cl_2$ and stirred for 2 h in a darkened flask at RT. A white precipitate was filtered off using celite and washed with a generous amount of $C_2H_4Cl_2$. The filtrate was concentrated under vacuum to give a white solid (3.7 mg, 1.4%). The poor yield was due to the poor solubility of PyH·PF_6 in organic solvents with the majority being filtered off with AgCl. ^{1}H NMR (400 MHz, acetone-d_6+D_2O): 6.15 (2H, d, J = 6.0 Hz, H_A), 5.96 (1H, m, H_C), 5.44 (2H, m, H_C); ^{19}F NMR (376 MHz, $C_2D_2Cl_4$): -74.60 (6F, d, J_{FP} = 708.7 Hz, PF_6^-).

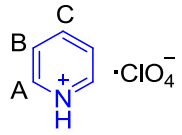

PyH·ClO_4

PyH·ClO_4 was synthesised following the literature procedure by O. Kolodyazhnaya *et al.*.[41] ^{1}H NMR (400 MHz, $C_2D_2Cl_4$): 8.83 (2H, d, J = 4.8 Hz, H_A), 8.60 (1H, m, H_C), 8.08 (2H, m, H_C).

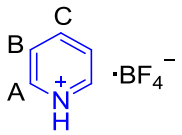

PyH·BF_4

PyH·BF_4 was synthesised following a similar procedure to that for PyH·ClO_4. To a cooled (0 °C) pyridine (7.54 g, 0.095 mol), water (85 mL) solution was charged a 10% HBF_4 (8.36 g, 0.095 mol) acid solution in water (85 mL). The solution was stirred for 1 h at 0 °C, before being concentrated to ~5 mL on the rotary evaporator. A precipitate was isolated and washed with water, methanol and diethyl ether to give a white crystalline product (2.21 g, 14%). ^{1}H NMR (400 MHz, $C_2D_2Cl_4$): 8.81 (2H, d, J = 5.2 Hz,

H_A), 8.58 (1H, m, H_C), 8.05 (2H, m, H_C). ^{19}F NMR (376 MHz, $C_2D_2Cl_4$): -149.80 (4F, d, J_{BF} = 19.9 Hz, BF_4^-).

4.5.2.7 Synthesis of *Λ*-[(Ir(ppy)$_2$)$_3$(tcb)$_3$](NTf$_2$)$_3$

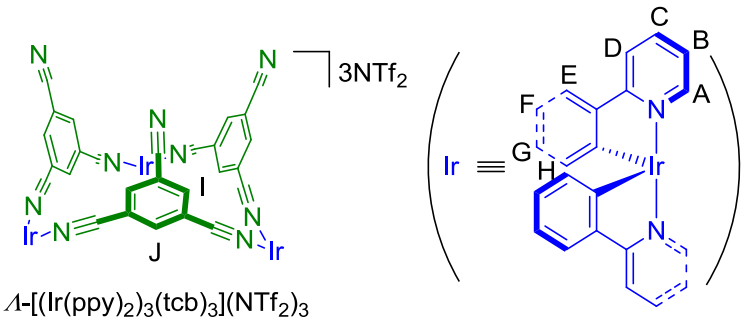

To *Λ*-[(Ir(ppy)$_2$Cl)$_2$] (11.1mg, 0.010 mmol) in THF (5 mL) was added $AgNTf_2$ (8.0 mg, 0.020 mmol) and the solution stirred at RT in a darkened flask for 2 h. The formed AgCl was filtered off through celite and the filtrate concentrated under pressure on the rotary evaporator. The crude intermediate, [Ir(ppy)$_2$THF$_2$]NTf$_2$, was re-dissolved in $C_2H_4Cl_2$ (1 mL), tcb charged (3.2 mg, 0.010 mmol) and the solution stirred for 4 h at RT. The homogeneous mixture was concentrated under pressure and with slow diffusion of ether an orange precipitate isolated (13.0 mg, 66%). ^{1}H NMR (500 MHz, $C_2D_2Cl_4$): (see Figure 4.9b). Excess tcb (1.0 mg, 0.006 mmol) was charged to the NMR solution in $C_2D_2Cl_4$ and the ^{1}H NMR re-run. ^{1}H NMR (500 MHz, $C_2D_2Cl_4$): 9.19 (6H, d, J = 5.7 Hz, H_A), 8.92 (3H, m, H_J), 8.18 (3H, s, $H_{free\text{-}tcb}$), 8.14 (6H, d, J_4 = 1.5 Hz, H_I), 7.94 (12H, m, H_{C+D}), 7.64 (6H, d, J = 7.1 Hz, H_E), 7.43 (6H, m, H_B), 7.04 (6H, m, H_F), 6.89 (6H, m, H_G), 6.15 (12H, d, J = 7.0 Hz, H_H); ^{19}F NMR (376 MHz, $C_2D_2Cl_4$): -78.49 (36F, s, NTf_2^-); nESI *m/z*: 1120.1 *Λ*-[(Ir(ppy)$_2$)$_3$(tcb)$_3$](NTf$_2$)$^{2+}$, 2522.2 *Λ*-[(Ir(ppy)$_2$)$_3$(tcb)$_3$](NTf$_2$)$_2^{1+}$.

4.5.2.8 Synthesis of *Δ*-[(Ir(ppy)$_2$)$_3$(dcmb)$_3$](NTf$_2$)$_3$

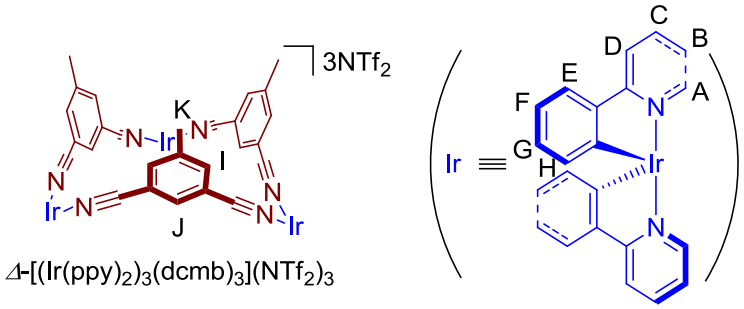

Δ-[(Ir(ppy)$_2$)$_3$(dcmb)$_3$](NTf$_2$)$_3$

To *Δ*-[(Ir(ppy)$_2$Cl)$_2$] (10.5mg, 0.0098 mmol) in THF (5 mL) was added AgNTf (7.6 mg, 0.0196 mmol) and the solution stirred at RT in a darkened flask for 2 h. The formed AgCl was filtered off through celite and the filtrate concentrated under pressure on the rotary evaporator. The crude intermediate was redissolved in $C_2H_4Cl_2$ (1 mL), tcb charged (2.8 mg, 0.0196 mmol) and the solution stirred for 4 h at RT. Precipitation occurred with ether diffusion into the reaction mixture from which a pale yellow solid was isolated (6.3 mg, 41%). ^{1}H NMR (500 MHz, $C_2D_2Cl_4$): two species present in a 1.8:1 ratio (see Figure 4.33).

4.5.2.9 Synthesis of *Λ*-[(Ir(ppy)$_2$)$_6$(tceb)$_4$](X)$_6$ where X = NTf$_2^-$ and OTf$^-$

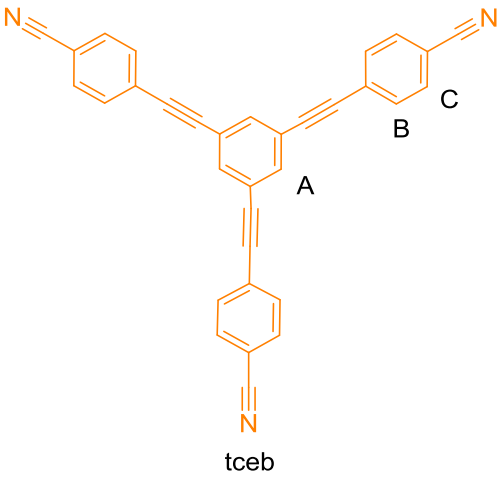

To N_2 purged THF (10 mL) was added Pd(AcO)$_2$ (22.8 mg, 0.10 mmol) and PPh_3 (52.5 mg, 0.20 mmol). The red reaction mixture was purged a further 3 times and CuI (58.1 mg, 0.2 mmol), 1,3,5-triethylbenzene (100 mg, 0.67 mmol) and 4-bromobenzonitrile

(364 mg, 2.0 mmol) were consecutively added. Et_3N (5 mL) was charged and the reaction stirred at RT for 1 h and 50 °C for 3 days. After 3 days, the reaction was cooled to RT, the solvent removed under vacuum and the organics extracted with DCM from an aqueous solution of NH_4Cl. The organic washes were combined, washed with bring, dried with $MgSO_4$ and concentrated on the rotary evaporator. The product was purified using flash silica column chromatography (hexane/DCM) to yield a white precipitate (50.1 mg, 17% yield). ^{1}H NMR (400 MHz, $CDCl_3$): 7.72 (3H, s, H_A), 7.67 (6H, d, J = 8.4 Hz, H_C), 7.62 (6H, d, J = 8.4 Hz, H_B). The ^{1}H NMR signals were an exact match to those reported by Y. Yamaguchi *et al.* for the same compound.[42]

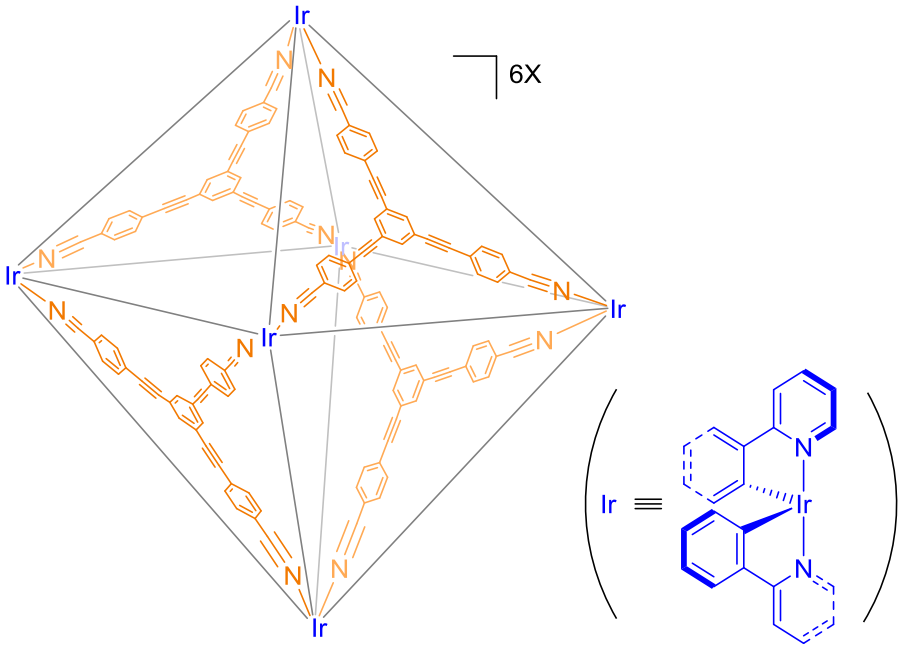

Λ-[(Ir(ppy)$_2$)$_6$(tceb)$_4$](X)$_6$
(where X = NTf_2^- or OTf^-)

To a previously synthesised stock solution of *Λ*-[Ir(ppy)$_2$THF$_2$]NTf_2 (3.9 mg, 0.0042 mmol) in $C_2D_2Cl_4$ was titrated tceb (1.27 mg, 0.0028 mmol) in $C_2D_2Cl_4$. No single species was observed to form by ^{1}H NMR or nESI-MS analysis.

Synthesis of *Λ*-[(Ir(ppy)$_2$)$_6$(tceb)$_4$](OTf)$_6$ was attempted in an analogous manner. To a stock solution of *Λ*-[(Ir(ppy)$_2$OTf)$_2$] (1.2 mg, 0.00092 mmol) in $C_2D_2Cl_4$ was titrated tceb (0.56 mg, 0.00123 mmol) in $C_2D_2Cl_4$. Once again, no single species was observed to form by ^{1}H NMR or nESI-MS analysis.

4.5.2.10 Synthesis of $[Ir(ppz)_2(NCC_6H_4F)_2](OTf)$

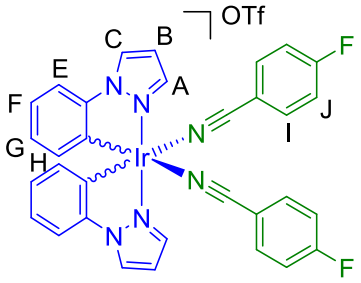

$[Ir(ppz)_2(NCC_6H_4F)_2]OTf$

$[Ir(ppz)_2(NCC_6H_4F)_2]OTf$ was synthesised starting from $[(Ir(ppz)_2Cl)_2]$ and AgOTf following an analogous procedure to $[Ir(ppy)_2(NCC_6H_4F)_2]OTf$ above.

Starting from *rac*-$[Ir(ppz)_2Cl)_2]$ (60.8 mg, 0.059 mmol), $[Ir(ppz)_2(NCC_6H_4F)_2]OTf$ was synthesised as a yellow solid (51.3 mg, 49.9% yield). ^1H NMR (400 MHz, $C_2D_2Cl_4$ + 10 eq NCC_6H_4F): 8.23 (2H, d, J = 2.5 Hz, H_A), 8.11 (2H, d, J = 1.9 Hz, H_C), 7.70 (m, H_I + $H_{NCC_6H_4F}$), 7.23 (m, H_{E+J} + $H_{NCC_6H_4F}$), 7.15 (2H, m, H_F), 6.89 (2H, m, H_B), 6.83 (2H, m, H_G), 6.16 (2H, d, J = 7.6 Hz, H_H); ^{19}F NMR (376 MHz, $C_2D_2Cl_4$ + 10 eq NCC_6H_4F): -77.38 (18F, s, OTf^-), -96.60 (2F, s, $NCC_6H_4F_{bound}$), -101.59 (s, $NCC_6H_4F_{free}$).

4.5.2.11 Synthesis of *Λ*/*Δ*-$[(Ir(ppz)_2)_6(tcb)_4](OTf)_6$ (*Λ*/*Δ*-2·6OTf)

Synthesis of intermediate [(*Λ*/*Δ*-$Ir(ppz)_2$)(L/D-serine)] follows a similar procedure to that of R. Urban *et. Al.*[43]

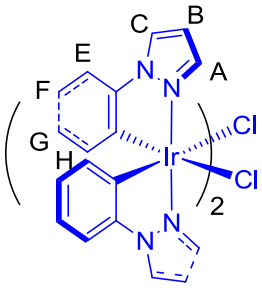

Λ-$[(Ir(ppz)_2Cl)_2]$

A mixture of *rac*-$[(Ir(ppz)_2Cl)_2]$ (138 mg, 0.134 mmol), L-serine (35.2 mg, 0.335 mmol) and NaOMe (18.1 mg, 0.335 mmol) in CH_3OH (15 mL) were stirred at 40 °C for 16 h. The solvent was removed under vacuum and the crude product purified using

solubility differences between the two diastereoisomers in CH_2Cl_2. On washing the crude mixture with CH_2Cl_2, *Λ*-[Ir(ppz)$_2$(L-serine)] was isolated from the filtrate due to its significantly greater solubility in the solvent than *Δ*-[Ir(ppz)$_2$(L-serine)]. The isolated *Λ*-[Ir(ppz)$_2$(L-serine)] was dissolved in CH_3OH (5 mL) and to this was added 1M HCl solution (1 mL). The formed precipitate was filtered off, washed with CH_3OH and Et_2O and air dried to give a white solid (16.4 mg, 24% (starting from *rac*-[(Ir(ppz)$_2$Cl)$_2$]). ^{1}H NMR (500 MHz, $C_2D_2Cl_4$): 8.16 (4H, d, J = 2.7 Hz, H_A), 7.82 (4H, d, J = 1.6 Hz, H_C), 7.17 (4H, d, J = 7.8 Hz, H_E), 6.90 (4H, m, H_F), 6.71 (4H, m, H_B), 6.62 (4H, m, H_G), 6.04 (4H, d, J = 7.6 Hz, H_H).

Δ-[(Ir(ppz)$_2$Cl)$_2$] was synthesised following the same procedure as above starting with *rac*-[(Ir(ppz)$_2$Cl)$_2$] (50.1 mg, 0.049 mmol), D-serine (12.9 mg, 0.123 mmol) and NaOMe (6.6 mg, 0.123 mmol). White solid obtained (4.1 mg, 16%). Characterisation as for *Λ*-[(Ir(ppz)$_2$Cl)$_2$].

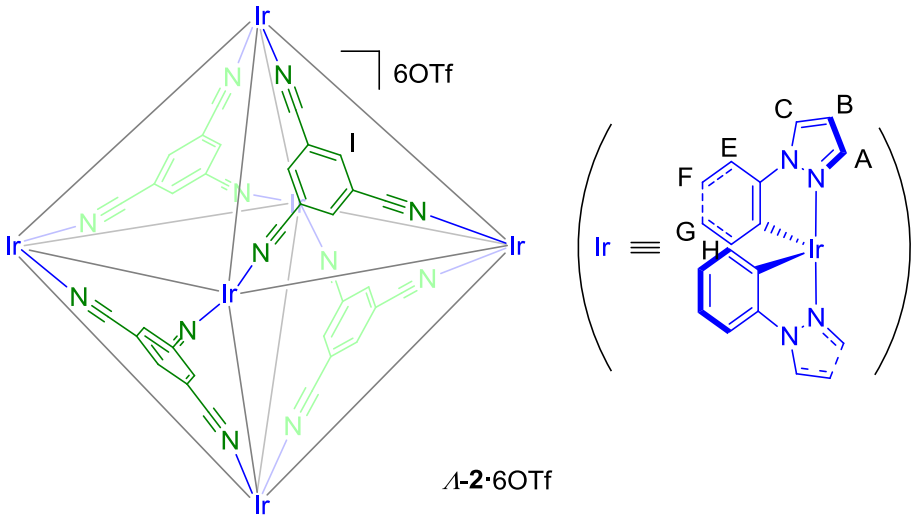

Λ-**2**·6OTf

Λ-[(Ir(ppz)$_2$)$_6$(tcb)$_4$](OTf)$_6$ (*Λ*-**2**·6OTf) was synthesised following the same procedure as for *Λ*/*Δ*-**1**·6OTf starting from *Λ*-[(Ir(ppz)$_2$Cl)$_2$] (16.2 mg, 0.0158 mmol). Using AgOTf (8.1 mg, 0.0316 mmol) and tcb (3.1 mg, 0.020 mmol), a pale yellow solid was obtained (3.8 mg, 16%). ^{1}H NMR (500 MHz, $C_2D_2Cl_4$): 8.55 (12H, d, J = 2.1 Hz, H_A), 8.44 (12H, s, H_I), 8.24 (12H, d, J = 2.7 Hz, H_C), 7.20 (12H, d, J = 8.0 Hz, H_E), 7.07 (12H, m, H_B), 6.97 (12H, m, H_F), 6.74 (12H, m, H_G), 6.17 (12H, d, J = 5.7 Hz, H_H); ^{13}C NMR (126 MHz, $C_2D_2Cl_4$): 143.0, 142.7, 141.7, 133.2, 127.1, 125.8, 124.6, 123.9, 114.2, 112.5, 111.2,

109.1; ^{19}F NMR (376 MHz, $C_2Cl_4D_2$): -78.27 (12F, bs, OTf^-); nESI *m/z*: 2040.2, *Λ*-[**2**·4OTf]$^{2+}$.

Δ-[(Ir(ppz)$_2$)$_6$(tcb)$_4$](OTf)$_6$ (*Δ*-**2**·6OTf) was synthesised using *Δ*-[(Ir(ppz)$_2$Cl)$_2$] (23.2 mg, 0.0226 mmol), AgOTf (11.6 mg, 0.0452mmol) and tcb (4.6 mg, 0.0301 mmol) in an analogous manner to *Λ*-**2**·6OTf above. A pale yellow solid was obtained (7 mg, 22%). Characterisation was identical to *Λ*-**2**·6OTf.

4.5.3 ^{1}H DOSY NMR spectra of *Λ*-1·6X

The NMR samples were only at a high enough concentration to obtain a ^{1}H DOSY NMR spectrum for *Λ*-**1**·6OTf (see section 3.5.6) and *Λ*-**1**·6BF_4 (see section 3.5.17). The ^{1}H DOSY spectrum for *Λ*-**1**·6ClO_4 was obtained by titrating excess Bu_4NClO_4 to *Λ*-**1**·6BF_4, the ^{1}H NMR spectrum was superimposable with authentic *Λ*-**1**·6ClO_4.

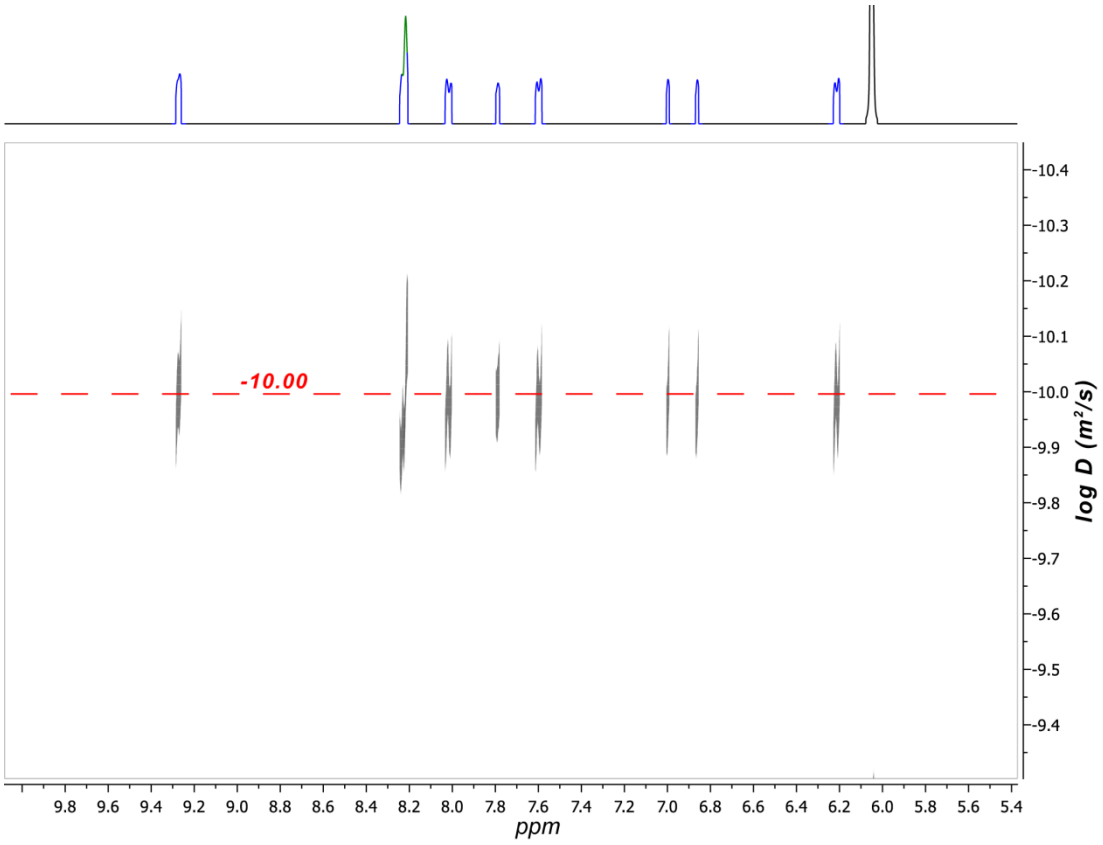

Figure 4.14. ^{1}H DOSY NMR (400 MHz, $C_2D_2Cl_4$, 298 K) spectrum of *Λ*-**1**·6PF_6. Corresponding log (*D* / m^2 s^{-1}) = -10.00.

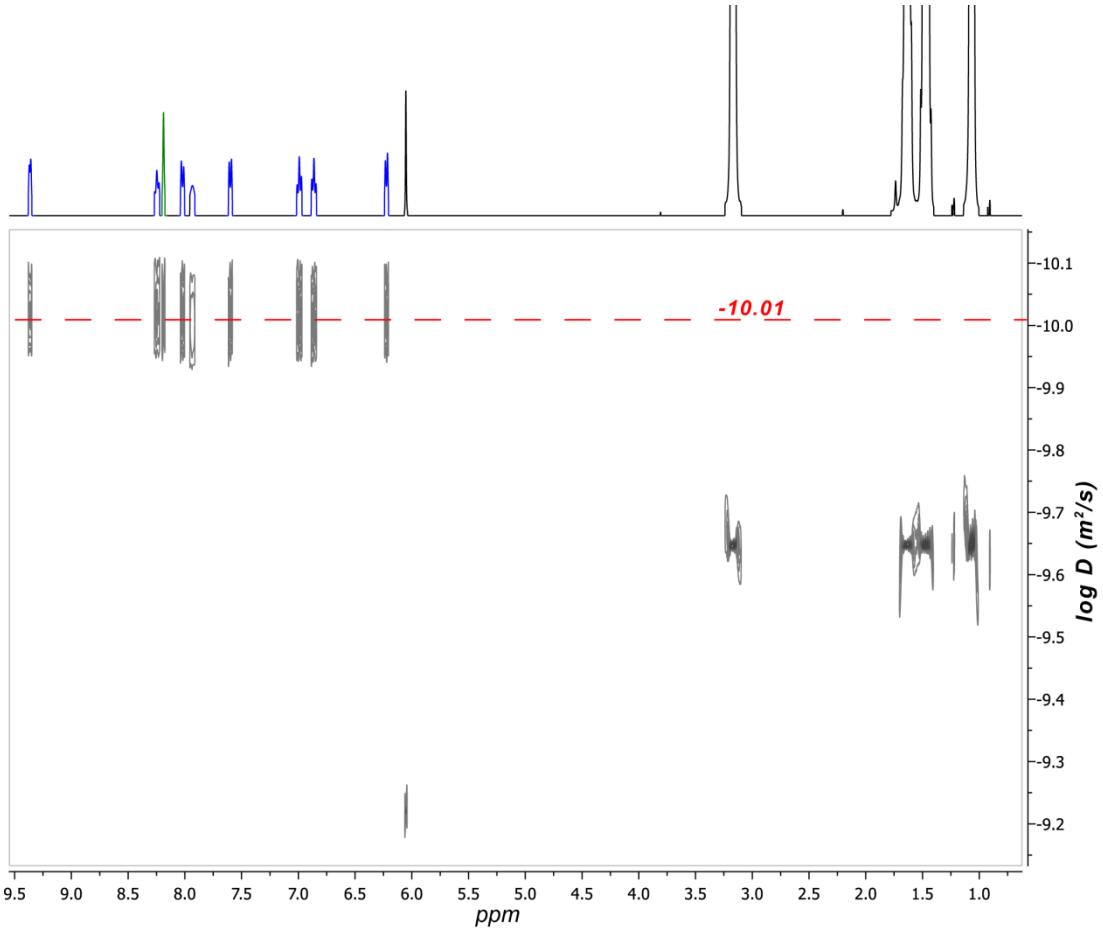

Figure 4.15. ^{1}H DOSY NMR (400 MHz, $C_2D_2Cl_4$, 298 K) spectrum of *Λ*-**1**·6ClO_4 obtained by titrating 60 eq Bu_4NClO_4 to *Λ*-**1**·6BF_4. Corresponding log (D / m^2 s^{-1}) = -10.01.

4.5.4 Mass spectra and isotopic distribution patterns for *Λ*-1·6PF_6 and *Λ*-1·6ClO_4

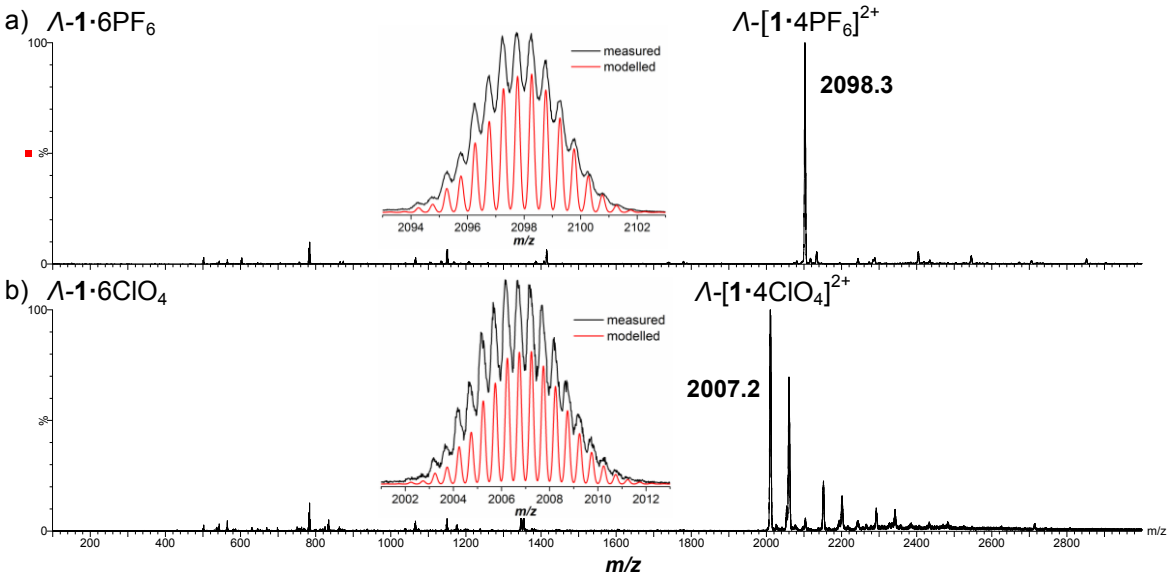

Figure 4.16. nESI mass spectra of a) *Λ*-**1**·6PF_6 and b) *Λ*-**1**·6ClO_4 with measured (black) versus modelled (red) isotopic distribution pattern for each [**1**·4X]$^{2+}$ ion (where X = PF_6^- and ClO_4^-, respectively), 50 μM in $C_2H_4Cl_2$.

4.5.5 ^{19}F DOSY and ^{19}F-^{1}H 2D HOESY NMR spectra of *Λ*-1·6PF$_6$

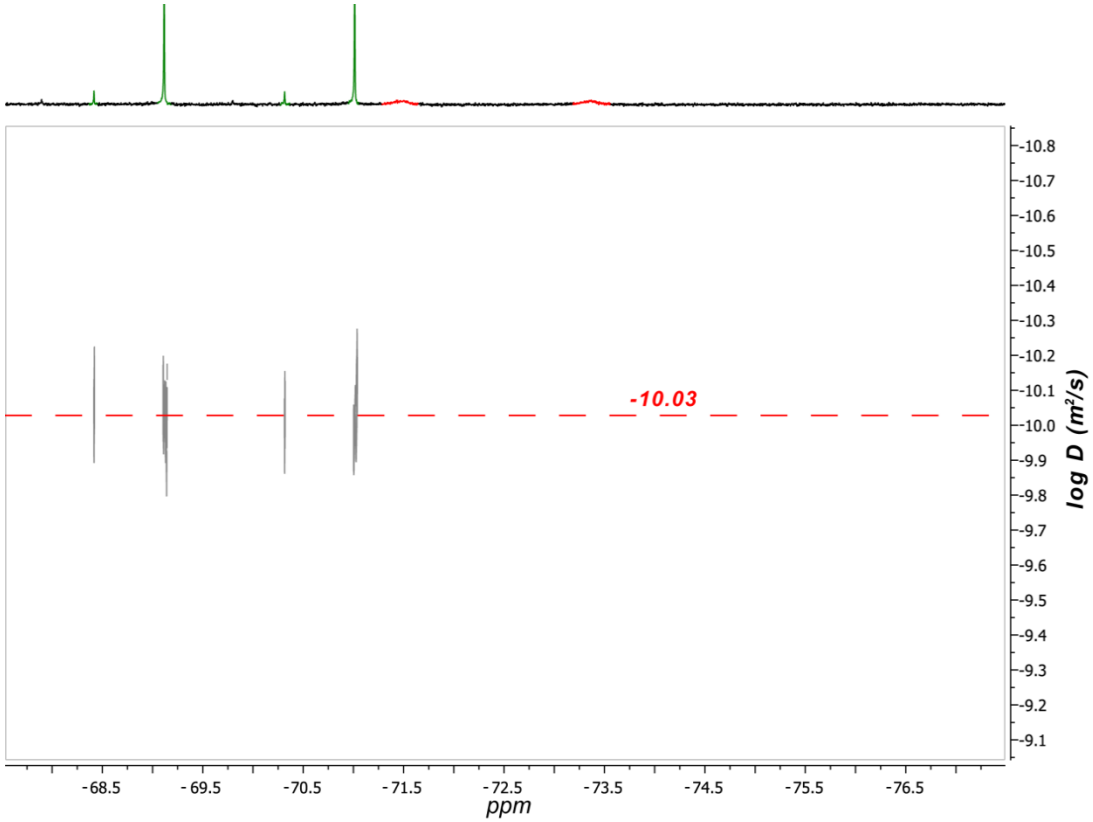

Figure 4.17. ^{19}F DOSY NMR (376 MHz, $C_2D_2Cl_4$, 298 K) spectrum of *Λ*-**1**·6PF$_6$. Corresponding log (D / m^2 s^{-1}) = -10.03.

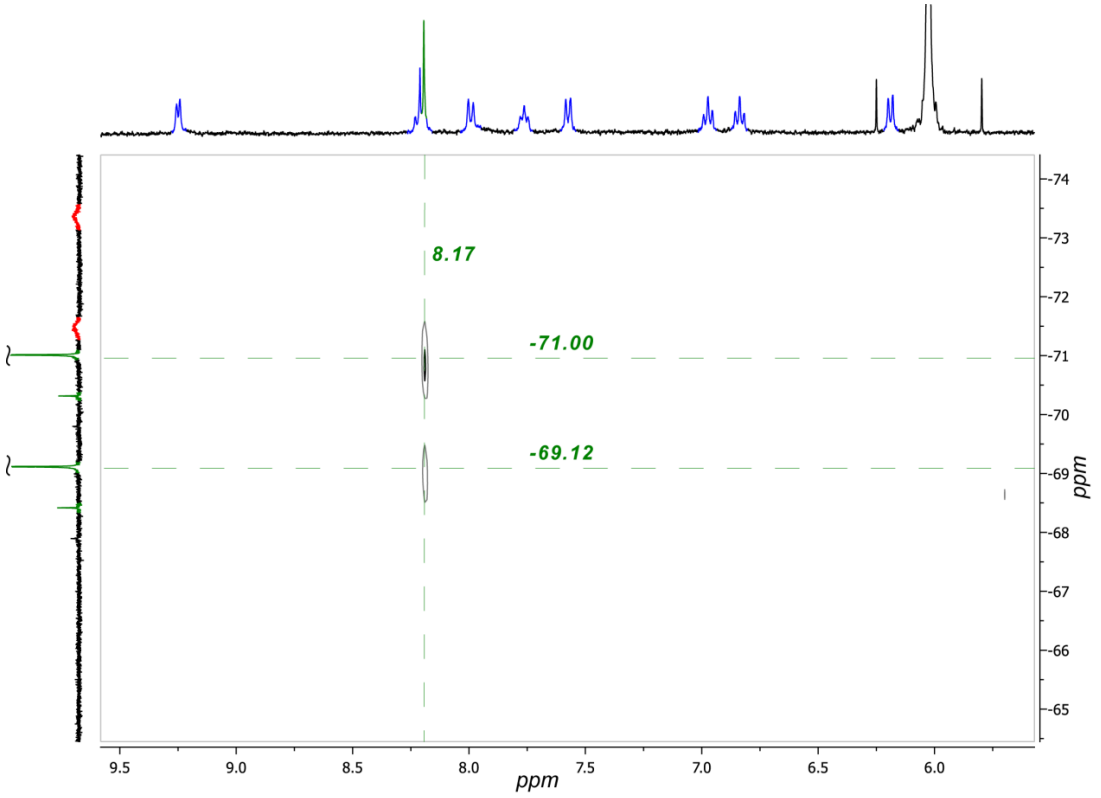

Figure 4.18. ^{19}F-^{1}H HOESY NMR (376 MHz, $C_2D_2Cl_4$, 298 K) spectrum of *Λ*-**1**·6PF_6. Cross-peak visible between split PF_6^- signal at -71.00 and -69.12 and the signal for proton H_I at 8.17.

4.5.6 Stability measurements of 1·6X (where X = OTf^-, PF_6^-, BF_4^- or ClO_4^-)

Λ-**1**·6OTf (170 μM solution in $C_2D_2Cl_4$, 0.5 mL) and *Δ*-**1**·6OTf (170 μM solution in $C_2D_2Cl_4$, 0.5 mL) were prepared in separate NMR tubes. ^{1}H NMR spectra was recorded for both samples prior and 0.5, 6, 24, 48, and 96 h post the combination of the two in a single NMR tube. Over time new peaks appeared on the ^{1}H NMR spectra. The concentration of homochiral *Λ*- and *Δ*-**1**·6OTf was monitored by relative integration of the H_I proton signal to the signal for C_2HDCl_4 (see Figure 4.5a). The experimental data of 1/[*Λ*/*Δ*-**1**·6OTf]-1/[*Λ*/*Δ*-**1**·6OTf]$_0$ was plotted against the scrambling time *t* to give a straight line with gradient = observed exchange rate constant k_{obs} (1.52 ×10^{-2} M^{-1} s^{-1}) and half-life, $t_{1/2}$ = 1/(k_{obs}×[*Λ*/*Δ*-**1**·6OTf]$_0$) (4.48 days). Stability measurements for **1**·6PF_6 (135 μM), **1**·6ClO_4 (144 μM) and **1**·6BF_4 (156 μM) were performed following the

same procedure as for **1**·6OTf, with the scrambling time measurements taken at suitable intervals relative to the stability of each system.

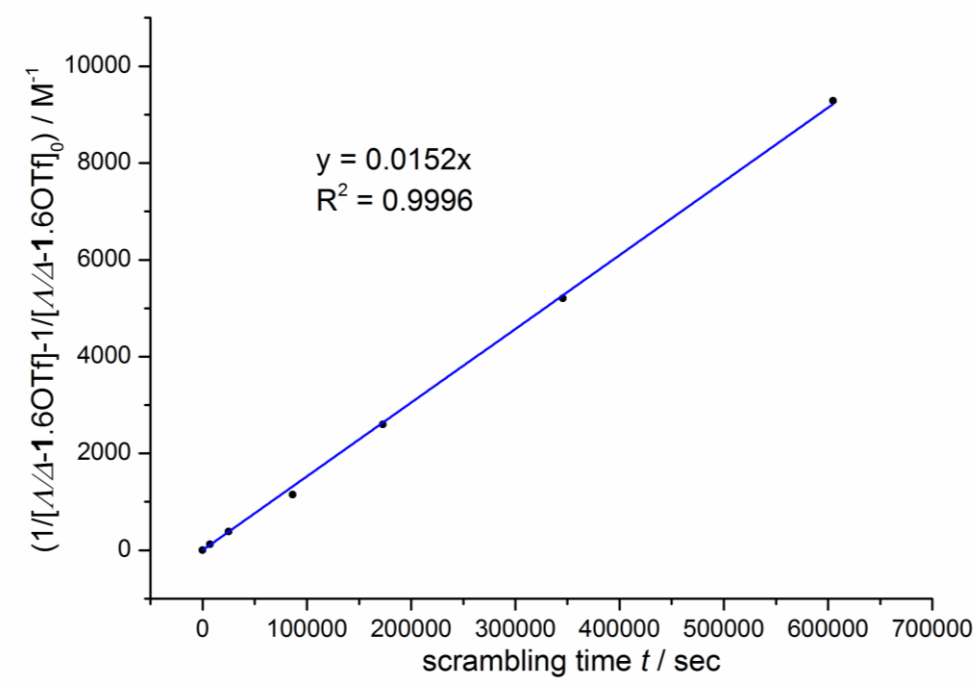

Figure 4.19. $1/[\Lambda/\Delta\text{-}\mathbf{1}\cdot 6\text{OTf}]\text{-}1/[\Lambda/\Delta\text{-}\mathbf{1}\cdot 6\text{OTf}]_0$ versus scrambling time *t*.

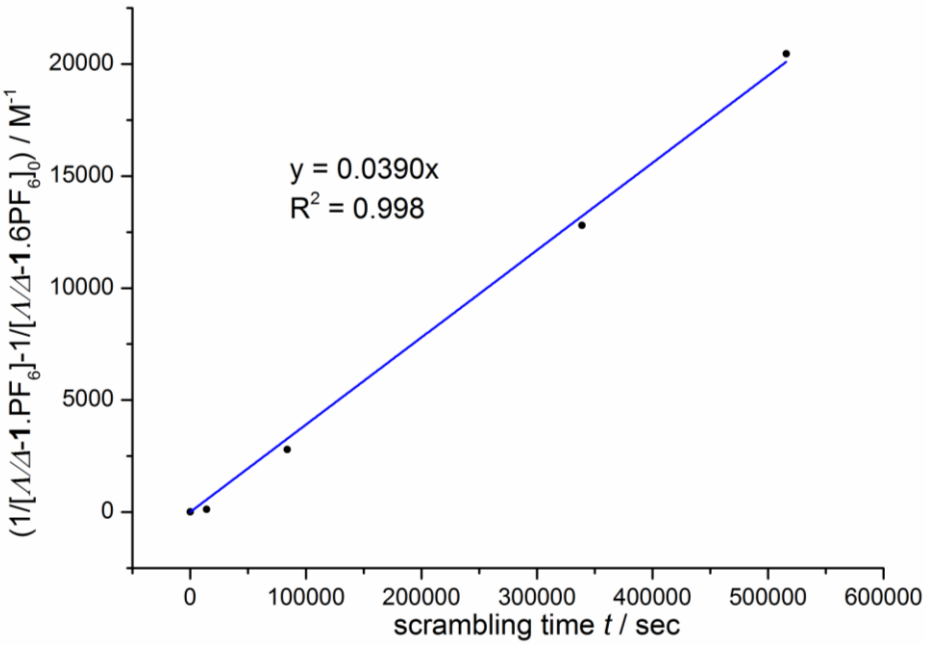

Figure 4.20. $1/[\Lambda/\Delta\text{-}\mathbf{1}\cdot 6\text{PF}_6]\text{-}1/[\Lambda/\Delta\text{-}\mathbf{1}\cdot 6\text{PF}_6]_0$ versus scrambling time *t*.

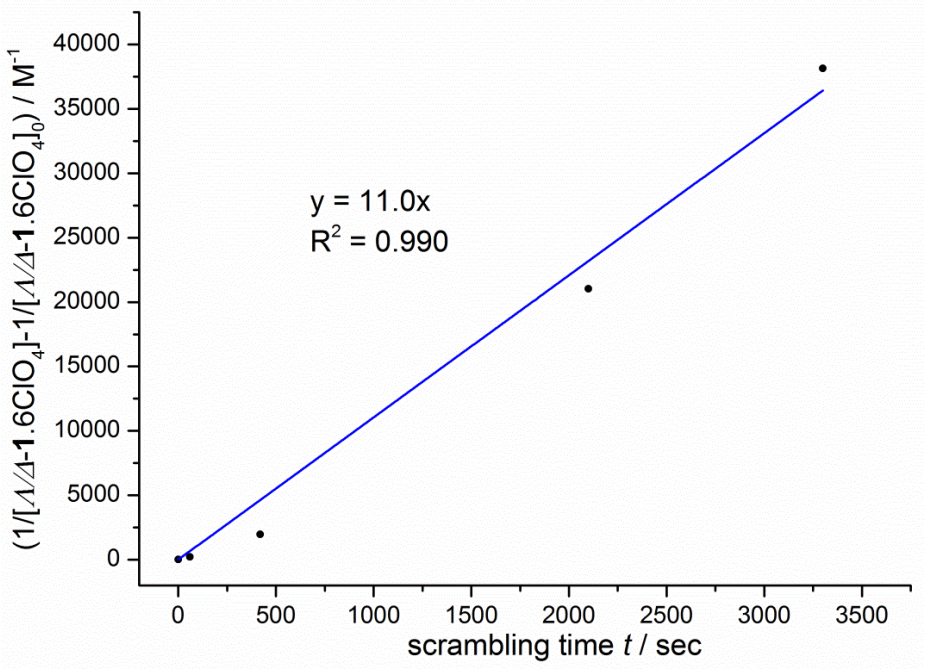

Figure 4.21. (1/[*Λ*/*Δ*-**1**·6ClO_4]-1/[*Λ*/*Δ*-**1**·6ClO_4]$_0$) versus scrambling time *t*.

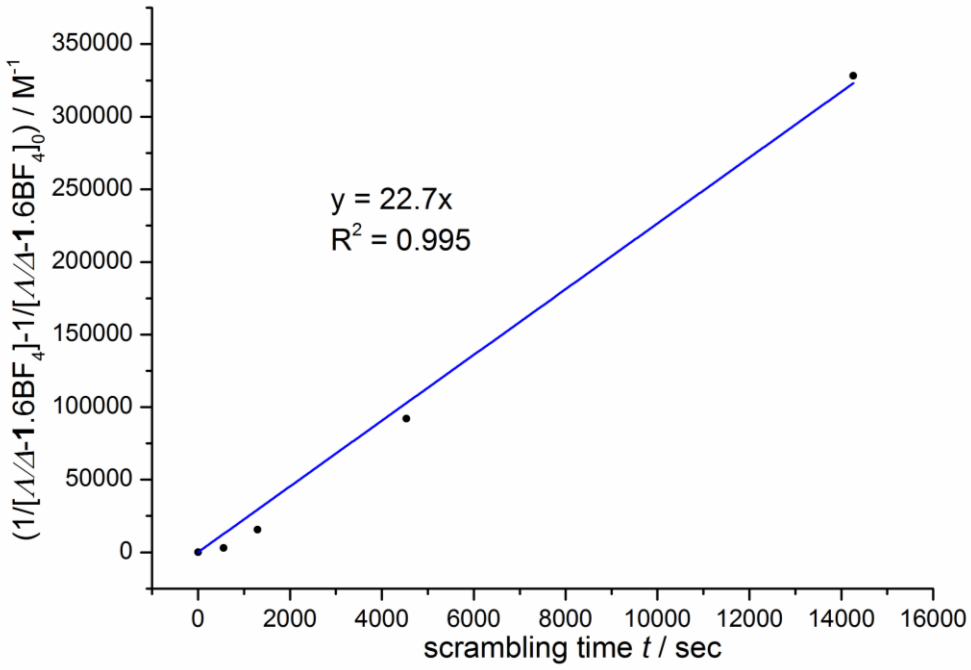

Figure 4.22. 1/[*Λ*/*Δ*-**1**·6BF_4]-1/[*Λ*/*Δ*-**1**·6BF_4]$_0$ versus scrambling time *t*.

4.5.7 Exchange Spectroscopy (2D-EXSY) investigation into Ir-nitrile bond strengths and *guest* binding within $\mathbf{1}^{6+}$

^{19}F 2D-EXSY was used to investigate the kinetics of a) NCC_6H_4F ligand exchange for $[Ir(ppy)_2(NCC_6H_4F)_2]X$ (where X = OTf^-, PF_6^-, BF_4^- and ClO_4^-), b) PF_6^- counterion exchange between the different environments of capsule *Δ*-**1**·6PF_6, c) NCC_6H_4F ligand exchange for $[Ir(ppz)_2(NCC_6H_4F)_2]OTf$ and d) OTf^- counterion exchange between the two different environments of capsule *Λ*-**2**·6OTf. All spectra were recorded on a Bruker 400 MHz NMR spectrometer at 298 K with the mixing time, τ_m, set to either 0.2, 0.4, 0.6, 0.8 or 1.0 s. Using *equation 1* shown below, where I_{AA}, I_{BB}, I_{CC} and I_{DD} are the diagonal peak intensities and I_{AB}, I_{BA}, I_{AC}, I_{CA}, I_{BD} and I_{DB} are the cross-peak intensities, r was calculated. The values for k were obtained for a) from 1/gradient of the linear plot of ln((r+1)/(r-1)) versus τ_m and for b), c) and d) using *equation 2-3*. As k is the sum of the forward, k_1, and backward, k_{-1}, pseudo-first order rate constants, which are presumed equal ($k_1 = k_{-1}$), the observed pseudo-first order rate constant, k_{obs}, was determined from *equation 4*. k_{obs} was used in the Eyring equation (*equation 5*) to determine the change in Gibbs free energy, $\Delta G^{\ddagger}$, for the exchange processes. Being first order kinetics it was also possible to obtain the $t_{1/2}$ for the exchange reaction using k_{obs} in *equation 6*.

$$r = \frac{(I_{AA} + I_{BB})}{(I_{AB} + I_{BA})} \text{ or } r = \frac{(I_{AA} + I_{BB} + I_{CC} + I_{DD})}{(I_{AC} + I_{CA} + I_{BD} + I_{DB})} \text{ used for } \Delta\text{-}\mathbf{1}\cdot 6PF_6 \qquad (1)$$

$$HG_n + G^* \underset{k_{-1}}{\overset{k_1}{\rightleftharpoons}} HG_{n-1}G^* + G \qquad (2)$$

$$k = \frac{1}{\tau_m} \times \ln\frac{r+1}{r-1} \qquad (3)$$

$$k = k_1 + k_{-1} = 2 \times k_{obs} \qquad (k_1 = k_{-1} = k_{obs}) \qquad (4)$$

$$\Delta G^{\ddagger} = -RT \ln \frac{k_{obs} h}{k_B T} \qquad (5)$$

(R = 1.9872 *cal K*$^{-1}$ *mol*$^{-1}$, k_B = 3.30 x 10^{-24} *cal K*$^{-1}$, h = 1.58 x 10^{-34} *cal s*)

$$t_{1/2} = \frac{\ln 2}{k_{obs}} \qquad (6)$$

4.5.7.1 NCC_6H_4F ligand exchange for $[Ir(ppy)_2(NCC_6H_4F)_2]X$ (where X = OTf^-, PF_6^-, BF_4^- and ClO_4^-)

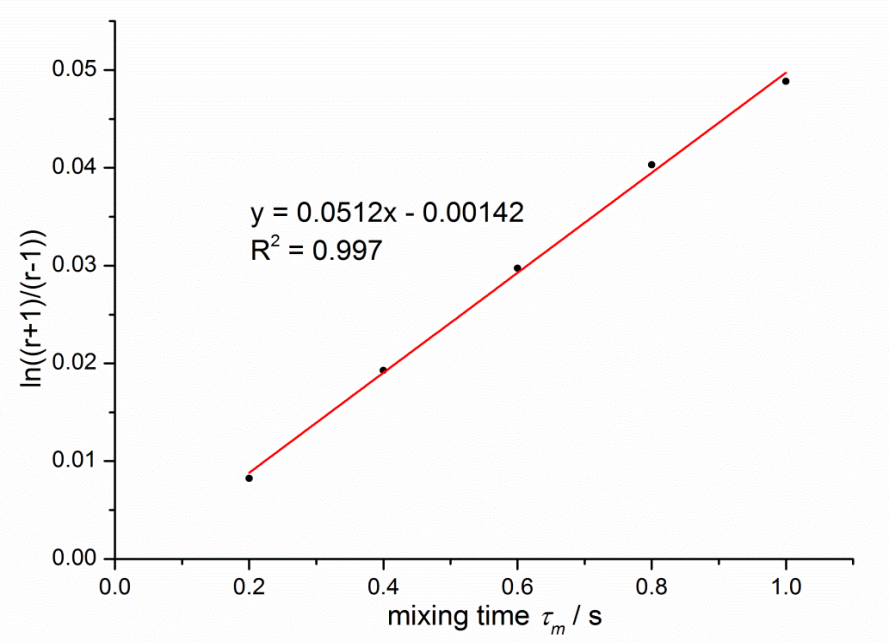

Figure 4.23. Plot of ln((r+1)/(r-1)) versus mixing time τ_m for $[Ir(ppy)_2(NCC_6H_4F)_2]OTf$ in $C_2D_2Cl_4$ with 10 eq NCC_6H_4F obtained from ^{19}F EXSY NMR measurements.

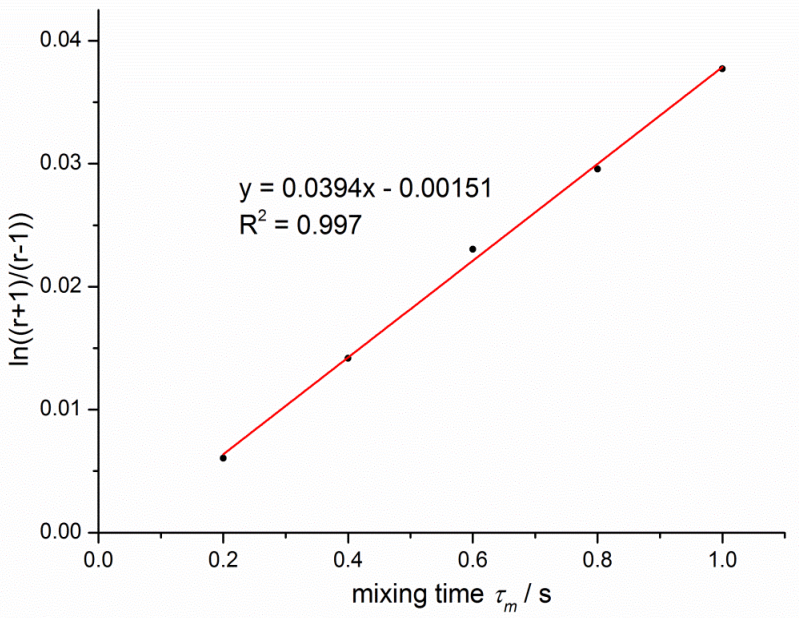

Figure 4.24. Plot of ln((r+1)/(r-1)) versus mixing time τ_m for $[Ir(ppy)_2(NCC_6H_4F)_2]PF_6$ in $C_2D_2Cl_4$ with 10 eq NCC_6H_4F obtained from ^{19}F EXSY NMR measurements.

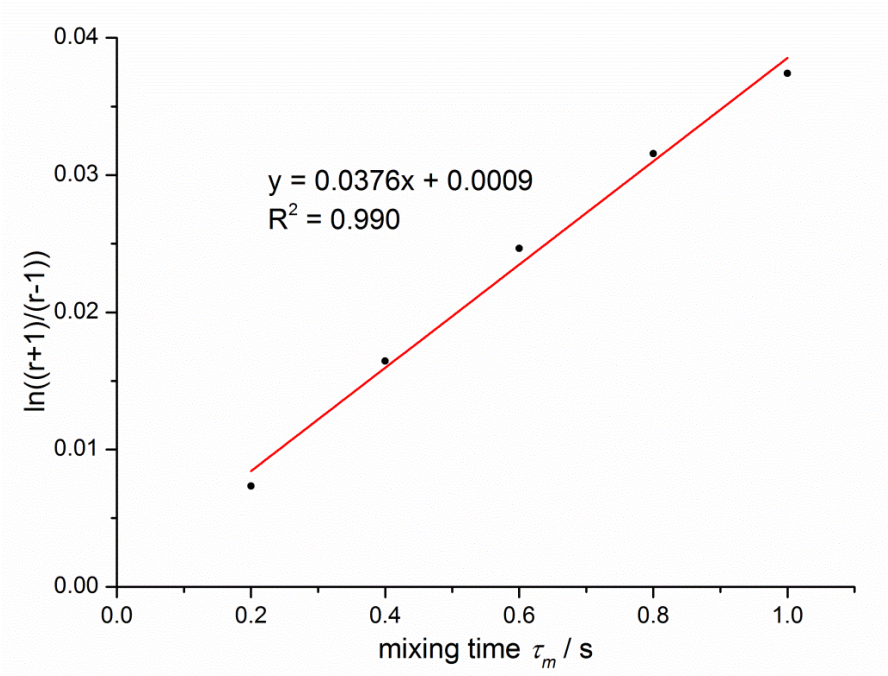

Figure 4.25. Plot of ln((r+1)/(r-1)) versus mixing time τ_m for $[Ir(ppy)_2(NCC_6H_4F)_2]ClO_4$ in $C_2D_2Cl_4$ with 10 eq NCC_6H_4F obtained from ^{19}F EXSY NMR measurements.

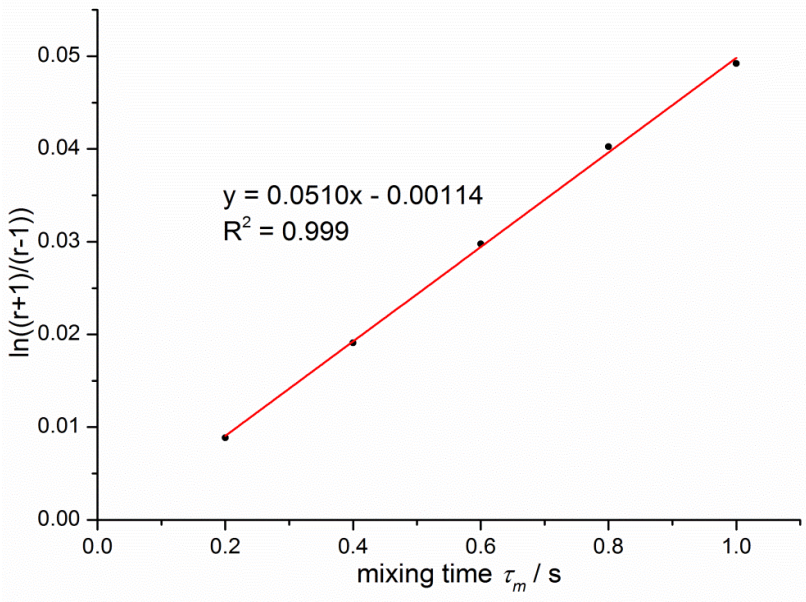

Figure 4.26. Plot of ln((r+1)/(r-1)) versus mixing time τ_m for $[Ir(ppy)_2(NCC_6H_4F)_2]BF_4$ in $C_2D_2Cl_4$ with 10 eq NCC_6H_4F obtained from ^{19}F EXSY NMR measurements.

4.5.7.2 PF_6^- counterion exchange of *Δ*-1·6PF_6

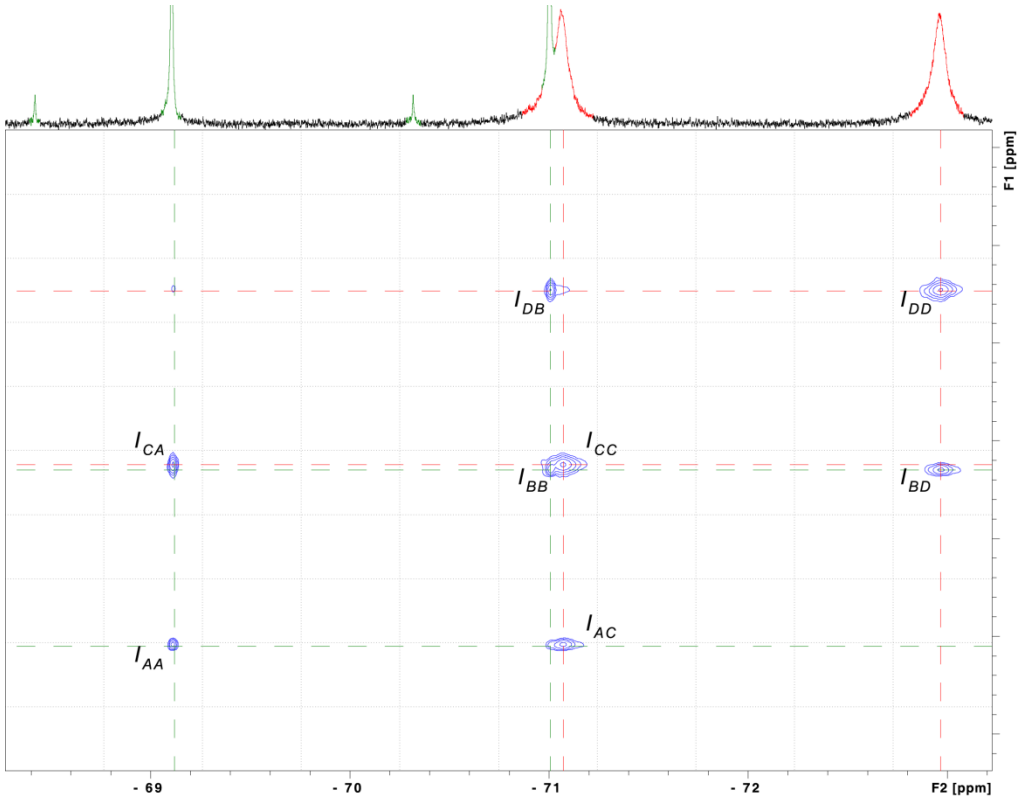

Figure 4.27. Partial ^{19}F 2D-EXSY (376 MHz, $C_2D_2Cl_4$, 298 K) spectrum of *Δ*-**1**·6PF_6 with excess Bu_4NPF_6.

	I_{AA}	I_{AC}	I_{CA}	$I_{BB} + I_{CC}$	I_{BD}	I_{DB}	I_{DD}	k_{obs} / s^{-1}	$\Delta G^{\ddagger}$ / kcal mol^{-1}
F_{PF6}	0.1100	0.3258	0.2834	1.0000	0.3220	0.3098	0.2432	0.80	17.6

Table 4.3. Kinetic parameters for PF_6^- counterion exchange for *Δ*-**1**·6PF_6 in $C_2D_2Cl_4$.

4.5.7.3 NCC_6H_4F ligand exchange for $[Ir(ppz)_2(NCC_6H_4F)_2]OTf$

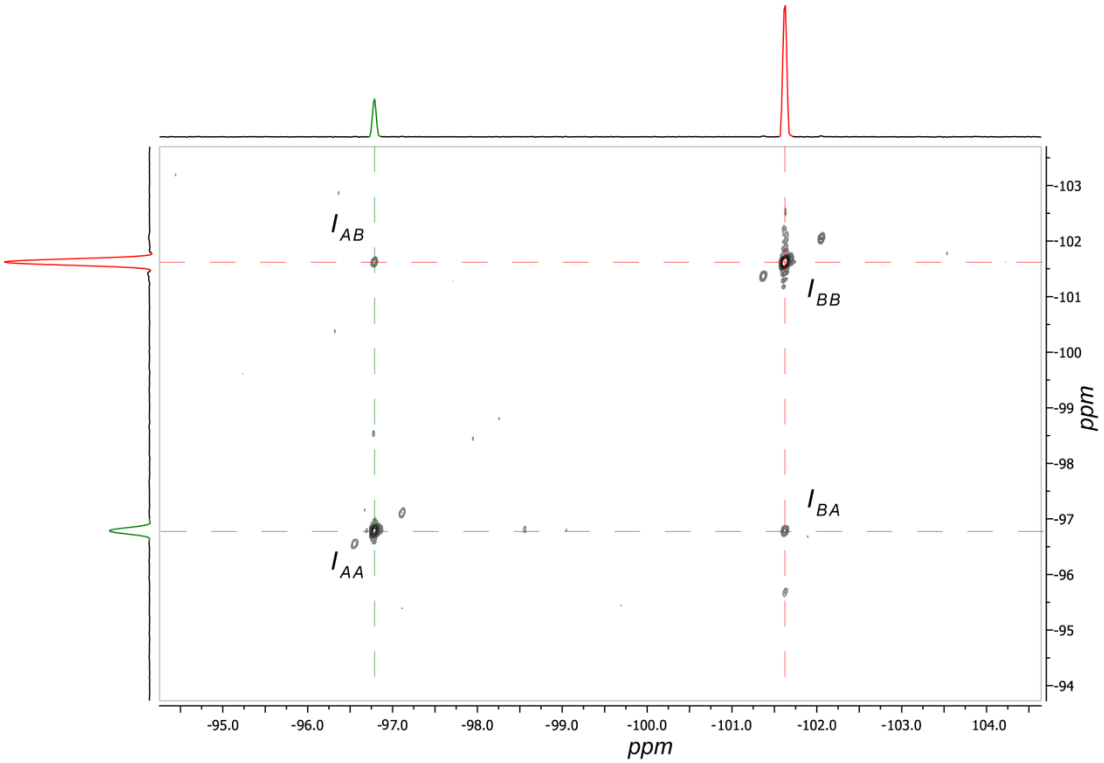

Figure 4.28. Partial ^{19}F 2D-EXSY (376 MHz, $C_2D_2Cl_4$, 298 K) spectrum of $[Ir(ppz)_2(NCC_6H_4F)_2]OTf$ with 10 eq NCC_6H_4F.

	I_{AA}	I_{AB}	I_{BA}	I_{BB}	k_{obs} / s^{-1}	$\Delta G^{\ddagger}$ / kcal mol^{-1}
$F_{NCC6H4F}$	0.2707	0.0032	0.0065	1.0000	0.0076	20.3

Table 4.4. Kinetic parameters for NCC_6H_4F ligand exchange of $[Ir(ppz)_2(NCC_6H_4F)_2]OTf$ in $C_2D_2Cl_4$ with 10 eq NCC_6H_4F.

4.5.7.4 OTf^- counterion exchange of *Λ*-**2**·6OTf

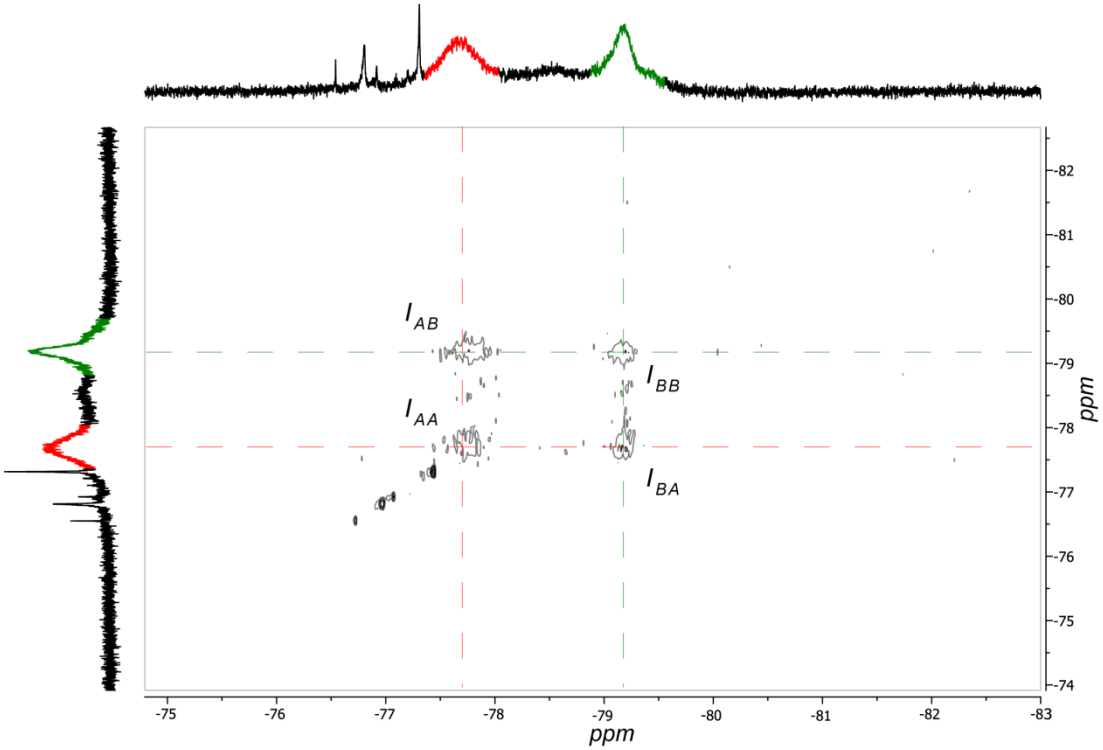

Figure 4.29. Partial ^{19}F 2D-EXSY (376 MHz, $C_2D_2Cl_4$, 273 K) spectrum of *Λ*-**2**·6OTf.

	I_{AA}	I_{AB}	I_{BA}	I_{BB}	k_{obs} / s^{-1}	$\Delta G^{\ddagger}$ / kcal mol^{-1}
F_{OTf}	0.7842	0.8070	0.6905	1.0000	1.22	15.8

Table. Kinetic parameters for OTf^- counterion exchange for *Λ*-**2**·6OTf in $C_2D_2Cl_4$.

4.5.8 ^{19}F NMR of 1·6OTf in a mixed $CD_3NO_2/C_2D_2Cl_4$ solvent system

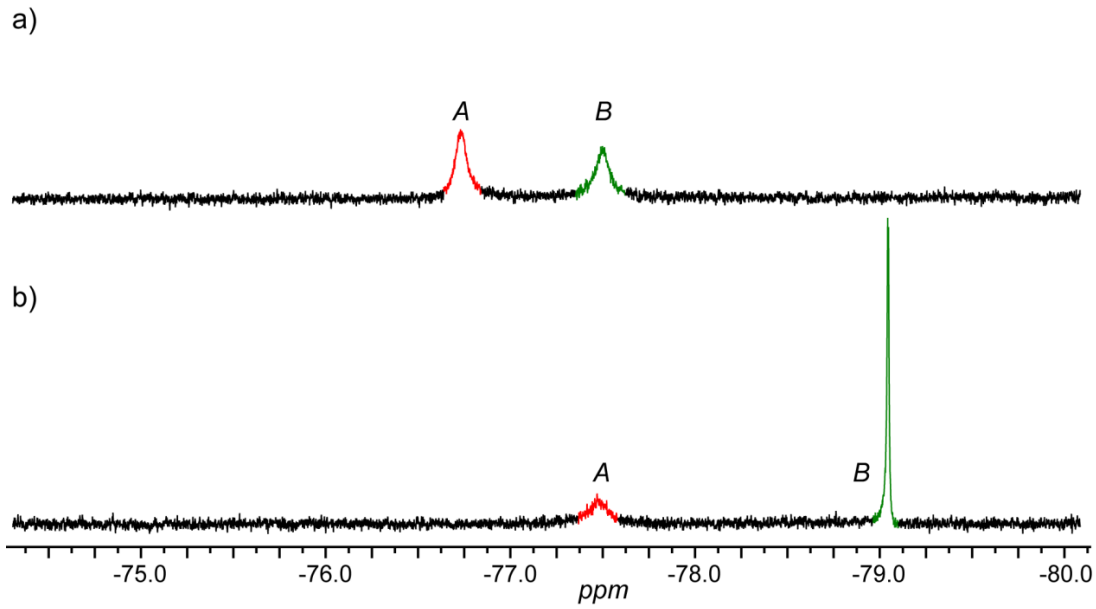

Figure 4.30. ^{19}F NMR (376 MHz, $C_2D_2Cl_4$, 298 K) spectra of *Δ*-**1**·6OTf in a) 1:2 $CD_3NO_2/C_2D_2Cl_4$ and b) neat $C_2D_2Cl_4$. Green singlet (*B*) corresponds to encapsulated OTf^- and red singlet (*A*) is for free OTf^-.

4.5.9 ^{1}H DOSY NMR spectrum of *Λ*-$[(Ir(ppy)_2)_3(tcb)_3](NTf_2)_3$

The hydrodynamic radius of *Λ*-$[(Ir(ppy)_2)_3(tcb)_3](NTf_2)_3$ in $C_2D_2Cl_4$ was determined using ^{1}H DOSY NMR spectroscopy. From the ^{1}H DOSY NMR spectrum (see Figure 4.31), the measured diffusion coefficient *D* was used in the Stokes-Einstein equation (*equation 7*) to calculate the effective hydrodynamic radius R_H.

$$R_H = \frac{k_B T}{6\pi\eta D} \qquad (7)$$

where k_B is the Boltzmann constant, *T* absolute temperature and *η* the viscosity of the solvent. The viscosity of $C_2D_2Cl_4$ not being available, that of $C_2H_2Cl_4$ (1.456 mPa.s)[44] at 298 K was used instead. The diffusion coefficient and computed Stokes-Einstein radius are listed in Table 4.5.

	log D	*D* / m^2 s^{-1}	Stokes-Einstein radius / Å
Λ-[(Ir(ppy)$_2$)$_3$(tcb)$_3$](NTf$_2$)$_3$	-9.86	1.38×10^{-10}	10.9

Table 4.5. Diffusion coefficient and computed Stokes-Einstein radius of *Λ*-[(Ir(ppy)$_2$)$_3$(tcb)$_3$](NTf$_2$)$_3$ in $C_2D_2Cl_4$ at 298 K.

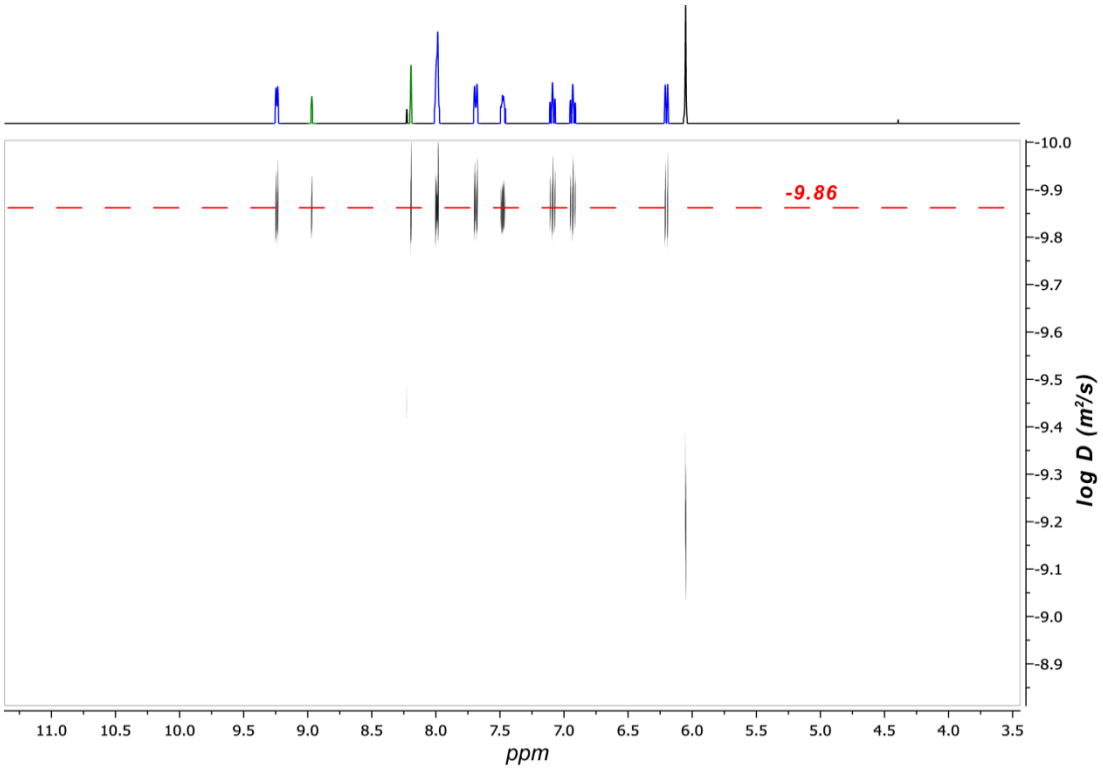

Figure 4.31. ^{1}H DOSY NMR (400 MHz, $C_2D_2Cl_4$, 298 K) spectrum of *Λ*-[(Ir(ppy)$_2$)$_3$(tcb)$_3$](NTf$_2$)$_3$ with 6 eq of tcb added. Corresponding log (*D* / m^2 s^{-1}) = -9.86.

4.5.10 Mass spectra and isotopic distribution patterns for *Λ*-[(Ir(ppy)$_2$)$_3$(tcb)$_3$](NTf$_2$)$_3$

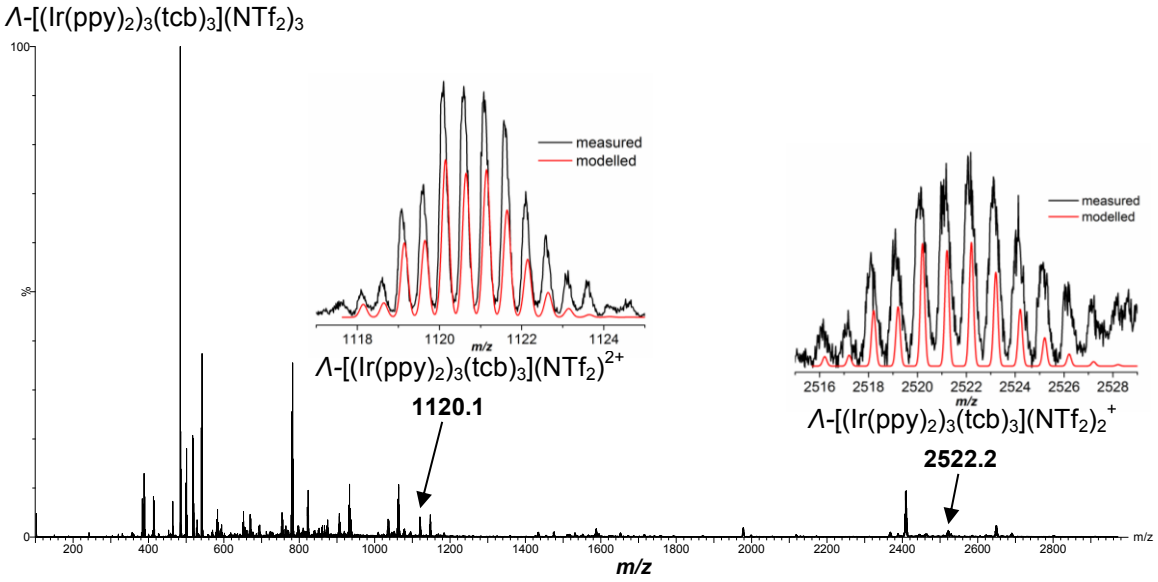

Figure 4.32. nESI mass spectra of *Λ*-[(Ir(ppy)$_2$)$_3$(tcb)$_3$](NTf$_2$)$_3$ with measured (black) versus modelled (red) isotopic distribution patterns for *Λ*-[(Ir(ppy)$_2$)$_3$(tcb)$_3$](NTf$_2$)$^{2+}$ and *Λ*-[(Ir(ppy)$_2$)$_3$(tcb)$_3$](NTf$_2$)$_2^+$ ion, 50 μM in $C_2H_4Cl_2$.

4.5.11 ^{1}H NMR spectra of *Λ*-[(Ir(ppy)$_2$)$_3$(tcb)$_3$](NTf$_2$)$_3$ and *Δ*-[(Ir(ppy)$_2$)$_3$(dcmb)$_3$](NTf$_2$)$_3$.

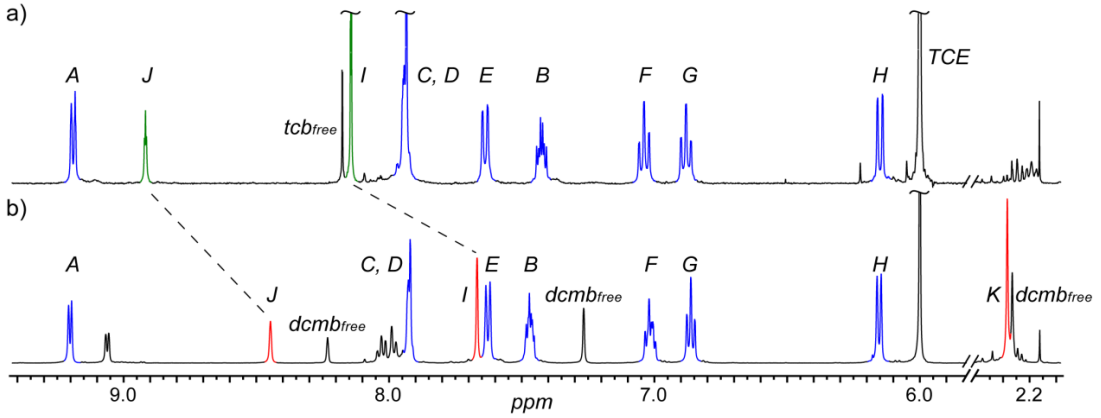

Figure 4.33. ^{1}H NMR (500 MHz, $C_2D_2Cl_4$, 298 K) spectra of a) *Δ*-[(Ir(ppy)$_2$)$_3$(tcb)$_3$](NTf$_2$)$_3$ with excess tcb and b) *Δ*-[(Ir(ppy)$_2$)$_3$(dcmb)$_3$](NTf$_2$)$_3$ as the major species. The assignments correspond to the lettering shown in section 4.5.2.7 for a) and section 4.5.2.8 for b).

4.5.12 ^{1}H and ^{1}H DOSY NMR spectra of *Λ*-2·6OTf

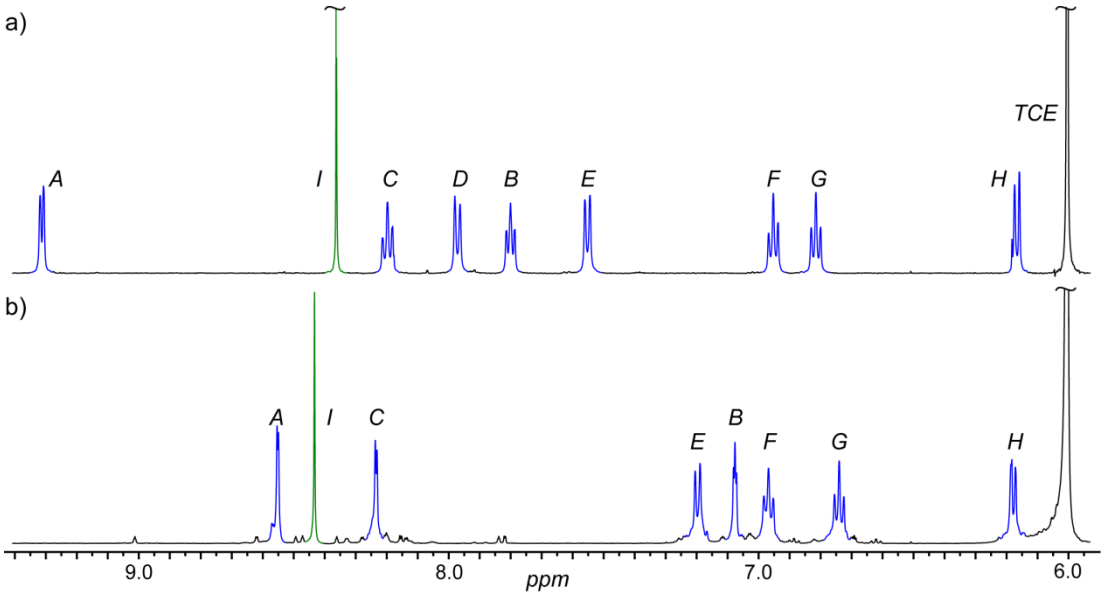

Figure 4.34. ^{1}H NMR (500 MHz, $C_2D_2Cl_4$, 298 K) spectra of a) *Λ*-**1**·6OTf and b) *Λ*-**2**·6OTf. The assignments correspond to the lettering shown in Scheme 4.1 for a) and 4.7 for b).

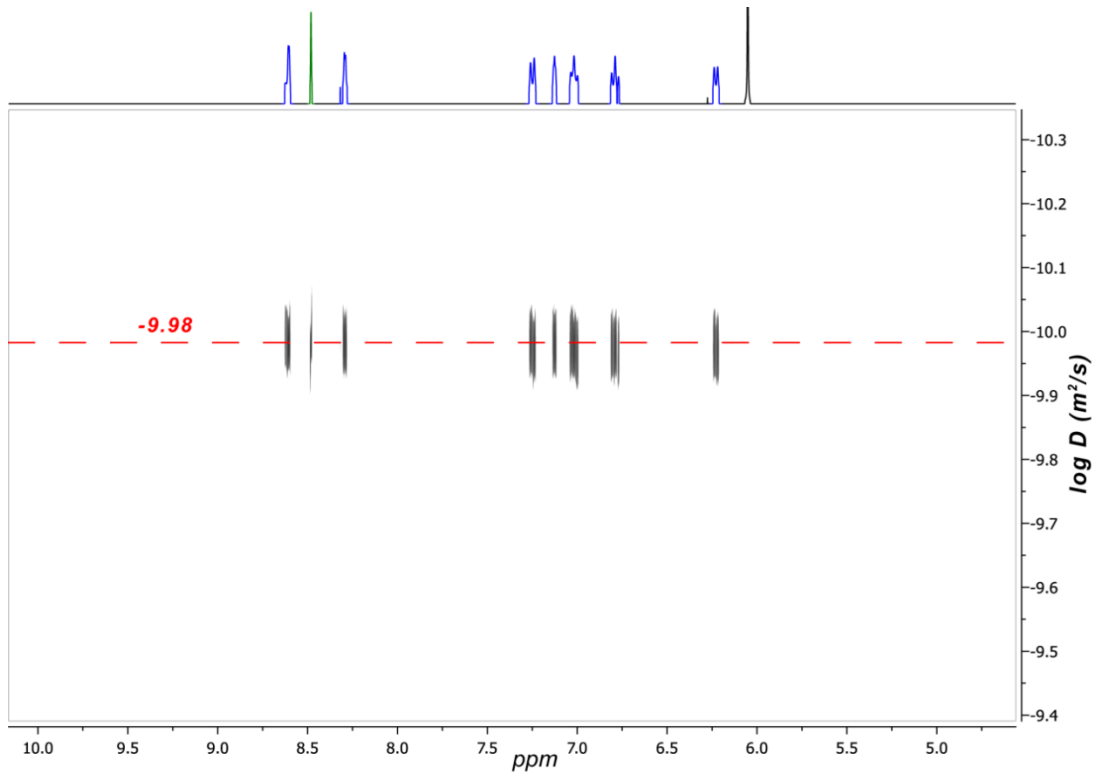

Figure 4.35. ^{1}H DOSY NMR (400 MHz, $C_2D_2Cl_4$, 298 K) spectrum of *Δ*-**2**·6OTf. Corresponding log (D / m^2 s^{-1}) = -9.98.

4.5.13 Mass spectrum and isotopic distribution patterns for 2·6OTf

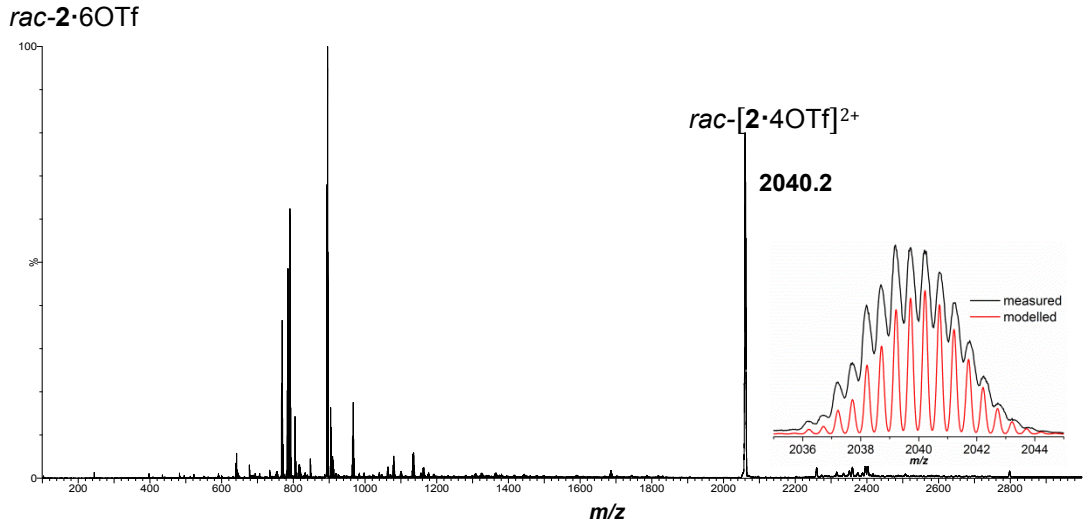

Figure 4.36. nESI mass spectra of *rac*-**2**·6OTf with measured (black) versus modelled (red) isotopic distribution pattern for the *rac*-[**2**·4OTf]$^{2+}$ ion, 50 μM in $C_2H_4Cl_2$.

4.5.14 X-ray crystal structure of *Δ*-2·6OTf

Structural data were collected at 93 K using a Rigaku Saturn diffractometer (MM007 high-flux RA/MoKa radiation, confocal optic). All data collection employed narrow frames (0.3-1.0) to obtain at least a full hemisphere of data. Intensities were corrected for Lorentz polarisation and absorption effects (multiple equivalent reflections). The structures were solved by direct methods, non-hydrogen atoms were refined anisotropically with CH protons being refined in riding geometries (SHELXTL) against F^2.

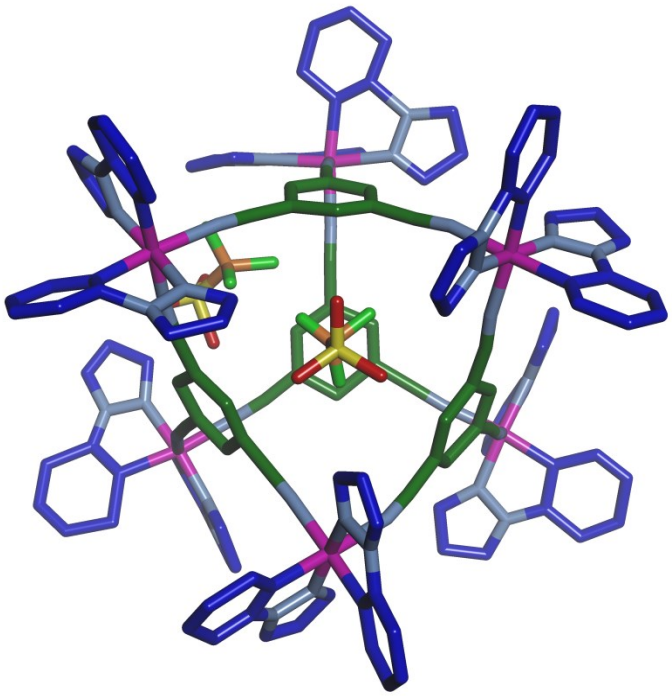

Figure 4.37. Preliminary X-ray crystal structure of *Δ*-**2**·6OTf. For clarity**,** non-encapsulated OTf^- counteranions, solvent molecules and hydrogens have been removed. The carbon atoms of ppy are shown in blue, tcb in dark green and OTf^- carbons in orange, iridium in pink, nitrogen in pale blue, sulfur in yellow, oxygen in red and fluorine in pale green.

Identification code	*Δ*-**2**·6OTf
Empirical formula	$C_{150}H_{96}F_{18}Ir_6N_{36}O_{18}S_6$
Formula weight	4378.29
Temperature	93(1) K
Wavelength	0.71075 Å
Crystal system	Primitive Monoclinic
Space group	$P2_1$
Unit cell dimensions	a = 17.773(5) Å α = 90°
	b = 34.303(9) Å β = 95.828(4)°
	c = 19.085(5) Å γ = 90°
Volume	11575(5) $Å^3$
Z	2
Density (calculated)	1.256 g cm^{-3}
Absorption coefficient	3.565 mm^{-1}
F(000)	4224

Crystal size	0.1 × 0.1 × 0.02 mm
Theta range for data collection	1.60 to 25.42°
Index ranges	-21<=h<=21, -41<=k<=41, -22<=l<=22
Reflections collected	117344
Independent reflections	42060 [R(int) = 0.0757]
Completeness to theta = 25.42°	99.2%
Absorption correction	Multiscan
Max. and min. transmission	0.931 and 0.690
Refinement method	Full-matrix least-squares on F^2
Data / restraints / parameters	42060 / 1 / 819
Goodness-of-fit on F^2	1.561
Final R indices [I>2sigma(I)]	R1 = 0.1684
R indices (all data)	wR2 = 0.4363
Absolute structure parameter	0.089(18)
Largest diff. peak and hole	6.420 and -2.540 e^- $Å^{-3}$

Table 4.6. Crystal data and structural refinement for *Δ*-**2**·6OTf.

4.5.15 ^{19}F VT NMR studies of 2·6OTf

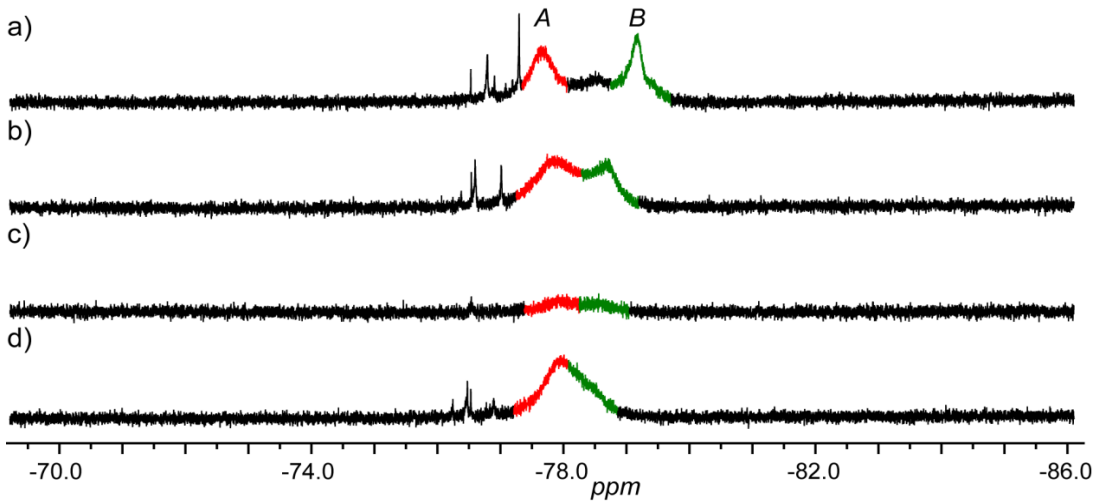

Figure 4.38. ^{19}F NMR (376 MHz, $C_2D_2Cl_4$) spectra of *Λ*-**2**·6OTf at a) 273K, b) 298K, c) 303K and d) 308K. Green peak (*B*) corresponds to encapsulated OTf^- and red peak (*A*) to free OTf^-.

4.5.16 Stability measurements for 2·6OTf

Stability measurements for **2**·6OTf (124 μM) were performed following a similar procedure to **1**·6OTf (see section 4.5.6), with the scrambling time measurements taken at 0, 0.5, 3, 6, 24, 48, 72 and 96 h. The experimental data of 1/[*Λ*/*Δ*-**2**·6OTf]-1/[*Λ*/*Δ*-**2**·6OTf]$_0$ was plotted against the scrambling time *t* from which k_{obs} and $t_{1/2}$ were calculated (see Table 4.7).

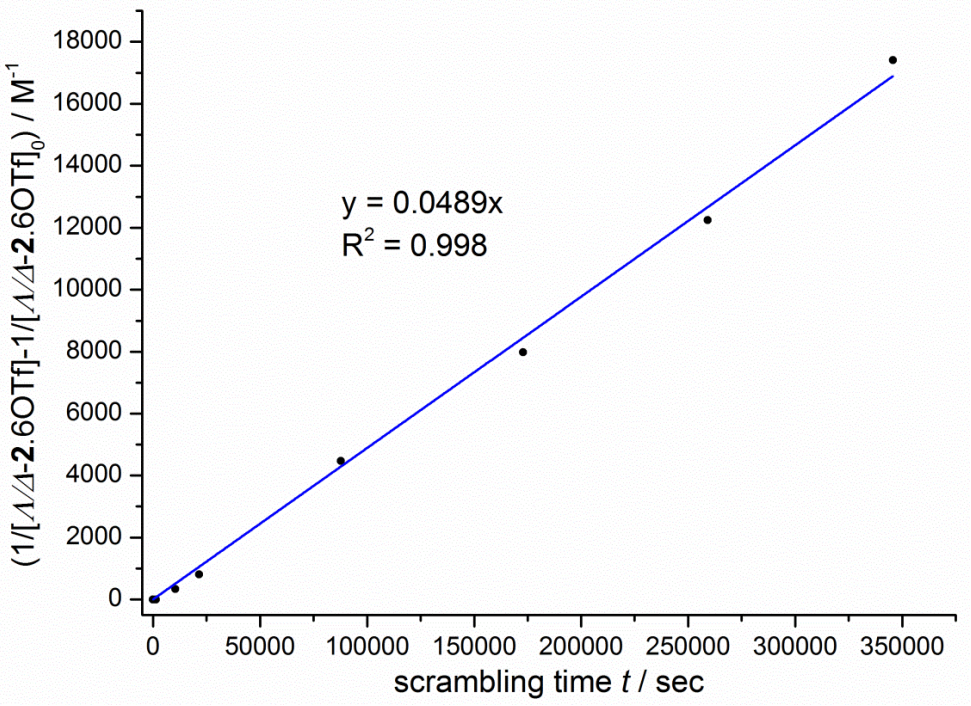

Figure 4.39. (1/[*Λ*/*Δ*-**2**·6OTf]-1/[*Λ*/*Δ*-**2**·6OTf]$_0$) versus scrambling time *t*.

	k_{obs} / M^{-1}s^{-1}	$t_{1/2}$ / day(s)
Λ/*Δ*-**2**·6OTf	4.89×10^{-2}	1.9

Table 4.7. The observed exchange rate constant, k_{obs}, and half-life, $t_{1/2}$, values for **2**·6OTf derived from Figure 4.39.

4.5.17 Emission Data

Steady-state luminescence spectra were measured using a Fluoromax (Horiba Jobin Yvon) photon-counting spectrofluorometer. Spectra were recorded with a bandpass of 3 nm for both excitation and emission monochromators and were corrected for variation in the excitation lamp intensity and the wavelength-dependence of the detector response. The data was further corrected with background subtraction and baseline correction. Spectral intensities were determined by integration over entire emission peaks bandwidth. Samples were measured in 1,1,2,2-tetrachloroethane (TCE) at RT using a fused silica cuvette (Starna Ltd.) with a 10 mm path length. The luminescence intensity for each sample was measured at an absorbance between 0.01 and 0.1, with an excitation wavelength of 413 nm. Emission quantum yields (Φ) were determined using $[Ru(bipy)_3](PF_6)_2$ (Φ_{air} = 0.018 in acetonitrile)[45] as reference with coumarin 153 (Φ_{air} = 0.58 in ethanol)[46] as a second reference to verify the yields. The quantum yields were calculated using the expression $\Phi_X = \Phi_R(m_X/m_R)(\eta_X^2/\eta_R^2)$, where X and R denote sample being measured and reference respectively, m is the gradient from the plot of integrated luminescence intensity *vs*. absorbance, which passes through (0, 0) and η is the refractive index of the solvent (η_{TCE} = 1.494, $\eta_{acetonitrile}$ = 1.344 and $\eta_{ethanol}$ = 1.361)[47].

	Emission Max (λ_{max}) / nm	Quantum yields (Φ) / %
Λ-**1**·6OTf	560	4.1
Λ-**1**·6PF_6	573	0.6
Δ-**1**·6ClO_4	577	1.2
Λ-**1**·6BF_4	545	0.6
Δ-$[(Ir(ppy)_2)_3(tcb)_3](NTf_2)_3$	589	0.6
Λ-**2**·6OTf	551	5.7

Table 4.8. Measured quantum yields of *Λ*-**1**·6OTf (2 μM), *Λ*-**1**·6PF_6 (2 μM), *Δ*-**1**·6ClO_4 (2 μM), *Λ*-**1**·6BF_4 (2 μM), *Δ*-$[(Ir(ppy)_2)_3(tcb)_3](NTf_2)_3$ (6 μM with 100 eq of tcb) and *Λ*-**2**·6OTf (2 μM) in $C_2H_2Cl_4$.

4.6 Notes and References

[1] B. Brune, *Cell Death Differ.* **2003**, *10*, 864-869.

[2] a) J. E. M. Lewis, E. L. Gavey, S. A. Cameron, J. D. Crowley, *Chem. Sci.* **2012**, *3*, 778-784; b) Y. Yamauchi, M. Yoshizawa, M. Akita, M. Fujita, *J. Am. Chem. Soc.* **2010**, *132*, 960-966; c) P. Mal, B. Breiner, K. Rissanen, J. R. Nitschke, *Science* **2009**, *324*, 1697-1699; d) M. D. Ward, *Chem. Commun.* **2009**, 4487-4499; e) T. Sawada, M. Yoshizawa, S. Sato, M. Fujita, *Nat. Chem.* **2009**, *1*, 53-56; f) B. Therrien, G. Süss-Fink, P. Govindaswamy, A. K. Renfrew, P. J. Dyson, *Angew. Chem. Int. Ed.* **2008**, *47*, 3773-3776; g) V. M. Dong, D. Fiedler, B. Carl, R. G. Bergman, K. N. Raymond, *J. Am. Chem. Soc.* **2006**, *128*, 14464-14465; h) M. Kawano, Y. Kobayashi, T. Ozeki, M. Fujita, *J. Am. Chem. Soc.* **2006**, *128*, 6558-6559; i) M. Yoshizawa, T. Kusukawa, M. Fujita, K. Yamaguchi, *J. Am. Chem. Soc.* **2000**, *122*, 6311-6312; j) T. Murase, Y. Nishijima, M. Fujita, *J. Am. Chem. Soc.* **2012**, *134*, 162-164; k) C. J. Hastings, M. D. Pluth, R. G. Bergman, K. N. Raymond, *J. Am. Chem. Soc.* **2010**, *132*, 6938-6940; l) C. J. Brown, R. G. Bergman, K. N. Raymond, *J. Am. Chem. Soc.* **2009**, *131*, 17530-17531; m) S. J. Lee, S.-H. Cho, K. L. Mulfort, D. M. Tiede, J. T. Hupp, S. T. Nguyen, *J. Am. Chem. Soc.* **2008**, *130*, 16828-16829; n) M. Yoshizawa, M. Tamura, M. Fujita, *Science* **2006**, *312*, 251-254; o) M. Wang, V. Vajpayee, S. Shanmugaraju, Y.-R. Zheng, Z. Zhao, H. Kim, P. S. Mukherjee, K.-W. Chi, P. J. Stang, *Inorg. Chem.* **2011**, *50*, 1506-1512; p) S. Ghosh, P. S. Mukherjee, *Organomet.* **2008**, *27*, 316-319; q) D. Xu, B. Hong, *Angew. Chem. Int. Ed.* **2000**, *39*, 1826-1829; r) S.-S. Sun, A. J. Lees, *J. Am. Chem. Soc.* **2000**, *122*, 8956-8967.

[3] a) A. R. Stefankiewicz, M. R. Sambrook, J. K. M. Sanders, *Chem. Sci.* **2012**, *3*, 2326-2329; b) M. C. O'Sullivan, J. K. Sprafke, D. V. Kondratuk, C. Rinfray, T. D. W. Claridge, A. Saywell, M. O. Blunt, J. N. O'Shea, P. H. Beton, M. Malfois, H. L. Anderson, *Nature* **2011**, *469*, 72-75; c) J. Freudenreich, J. Furrer, G. Süss-Fink, B. Therrien, *Organomet.* **2011**, *30*, 942-951; d) K. Kumazawa, K. Biradha, T. Kusukawa, T. Okano, M. Fujita, *Angew. Chem. Int. Ed.* **2003**, *42*, 3909-3913; e) F. Ibukuro, T. Kusukawa, M. Fujita, *J. Am. Chem. Soc.* **1998**, *120*, 8561-8562; f) S. Anderson, H. L. Anderson, J. K. M. Sanders, *Acc. Chem. Res.* **1993**, *26*, 469-475.

[4] I. A. Riddell, Y. R. Hristova, J. K. Clegg, C. S. Wood, B. Breiner, J. R. Nitschke, *J. Am. Chem. Soc.* **2013**, *135*, 2723-2733.

[5] S. Sato, Y. Ishido, M. Fujita, *J. Am. Chem. Soc.* **2009**, *131*, 6064-6065.

[6] a) I. A. Riddell, M. M. J. Smulders, J. K. Clegg, Y. R. Hristova, B. Breiner, J. D. Thoburn, J. R. Nitschke, *Nat. Chem.* **2012**, *4*, 751-756; b) C. R. K. Glasson, G. V. Meehan, J. K. Clegg, L. F. Lindoy, J. A. Smith, F. R. Keene, C. Motti, *Chem. Eur. J.* **2008**, *14*, 10535-10538.

[7] a) J. Bunzen, J. Iwasa, P. Bonakdarzadeh, E. Numata, K. Rissanen, S. Sato, M. Fujita, *Angew. Chem. Int. Ed.* **2012**, *51*, 3161-3163; b) W. Meng, J. K. Clegg, J. D. Thoburn, J. R. Nitschke, *J. Am. Chem. Soc.* **2011**, *133*, 13652-13660; c) Q.-F. Sun, J. Iwasa, D. Ogawa, Y. Ishido, S. Sato, T. Ozeki, Y. Sei, K. Yamaguchi, M. Fujita, *Science* **2010**, *328*, 1144-1147; d) D. L. Caulder, K. N. Raymond, *Acc. Chem. Res.* **1999**, *32*, 975-982.

[8] a) J. K. Clegg, J. Cremers, A. J. Hogben, B. Breiner, M. M. J. Smulders, J. D. Thoburn, J. R. Nitschke, *Chem. Sci.* **2013**, *4*, 68-76; b) F. Cui, S. Li, C. Jia, J. S. Mathieson, L. Cronin, X.-J. Yang, B. Wu, *Inorg. Chem.* **2011**, *51*, 179-187; c) M. Scherer, D. L. Caulder, D. W. Johnson, K. N. Raymond, *Angew. Chem. Int. Ed.* **1999**, *38*, 1587-

1592; d) R. Custelcean, P. V. Bonnesen, N. C. Duncan, X. Zhang, L. A. Watson, G. Van Berkel, W. B. Parson, B. P. Hay, *J. Am. Chem. Soc.* **2012**, *134*, 8525-8534.
[9] K. Suzuki, M. Kawano, M. Fujita, *Angew. Chem. Int. Ed.* **2007**, *46*, 2819-2822.
[10] O. Chepelin, J. Ujma, X. Wu, A. M. Z. Slawin, M. B. Pitak, S. J. Coles, J. Michel, A. C. Jones, P. E. Barran, P. J. Lusby, *J. Am. Chem. Soc.* **2012**, *134*, 19334-19337.
[11] a) A. M. Johnson, O. Moshe, A. S. Gamboa, B. W. Langloss, J. F. K. Limtiaco, C. K. Larive, R. J. Hooley, *Inorg. Chem.* **2011**, *50*, 9430-9442; b) Y.-R. Zheng, P. J. Stang, *J. Am. Chem. Soc.* **2009**, *131*, 3487-3489; c) E. S. Barrett, T. J. Dale, J. Rebek, *J. Am. Chem. Soc.* **2007**, *129*, 8818-8824; d) K. S. Chichak, S. J. Cantrill, J. F. Stoddart, *Chem. Commun.* **2005**, 3391-3393.
[12] Energy barrier calculated for PF_6^- exchange between the $[5PF_6 \subset \mathbf{1}]^+$ species and the unencapsulated counterions.
[13] A. V. Davis, D. Fiedler, G. Seeber, A. Zahl, R. van Eldik, K. N. Raymond, *J. Am. Chem. Soc.* **2006**, *128*, 1324-1333.
[14] S. Mecozzi, J. J. Rebek, *Chem. Eur. J.* **1998**, *4*, 1016-1022.
[15] Y. R. Hristova, M. M. J. Smulders, J. K. Clegg, B. Breiner, J. R. Nitschke, *Chem. Sci.* **2011**, *2*, 638-641.
[16] Without an X-ray crystal structure for *Λ*/*Δ*-**1**·6PF_6 we were unable to measure the exact volume occupied by 5 PF_6^- anions encapsulated within $\mathbf{1}^{6+}$. The anions were however modelled using Spartan '10 and the energy minimised volume of PF_6^- was measured as 75.0 Å^3. The cummulative volume for 4 and 5 PF_6^- anions is therefore 300 Å^3 and 375.0 Å^3, respectively. From Chapter 3, the volume of the cavity was calculated as 623.3 Å^3 based on the XRD data of *Δ*-**1**·6OTf.
[17] a) C. R. K. Glasson, G. V. Meehan, J. K. Clegg, L. F. Lindoy, P. Turner, M. B. Duriska, R. Willis, *Chem. Commun.* **2008**, 1190; b) R.-D. Schnebeck, E. Freisinger, B. Lippert, *Angew. Chem. Int. Ed.* **1999**, *38*, 168-171.
[18] R. Lin, J. H. K. Yip, K. Zhang, L. L. Koh, K.-Y. Wong, K. P. Ho, *J. Am. Chem. Soc.* **2004**, *126*, 15852-15869.
[19] T. K. Ronson, C. Giri, N. Kodiah Beyeh, A. Minkkinen, F. Topić, J. J. Holstein, K. Rissanen, J. R. Nitschke, *Chem. Eur. J.* **2013**, *19*, 3374-3382.
[20] PyH^+ salts were used due to their partial solubily in $C_2D_2Cl_4$. Bu_4N^+ salts were too soluble to make a direct comparison between their solubilities.
[21] J. S. Murray, K. Sen, *Molecular Electrostatic Potentials: Concepts and Applications*, Elsevier Science, **1996**.
[22] R. Cabot, C. A. Hunter, L. M. Varley, *Org. Biomol. Chem.* **2010**, *8*, 1455-1462.
[23] S. Mecozzi, A. P. West, D. A. Dougherty, *Proc. Natl. Acad. Sci.* **1996**, *93*, 10566-10571.
[24] a) E. G. Hohenstein, C. D. Sherrill, *J. Phys. Chem. A* **2009**, *113*, 878-886; b) S. L. Cockroft, J. Perkins, C. Zonta, H. Adams, S. E. Spey, C. M. R. Low, J. G. Vinter, K. R. Lawson, C. J. Urch, C. A. Hunter, *Org. Biomol. Chem.* **2007**, *5*, 1062-1080.
[25] a) C. Zonta, S. Cossu, Ottorino D. Lucchi, *Eur. J. Org. Chem.* **2000**, *2000*, 1965-1971; b) C. A. Schalley, R. K. Castellano, M. S. Brody, D. M. Rudkevich, G. Siuzdak, J. Rebek, *J. Am. Chem. Soc.* **1999**, *121*, 4568-4579; c) M. Kamieth, F.-G. Klärner, F. Diederich, *Angew. Chem. Int. Ed.* **1998**, *37*, 3303-3306.
[26] The anions were energy minimised and the electrostatic potential surfaces modelled using DFT calculations with B3LYP/6-31G** as the basis set in Spartan '10, Wavefunction, Inc., Irvine, CA, USA.
[27] S. Leininger, J. Fan, M. Schmitz, P. J. Stang, *Proc. Natl. Acad. Sci.* **2000**, *97*, 1380-1384.
[28] P. D. Frischmann, M. J. MacLachlan, *Chem. Soc. Rev.* **2013**, *42*, 871-890.

[29] Z. Laughrey, B. Gibb, *Templates in Chemistry II, Vol. 249* (Eds.: C. Schalley, F. Vögtle, K. Dötz), Springer Berlin Heidelberg, **2005**, 67-125.
[30] J. E. Beves, B. A. Blight, C. J. Campbell, D. A. Leigh, R. T. McBurney, *Angew. Chem. Int. Ed.* **2011**, *50*, 9260-9327.
[31] N. Gimeno, R. Vilar, *Coord. Chem. Rev.* **2006**, *250*, 3161-3189.
[32] a) R. L. Paul, Z. R. Bell, J. C. Jeffery, J. A. McCleverty, M. D. Ward, *Proc. Natl. Acad. Sci.* **2002**, *99*, 4883-4888; b) J. S. Fleming, K. L. V. Mann, C.-A. Carraz, E. Psillakis, J. C. Jeffery, J. A. McCleverty, M. D. Ward, *Angew. Chem. Int. Ed.* **1998**, *37*, 1279-1281.
[33] B. L. Schottel, H. T. Chifotides, K. R. Dunbar, *Chem. Soc. Rev.* **2008**, *37*, 68-83.
[34] a) S. Freye, J. Hey, A. Torras-Galán, D. Stalke, R. Herbst-Irmer, M. John, G. H. Clever, *Angew. Chem. Int. Ed.* **2012**, *51*, 2191-2194; b) T. D. Hamilton, G. S. Papaefstathiou, L. R. MacGillivray, *J. Am. Chem. Soc.* **2002**, *124*, 11606-11607.
[35] J. M. Klein, V. Saggiomo, L. Reck, U. Luning, J. K. M. Sanders, *Org. Biomol. Chem.* **2012**, *10*, 60-66.
[36] K. Suzuki, S. Sato, M. Fujita, *Nat. Chem.* **2010**, *2*, 25-29.
[37] For the IR stretching frequencies of OTf^-, PF_6^-, ClO_4^- and BF_4^-, see: T. H. Noh, J. Ahn, Y. M. Na, O.-S. Jung, *Bull. Korean Chem. Soc.* **2011**, *32*, 2795-2798.
[38] M. Nonoyama, *Bull. Chem. Soc. Jpn.* **1974**, *47*, 767-768.
[39] A. B. Tamayo, S. Garon, T. Sajoto, P. I. Djurovich, I. M. Tsyba, R. Bau, M. E. Thompson, *Inorg. Chem.* **2005**, *44*, 8723-8732.
[40] a) F. L. Weitl, K. N. Raymond, *J. Am. Chem. Soc.* **1979**, *101*, 2728-2731; b) A. S. Bailey, B. R. Henn, J. M. Langdon, *Tetrahedron* **1963**, *19*, 161-167.
[41] O. O. Kolodyazhnaya, O. I. Kolodyazhnyi, *Russ. J. Gen. Chem.* **2011**, *81*, 307-314.
[42] Y. Yamaguchi, T. Ochi, S. Miyamura, T. Tanaka, S. Kobayashi, T. Wakamiya, Y. Matsubara, Z.-i. Yoshida, *J. Am. Chem. Soc.* **2006**, *128*, 4504-4505.
[43] R. Urban, R. Krämer, S. Mihan, K. Polborn, B. Wagner, W. Beck, *J. Organomet. Chem.* **1996**, *517*, 191-200.
[44] J. A. Riddick, W. B. Bunger, T. K. Sakano, *Organic Solvents: Physical Properties and Methods of Purification, 4th Edition*, Wiley Interscience, New York, **1986**.
[45] K. Suzuki, A. Kobayashi, S. Kaneko, K. Takehira, T. Yoshihara, H. Ishida, Y. Shiina, S. Oishi, S. Tobita, *Phys. Chem. Chem. Phys.* **2009**, *11*, 9850-9860.
[46] R. F. Kubin, A. N. Fletcher, *Chem. Phys. Lett.* **1983**, *99*, 49-52.
[47] W. M. Haynes (Ed.), *Handbook of Chemistry and Physics*, 92nd ed., CRC press, **2011**.

Conclusion and Outlook

The versatility of cyclometalated Pt(II) and Ir(III) 2-phenylatopyridyl moieties in directing the self-assembly of multiple aggregates into metallosupramolecular capsules has been exposed.

In Chapter 2, the bias imposed by the *trans*-influence of the auxiliary 2-phenylatopyridyl ligands on the binding kinetics of the *cis*-exchangeable sites on Pt(II) was used to self-assemble trigonal prisms under an unusual kinetically controlled protocol, where-by the sequence of addition of the ditopic and tritopic pyridyl ligands determined the stereo-conformation of the product. This synthetic approach has the potential to generate other more complex supramolecular assemblies with shape-specific cavities that are highly selective in *guest* binding and can catalyse both regio- and stereo-specific reactions.

In Chapters 3 and 4, 2-phenylatopyridine was also used to labilise the *cis*-exchangeable sites on Ir(III) and together with a tritopic nitrile ligand the synthesis of the first photoactive [Ir(ppy)$_2$]-based capsule was achieved. Following the development of a novel method to resolve the racemic [(Ir(ppy)$_2$Cl)$_2$] starting material into its enantiopure forms, both the homochiral *Λ*- and *Δ*-Ir capsules were assembled. The octahedral capsules were shown to encapsulate an unusually large number of anions that were exchangeable for other anionic guests and, coupled with the luminescent properties, ion sensing was demonstrated. The associated counterions were highly crucial to the Ir capsules; both in templating their self-assembly and controlling their stability. Thus, substituting the anions for neutral guests was not possible nor was the synthesis of similar M_6L_4 assemblies with 'empty' cavities. The synthesis of photo-active assemblies with accessible internal space is of particular interest in the field of *host-guest* chemistry and photo-catalysis. Several projects are currently underway in the Lusby group, exploring the catalytic potential of alternative cyclometalated Ir-based systems. The use of other more kinetically robust ligands with the [Ir(ppy)]$^+$ moiety as well as appending the light harvesting unit to the periphery of alternative conjugated metallosupramolecular capsules is currently being pursued. Making these systems water soluble will also be addressed in future work.

In the more remote future, metallosupramolecular assemblies have the potential to be used as enzyme-like environmentally benign microreactors powered by light energy to catalyse selective and stereo-specific reactions. Or within the medicinal world, as site-specific drug delivery systems and biosensors.

Appendix: Published papers

"*Sequential, kinetically controlled synthesis of multicomponent stereoisomeric assemblies"* O. Chepelin, J. Ujma, P. E. Barran, P. J. Lusby, *Angew. Chem. Int. Ed.* **2012**, *51*, 4194-4197.

"Shapes of supramolecular cages by ion mobility mass spectrometry" J. Ujma, M. De Cecco, O. Chepelin, H. Levene, C. Moffat, S. J. Pike, P. J. Lusby, P. E. Barran, *Chem. Commun.*, **2012**, 48, 4423-4425.

"*Luminescent, Enantiopure, Phenylatopyridine Iridium-Based Coordination Capsules"* O. Chepelin, J. Ujma, X. Wu, A. M. Z. Slawin, M. B. Pitak, S. J. Coles, J. Michel, A. C. Jones, P. E. Barran, P. J. Lusby, *J. Am. Chem. Soc.*, **2012**, *134*, 19334–19337.

A Journal of the Gesellschaft Deutscher Chemiker

Angewandte Chemie

International Edition

GDCh

www.angewandte.org

2012–51/17

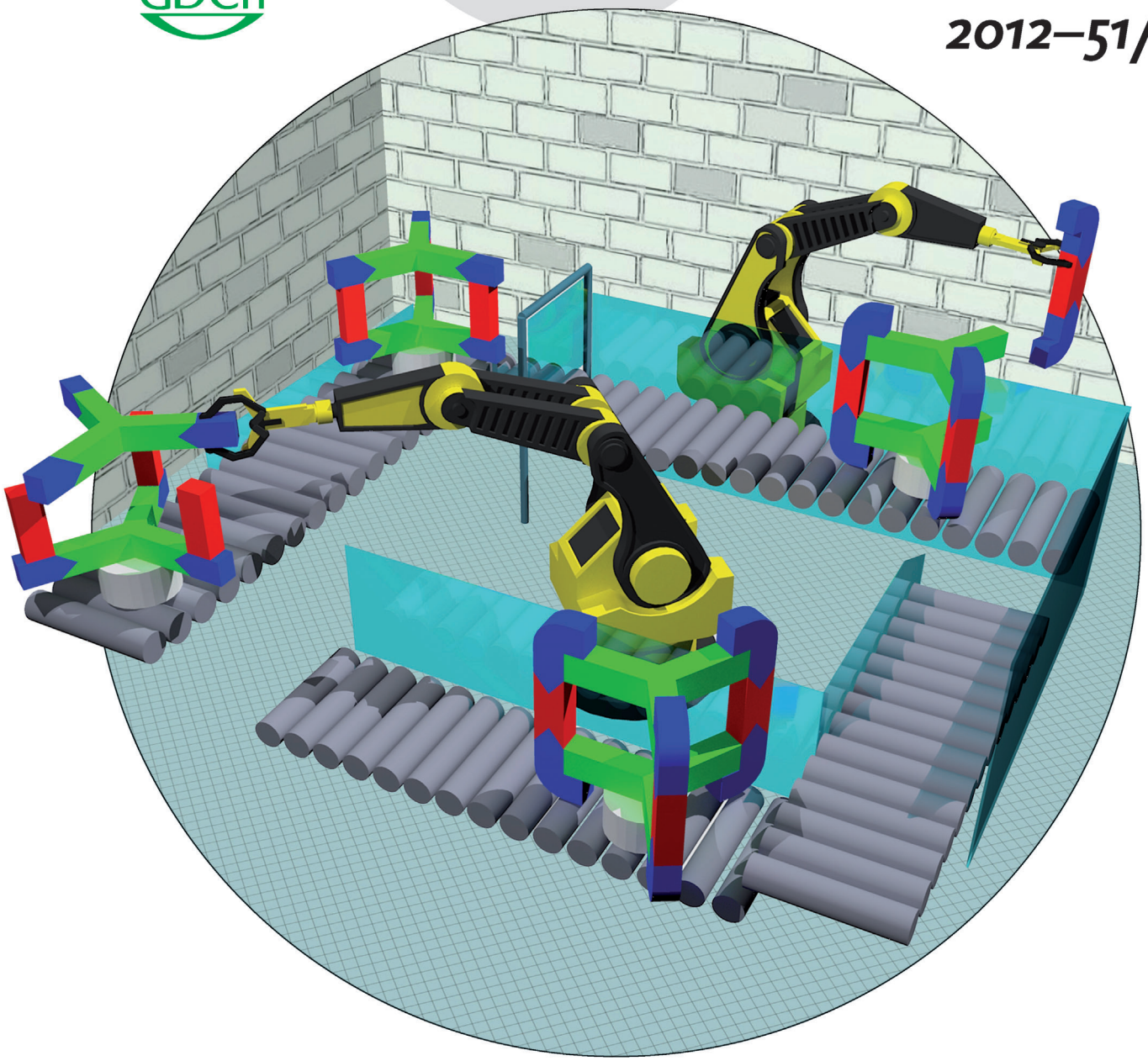

A kinetically controlled approach ...

… to metallosupramolecular assembly has been demonstrated by P. J. Lusby and co-workers in their Communication on page 4194 ff. By exploiting asymmetric cyclometalated platinum corner units that possess both labile and nonlabile *cis*-coordination sites, trigonal prismatic stereoisomeric architectures have been selectively prepared by altering the sequence of addition of molecular structural components using a template-free method.

WILEY-VCH

VIP Self-Assembly

DOI: 10.1002/anie.201108994

Sequential, Kinetically Controlled Synthesis of Multicomponent Stereoisomeric Assemblies**

Oleg Chepelin, Jakub Ujma, Perdita E. Barran, and Paul J. Lusby**

The reversibility of noncovalent and metal–ligand interactions has widely been exploited to synthesize a plethora of supramolecular and coordination-based assemblies under thermodynamic control.[1] Occasionally, entrapment in local energy minima leads to the formation of metastable products, which are often converted into lower-energy products upon prolonged reaction times.[2] In contrast, self-assembled products in nature almost always arise according to the most expedient reaction pathway, that is, the kinetically selected.[3] Herein we demonstrate a kinetically controlled approach to self-assembly, in which the sequence of addition[4] of molecular structural units leads to the stereoselective formation of metallosupramolecular isomers.

The use of platinum(II) (and other third-row transition metals) is particularly well-suited to a kinetic approach to self-assembly, not just because Pt–ligand bonds can be kinetically inert, but also because the metal ion can be conveniently tuned to produce a vast range of different ligand-exchange labilities. For instance, assemblies that utilize bis(phosphine) ligands as corner protecting groups often readily assemble at room temperature,[5] while those that exploit neutral N-donor bidentate ligands, such as ethylene diamine, typically require several hours at elevated temperature to reach equilibrium.[6] Furthermore, the mechanism of labilization, that is, the trans effect, is such that it is possible for a single metal center to possess *cis* exchangeable sites with dramatically different kinetic properties. We have recently prepared a metallosupramolecular trigonal prism that possesses an unsymmetrical cyclometalated $\widehat{CN}$ corner protecting group, which was assembled in two steps by treating [$\mathbf{L^1}$Pt(dmso)] (where $H_2\mathbf{L^1}$ = 2,6-diphenylpyridine) sequentially with 4,4′-bipy and tpt.3CSA (Scheme 1, steps a and b).[7] The isolation of a single isomeric product from a possible fourteen products, as indicated by the ^{1}H NMR spectrum of the hexa-PF_6 salt (see the Supporting Information, Figure S1a), led us to ask, was this selectivity a result of each Pt center possessing one labile and one inert exchangeable site, or was the selectivity thermodynamic in origin?

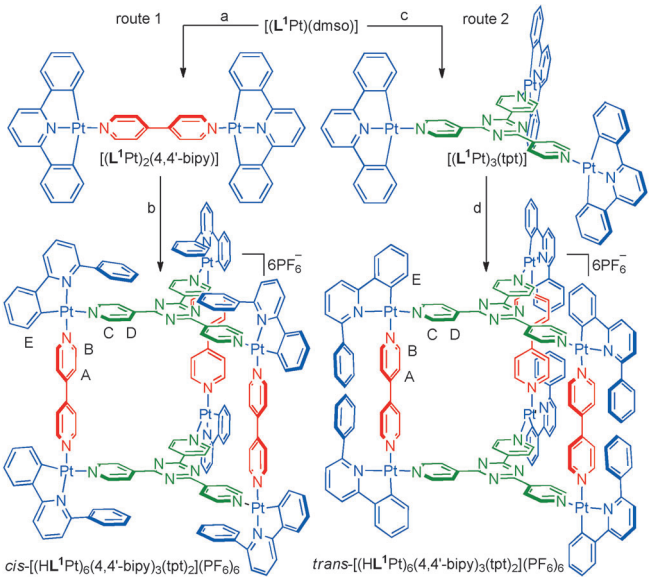

Scheme 1. Sequence-specific control over the formation of metallosupramolecular stereochemical isomers. a) 4,4′-bipy, CH_2Cl_2, RT, 18 h, 77%; b) (i) tpt·3CSA, CH_2Cl_2, RT, 1 h; (ii) NH_4PF_6, 97%; c) tpt, CH_2Cl_2, 18 h, 85%; d) (i) 4,4′-bipy·2CSA, CH_2Cl_2, RT, 3 h; (ii) NH_4PF_6, 99%. bipy = bipyridine, CSA = camphorsulfonic acid, dmso = dimethylsulfoxide, tpt = tris(4-pyridyl)triazine.

To answer this question, the sequence in which 4,4′-bipy and tpt were added to [$\mathbf{L^1}$Pt(dmso)] was reversed. [$\mathbf{L^1}$Pt(dmso)] was first treated with a third of an equivalent of tpt at room temperature in CH_2Cl_2 to give [($\mathbf{L^1}$Pt)$_3$(tpt)] (Scheme 1, step c), which was then treated with 4,4′-bipy·2CSA, and after metathesis with NH_4PF_6, the hexa-PF_6 salt was isolated in 99% yield (Scheme 1, step d). The ^{1}H NMR spectrum of this product (see the Supporting Information, Figure S1b) also indicated the formation of a single species, yet there were clear differences between the spectra of the two isomers, in particular, for resonances $H_{A\text{-}E}$. The product from route 1 was assigned as *cis*-[(H$\mathbf{L^1}$Pt)$_6$(4,4′-bipy)$_3$(tpt)$_2$](PF$_6$)$_6$, in which the tpt ligand is coordinated *cis* to the nitrogen of the 2,6-diphenylpyridine ligand, and the product from route 2 was assigned as *trans*-[(H$\mathbf{L^1}$Pt)$_6$(4,4′-bipy)$_3$(tpt)$_2$](PF$_6$)$_6$, in which the tpt ligand is coordinated *trans* to the nitrogen of the 2,6-diphenylpyridine ligand. This absolute assignment was made on the basis that a) the resonance of the *ortho* proton of tpt (H_C) is more deshielded in the *trans*-to-nitrogen coordination site in comparison to the *ortho* proton 4,4′-bipy (H_B), and b) the large and small relative separations between the resonances of H_A and H_B, and between the resonances of H_C and H_D.

[*] O. Chepelin, J. Ujma, Dr. P. E. Barran, Dr. P. J. Lusby
EaSTCHEM School of Chemistry, University of Edinburgh
The King's Buildings, West Mains Road, Edinburgh EH9 3JJ (UK)
E-mail: perdita.barran@ed.ac.uk
paul.lusby@ed.ac.uk
Homepage: http://www.chem.ed.ac.uk/staff/academic/lusby.html

[**] This work was supported by the EPSRC and the Royal Society. P.J.L. is a Royal Society University Research Fellow.

Supporting information (including full synthetic details and compound characterization) for this article is available on the WWW under http://dx.doi.org/10.1002/anie.201108994.

To corroborate the structure assignment of the isomers in solution, analysis was undertaken using nanoelectrospray mass spectrometry (nESI). While samples of the presumed *cis* and *trans* isomers both showed peaks that matched the predicted isotope pattern for the intact 3+ and 2+ charged cages (1360 and 2114 *m/z*, respectively), their collision-induced dissociation (CID) pathways differed significantly. For instance, MS–MS experiments showed that with increasing kinetic energy, the isolated intact 3+ charged cage $[[(H\mathbf{L}^{1}Pt)_6(4,4'\text{-bipy})_3(tpt)_2](PF_6)_3]^{3+}$ of the *cis* isomer initially fragments to give ions at 1308 and 1464 *m/z*, which then fragment further to a dominant species at 1152 *m/z* (Figure 1a). Although the singly charged peak at 1152 *m/z* unambiguously corresponds to $[[(H\mathbf{L}^{1}Pt)_2(4,4'\text{-bipy})]PF_6]^{+}$, and thus supports the assignment of the *cis* isomer, in which

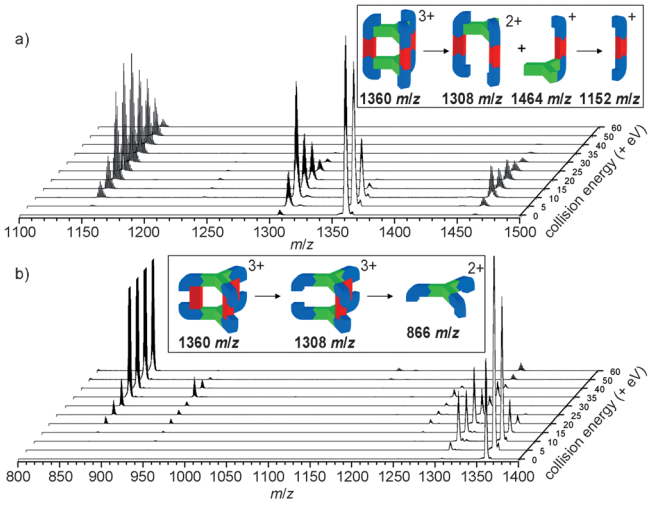

Figure 1. Partial nESI spectra with increasing collisional energy of the +3 charged intact prism (1360 *m/z*) to illuminate the CID pathways (see insets) for a) *cis*- and b) *trans*-$[(H\mathbf{L}^{1}Pt)_6(4,4'\text{-bipy})_3(tpt)_2](PF_6)_6$.

the weaker *trans*-to-phenylato Pt–tpt bond undergoes selective dissociation at lower potential, the peaks at both 1308 (+2) and 1464 (+1) *m/z* could correspond to more than one different structure with the formulas of $[[(H\mathbf{L}^{1}Pt)_4(4,4'\text{-bipy})_2(tpt)](PF_6)_2]^{2+}$ and $[[(H\mathbf{L}^{1}Pt)_2(4,4'\text{-bipy})(tpt)]PF_6]^{+}$, respectively. However, MS^3 experiments of both the species at 1308 and 1464 *m/z* showed the predominant appearance of the +1 ion at 1152 *m/z* ($[[(H\mathbf{L}^{1}Pt)_2(4,4'\text{-bipy})]PF_6]^{+}$). This finding suggests that the ions at 1308 and 1464 *m/z* correspond to tpt coordinated with two and one $[(H\mathbf{L}^{1}Pt)_2(4,4'\text{-bipy})]$ unit(s), respectively, and that initial fragmentation of the cage results from cleavage of Pt–tpt bonds from adjacent panels (Figure 1a, inset). When the isolated 3+ ion from the *trans* isomer was subjected to the same CID experiment, a signal at 1308 *m/z* was also observed at low voltage (Figure 1b), yet the different charge state (+3) indicates that the initial fragmentation involves the loss of a single 4,4′-bipy ligand to give $[[(H\mathbf{L}^{1}Pt)_6(4,4'\text{-bipy})_2(tpt)_2](PF_6)_3]^{3+}$ (Figure 1b, inset). At higher potential, this peak diminishes with a concomitant appearance of a +2 ion at 866 *m/z*, which unequivocally corresponds to $[(H\mathbf{L}^{1}Pt)_3(tpt)]^{3+}$. This fits with a preferential, low-energy dissociation of the weaker Pt-4,4′-bipy bond from the *trans* isomer (Figure 1b, inset).

To ascertain whether a kinetic self-assembly strategy could be used if the labile coordination site isn't initially masked, we have investigated the sequential addition of tpt and 4,4′-bipy to both $[(\mathbf{L}^{2}Pt)_2Cl_2]$ and $[(\mathbf{L}^{2}Pt)Cl_2]NBu_4$, where $H\mathbf{L}^{2}$ is the bidentate CN ligand 2-phenylpyridine (Scheme 2). The ^{1}H NMR spectrum of a mixture of $[(\mathbf{L}^{2}Pt)_2Cl_2]$ and 0.5 equivalents of 4,4′-bipy (Scheme 2, route 1, step a) showed

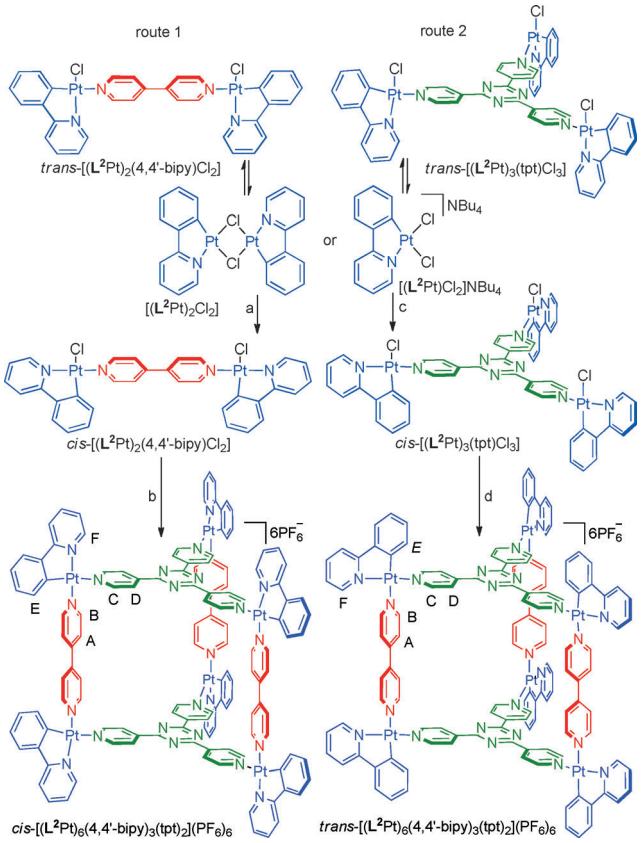

Scheme 2. Kinetically controlled synthesis using an "unmasked" corner protecting ligand. a) 4,4′-bipy, $C_2H_2Cl_4$, 45 °C, 24 h; b) (i) AgCSA, $C_2H_2Cl_4$, RT, 3 h; (ii) tpt, $C_2H_2Cl_4$, RT, 24 h; (iii) NH_4PF_6, 98% (starting from $[(\mathbf{L}^{2}Pt)_2Cl_2]$); c) tpt, $C_2H_2Cl_4$, 45 °C, 24 h; d) (i) AgCSA, $C_2H_2Cl_4$, RT, 3 h; (ii) 4,4′-bipy, $C_2H_2Cl_4$, RT, 24 h; (iii) NH_4PF_6, 77% (starting from $[(\mathbf{L}^{2}Pt)_2Cl_2]$).

the appearance of several new peaks after 5 minutes (see the Supporting Information, Figure S2b); these peaks differed from those of the $[(\mathbf{L}^{2}Pt)_2Cl_2]$ starting material (see the Supporting Information, Figure S2a). However, the gradual disappearance of these initial peaks and the concomitant appearance of a new set of signals, which converged to a single species after 24 hours at 45 °C, was observed (see the Supporting Information, Figure S2c). Based on the relative chemical shifts, and in particular the significant differences of H_E and H_F in the initial and final compounds (which is caused by shielding by the coordinated 4,4′-bipy ligand), it appears that *trans*-$[(\mathbf{L}^{2}Pt)_2(4,4'\text{-bipy})Cl_2]$ is the initial kinetic product, which rearranges into the thermodynamically (and kineti-

cally) more-stable *cis*-[($\mathbf{L^2}$Pt)$_2$(4,4′-bipy)Cl$_2$] (Scheme 2, route 1, step a).[8] After halide extraction using AgCSA, treatment with tpt, and then anion exchange with NH_4PF_6, *cis*-[($\mathbf{L^2}$Pt)$_6$(4,4′-bipy)$_3$(tpt)$_2$](PF$_6$)$_6$ was isolated in virtually quantitative yield (Scheme 2, route 1, step b). The ^{1}H NMR spectrum of this product (see the Supporting Information, Figure S2d) again suggested the formation of a single isomer. When the sequence of addition of 4,4′-bipy and tpt to [($\mathbf{L^2}$Pt)$_2$Cl$_2$] was switched (Scheme 2, route 2) a single, yet different product was obtained. A comparison of the ^{1}H NMR spectra of the two isomers showed significant differences (see Supporting Information, Figure S2d and S2e), particularly in resonances H_{A-F}.

The nESI mass spectra of *cis* and *trans*-[($\mathbf{L^2}$Pt)$_6$(4,4′-bipy)$_3$(tpt)$_2$](PF$_6$)$_6$ showed identical peaks at 1208 and 1884 *m*/*z*, which matched the predicted isotope patterns for the intact +3 and +2 charged prisms, respectively (not shown). However, in contrast to the analogous experiments with *cis* and *trans*-[(H$\mathbf{L^1}$Pt)$_6$(4,4′-bipy)$_3$(tpt)$_2$](PF$_6$)$_6$, the CID of the *cis* and *trans* isomers of [($\mathbf{L^2}$Pt)$_6$(4,4′-bipy)$_3$(tpt)$_2$](PF$_6$)$_6$ showed mainly peaks that did not correspond to any sensible combinations of $\mathbf{L^2}$Pt, 4,4′-bipy, tpt, and PF$_6$. Instead, the dominant CID pathway for both *cis* and *trans*-[[($\mathbf{L^2}$Pt)$_6$(4,4′-bipy)$_3$(tpt)$_2$](PF$_6$)$_3$]$^{3+}$ involves fluoride abstraction from the PF$_6$ counteranions. With the *cis* isomer, the disappearance of the 1208 *m*/*z* peak is initially accompanied by a dominant species at 1093 *m*/*z*, which corresponds to the formula [[($\mathbf{L^2}$Pt)$_4$(4,4′-bipy)$_2$(tpt)F]PF$_6$]$^{2+}$ (Figure 2a). In an analogous manner to *cis* isomer of [(H$\mathbf{L^1}$Pt)$_6$(4,4′-bipy)$_3$(tpt)$_2$](PF$_6$)$_6$, it appears that the initial fragmentation pathway involves the cleavage of the weaker Pt–tpt bonds from adjacent panels (also supported by a smaller intensity ion at 1311 *m*/*z*, which corresponds to [[($\mathbf{L^2}$Pt)$_2$(4,4′-bipy)(tpt)]PF$_6$]$^+$), a route that is either promoted or stabilized by abstraction of fluoride from one of the PF$_6$ counteranions (Figure 2a, inset). MS^3 experiments show that the disappearance of this 1093 *m*/*z* ion results from the dissociation into a low-intensity ion at 873 *m*/*z*, which matches [($\mathbf{L^2}$Pt)$_2$(4,4′-bipy)F]$^+$, and subsequent MS^4 experiments show that this fragments into a singly charged ion at 505 *m*/*z*, by loss of the neutral [($\mathbf{L^2}$Pt)F] from [($\mathbf{L^2}$Pt)$_2$(4,4′-bipy)F]$^+$. For the *trans* isomer, the fragmentation pathway appears to first involve loss of a single 4,4′-bipy, again either promoted or stabilized by fluoride abstraction from the counter anion, to give [[($\mathbf{L^2}$Pt)$_6$(4,4′-bipy)$_2$(tpt)$_2$F]-(PF$_6$)$_2$]$^{3+}$ (1114 *m*/*z*), which subsequently looses another 4,4′-bipy by a fluoride promoted/stabilized route to produce [[($\mathbf{L^2}$Pt)$_6$(4,4′-bipy)(tpt)$_2$F$_2$](PF$_6$)$_2$]$^{3+}$ (1020 *m*/*z*). Again, the selective loss of 4,4′-bipy ligands from the weaker *trans*-to-phenylato coordination sites supports the formation of *trans*-[($\mathbf{L^2}$Pt)$_6$(4,4′-bipy)$_3$(tpt)$_2$](PF$_6$)$_6$.

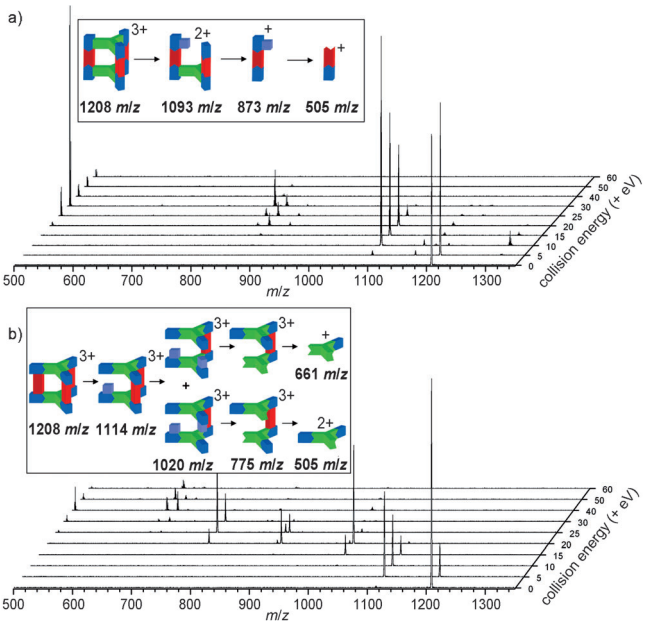

Figure 2. Partial nESI mass spectra with increasing collisional energy of the +3 charged intact prism (1208 *m*/*z*) to illuminate the fluoride-induced CID pathways (see insets) for a) *cis*- and b) *trans*-[($\mathbf{L^2}$Pt)$_6$(4,4′-bipy)$_3$(tpt)$_2$](PF$_6$)$_6$.

The four metallosupramolecular stereochemical isomers do not undergo isomerization, or reassemble to generate other assemblies (e.g. Pt$_4$ squares or Pt$_6$(tpt)$_4$ cages) at room temperature in solution.[9] We attribute this stability to the unlabile Pt–N bonds *trans* to the nitrogen donors of H$\mathbf{L^1}$/$\mathbf{L^2}$; although these bonds form readily at room temperature (or just above in the case of $\mathbf{L^2}$) from the corresponding solvato/halide complexes, the activation barrier for de-coordination is such that this step is essentially irreversible under ambient conditions. Therefore the sequence in which the N-donor bridging ligands are added to the starting platinum complexes determines the stereochemical outcome of the reaction. In this regard, the synthesis of these metallosupramolecular isomers combines elements of covalent (irreversible) synthesis and noncovalent (reversible) thermodynamically controlled assembly. It could also be expected that the isomers would show some thermodynamic bias towards either the *cis* or the *trans* form, however, heating samples of either *cis* or *trans*-[(H$\mathbf{L^1}$/$\mathbf{L^2}$Pt)$_6$(4,4′-bipy)$_3$(tpt)$_2$](PF$_6$)$_6$ at 80 °C for 24 hours results in a complex mixture with no obvious preference for a single species. This is perhaps unsurprising as to gain greater than 95% selectivity for a single species, an energy difference greater than 1.74 kcal mol^{-1} would be required. This is in marked contrast to the sequential, kinetically controlled syntheses described herein; these syntheses give greater than 95% selectivity for single stereochemical isomers, thus highlighting the potential benefits of exploiting differences in rates of assembly, rather than simply considering ground-state energies, for the preparation of multicomponent systems.

The vast difference in labilities of *cis* exchangeable platinum coordination sites have been exploited to selectively synthesize multicomponent stereoisomeric assemblies using a template-free, sequential, kinetically controlled approach. We anticipate that this approach to noncovalent, and in particular coordination driven self-assembly will facilitate the generation of multicomponent, ultimately functional systems.

Received: December 20, 2011
Published online: March 5, 2012

Keywords: cyclometalated complexes · kinetic control · platinum · self-assembly · supramolecular chemistry

[1] For recent examples, see a) Q.-F. Sun, J. Iwasa, D. Ogawa, Y. Ishido, S. Sato, T. Ozeki, Y. Sei, K. Yamaguchi, M. Fujita, *Science* **2010**, *328*, 1144 – 1147; b) M. Wang, Y.-R. Zheng, K. Ghosh, P. J. Stang, *J. Am. Chem. Soc.* **2010**, *132*, 6282 – 6283; c) S. Hiraoka, M. Kiyokawa, S. Hashida, M. Shionoya, *Angew. Chem.* **2010**, *122*, 142 – 147; *Angew. Chem. Int. Ed.* **2010**, *49*, 138 – 143; d) C. J. Hastings, M. D. Pluth, R. G. Bergman, K. N. Raymond, *J. Am. Chem. Soc.* **2010**, *132*, 6938 – 6940; e) T. Liu, Y. Liu, W. Xuan, Y. Cui, *Angew. Chem.* **2010**, *122*, 4215 – 4218; *Angew. Chem. Int. Ed.* **2010**, *49*, 4121 – 4124; f) A. Kaloudi-Chantzea, N. Karakostas, C. P. Raptopoulou, V. Psycharis, E. Saridakis, J. Griebel, R. Hermann, G. Pistolis, *J. Am. Chem. Soc.* **2010**, *132*, 16327 – 16329; g) J. Dömer, J. C. Slootweg, F. Hupka, K. Lammertsma, F. E. Hahn, *Angew. Chem.* **2010**, *122*, 6575 – 6578; *Angew. Chem. Int. Ed.* **2010**, *49*, 6430 – 6433; h) K. E. Allen, R. A. Faulkner, L. P. Harding, C. R. Rice, T. Riis-Johannessen, M. L. Voss, M. Whitehead, *Angew. Chem.* **2010**, *122*, 6805 – 6808; *Angew. Chem. Int. Ed.* **2010**, *49*, 6655 – 6658; i) X. Kuang, X. Wu, R. Yu, J. P. Donahue, J. Huang, C.-Z. Lu, *Nat. Chem.* **2010**, *2*, 461 – 465; j) M. Beyler, V. Heitz, J.-P. Sauvage, *J. Am. Chem. Soc.* **2010**, *132*, 4409 – 4417; k) J.-R. Li, H.-C. Zhou, *Nat. Chem.* **2010**, *2*, 893 – 898; l) J. L. Atwood, E. K. Brechin, S. J. Dalgarno, R. Inglis, L. F. Jones, A. Mossine, M. J. Paterson, N. P. Power, S. J. Teate, *Chem. Commun.* **2010**, *46*, 3484 – 3486; m) S. Perera, X. Li, M. Soler, A. Schultz, C. Wesdemiotis, C. N. Moorefield, G. R. Newkome, *Angew. Chem.* **2010**, *122*, 6689 – 6694; *Angew. Chem. Int. Ed.* **2010**, *49*, 6539 – 6544; n) J. Gao, J. Yan, S. G. Mitchell, H. N. Miras, A. G. Boulay, D.-L. Long, L. Cronin, *Chem. Sci.* **2011**, *2*, 1502 – 1508; o) A. Lledó, S. Kamioka, A. C. Sather, J. Rebek, *Angew. Chem.* **2011**, *123*, 1335 – 1337; *Angew. Chem. Int. Ed.* **2011**, *50*, 1299 – 1301; p) W. Meng, B. Breiner, K. Rissanen, J. D. Thoburn, J. K. Clegg, J. R. Nitschke, *Angew. Chem.* **2011**, *123*, 3541 – 3545; *Angew. Chem. Int. Ed.* **2011**, *50*, 3479 – 3483; q) A. Granzhan, C. Schouwey, T. Riis-Johannessen, R. Scopelliti, K. Severin, *J. Am. Chem. Soc.* **2011**, *133*, 7106 – 7115; r) M. Schmittel, M. Lal Saha, J. Fan, *Org. Lett.* **2011**, *13*, 3916 – 3919; s) Y. Liu, C. Hu, A. Comotti, M. D. Ward, *Science* **2011**, *333*, 436 – 440; t) A. Stephenson, S. P. Argent, T. Riis-Johannessen, I. S. Tidmarsh, M. D. Ward, *J. Am. Chem. Soc.* **2011**, *133*, 858 – 870; u) C. R. K. Glasson, J. K. Clegg, J. C. McMurtrie, G. V. Meehan, L. F. Lindoy, C. A. Motti, B. Moubaraki, K. S. Murray, J. D. Cashion, *Chem. Sci.* **2011**, *2*, 540 – 543.

[2] a) B. Hasenknopf, J.-M. Lehn, N. Boumediene, E. Leize, A. Van Dorsselaer, *Angew. Chem.* **1998**, *110*, 3458 – 3460; *Angew. Chem. Int. Ed.* **1998**, *37*, 3265 – 3268; b) V. Paraschiv, M. Crego-Calama, T. Ishi-i, C. J. Padberg, P. Timmerman, D. N. Reinhoudt, *J. Am. Chem. Soc.* **2002**, *124*, 7638 – 7639; c) B. J. Holliday, Y.-M. Jeon, C. A. Mirkin, C. L. Stern, C. D. Incarvito, L. N. Zakharov, R. D. Sommer, A. L. Rheingold, *Organometallics* **2002**, *21*, 5713 – 5725; d) S. Tashiro, M. Tominaga, T. Kusukawa, M. Kawano, S. Sakamoto, K. Yamaguchi, M. Fujita, *Angew. Chem.* **2003**, *115*, 3389 – 3392; *Angew. Chem. Int. Ed.* **2003**, *42*, 3267 – 3270; e) A. Hori, K. Yamashita, M. Fujita, *Angew. Chem.* **2004**, *116*, 5126 – 5129; *Angew. Chem. Int. Ed.* **2004**, *43*, 5016 – 5019; f) J. D. Badjić, S. J. Cantrill, J. F. Stoddart, *J. Am. Chem. Soc.* **2004**, *126*, 2288 – 2289; g) J. T. Davis, M. S. Kaucher, F. W. Kotch, M. A. Iezzi, B. C. Clover, K. M. Mullaugh, *Org. Lett.* **2004**, *6*, 4265 – 4268; h) A. Lohr, M. Lysetska, F. Würthner, *Angew. Chem.* **2005**, *117*, 5199 – 5202; *Angew. Chem. Int. Ed.* **2005**, *44*, 5071 – 5074; i) P. Mukhopadhyay, P. Y. Zavalij, L. Isaacs, *J. Am. Chem. Soc.* **2006**, *128*, 14093 – 14102; j) M. Yamanaka, Y. Yamada, Y. Sei, K. Yamaguchi, K. Kobayashi, *J. Am. Chem. Soc.* **2006**, *128*, 1531 – 1539; k) C. G. Claessens, M. J. Vicente-Arana, T. Torres, *Chem. Commun.* **2008**, 6378 – 6380; l) V. M. Cangelosi, T. G. Carter, L. N. Zakharov, D. W. Johnson, *Chem. Commun.* **2009**, 5606 – 5608; m) W. Jiang, A. Schäfer, P. C. Mohr, C. A. Schalley, *J. Am. Chem. Soc.* **2010**, *132*, 2309 – 2320.

[3] a) P. A. Jennings, P. E. Wright, *Science* **1993**, *262*, 892 – 896; b) R. Pellarin, P. Schuetz, E. Guarnera, A. Caflisch, *J. Am. Chem. Soc.* **2010**, *132*, 14960 – 14970.

[4] Y. Sakata, S. Hiraoka, M. Shionoya, *Chem. Eur. J.* **2010**, *16*, 3318 – 3325.

[5] a) P. J. Stang, D. H. Cao, S. Saito, A. M. Arif, *J. Am. Chem. Soc.* **1995**, *117*, 6273 – 6283; b) A. Rang, M. Nieger, M. Engeser, A. Lützen, C. A. Schalley, *Chem. Commun.* **2008**, 4789 – 4791.

[6] M. Fujita, F. Ibukuro, K. Yamaguchi, K. Ogura, *J. Am. Chem. Soc.* **1995**, *117*, 4175 – 4176.

[7] P. J. Lusby, P. Müller, S. J. Pike, A. M. Z. Slawin, *J. Am. Chem. Soc.* **2009**, *131*, 16398 – 16400.

[8] D. S. Black, G. B. Deacon, G. L. Edwards, *Aust. J. Chem.* **1994**, *47*, 217 – 227. Possible thermodynamic driving forces for the formation of *cis*-$[(\mathbf{L}^2\mathrm{Pt})_2(4,4'\text{-bipy})\mathrm{Cl}_2]$ may include minimization of the repulsive interaction between partial positively charged pyridyl donors (see Y.-R. Zheng, Z. Zhao, M. Wang, K. Ghosh, J. B. Pollock, T. R. Cook, P. J. Stang, *J. Am. Chem. Soc.* **2010**, *132*, 16873 – 16882.) and/or entropic factors related to desolvation upon lowering the dipole moment at the Pt center (see F. Basolo, R. G. Pearson, *Mechanisms of inorganic reactions: a study of metal complexes in solution*, Wiley, London, **1967**).

[9] The corresponding CSA salts are also stable in 1,1,2,2-tetrachloroethane at room temperature.

ChemComm

Cite this: *Chem. Commun.*, 2012, **48**, 4423–4425

www.rsc.org/chemcomm

COMMUNICATION

Shapes of supramolecular cages by ion mobility mass spectrometry†‡

Jakub Ujma, Martin De Cecco, Oleg Chepelin, Hannah Levene, Chris Moffat, Sarah J. Pike, Paul J. Lusby* and Perdita E. Barran*

Received 3rd February 2012, Accepted 8th March 2012
DOI: 10.1039/c2cc30778b

Mass spectrometry and drift tube ion mobility mass spectrometry have been used to analyse several isobaric, multicomponent cages yielding information on three dimensional structure, interactions and dynamics of assembly in the gas phase.

Unambiguous characterisation of supramolecular and polynuclear coordination-based assemblies presents a significant challenge. Such analysis is crucial to understanding structure–activity relationships with respect to a myriad of applications, such as sensing, catalysis and drug delivery. In the absence of X-ray crystallographic data, irrefutable evidence for the precise configuration and conformation of complex 3D architectures is difficult to obtain solely from NMR spectroscopic methods. In recent years the use of nano-electrospray ionisation (n-ESI) coupled with mass spectrometry has allowed analysis of intact biological non-covalent assemblies (for example pre-fibrillar amyloid clusters,[1] or heterogenic protein complexes[2]) as well as inorganic supramolecular self-assemblies.[3,4] Mass spectrometry based methods can provide detailed information of the stoichiometry of complexes, as well as on structural integrity *via* the use of collisional activation.

Ion Mobility Mass Spectrometry (IM-MS) is increasingly utilised for structural analysis of ions following n-ESI.[5] In drift tube based IM-MS (DT IM-MS), ions are allowed to drift through a cell of defined length filled with an inert buffer gas under the influence of a weak electric field and their arrival time at a subsequent detector is recorded. An ion will undergo many collisions in the drift cell and its mobility (K) in the cell is given by the ratio of the drift velocity (v_d) to the applied electric field (E). K is related to the temperature (T) dependent collision cross section (Ω) of the ion according to a modified form of the relationship below:[6]

$$K_0 = \frac{3ze}{16N_0}\left(\frac{2\pi}{\mu k_B T}\right)^{\frac{1}{2}}\frac{1}{\Omega}$$

where z is the charge on the ion, and N_0 is the number gas density. Coupling ion mobility (IM) with mass spectrometry (MS) has produced the hybrid technique (IM-MS) where both the m/z and the 'shape' of the molecular ion can be determined. IM-MS has risen to prominence in its study of large intact non-covalent biological systems but recent work has shown that it also can be applied to supramolecular inorganic systems.[7]

Schalley and co-workers applied IM-MS to distinguish between isobaric catenane and octalactam macrocycles.[7a] The Bowers group, have utilized DT IM-MS techniques to study various polyhedral oligomeric silsequioxanes polymers (POSS)[7b] and recently also metallosupramolecular cage systems.[7c] Chan *et al.* applied the travelling wave version of IM-MS to examine isobaric complexes and conformations of a hexacadmium macrocycle using a Synapt G2 platform.[7d] and recently Thiel *et al.* used IM-MS to distinguish between structural isomers of hybrid Mn-Anderson clusters.[8]

We have applied DT IM-MS to examine isobaric self assembled trigonal prismatic cage isomers of two related systems ((H**L**^{1}Pt) and (**L**^{2}Pt); Fig. 1). These are species which differ only in the relative orientation (*cis* or *trans*) of the bidentate cyclometallated ligand with respect to the other components.

Remarkably, DT IM-MS is able to readily distinguish these isomers, despite, in the case of the (**L**^{2}Pt) system, the isomers only really differing in the relative position of N and C atoms. Under identical n-ESI conditions, each of the cages produces a distinctive mass spectrum, with differing intensities of intact

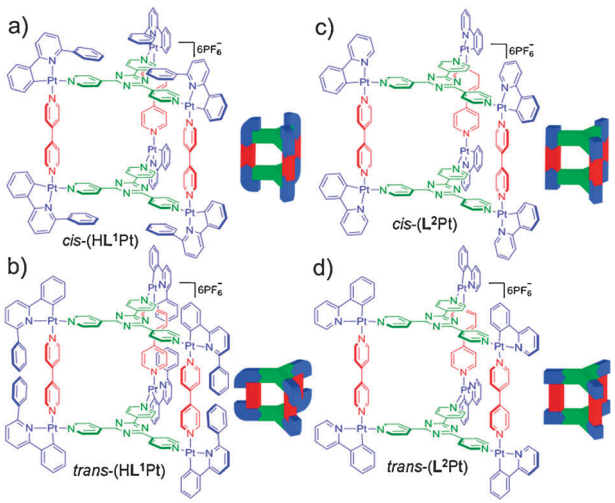

Fig. 1 Isobaric self-assembled systems examined by IM-MS and their cartoon representations. Each cage consists of tpt and 4,4′-bipy groups bridged by (a) *cis*-(H**L**^{1}Pt); (b) *trans*-(H**L**^{1}Pt); (c) *cis*-(**L**^{2}Pt); (d) *trans*-(**L**^{2}Pt); corner groups. Corner block shape represents ligand type.

EastChem, School of Chemistry, University of Edinburgh, West Mains Road, Edinburgh EH9 3JJ. E-mail: paul.lusby@ed.ac.uk, perdita.barran@ed.ac.uk

† Electronic supplementary information (ESI) available. See DOI: 10.1039/c2cc30778b

‡ This research was funded by EPSRC, EastChem, and the BMSS. PL is a Royal Society University Research Fellow.

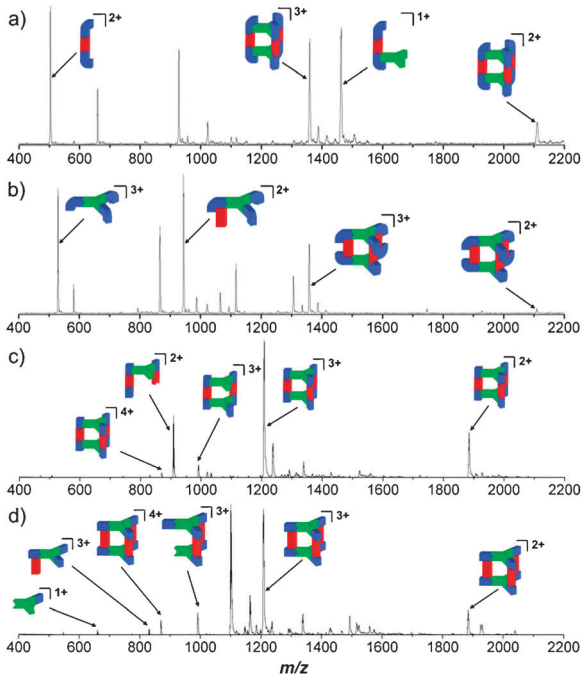

Fig. 2 Nano-ESI mass spectra of the cage systems: (a) *cis*-(HL^{1}Pt); (b) *trans*-(HL^{1}Pt); (c) *cis*-(L^{2}Pt); (d) *trans*-(L^{2}Pt).

species as well as different fragments ions, suggesting both differing gas-phase stabilities and diagnostic isomer-specific fragmentation pathways. Our peak assignment procedure is outlined in supplementary data (Fig. S1†).

Focusing first on the *cis* and *trans* isomers of (HL^{1}Pt), their n-ESI mass spectra reveal differences in the inherent stability of each isomer (Fig. 2a and b). For both, intact cages are present as ions of the general form $[M\text{-}nPF_6]^{6-n+}$, where loss of counterions allows positively charged ions to be observed; peaks at 1361 *m*/*z* and 2113 *m*/*z* corresponding to the $[M\text{-}3PF_6]^{3+}$, and $[M\text{-}2PF_6]^{2+}$ species respectively. The *cis* isomer of (HL^{1}Pt) (Fig. 2a) appears more resistant to dissociation during the nESI desolvation process than the corresponding *trans* isomer.

For both isomers of (HL^{1}Pt), some 'in-source' fragmentation is observed, resulting in spectra that are both diagnostic and informative on the relative stabilities of the molecular ions from these isobaric species. For the (L^{2}Pt) cages we also observe a different mass spectrum for the *cis* and *trans* forms (Fig. 2c and d). Again the relative intensities of intact cages and fragments are different for each molecular species.

Using DT-IM-MS we have measured rotationally averaged collision cross sections (CCS), on all the intact cages. Our analysis allows us to determine the shape with respect to number of counter ions present. Fig. 3 shows arrival time distributions (ATDs) obtained for the two charge states of each of the (HL^{1}Pt) cage isobarimers following mobility based separation. For the most dominant intact cage in the mass spectrum, $[M\text{-}3PF_6]$, the ATDs for the *cis*-(HL^{1}Pt) and *trans*-(HL^{1}Pt) cage isomers show a single resolvable conformation (or a smooth distribution of rapidly interconverting conformations) but with different, distinguishable CCS. With three counter anions, the *cis*-(HL^{1}Pt) cage has a smaller CCS in comparison to the *trans* isomer (Fig. 3a, Table 1). We associate this difference to positions of the non-coordinating phenyl groups (Fig. 1) on

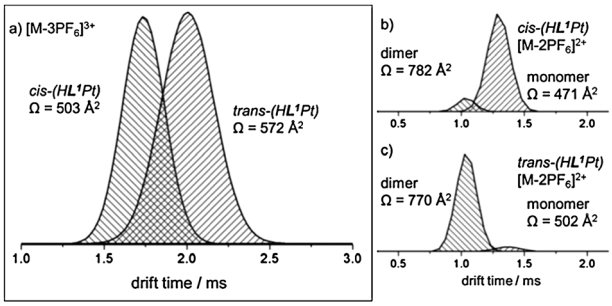

Fig. 3 ATDs for the (HL^{1}Pt) cages: (a) ATDs for *trans* and *cis* isomers for $[M\text{-}3PF_6]^{3+}$ at 1361 *m*/*z*; (b) and (c) presents ATDs for the *cis* and *trans* isomers respectively, for the peak attributed to $[M\text{-}2PF_6]^{2+}$ at 2113 *m*/*z*.

two isomeric forms of (HL^{1}Pt) corner group. Moreover, we anticipate different arrangement of counterions in *cis* and *trans* forms due to both electronic and steric factors.

For the lower charge state ions, $[M\text{-}2PF_6]^{2+}$, both the *cis* and *trans* isomers present two distinct species in the ATDs (Fig. 3b and c). We assign these as a monomer and a *m*/*z* coincident dimer, separated by ion mobility; since the dimer $[2M\text{-}4PF_6]^{4+}$ has twice the charge of the monomer, it arrives earlier. For the *cis*-(HL^{1}Pt) cage the monomer is the dominant form with a CCS of 471 Å^2, and the earlier arriving dimer with a CCS of 782 Å^2 (Fig. 3b). The relative intensities of these species are switched for the *trans*-(HL^{1}Pt) cage (Fig. 3c) now the dimer dominates, and has a similar CCS as for the *cis* cage (770 Å^2). The monomer is much lower in intensity and has a somewhat larger CCS than for the *cis* cage, (502 Å^2).

Although we do not obtain baseline resolution for ions of the size of the $[2M\text{-}4PF_6]^{4+}$ species, ion mobility easily separates these species, as well as providing diagnostic size information. A similar benefit of IM-MS analysis has been previously reported by Chen *et al.* on a hexacadmium metallocycle system.[7d]

Interestingly, additional counterions reduce the CCS. The *cis*-(HL^{1}Pt) cage $[M\text{-}2PF_6]^{2+}$ species is slightly smaller than that measured for $[M\text{-}3PF_6]^{3+}$, for the corresponding *trans*-isomer a much more significant difference in size is noted between the $[M\text{-}2PF_6]^{2+}$ and the $[M\text{-}3PF_6]^{3+}$, 503 Å^2 *versus* 572 Å^2 (Fig. 1a and b, Table 1). We attribute this either to an opening of the cage for the more abundant $[M\text{-}3PF_6]^{3+}$ or a rearrangement of counterions involving more efficient packing. The former is a more likely explanation, which is supported by the very small signal for the monomeric species of *trans*-(HL^{1}Pt) cage (Fig. 3c), which suggest that the fully closed intact species is not stable as a monomer in the gas-phase, also borne out by the more extensive in-source fragmentation for the *trans* isomer (Fig. 2b). Dimers for both isomers provide identical CCS so the packing arrangement of these must result in a similar gas phase shape, albeit one that is favoured by the *trans* isomer.

Similar IM-MS analysis has been performed for isomers of the (L^{2}Pt) system. This presents in three charge states, all of which, as expected, exhibit smaller CCS values than the corresponding values for the (HL^{1}Pt) structures. As already discussed for the (HL^{1}Pt) system, the more counter ions present, the smaller the measured CCS (Table 1).

The decrease in CCS on addition of counterions can be attributed to the effect of a larger number of favourable coulombic

Table 1 Average experimental collision cross sections for the intact cages. Each value is the average of at least three measurements accompanied by the statistical uncertainty. (see experimental section and supplementary information)

Collision Cross Section (Å^2)				
Molecular Species	$[M\text{-}4PF_6]^{4+}$	$[M\text{-}3PF_6]^{3+}$	$[M\text{-}2PF_6]^{2+}$	$[2M\text{-}4PF_6]^{4+}$
cis-(**HL^{1}Pt**)	—	503 ± 4	471 ± 4	770 ± 20
trans-(**HL^{1}Pt**)	—	572 ± 5	502 ± 4	782 ± 9
cis-(**L^{2}Pt**)	443 ± 8 692 ± 15	425 ± 8	425 ± 3	626 ± 29
trans-(**L^{2}Pt**)	467 ± 12	479 ± 4	431 ± 7	708 ± 18

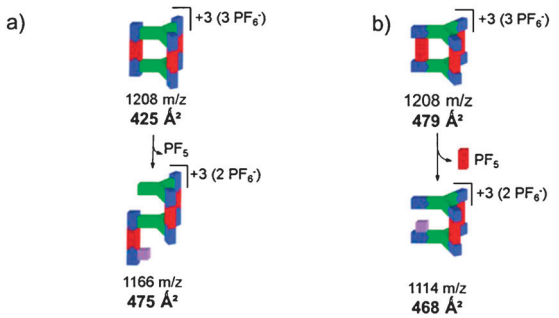

Scheme 1 Fragmentation pathways from CID experiments correlated with CCS values of fragments of $[M\text{-}3PF_6]^{3+}$ ion for *cis* (a) and *trans* (b) isomers of (**L^{2}Pt**).

interactions, to the cationic cage systems. The more counterions that are present, the greater the chance for ion pairs to form which will restrict and compact the structures. Contrary to the (**HL^{1}Pt**) cages isomers, the *cis* and *trans* isomeric forms of (**L^{2}Pt**) are isoteric and therefore structural/shape differences between the naked cages without counter anions should be minimal (Fig. 1). Nevertheless, our IM-MS results show prominent differences in the mobility for certain charge states. As with (**HL^{1}Pt**) cages, the *trans* isomer for each charge state has larger CCS than the *cis* form (Figure S2†), probably due to placement of counterions, in turn afforded by the steric differences. The $[M\text{-}4PF_6]^{4+}$ ion of the *cis* isomer also presents two distinct species in its ATD (Figure S2a†), which we interpret as closed cage and an open, more extended structure. The corresponding *trans* ion presents only one distinguishable species in its ATD at the +4 charge state suggesting an increased stability towards fragmentation.

As was observed for the (**HL^{1}Pt**) system, the lowest observed charge states give bimodal ATD which we interpret as monomeric and dimeric species. In contrast to the (**HL^{1}Pt**) system in which the *trans* isomer shows highest propensity to dimerize, with (**L^{2}Pt**) both the *cis* and *trans* form roughly equal proportions of dimer and monomer, although the CCS in the dimeric form appears to be quite different.

As well as exploring intact cages IM-MS analysis has also been applied to fragment species (Scheme 1 and supplementary data Table S1†). CID experiments[9b] indicate that fragmentation of the (**L^{2}Pt**) system proceeds *via* abstraction of fluoride from the PF_6^- counterion.

Here we observe such species from in-source fragmentation. In the case of the *cis* isomer we observe a significant increase in CCS upon fluoride abstraction (425Å^2 to 475Å^2), consistent with an increase in conformational flexibility. Contrary, in the *trans* isomer, fluoride abstraction occurs together with loss of 4-4′-bipy. This does not seem to affect the contracted geometry, CCS values of intact cage and 1114 *m*/*z* fragment differ only marginally (479 Å^2 to 468 Å^2). Again, this is rationalised by different *trans*-effects at metal centres of isobaric species.

While the (**HL^{1}Pt**) system has slightly larger CCS than the (**L^{2}Pt**) system, statistical uncertainties in CCSs of (**L^{2}Pt**) are often larger (Table 1). From this, we can speculate that the conformational dynamics of the two systems are different. The (**HL^{1}Pt**) system appears restricted whereas the (**L^{2}Pt**) cages are certainly more dynamic. This may be related to the positioning of the PF_6 counterions with respect to the Pt centres. For (**HL^{1}Pt**), the non-coordinating phenyl group masks Pt from the counterion, thus preventing fluoride abstraction. No analogous effects were observed in solution studies.

DT IM-MS has been used to investigate three-dimensional structures of metallosupramolecular stereochemical isomers. Despite the increasing use of commercial travelling wave based ion-mobility instrumentation, there is not yet a suitable set of calibrants for inorganic macromolecular species from which to provide accurate CCS from arrival time data. DT IM-MS data such as that shown here (Table 1, Table S1†), will start to address this. We have shown how this technique can be used to distinguish isobaric species, which has potential for checking the progress of isomerisation. IM-MS analysis has revealed how subtle structural differences significantly alter the stabilities of these species, highlighting the benefit of this analytical method. In the absence of X-ray crystallographic data, often difficult to obtain for self-assembling systems, IM-MS provides diagnostic structural information. Insights from the combination of n-ESI and IM-MS will be used to inform future supramolecular synthetic strategies.

Notes and references

1 H. L. Cole, J. M. Kalapothakis, G. Bennett, P. E. Barran and C. E. Macphee, *Angew. Chem., Int. Ed.*, 2010, **49**, 9448–9451.
2 M. Jenner, J. Ellis, W.-C. Huang, E. Lloyd Raven, G. C. K. Roberts and N. J. Oldham, *Angew. Chem., Int. Ed.*, 2011, **50**, 8291–8294.
3 (*a*) A. Marquis-Rigault, A. Dupont-Gervais, P. N. W. Baxter, A. Van Dorsselaer and J.-M. Lehn, *Inorg. Chem.*, 1996, **35**, 2307–2310; (*b*) Y. R. Zheng, K. Ghosh, H. B. Yang and P. J. Stang, *Inorg. Chem.*, 2010, **49**, 4747–4749.
4 C. A. Schalley, *Int. J. Mass Spectrom.*, 2000, **194**, 11–39.
5 S. R. Harvey, C. E. Macphee and P. E. Barran, *Methods*, 2011, **54**, 454–461.
6 E. A. Mason and E. W. McDaniel, *Transport properties of ions in gases*, Wiley, New York, 1988.
7 (*a*) C. A. Schalley, J. Hoernschemeyer, X. Li, G. Silva and P. Weis, *Int. J. Mass Spectrom.*, 2003, **228**, 373–388; (*b*) J. Gidden, P. R. Kemper, E. Shammel, D. P. Fee, S. Anderson and M. T. Bowers, *Int. J. Mass Spectrom.*, 2003, **222**, 63–73; (*c*) E. R. Brocker, S. E. Anderson, B. H. Northrop, P. J. Stang and M. T. Bowers, *J. Am. Chem. Soc.*, 2010, **132**, 13486–13494; (*d*) Y.-T. Chan, X. Li, M. Soler, J.-L. Wang, C. Wesdemiotis and G. R. Newkome, *J. Am. Chem. Soc.*, 2009, **131**, 16395–16397.
8 J. Thiel, D. Yang, M. H. Rosnes, X. Liu, C. Yvon, S. E. Kelly, Y.-F. Song, D.-L. Long and L. Cronin, *Angew. Chem., Int. Ed.*, 2011, **50**, 8871–8875.
9 (*a*) P. J. Lusby, P. Muller, S. J. Pike and A. M. Z. Slawin, *J. Am. Chem. Soc.*, 2009, **131**, 16398–16399; (*b*) O. Chepelin, J. Ujma, P. E. Barran and P. J. Lusby, *Angew. Chem., Int. Ed.*, DOI: 10.1002/anie.201108994.

JACS
JOURNAL OF THE AMERICAN CHEMICAL SOCIETY

Communication

pubs.acs.org/JACS

Luminescent, Enantiopure, Phenylatopyridine Iridium-Based Coordination Capsules

Oleg Chepelin,[†] Jakub Ujma,[†] Xiaohua Wu,[†] Alexandra M. Z. Slawin,[‡] Mateusz B. Pitak,[§] Simon J. Coles,[§] Julien Michel,[†] Anita C. Jones,[†] Perdita E. Barran,[†] and Paul J. Lusby*[,†]

[†]EaStCHEM School of Chemistry, University of Edinburgh, The King's Buildings, West Mains Road, Edinburgh EH9 3JJ, U.K.

[‡]EaStCHEM School of Chemistry, University of St. Andrews, Purdie Building, St. Andrews, Fife KY16 9ST, U.K.

[§]UK National Crystallography Service, School of Chemistry, University of Southampton, Southampton, SO17 1BJ, U.K.

Supporting Information

ABSTRACT: The first molecular capsule based on an $[Ir(ppy)_2]^+$ unit (ppy = 2-phenylatopyridine) has been prepared. Following the development of a method to resolve *rac*-$[(Ir(ppy)_2Cl)_2]$ into its enantiopure forms, homochiral Ir_6L_4 octahedra where obtained with the tritopic 1,3,5-tricyanobenzene. Solution studies and X-ray diffraction show that these capsules encapsulate four of the six associated counteranions and that these can be exchanged for other anionic guests. Initial photophysical studies have shown that an ensemble of weakly coordinating ligands can lead to luminescence not present in comparable mononuclear systems.

The combination of transition metal ions and geometrically complementary, multitopic bridging organic ligands has led to the preparation of numerous molecular capsules and cages.[1] These assemblies possess well-defined internal cavities that promote the ingress of guest molecules so that interesting functions, such as catalysis or the stabilization of reactive species, may be observed.[1,2] By and large, the transition metal ions within these systems have played solely a structural role, offering advantages such as predictable, well-defined coordination preferences and bond strength.[3] However, transition metals and their complexes often possess many other notable features, such as interesting photophysical properties; arguably the most well-known class are the poly(pyridyl) complexes of ruthenium(II),[4] while more recently, analogous cyclometalated C^N iridium(III) complexes have found widespread use as luminescent biological probes[5] and as dopants in organic light-emitting devices.[6] Although Newkome has described the synthesis of several very elegant metallocycles which feature $[Ru(terpy)_2]^{2+}$ connections,[7] the use Ru poly(pyridyl) or cyclometalated Ir complexes as structural components in metallosupramolecular assemblies, in particular polyhedral architectures, remains rare.[7,8] Herein, we report the first molecular capsule based on an $[Ir(ppy)_2]^+$ (ppy = 2-phenylatopyridine) motif and demonstrate that incorporation of this unit into a multimetallic array leads to a significant luminescence enhancement with respect to a comparable mononuclear complex, thus paving the way to capsules with light-harvesting function and the development of devices with emergent luminescent properties.

It was initially envisaged that $[Ir(ppy)_2]^+$ could be used in an analogous fashion to *cis*-protected square planar complexes, such as $[Pd(en)]^{2+}$ or $[Pt(dppp)]^{2+}$,[9] and that the ppy ligands, arranged in a *C,C-cis-N,N-trans* orientation, would sufficiently labilize the exchangeable sites to facilitate self-assembly.[10] Targeting an M_6L_4 octahedron,[11] at first we chose to explore the reaction of tris(4-pyridyl)triazine with the known iridium compound, $[Ir(ppy)_2(CH_3CN)_2]OTf$. As no evidence could be gathered for the formation of the intact architecture, we decided to instead investigate the self-assembly of the same Ir starting material with 1,3,5-tricyanobenzene (tcb). While it was anticipated that acetonitrile substitution from $[Ir(ppy)_2(CH_3CN)_2]OTf$ by tcb to generate the M_6L_4 assembly should be entropically, if not enthalpically, favored, initial experiments suggested only partial displacement. Instead, what is presumed to be $[(Ir(ppy)_2OTf)_2]$,[12] prepared by treating $[(Ir(ppy)_2Cl)_2]$ with silver triflate in $C_2H_4Cl_2$, was reacted with tcb in the same solvent (Scheme 1, step a). While the product gave a relatively complex ^1H NMR spectrum (see the Supporting Information, Figure S1a), nanoelectrospray ionization mass spectrometry (n-ESI-MS) showed an intense 2+ peak at 2106 *m/z* (see Figure S2a), which matched the predicted isotope pattern for $[\mathbf{1}\cdot 4OTf]^{2+}$. A ^1H DOSY NMR spectrum of the product also showed that the multiple aromatic signals possessed similar diffusion coefficients (see Figure S3a). This led us to postulate that $\mathbf{1}\cdot 6OTf$ is formed as a complex mixture of diastereoisomers[13] when the synthesis commences from racemic $[(Ir(ppy)_2Cl)_2]$ (Scheme 1, route 1), and thus tcb does not efficiently transmit stereochemical information between adjacent metal centers.[14]

To eliminate the problem of mixed stereoisomer formation, we have developed a preparative method to resolve *rac*-$[(Ir(ppy)_2Cl)_2]$ into its enantiopure forms,[15] which involves chromatographic resolution of serine complexes (Scheme 1, steps b and c).[16] We have found that the most efficient method to obtain both enantiomers (which, as expected, exhibit mirror image circular dichroism (CD) spectra; see Figure S4) is to resolve with both D- and L-serine, as the similarity in R_f values on silica ensures that only the faster-running diastereoisomer can be obtained in significant quantities. Both enantiomers crystallize in the chiral space group $P2_12_12_1$ upon diethyl ether

Received: September 11, 2012
Published: November 8, 2012

dx.doi.org/10.1021/ja309031h | *J. Am. Chem. Soc.* 2012, 134, 19334−19337

Scheme 1. Synthesis of Heterochiral and Homochiral Hexanuclear Iridium Assemblies[a]

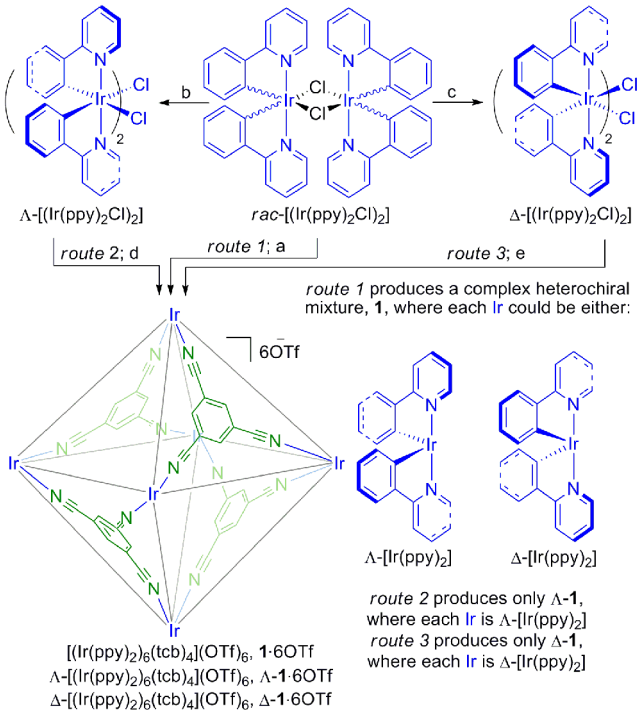

[a]Conditions: (a) (i) AgOTf, $C_2H_4Cl_2$, RT, 2 h; (ii) tcb, $C_2H_4Cl_2$, RT, 4 h, 48% (starting from *rac*-[(Ir(ppy)$_2$Cl)$_2$]). (b) (i) D-Serine, NaOMe, MeOH, 313 K, 16 h; (ii) 1 M HCl, MeOH, RT, 10 min, 50% (from *rac*-[(Ir(ppy)$_2$Cl)$_2$]). (c) L-Serine, NaOMe, MeOH, 313 K, 16 h; (ii) 1 M HCl, MeOH, RT, 10 min, 37% (from *rac*-[(Ir(ppy)$_2$Cl)$_2$]). (d) (i) AgOTf, $C_2H_4Cl_2$, RT, 2 h; (ii) tcb, $C_2H_4Cl_2$, RT, 5 h, 57% (starting from Λ-[(Ir(ppy)$_2$Cl)$_2$]). (e) (i) AgOTf, $C_2H_4Cl_2$, RT, 2 h; (ii) tcb, $C_2H_4Cl_2$, RT, 4 h, 68% (starting from Δ-[(Ir(ppy)$_2$Cl)$_2$]).

diffusion into saturated dichloromethane solutions; the solid-state structures (see Figure S5) reveal that the compound isolated following resolution with D-serine is Λ-[(Ir(ppy)$_2$Cl)$_2$], and that from L-serine is Δ-[(Ir(ppy)$_2$Cl)$_2$] (Scheme 1, steps b and c).[17]

When the self-assembly was commenced from either Λ- or Δ-[(Ir(ppy)$_2$Cl)$_2$] (Scheme 1, routes 2 and 3), a precipitate was observed shortly after the addition of tcb to what are presumed to be Δ- and Λ-[(Ir(ppy)$_2$OTf)$_2$], which was then isolated after a few hours of stirring at room temperature. We were delighted that the ^{1}H NMR spectra of the two products not only were indistinguishable (see Figure S1b,c) but also clearly showed single species with the number and ratio of tcb-to-ppy signals consistent with the sole formation of Λ- and Δ-**1**. CD confirmed that the two compounds were enantiomers (see Figure S4). The mass spectra also showed essentially a single species at 2106 *m*/*z*, which corresponds to the doubly charged [**1**·4OTf]$^{2+}$ (see Figure S2b,c). The surprising lack of other charge states in the mass spectra of Λ- and Δ-**1**·6OTf prompted us to look at the ^{19}F NMR spectra (see Figure S6a), which showed two distinct signals at −77.45 and −79.04 ppm in a ratio of 1:2, respectively. Addition of excess NBu_4OTf resulted in an increase in the intensity of the peak at −77.45 ppm (see Figure S6b), strongly suggesting that the peak at −79 ppm is due to encapsulated triflates. Other NMR techniques (HOESY and DOSY; see Figures S7 and S8) confirm this assignment and thus support the solution structure [4OTf⊂Δ-**1**]·2OTf. Further EXSY NMR experiments have shown that the *exo* and *endo* triflates are in slow exchange and that the activation barrier for this process is 18 kcal mol^{-1} (see Figure S9).

Corroboration of the capsule's structure (Figure 1) was obtained from X-ray diffraction (XRD) using single crystals

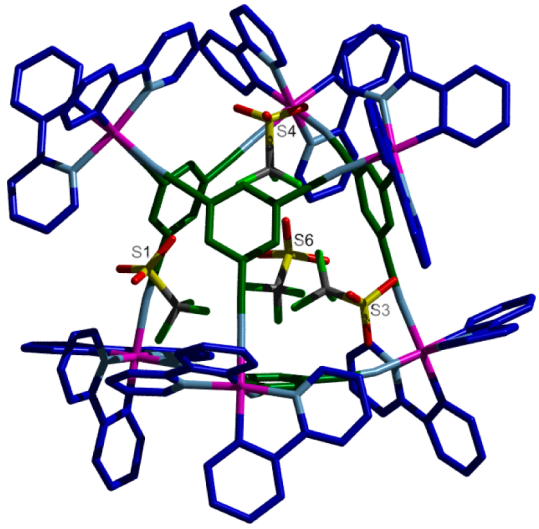

Figure 1. X-ray crystal structures of [4OTf⊂Δ-**1**]$^{2+}$. Color code: Ir, magenta; C(ppy), dark blue; C(tcb), dark green; C(OTf), gray; N, light blue; O, red; S, yellow; F, light green.

grown from benzene diffusion into a saturated dichloroethane solution of Δ-**1**·6OTf.[17,18] The solid-state structure supports the solution structure, [4OTf⊂Δ-**1**]$^{2+}$, showing triflates located in each of the octahedron "windows". For two encapsulated triflates (with S labels 3 and 4), the S−C axis points toward the center of these vacant windows (or, if viewed as a truncated tetrahedron, toward the vertex), forming a series of close contacts between the triflate oxygens and the hydrogen atoms attached to tcb and the *ortho* pyridyl positions. The other encapsulated anions (with S labels 1 and 6) are positioned in a slightly more "side-on" fashion, with the cage forming short contacts between two of the oxygen atoms and one of the fluorines. It seems probable that, in solution, these two distinct triflate co-conformations participate in a low-energy exchange process, thus explaining the presence of a single "encapsulated" signal in the ^{19}F NMR spectrum at room temperature.

To explore whether the structure and, in particular, the encapsulated anions are preserved under MS conditions, ion-mobility measurements have been undertaken.[19] For the ions at 2106 *m*/*z*, both samples gave superimposable arrival time distributions, consistent with a single species/conformation (see Figure S10). The observed rotationally averaged collision cross sections for Λ- and Δ-**1** were found to be 551 and 543 Å^2, respectively, virtually within error of each other. To validate these, ion-mobility simulations have been carried out using structures derived from the XRD data. The values calculated using either the exact hard-spheres scattering or trajectory method, 555 and 551 Å^2, respectively, agree remarkably well with the experimental data, suggesting that the counteranions remain within the capsule upon ionization into the gas phase.

Examples of metallocapsules which encapsulate multiple species of the same charge are very rare.[20] Clearly, the strong Coulombic attraction between the positively charged Ir vertices and negative counteranions, alongside the series of CH···X (X

dx.doi.org/10.1021/ja309031h | J. Am. Chem. Soc. 2012, 134, 19334−19337

= O, F) hydrogen bonds (*vide supra*), is enough to overcome the repulsion between same-charge ions. It could also be that the CF_3 groups, which are "meshed" together within the center of the cavity (C−C distances between encapsulated OTf counteranions range from 4.93 to 6.05 Å, with an average distance of 5.55 Å), act to insulate this charge. To probe further, we have calculated the capsule's occupancy. Based on an irregular hexadecahedron model (see Supporting Information for details), the volume of the empty cavity has been calculated to be 506 $Å^3$, of which the triflate counteranions occupy 280 $Å^3$, which equates to 55% filled cavity space, in line with previous observations made by Rebek.[21]

Held under a standard long-wavelength UV lamp, tetrachloroethane (TCE) solutions of Λ- and Δ-**1**·6OTf luminesce orange (Figure 2, inset). As most literature Ir complexes are

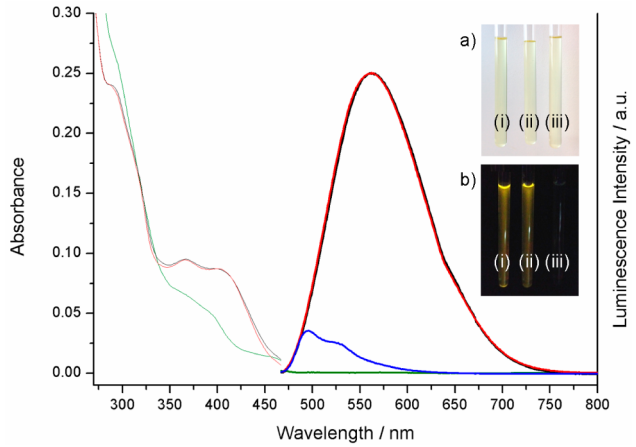

Figure 2. Absorption and emission (excitation at 413 nm) spectra of Λ- and Δ-**1**·6OTf. Λ = black line; Δ = red line; TCE, 2 μM. For comparison, the spectra of the mononuclear $[Ir(ppy)_2(PhCN)_2]OTf$ are also shown (Ir only = green line; Ir + 3000 equiv PhCN = blue line; TCE, 12 μM). Inset: Photographs of (i) Λ-**1**·6OTf, (ii) Δ-**1**·6OTf, and (iii) $[Ir(ppy)_2(PhCN)_2]OTf$ in NMR tubes held (a) in ambient lighting and (b) under a long-wavelength UV lamp.

luminescent, the significance of the capsules' photophysical properties only becomes apparent when compared against the representative mononuclear bis(benzonitrile) complex, $[Ir(ppy)_2(PhCN)_2]OTf$.[22] Placed next to the samples of Λ- and Δ-**1** under UV light (Figure 2, inset), there is no visible luminescence from $[Ir(ppy)_2(PhCN)_2]OTf$ in the same solvent (at equivalent [Ir]). The absorption and emission spectra of these samples confirm these visual observations (Figure 2). Even with a vast excess of benzonitrile, $[Ir(ppy)_2(PhCN)_2]OTf$ is only weakly luminescent (Figure 2). The emission of Λ- and Δ-**1**·6OTf is also broadened and red-shifted with respect to $[Ir(ppy)_2(PhCN)_2]OTf$ (in the presence of excess benzonitrile), signifying increased charge-transfer character of the emitting state. While the quantum yields for Λ- and Δ-**1**·6OTf, found to be 0.04 in air-equilibrated TCE (see the Supporting Information), are comparable to those for many cyclometalated Ir complexes under similar ambient conditions,[23] these often utilize either bidentate or strongly coordinating (and high ligand strength) monodentate ligands.[24] As far as we are aware, this is the first time a collection of weakly coordinating ligands has been used to inhibit nonradiative ligand dissociation pathways.[25] Interestingly, the emission intensity of Λ- and Δ-**1**·6OTf increases only marginally (by a factor of 1.1) when the samples are thoroughly degassed, in contrast to many other such Ir complexes,[23] suggesting that the metallosupramolecular architecture may also in some way inhibit collisional O_2 quenching.[23b] Alternatively, the presence of four desolvated anions located within the cavity of the capsule may provide such an efficient, alternative nonradiative decay pathway (e.g., via electron transfer) that the capsule is insensitive to the presence of O_2.

A preliminary investigation into the host−guest chemistry of $[4OTf⊂Δ/Λ\text{-}\mathbf{1}]^{2+}$ indicates that the encapsulated triflates can be exchanged for other anionic species. When NBu_4PF_6 is titrated into a sample of $[4OTf⊂Δ\text{-}\mathbf{1}]\cdot 2OTf$ in $C_2D_2Cl_4$, ^{19}F NMR spectroscopy (see Figure S12) shows multiple OTf and PF_6 signals at low $[PF_6]$, indicative of mixed PF_6−OTf host−guest complexes. At equimolar anionic concentrations, encapsulated OTf has mostly been displaced. This process has also been monitored by ^1H NMR spectroscopy (see Figure S13), which shows that while the overall symmetry is preserved, the proton signals closest to the anion binding sites (the tcb hydrogen atom and the *ortho* and *meta* pyridyl sites) are noticeably shifted. Similar experiments with NBu_4BF_4 and $NBu_4CF_3BF_3$, and additional titrations into Λ-**1**·6BF_4 (see Figures S14−S23), have ascertained that the overall affinity of perfluorinated anions for the cavity of $[Δ/Λ\text{-}\mathbf{1}]^{6+}$ follows the sequence PF_6 > OTf ≈ CF_3BF_3 > BF_4.[21c] While at present we are unable to rationalize this affinity, due to the fast exchange of some of the anionic species (even at low temperatures), additional DOSY measurements show that the cage remains intact following guest exchange. We have also ascertained that there is communication between the luminescent properties of $[Δ/Λ\text{-}\mathbf{1}]^{6+}$ and the cavity-bound guests, as evidenced by changes to the emission spectra during anion titration experiments (see the Supporting Information). As well as showing that $[Δ/Λ\text{-}\mathbf{1}]^{6+}$ acts as a luminescent anion sensor, this also suggests that it may be possible to tune luminescent properties of multimetallic Ir assemblies through supramolecular means rather than via conventional covalent modification. Our initial attempts to expand host−guest chemistry to neutral organic species have so far been hampered by the low solubility/stability of Λ/Δ-**1** in more polar solvents.

In summary, the first molecular capsule based on an $[Ir(ppy)_2]^+$ unit has been assembled using a multitopic nitrile ligand and enantiopure Ir starting materials. This incorporation leads to luminescence not present in a comparable mononuclear complex. In addition, we have shown that the same capsule is capable of binding multiple same-charge species and that these can be swapped for other anionic guests. We are currently exploring further aspects of this system, in particular how guest-binding features and photophysical properties relate, and whether the light-harvesting properties can be exploited in relation to potential substrate binding.

■ ASSOCIATED CONTENT

Supporting Information

Full synthetic details and compound characterization, crystallographic results in CIF fomat, details of IMMS calculations, and volume calculations. This material is available free of charge via the Internet at http://pubs.acs.org.

■ AUTHOR INFORMATION

Corresponding Author

Paul.Lusby@ed.ac.uk

Notes

The authors declare no competing financial interest.

■ ACKNOWLEDGMENTS

This work was supported by the EPSRC and the Royal Society. P.J.L. is a Royal Society University Research Fellow.

■ REFERENCES

(1) For recent reviews, see: (a) Chakrabarty, R.; Mukherjee, P. S.; Stang, P. J. *Chem. Rev.* **2011**, *111*, 6810. (b) Ward, M. D.; Raithby, P. R. *Chem. Soc. Rev.* **2012**, DOI: 10.1039/c2cs35123d.

(2) (a) Hastings, C. J.; Backlund, M. P.; Bergman, R. G.; Raymond, K. N. *Angew. Chem., Int. Ed.* **2011**, *50*, 10570. (b) Murase, T.; Nishijima, Y.; Fujita, M. *J. Am. Chem. Soc.* **2012**, *134*, 162. (c) Horiuchi, S.; Murase, T.; Fujita, M. *J. Am. Chem. Soc.* **2011**, *133*, 12445. (d) Mal, P.; Breiner, B.; Rissanen, K.; Nitschke, J. R. *Science* **2009**, *324*, 1697.

(3) For examples of capsules which exploit hydrogen-bonding, see: (a) Liu, Y.; Hu, C.; Comotti, A.; Ward, M. D. *Science* **2011**, *333*, 436. (b) MacGillivray, L. R.; Atwood, J. L. *Nature* **1997**, *389*, 469. (c) Wyler, R.; de Mendoza, J.; Rebek, J. *Angew. Chem., Int. Ed.* **1993**, *32*, 1699.

(4) Juris, A.; Balzani, V.; Barigelleti, F.; Campagna, S.; Belser, P.; von Zelewsky, A. *Coord. Chem. Rev.* **1988**, *84*, 85.

(5) Lo, K. K.-W.; Zhang, K. Y.; Leung, S.-K.; Tang, M.-C. *Angew. Chem., Int. Ed.* **2008**, *47*, 2213.

(6) Baldo, M.; Thompson, M.; Forrest, S. *Nature* **2000**, *403*, 750.

(7) For metallocycles which feature $[Ru(terpy)_2]^{2+}$ connections, see: (a) Chan, Y.-T.; Li, X.; Moorefield, C. N.; Wesdemiotis, C.; Newkome, G. R. *Chem. Eur. J.* **2011**, *17*, 7750. (b) Chan, Y.-T.; Li, X.; Yu, J.; Carri, G. A.; Moorefield, C. N.; Newkome, G. R.; Wesdemiotis, C. *J. Am. Chem. Soc.* **2011**, *133*, 11967. (c) Wang, P.; Moorefield, C. N.; Jeong, K.-U.; Hwang, S.-H.; Li, S.; Cheng, S. Z. D.; Newkome, G. R. *Adv. Mater.* **2008**, *20*, 1381. (d) Newkome, G. R.; Wang, P.; Moorefield, C. N.; Cho, T. J.; Mohapatra, P. P.; Li, S.; Hwang, S.-H.; Lukoyanova, O.; Echegoyen, L.; Palagallo, J. A.; Iancu, V.; Hla, S.-W. *Science* **2006**, *312*, 1782. (e) Sun, S.-S.; Lees, A. J. *Inorg. Chem.* **2001**, *40*, 3154. For grid-type arrays, see: (f) Bassani, D. M.; Lehn, J.-M.; Fromm, K.; Fenske, D. *Angew. Chem., Int. Ed.* **1998**, *37*, 2364. For helicates based on $[Ru(bipy)_3]^{2+}$ motifs, see: (g) Glasson, C. R. K.; Meehan, G. V.; Clegg, J. K.; Lindoy, L. F.; Smith, J. A.; Keene, F. R.; Motti, C. *Chem. Eur. J.* **2008**, *14*, 10535. For Ru poly(pyridyl) metallodendrimers, see: (h) Constable, E. C.; Harverson, P.; Oberholzer, M. *Chem. Commun.* **1996**, *32*, 1821.

(8) (a) Baranoff, E.; Orselli, E.; Allouche, L.; Di Censo, D.; Scopelliti, R.; Grätzel, M.; Nazeeruddin, M. K. *Chem. Commun.* **2011**, *47*, 2799. (b) Chandrasekhar, V.; Hajra, T.; Bera, J. K.; Rahaman, S. M. W.; Satumtira, N.; Elbjeirami, O.; Omary, M. A. *Inorg. Chem.* **2012**, *51*, 1319. For luminescent metallopolymers, see: (c) Eryazici, I.; Farha, O. K.; Compton, O. C.; Stern, C.; Hupp, J. T.; Nguyen, S. T. *Dalton Trans.* **2011**, *40*, 9189. For three-dimensional assemblies based on M(arene) building blocks (where M = Ru or Ir, arene = Cp*, *p*-cymene), see: (d) Schmitt, F.; Freudenreich, J.; Barry, N. P. E.; Juillerat-Jeanneret, L.; Süss-Fink, G.; Therrien, B. *J. Am. Chem. Soc.* **2012**, *134*, 754. (e) Han, Y.-F.; Jia, W.-G.; Lin, Y.-J.; Jin, G.-X. *Angew. Chem., Int. Ed.* **2009**, *48*, 6234. (f) Mirtschin, S.; Slabon-Turski, A.; Scopelliti, R.; Velders, A. H.; Severin, K. *J. Am. Chem. Soc.* **2010**, *132*, 14004. (g) Vajpayee, V.; Yang, Y. J.; Kang, S. C.; Kim, H.; Kim, I. S.; Wang, M.; Stang, P. J.; Chi, K.-W. *Chem. Commun.* **2011**, *47*, 5184.

(9) (a) Fujita, M.; Tominaga, M.; Hori, A.; Therrien, B. *Acc. Chem. Res.* **2005**, *38*, 369. (b) Seidel, S. R.; Stang, P. J. *Acc. Chem. Res.* **2002**, *35*, 972.

(10) (a) Lusby, P. J.; Müller, P.; Pike, S. J.; Slawin, A. M. Z. *J. Am. Chem. Soc.* **2009**, *131*, 16398. (b) Chepelin, O.; Ujma, J.; Barran, P. E.; Lusby, P. J. *Angew. Chem., Int. Ed.* **2012**, *51*, 4194.

(11) (a) Fujita, M.; Oguro, D.; Miyazawa, M.; Oka, H.; Yamaguchi, K.; Ogura, K. *Nature* **1995**, *378*, 469. (b) Leininger, S.; Fan, J.; Schmitz, M.; Stang, P. J. *Proc. Natl. Acad. Sci. U.S.A.* **2000**, *97*, 1380.

(12) Carlise, J. R.; Wang, X.-Y.; Weck, M. *Macromolecules* **2005**, *38*, 9000.

(13) There are a possible four enantiomeric pairs plus two *meso* compounds. This, and the lower symmetry of all but the homochiral assemblies, leads to the complex ^{1}H NMR spectrum. Prolonged heating of the sample does not significantly alter the complex pattern of signals.

(14) Meng, W.; Clegg, J. K.; Thoburn, J. D.; Nitschke, J. R. *J. Am. Chem. Soc.* **2011**, *133*, 13652.

(15) (a) Schaffner-Hamann, C.; von Zelewsky, A.; Barbieri, A.; Barigelletti, F.; Muller, G.; Riehl, J. P.; Neels, A. *J. Am. Chem. Soc.* **2004**, *126*, 9339. (b) Coughlin, F. J.; Oyler, K. D.; Pascal, R. A.; Bernhard, S. *Inorg. Chem.* **2008**, *47*, 974. (c) Keene, F. R. *Dalton Trans.* **2011**, *40*, 2405. (d) Marchi, E.; Sinisi, R.; Bergamini, G.; Tragni, M.; Monari, M.; Bandini, M.; Ceroni, P. *Chem. Eur. J.* **2012**, *18*, 8765.

(16) Urban, R.; Krämer, R.; Mihan, S.; Polborn, K.; Wagner, B.; Beck, W. *J. Organomet. Chem.* **1996**, *517*, 191.

(17) The crystallographic data for this paper have been deposited as CCDC 888469, 888470, and 898757. These data can be obtained free of charge from The Cambridge Crystallographic Data Centre via www.ccdc.cam.ac.uk/data_request/cif.

(18) Coles, S. J.; Gale, P. A. *Chem. Sci.* **2012**, *3*, 683.

(19) (a) Brocker, E. R.; Anderson, S. E.; Northrop, B. H.; Stang, P. J.; Bowers, M. T. *J. Am. Chem. Soc.* **2010**, *132*, 13486. (b) Chan, Y.-T.; Li, X.; Soler, M.; Wang, J.-L.; Wesdemiotis, C.; Newkome, G. R. *J. Am. Chem. Soc.* **2009**, *131*, 16395. (c) Thiel, J.; Yang, D.; Rosnes, M. H.; Liu, X.; Yvon, C.; Kelly, S. E.; Song, Y.-F.; Long, D.-L.; Cronin, L. *Angew. Chem., Int. Ed.* **2011**, *50*, 8871. (d) Ujma, J.; De Cecco, M.; Chepelin, O.; Levene, H.; Moffat, C.; Pike, S. J.; Lusby, P. J.; Barran, P. E. *Chem. Commun.* **2012**, *48*, 4423.

(20) (a) Argent, S. P.; Adams, H.; Harding, L. P.; Ward, M. D. *Dalton Trans.* **2006**, *35*, 542. (b) Clever, G. H.; Tashiro, S.; Shionoya, M. *Angew. Chem., Int. Ed.* **2009**, *48*, 7010. (c) Riddell, I. A.; J. Smulders, M. M.; Clegg, J. K.; Hristova, Y. R.; Breiner, B.; Thoburn, J. D.; Nitschke, J. R. *Nature Chem.* **2012**, *4*, 860.

(21) (a) Mecozzi, S.; Rebek, J. *Chem. Eur. J.* **1998**, *4*, 1016. (b) Pluth, M. D.; Johnson, D. W.; Szigethy, G.; Davis, A. V.; Teat, S. J.; Oliver, A. G.; Bergman, R. G.; Raymond, K. N. *Inorg. Chem.* **2009**, *48*, 111. (c) Hristova, Y. R.; Smulders, M. M. J.; Clegg, J. K.; Breiner, B.; Nitschke, J. R. *Chem. Sci.* **2011**, *2*, 638.

(22) In $C_2D_2Cl_4$, $[Ir(ppy)_2(PhCN)_2]OTf$ appears to be in a 3:1 equilibrium with a monobenzonitrile species; addition of a small excess of PhCN (10 equiv) shifts the equilibrium so that $[Ir(ppy)_2(PhCN)_2]OTf$ is the sole complex in solution (see Figure S27).

(23) There are only a few reported air-equilibrated quantum yields for Ir complexes, see: (a) Plummer, E. A.; Hofstraat, J. W.; De Cola, L. *Dalton Trans.* **2003**, *22*, 2080. This is because they exhibit strong O_2 quenching, e.g., for the ubiquitous $[Ir(ppy)_3]$, $\Phi = 0.71$, $\Phi_{air} = 0.03$, see: (b) Ruggi, A.; Berenguel Alonso, M.; Reinhoudt, D. N.; Velders, A. H. *Chem. Commun.* **2010**, *46*, 6726.

(24) Flamigni, L.; Barbieri, A.; Sabatini, C.; Ventura, B.; Barigelletti, F. *Top. Curr. Chem.* **2007**, *281*, 143.

(25) Schmid, B.; Garces, F. O.; Watts, R. J. *Inorg. Chem.* **1994**, *33*, 9.